Collaborate Research Meeting of Institute of Mathematics for Industry &
MEXT collaborative workshop of mathematics and mathematical sciences
with various sciences and industrial technologies 2011

"Multiscale Mathematics: Hierarchy of collective phenomena and interrelations between hierarchical structures"

Center No1, Ito Campus, Kyushu University
December9-11, 2011

Contents

December 8, 2011

December 10, 2011

December 11, 2011

Preface

Joint Research Workshop of Institute of Mathematics for Industry (IMI), Kyushu University

"Multiscale Mathematics: Hierarchy of Collective Phenomena and Interrelations between Hierarchical Structures"

was held at Ito Campus, Kyushu University, Fukuoka, from 9th through 11th, December 2011. This activity was organized also as one of Collaborative Workshops of Mathematics and Mathematical Sciences with Various Sciences and Industrial Technologies supported by the Ministry of Education, Culture, Sports, Science & Technology in Japan (MEXT). This volume collects the papers of all the talks presented at the workshop.

The workshop was built around an interdisciplinary subject "multiscale phenomenon". The difficulty of various problems in the modern world, such as climate change, global economy crisis, syndrome of sever accidents in high-tech systems, etc., is rooted in their fundamental complexity caused by intricate combinations, over various scales, of multiple elements. Many attempts to explore "complex systems," creating a variety of interdisciplinary collaborations encompassing natural sciences, various technologies, economics and social sciences, still fall short to present a satisfactory discourse on "complexity".

At the core of complexity, we find commonly a collective phenomenon, on various scale hierarchy, of involved elements, which exhibits complicated and diverse behavior. A macro-scale system necessarily correlates with underlying micro- or meso- (=intermediate) scale structures. By nonlinear couplings among different hierarchies, a single hierarchy does not allow a closed mathematical modeling, without having to include other hierarchies. If we assume the complicated movement in a micro-scale world to be random, whereby we build a mathematical modeling merely by statistical averages and dispersions, we neglect enriched diversity of the collective phenomena and are led to an inappropriate evaluation which hides the hierarchical correlation between sub-systems of different scales. In reality, many of high-performance numerical simulations rely on uncertain parameters and ad-hoc models, and have left aside the most important features of collective phenomena, by simply calling them "an anomalous something". Among the topics left unsolved over many years are "turbulent viscosity", "anomalous resistance" and properties of various materials associated with fracture and sudden symptoms. It is our challenge to understand the multi-scale structure of dynamics of a macroscopic system constituted by a number of micro-scale elements, and then to build a mathematical model which is capable of prediction as well as evaluation, in order to reduce uncertainty and to raise the accuracy of description, for instance, of the internal state of the earth consisting of heterogeneous substances, of meteorology influenced by coupling of atmosphere with ocean and with space as well, and for design and control large-scale artificial matters with some complexities. To develop such an innovative model of complex systems, we will need a solid mathematical basis that is different from conventional mathematics directed primarily to simplicity.

The aim of this collaboration is to develop new mathematical methods for analyzing the nonlinearity of a collective system with a hierarchical structure from micro- to macro scales, and consider the possibility of controlling the phenomena in specific ways. As an ultimate goal, establishment of multi-scale mathematics is in our view.

The presentations were invited from the fields of plasma science, solid earth science, meteorology, fluids, simulation science, material science, economy (monetary models and market system). This workshop was successful, collecting 40 participants. They sought issues jointly tackled by mathematicians and mathematical scientists, and also the way for collaboration between simulation science and mathematics. We are grateful to all the speakers and the participants who made fruitful discussions. The support by the staff of the MEXT and by Ms. Junko Yanagihara of the IMI is also gratefully acknowledged.

Organizers

Yasuhide Fukumoto (Institute of Mathematics for Industry, Kyushu University)

Zensho Yoshida (Graduate School of Frontier Sciences, University of Tokyo)

平成23年度九州大学マス・フォア・インダストリ研究所共同利用研究集会

マルチスケール数学
集団現象の多階層性と階層の連関

文部科学省
平成23年度数学・数理科学と諸科学・産業技術の
連携研究のためのワークショップ

拡がっていく数学
～期待される“見えない力”！

講演者氏名	所属
Snezhana I. Abarzhi	University of Chicago
Philip J. Morrison	University of Texas at Austin
Vadimír Chalupecký	九州大学 マス・フォア・インダストリ研究所
青柳　岳司	旭化成(株) 基盤技術研究所
浅井　光輝	九州大学 工学研究科
石村　直之	一橋大学 経済学研究科
神谷　和也	東京大学 経済学研究科
篠田　正人	奈良女子大学 理学部
高木　周	東京大学 工学系研究科
田上　大助	九州大学 マス・フォア・インダストリ研究所
鳥海　光弘	海洋研究開発機構 横浜研究所
中川　淳一	新日鐵(株) 先端技術研究所
沼田　龍介	兵庫県立大学 シミュレーション学研究科
廣田　真	日本原子力研究開発機構
古川　勝	東京大学 新領域創成科学研究科
余田　成男	京都大学 理学研究科
吉田　善章	東京大学 新領域創成科学研究科

運営責任者

吉田善章　東京大学 新領域創成科学研究科
福本康秀　九州大学 マス・フォア・インダストリ研究所

2011.12.9 Fri 13:00
～12.11 Sun 12:30

九州大学伊都キャンパス　センター1号館 第一会議室

〒819-0395 福岡市西区元岡744番地

お問合せ先　九州大学 マス・フォア・インダストリ研究所
TEL：092-802-4402
E-mail:kyodo_riyou@imi.kyushu-u.ac.jp

Joint Research Workshop of Institute of Mathematics for Industry, Kyushu University &
MEXT Collaborative Workshop of Mathematics and Mathematical Sciences with Various Sciences and Industrial Technologies 2011

Multiscale Mathematics: Hierarchy of Collective Phenomena and Interrelations between Hierarchical Structures

Center No1, Ito Campus, Kyushu University

December 9

13:00-13:10	**Opening**
13：10-13：50	**Junichi NAKAGAWA** Mathematical Modelling for soil contamination — Creating an interdisciplinary platform for taking aim at mathematical innovation — Nippon Steel Corporation
13:50-14:30	**Masato SHINODA** Existence of phase transition of percolation on fractal lattices Nara Women's University
14:30-15:10	**Vladmir CHALUPECKY** A Multi-scale model of biogenic concrete corrosion Kyushu University
15:10-15:40	COFFEE BREAK
15:40-16:20	**Shu TAKAGI** Surfactant effect on the multiscale structure of bubbly flows The University of Tokyo
16:20-17:00	**Takeshi AOYAGI** Multiscale simulation for polymer material design Asahi Kasei Corporation
17:00-17:40	**Ryusuke NUMATA** Multiscale simulation of nonlinear phenomena of plasmas University of Hyogo

December 10

9:20-9:30	**Review of the 1st day**
9:30-10:10	**Philip J. MORRISON** On the Hamilton-Jacobi vatiational formulation of the Vlasov equation University of Texas at Austin
10:10-10:50	**Masaru FURUKAWA** A new solution method for singular perturbation problems in magnetized plasmas The University of Tokyo
10:50-11:00	COFFEE BREAK
11:00-11:40	**Mitsuteru ASAI** Multi-scale modeling in heterogeneous material properties Kyushu University
11:40-12:20	**Daisuke TAGAMI** Efficient numerical computations on large scale electromagnetic field problems using an iterative domain decomposition method Kyushu University
12:20-13:40	LUNCH
13:40-14:20	**Makoto HIROTA** Variational approach to multi-scale dynamical system — an application to collisionless magnetic reconnection — Japan Atomic Energy Agency
14:20-15:00	**Shigeo YODEN** Multiscale characteristics of moist conventions and heavy precipitation in the tropics Kyoto University
15:00-15:40	**Mitsuhiro TORIUMI** Dimension reduction study of microseismicity rate in the plate boundary zones JAMESTEC
15:40-16:10	COFFEE BREAK
16:10-17:40	**Panel Discussion** Toward a mathematical understanding of multi-scales and its application
18:00-20:00	**Banquet** Chinese Restaurant "Ten Ten" Ito Campus

December 11

9:20-9:30	**Review of the 2nd day**
9:30-10:10	**Naoyuki ISHIMURA** On the evolution of copula Hitotsubashi University
10:10-10:50	**Kazuya KAMIYA** Real indeterminacy of stationary equilibria in matching models with divisible money The University of Tokyo
10:50-11:00	COFFEE BREAK
11:00-11:40	**Snezhana I. ABARZHI** The effect of heterogeneities and noise on pattern formation and chaos development University of Chicago
11:40-12:20	**Zensho YOSHIDA** Self-organization in a foliated phase space The University of Tokyo
12:20-12:30	**Closing**

Mathematical Modeling for Soil Contamination: Creating an Interdisciplinary Platform for Taking Aim at Mathematical Innovation

Junichi Nakagawa

Advanced Technology Research Laboratories, Nippon Steel Corporation, 20-1 Shintomi, Futtsu-City, Chiba, 293-8511, JAPAN

E-mail address: nakagawa.junichi@nsc.co.jp

Abstract

Nippon Steel knows that mathematics is a very powerful language that can describe the essence of problems and has been creating an interdisciplinary platform for taking aim at technological innovation based on mathematics. For this platform, mathematicians and engineers have come together, contemplating social problems and taking voluntary actions.

The scientific topic is the issue of anomalous diffusion in soil. The approach is highly diverse, with a boundary that encompasses mathematics, engineering, and industry. The ultimate objective is to determine the microstructure of soil through averaged spatial data analysis, such as contaminant concentration, and to predict the progress of soil contamination.

It is often the case with mass diffusion in a porous medium such as soil that the numerical simulations using traditional advection diffusion equations fail to predict the observation results of a real phenomenon observed in the field or in laboratory tests. The numerical experiments using CTRW says that the mean squared displacement of particles grows in proportion to the fractional power of time.

The CTRW is linked with the fractional order PDE in terms of time. This means that anomalous diffusion depends on the degree of history to be retained from the initial time to the current time. The smaller alpha is, the more history will be retained. We can combine the physical meaning of alpha (that stems from possible obstacles that delay the particle's jump) with the mathematical reasoning.

Thus, how do we combine the microstructure with the mechanism for determining the value? What are the geometric invariants? How do we combine the geometric invariants with the PDE in a mathematical framework? These are our next targets. The current progress of our discussion will be presented using the following methods.

.

Introduction

The steel making process requires control of a diverse range of phenomena involving mathematical applications for problem solving and modeling.

"Mathematics for industry" is aimed at extracting universal fundamental principles behind various natural phenomena and engineering problems, and crystallizing them into mathematical structures, and is essential for applying mathematics for industrial technology.

A methodology based on the mathematical thinking enables us to construct mathematical models that describe the essence of a phenomenon selectively. Such mathematical models serve as important basis for understanding and controlling a phenomenon. When a mathematical model describes the essence of a phenomenon as simply and comprehensibly as possible (a minimum necessary model), it becomes easier for engineers and researchers from a variety of technical fields to study, and it becomes easier to conceive ideas that can lead to innovations.

Nippon Steel has globally collaborated with mathematicians for decades and resolved industrial problems by enhancing practical insights with mathematical reasoning. Engineers in Nippon Steel have learnt how to understand the phenomena in the steel-making process only by the rules of pure logic, not by a posteriori ad hoc ways. On the other hand, mathematicians in universities have learnt how to link mathematics with the physical reality of the phenomena.

As a result, the collaborative research is playing a major role in mathematical innovation to broaden the diverse range of applications in mathematics and cultivation in both industry and the field of mathematics.

Collaboration Style

Figure 1 shows our style of collaboration with engineers and mathematicians in the case of Nippon Steel and the University of Tokyo. We formed international task force teams made up of faculty members, post-doctoral fellows and doctor course students. Team members are selected flexibly to create a task force according to the characteristics of the task. Our collaboration is composed of six indispensable phases.

The first is "intuition and expertise" from industry. Intuition and expertise can be carried out exclusively by insight based on observation of phenomena in the manufacturing process. The insight should be enhanced by mathematical reasoning. The second is "communication." Communication is bilateral translations: the translation of phenomena to mathematics and the translation of mathematics to phenomena. Engineers in industry need to understand real problems on site, express them in the language of physics, and offer possible model equations to mathematicians. Mathematicians explore the underlying mathematics to the model equations. This forum for communication through the interpretation of phenomena is extremely important in order that engineers and mathematicians may reach a common understanding of the nature of the problem and the mathematical components. The third is “logical path.” This corresponds to the extraction of mathematical principles from phenomena. Better communication can create a more logical path. The fourth is “analysis of data.” This means reasonable and quantitative interpretation of observations carried out on site. This enables us to extract the essence of phenomena. The fifth is “manufacturing theory.” This means the integration of logical paths from viewpoints of operation and economic rationality on site. The last is “activation to mathematics.” Motivation for mathematicians has launched new mathematical research fields.

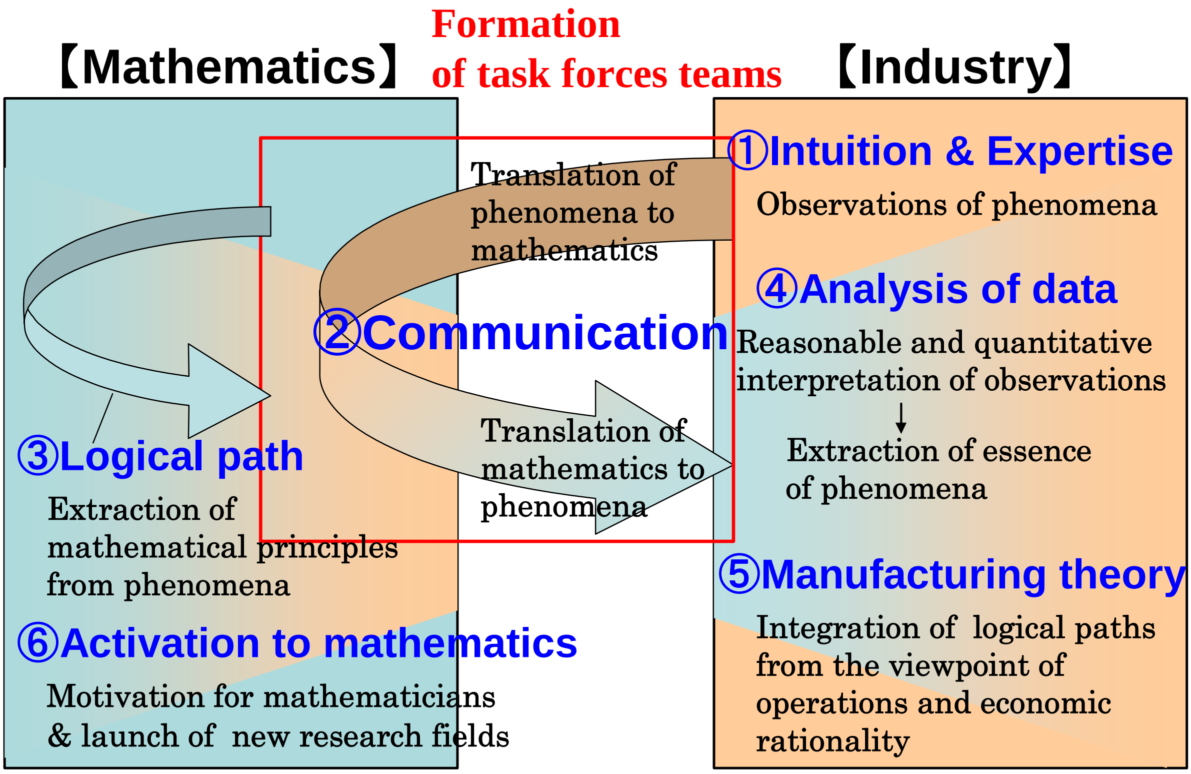

Fig.1 Collaboration with engineers and mathematicians in the case of Nippon Steel and the University of Tokyo

We, engineers in industry, have been eager to free ourselves from restrictions in our conventional thinking by making full use of mathematical reasoning that is free from specific industrial fields, through wider borderless collaborations. We have examined various conjectures by mathematicians and gained better practical solutions and further utilized analysis results. By repeating such phases of collaboration many times, we are able to pursue economic rationality, and mathematicians are able to find new results and describe them as theorem for future wider uses. It is important that mathematicians work not only for mathematical interests but also for the economic rationality through teamwork with engineers from a long-term point of view.

The cultivating interface between mathematics and industry has come into being as a forum for communication with the mathematicians mentioned above. Communication between the team members who are engineers in industry, and faculty members, post-doctoral fellows and doctor course students in university mathematical departments, has enhanced their communication skills day by day. As a result, several new themes have been launched.

Example of interdisciplinary collaboration

Figure 2 shows a challenge faced by Dr. Yuko Hatano. She is an associate professor affiliated with the University of Tsukuba whose major is Risk Engineering, and she had already collaborated with Nippon Steel on another subject.

The objective is to predict the progress of soil contamination. It is often the case with mass diffusion in a porous medium such as soil that numerical simulations using traditional advection diffusion equations fail to predict observation results of a real phenomenon observed in the field or laboratory tests. For instance, there are cases where actually the concentration is beyond the environmental standard as shown in Fig.3, even when a simulation indicates that the concentration of the pollutant is below the relevant environmental standard and the danger of soil pollution is unlikely. Diffusion not following the prediction based on such a simulation is called anomalous diffusion, in contrast to the traditional diffusion equations, and is often observed in different manners with various substances in the soil or atmosphere in the real environment.

The above is the kind of problem that we encounter when numerically simulating a soil system in which voids are distributed unevenly between particles, using a grid for calculation larger than the voids. This type of problem will not occur when the grid spacing is smaller than the voids between soil particles, for instance, about 0.1 mm. However, since several kilometers or more is the normal scale for environmental studies, in view of computer load the use of such a fine grid for a three-dimensional case is extremely difficult, and is practically unsuitable for on-line field analysis. Moreover, whereas a model test covers a time scale of as short as minutes to days, the prediction of a real environmental problem must deal with a time scale as large as a few years to tens of years.

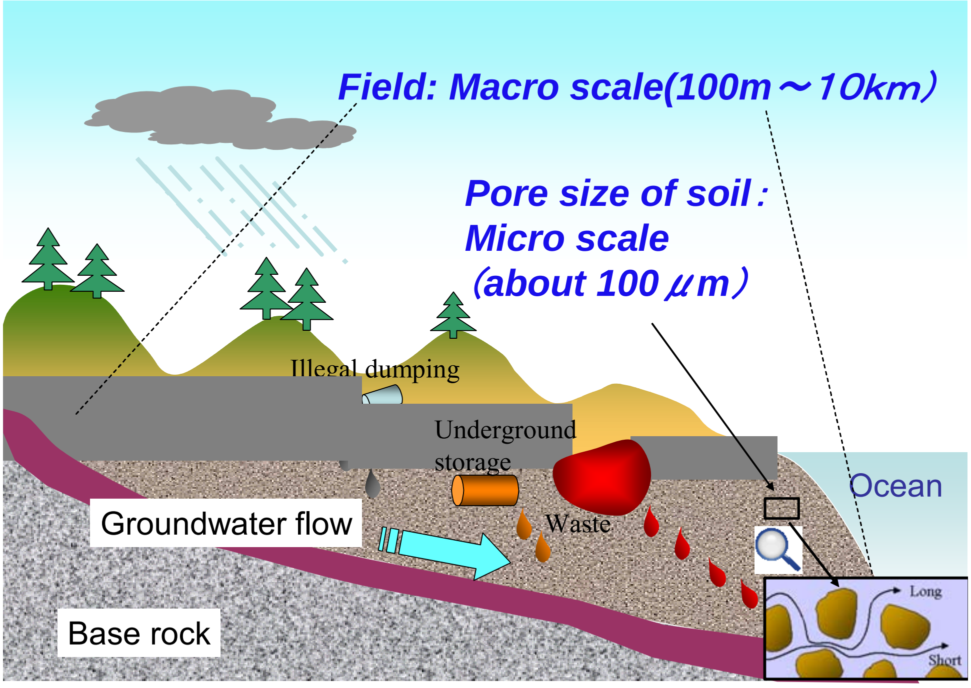

Fig.2 Prediction of soil contamination in large scale and long term

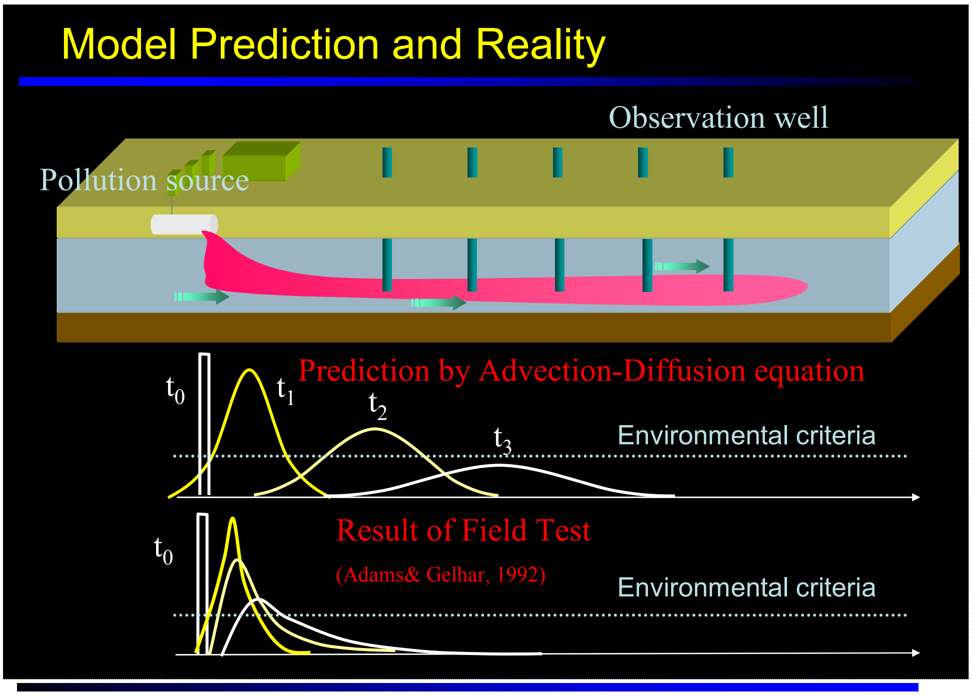

Model Prediction and Reality

Fig.3 Comparison between model prediction and results of field tests

Although we have to treat widely varied sizes of data obtained through physical and numerical tests based upon different scales of space and time, the scaling law allows us to combine those data together in accordance with principles of phenomena.

Large-scale numerical simulation is the principal method for the dynamic analysis of substances in any environmental medium: air, water or soil. Many detailed chemical and biochemical reactions are incorporated in the program codes for environmental simulation, and as a result, simulation programs seem to be becoming increasingly complicated these days. While a great number of numerical simulations are conducted on environmental issues, it is often difficult to tell whether each of such simulation results is valid, which fact is most serious for the problems.

Therefore the present study aims at dynamic prediction of environmental phenomena not totally depending on conventional numerical simulations but also employing mathematical methods typically such as scaling law. Toward this end, it is desirable to create a new field of environmental study involving mathematicians.

Launch of new research field in mathematics

A stochastic method employing random walk in consideration of the distribution of the waiting time of particles is used for describing mass transfer in soil. The stochastic method is called as CTRW that stands for Continuous Random Walk). The CTRW method has been effective when applied to the small space dealt with in laboratory tests, but the limitation on the number of particles is a bottleneck due to the limit of computer capacity, and thus the method cannot respond effectively to more pragmatic requirements of calculation in a larger volume of space.

On the other hand, some fields of physics and engineering employ numerical simulation based on a diffusion equation that includes a fractional-order derivative in time. While the concept of a fractional-order derivative can be traced back to as long ago as Leibniz (see [2]), a theory of partial differential equation that is applicable to such numerical simulation has not yet been established, and the application of such a method has so far been limited to very special cases where the space has only one dimension. It is reported in the literature [3] that, according to the scaling law to the effect that the root mean square of the displacement of particles is in proportion to time raised to the *k*th power (t^k), the stochastic method using the random walk mentioned earlier is closely related to the Fokker-Planck equation, which leads to a fractional-order derivative:

$$(\partial/\partial t)^k u(x, t) = \nabla \cdot (\kappa \nabla u(x, t)) - \mu \cdot \nabla u(x, t),$$

where u(x, t), κ and μ are the probability density function of particles, their diffusion coefficient, and mobility acting on them, respectively. It is expected that a scaling law combines stochastic methods such as the random-walk model for anomalous diffusion with the theory of partial differential equation including a fractional-order derivative to form a new field of research for mathematical concept and methodology. In [1], we discuss a related topic with such a theory.

Besides the above, Hatano et al. found that a formula empirically derived from two short-term atmospheric pollution cases (emission of inert gas Kr-85 from a nuclear plant in U.S.A. and the data of aerosol collected by an international team on global warming in the Arctic Ocean region) can describe the behavior of the pollutant of a long-term atmospheric pollution case (the accident of the Chernobyl Nuclear Power Plant) reasonably well [4], [5]. The formula is also written as a scaling law, but it is not yet been fully clarified why the formula has such a form.

Fig. 4 shows that CTRW is linked with the fractional order PDE in terms of time [6]. This means that anomalous diffusion depends on the degree of history to be retained from the initial time to the current time. The smaller α is, the more history will be retained. We can combine the physical meaning of alpha (that stems from possible obstacles that delay the particle's jump) with the mathematical reasoning.

Thus, how do we combine the microstructure with the mechanism for determining the value? What are the geometric invariants? How do we combine the geometric invariants with the PDE in a mathematical framework? These are our next targets. The current progress of our discussion will be presented using the following methods.

1. Analytical description for mathematically explaining the facts discovered by the experiments (a macro-scale viewpoint)
2. Characterization of the geometric features of the specimens of a 3D CT-image (a micro-scale viewpoint)
3. Deductive reasoning to derive a fractional differential equation using the homogenization method (a multi-scale viewpoint)

Thus, through the collaboration of mathematicians and engineers from both academic and industrial fields, the present study establishes the fundamental logical structure that lies behind the scaling law observed in the behavior of pollutants in different environmental media such as soil and atmosphere, and thus clarifying the universal characteristics of scaling law.

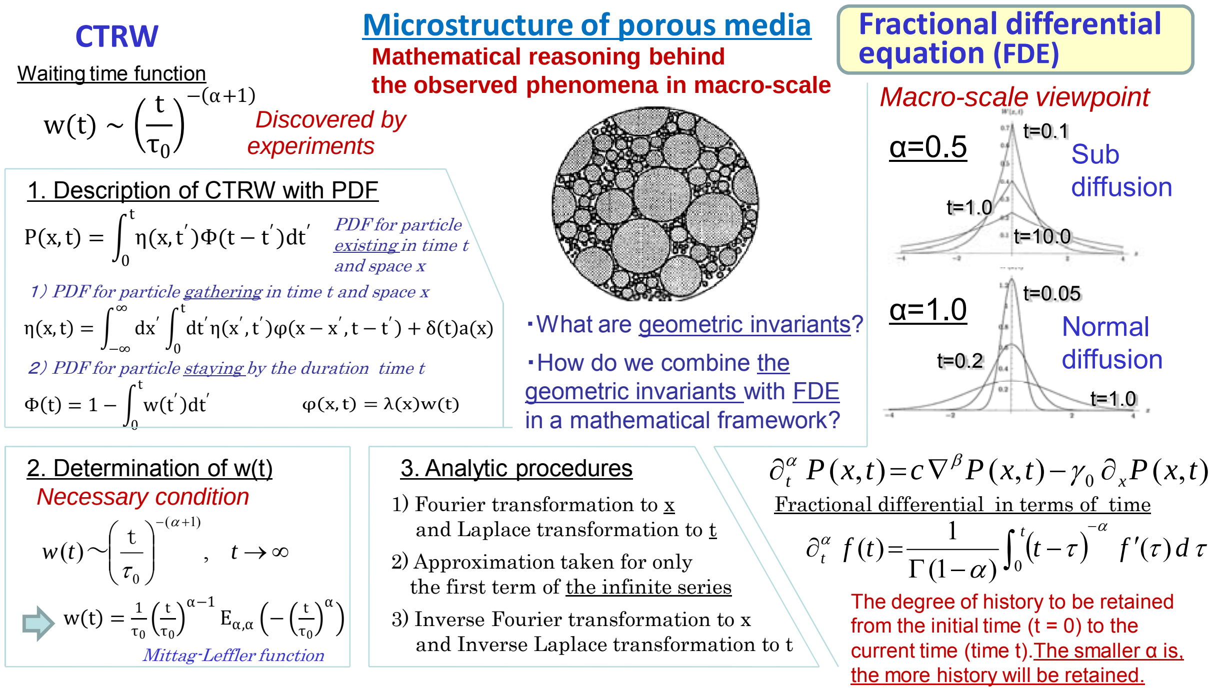

CTRW

Waiting time function

$$w(t) \sim \left(\frac{t}{\tau_0}\right)^{-(\alpha+1)}$$

Discovered by experiments

1. Description of CTRW with PDF

$$P(x,t) = \int_0^t \eta(x,t')\Phi(t-t')dt'$$

PDF for particle existing in time t and space x

1) PDF for particle gathering in time t and space x

$$\eta(x,t) = \int_{-\infty}^{\infty} dx' \int_0^t dt' \eta(x',t')\varphi(x-x',t-t') + \delta(t)a(x)$$

2) PDF for particle staying by the duration time t

$$\Phi(t) = 1 - \int_0^t w(t')dt' \qquad \varphi(x,t) = \lambda(x)w(t)$$

2. Determination of w(t)

Necessary condition

$$w(t) \sim \left(\frac{t}{\tau_0}\right)^{-(\alpha+1)}, \quad t \to \infty$$

$$\Rightarrow w(t) = \frac{1}{\tau_0}\left(\frac{t}{\tau_0}\right)^{\alpha-1} E_{\alpha,\alpha}\left(-\left(\frac{t}{\tau_0}\right)^{\alpha}\right)$$

Mittag-Leffler function

3. Analytic procedures

1) Fourier transformation to x and Laplace transformation to t
2) Approximation taken for only the first term of the infinite series
3) Inverse Fourier transformation to x and Inverse Laplace transformation to t

Microstructure of porous media

Mathematical reasoning behind the observed phenomena in macro-scale

- What are geometric invariants?
- How do we combine the geometric invariants with FDE in a mathematical framework?

Fractional differential equation (FDE)

Macro-scale viewpoint

$$\partial_t^{\alpha} P(x,t) = c\nabla^{\beta} P(x,t) - \gamma_0 \partial_x P(x,t)$$

Fractional differential in terms of time

$$\partial_t^{\alpha} f(t) = \frac{1}{\Gamma(1-\alpha)}\int_0^t (t-\tau)^{-\alpha} f'(\tau)d\tau$$

The degree of history to be retained from the initial time ($t = 0$) to the current time (time t). The smaller α is, the more history will be retained.

Fig. 4 Analytical descriptions for explaining mathematically the facts discovered by experiments

Future Plan

In industrial practice, a reduced-scale model is constructed to analyze a phenomenon that takes place in real-size equipment, significant physical values for the phenomenon in question are described by dimensionless numbers, and the dimensionless numbers obtained from the model analysis are made to match with those of real-size equipment. This matching operation secures the similarity of the dynamic physical values between the model and real-size equipment. This similarity refers also to the scaling law. It has been found from the above viewpoint of scaling law that, in addition to the physical values such as time and length which have been conventionally used for scaling up, the fractional powers in the differentiation of time and space are essential. This means that mathematics is expected to present a new “angle of view” for the scaling law that deals with inhomogeneous media. Practically, environmental analysis deals with a scale of several kilometers or more in size. In this relation, establishment of scaling laws including an a priori choice of an exponent will make it possible to appropriately use results obtained through reduced-scale tests and clarify a real phenomenon across a large space.

By establishing scaling laws and developing mathematical methods based thereon, we can significantly reduce costs for producing high-quality products as well as energy consumption and CO_2 emission by improving production efficiency in various problems of manufacturing industries such as monitoring of sintering processes, reactions in a blast furnace, and other metallurgical reactions in steel-making processes as shown in Fig.5.

Scaling laws and mathematical methods are applicable also to a wide variety of fields such as chemical engineering, mechanical engineering, geotechnical engineering, biotechnology, etc., and therefore, the establishment of such scaling laws is expected to be useful in remarkably accelerating the development of science and technology through the solution of important industrial problems.

Furthermore, the concept of scaling law combining micro- and macroscopic aspects is closely related to that of multi-scale modeling, the application of which is rapidly expanding in material science, chemistry, and other widely varied fields. The present study is expected to lead to proposals of new mathematical concepts and methodologies for multi-scale modeling, bringing about new problem recognition and methodology to mathematics.

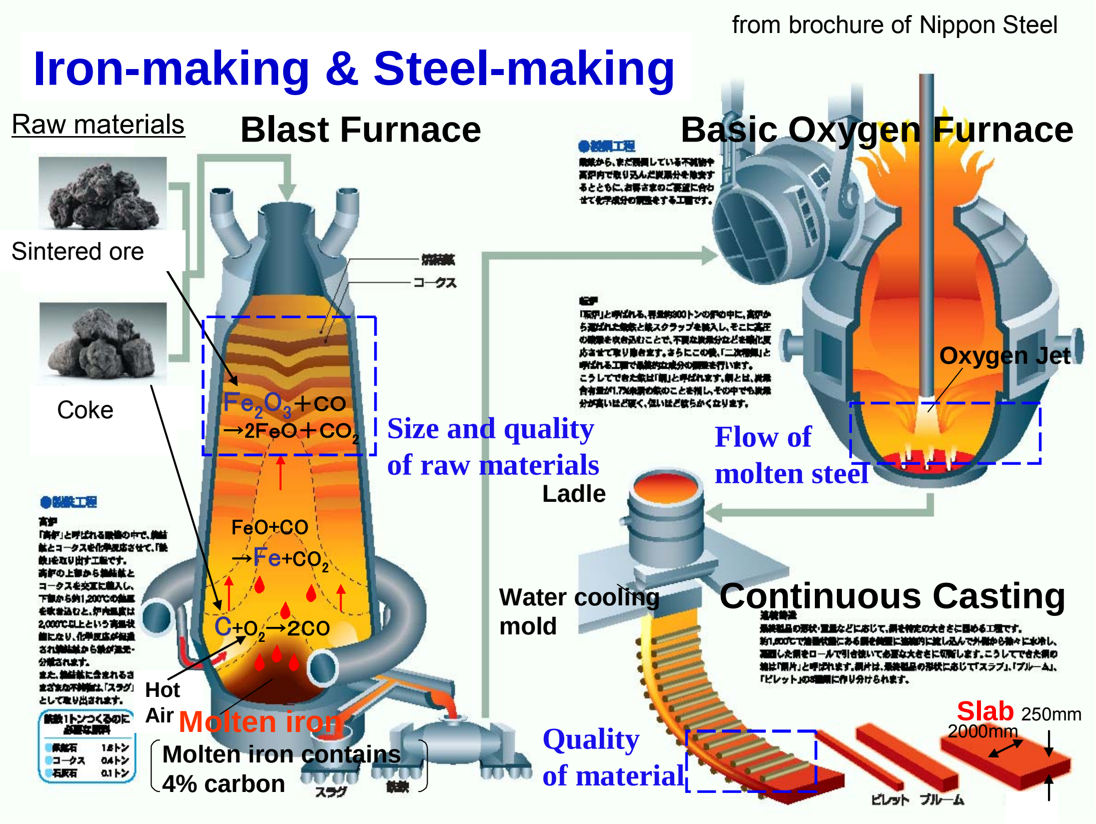
from brochure of Nippon Steel

Fig.5 Example of inhomogeneous media in iron making and steel making process

“Mathematics for indutry” will be the key for combining mathematics with industrial technology. Mathematical science can be understood as mathematics for phenomena; it is aimed at extracting fundamental principles behind different natural phenomena and engineering problems, and crystallizing them into mathematical structures.

Beyond the simple numerical operation of physical model equations, a methodology based on the principles and rules of mathematics makes it possible to construct mathematical models that describe the essence of a phenomenon selectively. Such mathematical models serve as important basis for understanding and controlling a phenomenon. When a mathematical model describes the essence of a phenomenon as simply and comprehensibly as possible (a minimum necessary model), it becomes easier for engineers and researchers from a variety of technical fields to study, and it becomes easier to conceive ideas that can lead to innovations.

In order to construct such a minimum necessary mathematical model that describes the essence of a phenomenon efficiently, a framework is required for the joint work of mathematicians and engineers from academic and industrial fields where they can thoroughly discuss subject phenomena and define suitable targets and milestones for different study stages. In addition, it is indispensable to mutually confirm work progress. At present, however, applied mathematics in Japan, compared with other developed countries, seems to lack such teamwork experience that helps to combine a phenomenon with mathematical methodology. In order to solve a problem as promptly as required in industry, it is too late to begin studying methodology after posing of the problem. It is necessary to continue to improve the skill to combine a phenomenon with mathematical methodology for its prompt application, and in this respect, each individual must improve their qualification to be "the right person" who can meet the above conditions and the role.

It is desirable that both mathematics and industry foster people capable of working jointly with each other from the viewpoint of "mathematics for phenomena" through academic-industrial collaboration. Towards this end, it is necessary to create a new framework independent of the structure of present industry and academic organizations. We must reinterpret and reconstruct the fundamental concept of manufacturing based on field practice, which constitutes the competitive edge in developed countries, from the standpoint of mathematical methodology while learning about interdisciplinary collaboration from abroad. By so doing, we will be able to command the most advanced industrial technology of the world.

References

[1] Cheng, J., Nakagawa, J., Yamamoto, M., Yamazaki, T.,

Uniqueness in an inverse problem for one-dimensional fractional diffusion equation, to appear in "Inverse Problems" (2009).

[2] Podlubny, I., Fractional Differential Equations, Academic Press, San Diego, 1999

[3] Sokolov, I, M., Klafter J., Blumen A., “Fractional Kinetics,” Physics Today, November 2002, pp. 48-54.

[4]Y. Hatano and N. Hatano: “Aeolian migration of radioactive dust in Chernobyl,” Zeitschrift fur Geomorphologie, 116 (1999) pp. 45-58.

[5]Y. Hatano and N. Hatano, Fractal fluctuation of aerosol migration near Chernobyl. Atmospheric Environment, 31, 2297-2303 (1997).

[6] J. Nakagawa, K. Sakamoto, M. Yamamoto, Overview to mathematical analysis for fractional diffusion equations-new mathematical aspects motivated by industrial collaboration, Journal for Math-for-industry, Vol.1 (2009B-9), 00.157-163

Existence of phase transition of percolation on fractal lattices

Masato SHINODA*
Faculty of science, Nara Women's University

Abstract

We study several bond percolation models on Sierpinski carpet lattices, which is a class of graphs corresponding to generalized Sierpinski carpets. In this paper we give some sufficient conditions for the existence of phase transition of percolation on the lattices.

1 Introduction

Percolation is studied as a very important subject in statistical mechanics because this is one of the simplest models which contains phase transitions of disordered media. Percolation has close relations to disordered electrical networks, ferromagnetism, epidemic models and so on. Percolation models were proposed by Broadbent-Hammersley [BH57], and have been well studied in the last forty years. See Grimmett [G99] to view the whole of this field.

We consider percolation on *fractal lattices*. Fractal lattices are graphs which correspond to fractals. All of them have a kind of self-similarity, but most of them have no translation invariances. Especially we study bond percolation, oriented percolation and stiff percolation on Sierpinski carpet lattices. In percolation model each bond is open with probability p and closed otherwise, independently of all other bonds. We think of open bonds as connections of vertices. The Sierpinski carpet lattice (that is a typical example of Sierpinski carpet lattices) and a sample configuration is shown in Figure 1. As for percolation on the Sierpinski carpet lattice, the following facts are known.

- There exists a phase transition of percolation. [K97]
- There exists no phase transition of oriented percolation. [S03]

In this paper we give a brief review about the existence of phase transition of percolation on fractal lattices. In Section 2 we define bond percolation on generalized Sierpinski carpet lattices and we show some sufficient conditions for the existence of phase transition. We also give an improved upper bound of the critical probability of

---

*e-mail:shinoda@cc.nara-wu.ac.jp

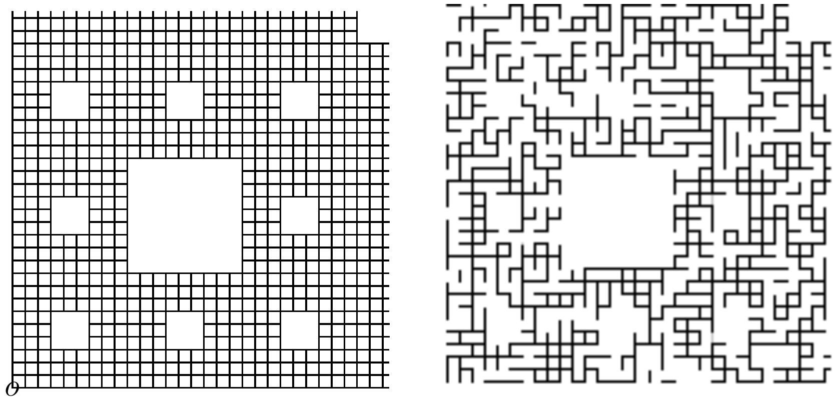

Figure 1: Bond percolation on the Sierpinski carpet lattice

bond percolation on the Sierpinski carpet lattice. In Section 3 we consider oriented percolation and stiff percolation. In these percolation models, going to certain directions are prohibited. We show sufficient conditions for the non-existence of phase transition. In section 4 we give proofs of some theorems.

2 Bond percolation on Sierpinski carpet lattices

We explain two well-known examples of fractals, *the Sierpinski gasket* and *the Sierpinski carpet*. The former is a *finite* ramified fractal (that is, it can be disconnected by removing a finite number of points) and the latter is an *infinite* ramified fractal. See Mandelbrot [M82] for details of fractals. In [S96] we analysed percolation on the Sierpinski gasket lattice, which has no phase transition. The non-existence of phase transition is induced by the character of finite ramified fractals.

Now we focus on Sierpinski carpet lattices. We define the Sierpinski carpet and generalized Sierpinski carpets on $\mathbb{R}^2$ as follows. Set $L \geq 2$ to be an integer and set $\mathbf{T}_L = \{0, 1, \ldots, L-1\}^2$. For $(i, j) \in \mathbf{T}_L$, we set an affine map $\Psi_{(i,j)}$ from $[0,1]^2$ to $[i/L, (i+1)/L] \times [j/L, (j+1)/L]$ which preserves the directions. For a nonempty subset $T \subset \mathbf{T}_L$, it is well-known (see Falconer [F85], for example) that there exists a unique nonempty compact set $K_T \subset [0,1]^2$ which satisfies the equation

$$K_T = \bigcup_{t \in T} \Psi_t(K_T).$$

We call these K_T's generalized Sierpinski carpets. The Sierpinski carpet is an element of generalized Sierpinski carpets.

Example 2.1 Set $L = 3$ and $T = \mathbf{T}_3 \setminus \{(1,1)\}$. K_T is the Sierpinski carpet.

We remark that the Sierpinski gasket is also an element of generalized Sierpinski carpets.

Example 2.2 Set $L = 2$ and $T = \mathbf{T}_2 \setminus \{(1,1)\}$. K_T is the Sierpinski gasket.

Let us define the graph corresponding to K_T. Set

$$F_T^n = \bigcup_{t_1,t_2,\cdots,t_n \in T} \Psi_{t_1} \circ \Psi_{t_2} \circ \cdots \circ \Psi_{t_n}([0,1]^2).$$

K_T can be constructed as the limit of F_T^n. Set a graph $G_T^n = (V(G_T^n), E(G_T^n))$ where $V(G_T^n) = \mathbb{Z}^2 \cap L^n F_T^n$ and $E(G_T^n) = \{\langle u,v\rangle : u,v \in V(G_T^n), |u-v|_1 = 1\}$. Here we write $\langle u,v\rangle$ as a bond with endvertices u and v. From now on we assume through this paper that K_T is connected and

$$(0,0) \in T. \tag{1}$$

Under these assumptions we set $G_T = \bigcup_{n=1}^{\infty} G_T^n$. That is, $V(G_T) = \bigcup_{n=1}^{\infty} V(G_T^n)$ and $E(G_T) = \bigcup_{n=1}^{\infty} E(G_T^n)$. Note that $V(G_T^n)$ and $E(G_T^n)$ are increasing sequences with respect to n under (1). We call the family of G_T corresponding K_T's *generalized Sierpinski carpet lattices. The Sierpinski carpet lattice* given in Figure 1 is an example of generalized Sierpinski carpet lattices, and we sometimes denote the graph by S.C..

We consider bond percolation on G_T. Set $0 \le p \le 1$. Each $e \in E(G_T)$ is declared to be *open* with probability p and *closed* with probability $1-p$ independently. We denote the product measure by P_p. Let us consider a sequence of vertices $\pi = (v_0, v_1, \cdots, v_m)$ where $v_i \in V(G_T)$ for $0 \le i \le m$. We say π is a *path* when $\langle v_{i-1}, v_i\rangle \in E(G_T)$ for $1 \le i \le m$ and $v_i \ne v_j$ for $i \ne j$. We write $u \leftrightarrow v$ if and only if there exists a path π with $v_0 = u$, $v_m = v$ and $\langle v_{i-1}, v_i\rangle$ are open for $1 \le i \le m$. We write $C(v) = \{u \in V(G_T) | v \leftrightarrow u\}$. We define $\theta(p) = P_p(|C(o)| = \infty)$ where o is the origin and $|C(o)|$ is the number of vertices in $C(o)$. Let $p_c(G_T) = \inf\{p : \theta(p) > 0\}$. We study the problem of finding necessary and sufficient conditions for $p_c(G_T) < 1$. Häggström [H00] showed that if the maximum degree of the vertices is finite then the existence of phase transitions of bond percolation, site percolation and the Ising model are equivalent. So we can consider the critical phenomena of bond, site percolation or the Ising model on Sierpinski carpet lattices simultaneously.

The difficulty of this problem is that we can not apply Peierl's argument (see [G99], for example) because the ratio of the holes of G_T tends to 1. In the case of $L = 2$, we can completely answer the problem; $P_c(G_T) < 1$ if and only if $T = \mathbf{T}_2$. Hereafter we assume $L \ge 3$. In [K97] Kumagai obtained a sufficient condition for this problem. Set $\partial_{int}\mathbf{T} = \{(0,j) : 0 \le j \le L-1\} \cup \{(L-1,j) : 0 \le j \le L-1\} \cup \{(i,0) : 0 \le i \le L-1\} \cup \{(i,L-1) : 0 \le i \le L-1\}$.

Theorem 2.3 ([K97]) *If* $\partial_{int}\mathbf{T} \subset T$, *then* $p_c(G_T) < 1$.

In [S02] we gave a weaker condition than the theorem above. We write $T_l = \{j : (0,j) \in T\}$, $T_r = \{j : (L-1,j) \in T\}$, $T_d = \{i : (i,0) \in T\}$ and $T_u = \{i : (i,L-1) \in T\}$. We say T *is connected* if for any $t, t' \in T$ there exists a sequence $t_1 = t$, t_2, ..., $t_n = t'$ which satisfies $t_i \in T$ and $|t_i - t_{i+1}|_1 = 1$ for $1 \le i \le n-1$.

Theorem 2.4 ([S02]) *Assume*

$$T \setminus \{t\} \text{ is connected for any } t \in T \tag{2}$$

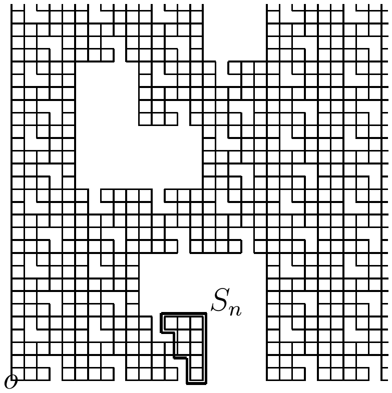

Figure 2: G_T for $T = \mathbf{T}_5 \setminus \{(1,3),(1,4),(2,1),(2,3),(3,0),(3,1)\}$

and

$$|T_l \cap T_r| \geq 2 \text{ and } \ |T_d \cap T_u| \geq 2. \tag{3}$$

Then $p_c(G_T) < 1$.

A proof of this theorem was given in [S02]. $\partial_{int}\mathbf{T}$ satisfies (2) and (3), so this theorem contains Theorem 2.3. There are some examples to which Theorem 2.4 is applicable and Theorem 2.3 is not.

Example 2.5 Set $L \geq 3$ and $T = \{(i,j) \in \mathbf{T}_L : i \in \{0,1\} \text{ or } j \in \{0,1\}\}$. Theorem 2.3 is not applicable to this graph. We see $p_c(G_T) < 1$ from (2) and (3).

We note the existence of phase transition on general graphs. For a general connected graph G, we define *isoperimetric dimension* $\mathrm{Dim}(G)$ by

$$\mathrm{Dim}(G) = \sup\Big\{D > 0 : \inf \frac{|\partial S|}{|S|^{\frac{D-1}{D}}} > 0\Big\}$$

where S is a finite connected subset of the bonds of G and ∂S is the outer boundary of S. For example $\mathrm{Dim}(\mathbb{Z}^d) = d$, and $\mathrm{Dim}(\mathrm{S.C.}) = 3/2$ (See [Os90]). We hope to clarify the relation between $\mathrm{Dim}(G)$ and $p_c(G)$. In [BS96], Benjamini and Schramm proposed the problem of whether $\mathrm{Dim}(G) > 1$ implies $p_c(G) < 1$. We check this problem in the case of Sierpinski carpet lattices. Now we can say only that it seems that $\mathrm{Dim}(G_T) > 1$ implies $p_c(G_T) < 1$, but we do not yet have the proof, and $\mathrm{Dim}(G_T) = 1$ does not imply $p_c(G_T) = 1$.

Example 2.6 Set $L = 5$ and $T = \mathbf{T}_5 \setminus \{(1,3),(1,4),(2,1),(2,3),(3,0),(3,1)\}$. In this case $\mathrm{Dim}(G_T) = 1$ because we can take $\{S_n\}$ as in Figure 2 to satisfy $|\partial S_n| = 2$. On this graph $p_c(G_T) < 1$. In this example the component corresponding to $(2,0)$ seems a dangling subgraph, but if we delete $(2,0)$ from T then $p_c(G_T) = 1$.

As for the Sierpinski gasket lattice, we showed that $p_c(\mathrm{S.C.}) < 0.9224$ in [S02]. $p_c(\mathrm{S.C.}) \sim 0.56$ is suggested by numerical simulations ([Ot12]). In this paper we show the following estimate.

Theorem 2.7

$$p_c(\text{S.C.}) < 0.7.$$

We will give a proof of this estimate in Section 4.

3 Oriented percolation on the Sierpinski carpet lattice

In this section we study oriented percolation and stiff percolation on the Sierpinski carpet lattice. We give a partial order on $\mathbb{Z}^2$ such that $(x_1, x_2) \le (y_1, y_2)$ if and only if $x_1 \le y_1$ and $x_2 \le y_2$. We say $\pi = (v_0, v_1, \ldots, v_m)$ is an *oriented path* when π is a path and $v_{i-1} \le v_i$ for $1 \le i \le m$. We write $u \to v$ if and only if there exists an oriented path π with $v_0 = u$, $v_m = v$ and $\langle v_{i-1}, v_i \rangle$ are open for $1 \le i \le m$. We define $\overrightarrow{C}(v) = \{u \in V(G_T) |\ v \to u\}$, $\overrightarrow{\theta}(p)$ and $\overrightarrow{p_c}(G_T)$ as before.

Oriented percolation is also significant as a model of disordered media because it has close relations to media of semiconductors, contact processes and so on. On $\mathbb{Z}^2$ we may regard this model as a one-dimensional contact process in discrete time. See Durrett [D84] and [G99] for details. On $\mathbb{Z}^d$ $(d \ge 2)$, it is well-known that the critical probability $p_c(\mathbb{Z}^d)$ of percolation and that $\overrightarrow{p_c}(\mathbb{Z}^d)$ of oriented percolation are strictly less than 1. In particular, $p_c(\mathbb{Z}^2) = 1/2$ has been shown by Kesten [K97] and $\overrightarrow{p_c}(\mathbb{Z}^2) \le 2/3$ has been shown by Liggett [L95]. We devote to determine the critical probability of oriented percolation on the Sierpinski carpet lattice. By definition $p_c(\text{S.C.}) \le \overrightarrow{p_c}(\text{S.C.})$ is clear.

Let a and b be positive integers. We write $L = 2a + b$. Set

$$T_{a,b} = \mathbf{T}_L \backslash \Big\{ (x_1, x_2) \in \{0, 1, \ldots, L-1\}^2 \ \Big|\ a \le x_1 \le a+b-1 \text{ and } a \le x_2 \le a+b-1 \Big\}.$$

Generalized Sierpinski carpet lattice $G_{T_{a,b}}$ is determined by $T_{a,b}$ in the same way as in Section 2. We write abbreviately $G_{a,b}$ instead of $G_{T_{a,b}}$. We remark that $G_{1,1}$ is the Sierpinski carpet lattice. We showed the following theorem.

Theorem 3.1 ([S03]) *If $a \le b$, then $\overrightarrow{p_c}(G_{a,b}) = 1$. In particular, $\overrightarrow{p_c}(\text{S.C.}) = 1$.*

A proof of Theorem 3.1 was shown in [S03]. This result is interesting because it shows a remarkable difference between the Sierpinski carpet lattice and $\mathbb{Z}^2$ lattice. This theorem says that there exists no phase transition of oriented percolation on the Sierpinski carpet lattice, in spite of the existence of phase transition of percolation on the graph. It says also that the contact process will die out if $p < 1$ on the Sierpinski carpet lattice. We do not know whether $\overrightarrow{p_c}(G_{a,b}) = 1$ for *all* a and b. This is a significant open problem.

As an intermediate probabilistic model between percolation and oriented percolation, we introduce *stiff* percolation. For (x_1, x_2) and (y_1, y_2) we write $(x_1, x_2) \preceq (y_1, y_2)$ if and only if $x_1 \le y_1$. We say $\pi = (v_0, v_1, \ldots, v_m)$ is an *stiff path* when π is a path and $v_{i-1} \preceq v_i$ for $1 \le i \le m$. We write $u \rightsquigarrow v$ if and only if there exists an stiff path π with $v_0 = u$, $v_m = v$ and $\langle v_{i-1}, v_i \rangle$ are open for $1 \le i \le m$. We define $\tilde{\theta}(p)$ and $\tilde{p_c}(G_T)$ as usual. We prove the following theorem.

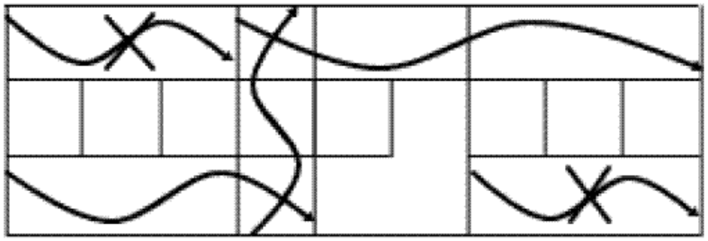

Figure 3: The event C_n

Theorem 3.2 *If* $L \geq 4$*, then* $\tilde{p_c}(G_{1,L-2}) = 1$.

This theorem says that there is no phase transition of stiff percolation on Sierpinski carpet lattices if the ratio of its hole is large enough. We shall give a proof of this theorem in the next section.

4 Proof of theorems

In the beginning of this section we give a proof of Theorem 2.7. Here we consider bond percolation on the Sierpinski carpet lattice, and we set $T = \mathbf{T}_3 \setminus \{(1,1)\}$. For a rectangle $R \subset \mathbb{R}^2$, we say *left-right crossing* (respectively *bottom-top crossing*) of R exists if $u \leftrightarrow v$ in R for some u on the left (respectively lower) side of R and some v on the right (respectvely upper) side of R. We denote this event by $LR(R)$ (respectively $BT(R)$). This event depends only on the bonds in R. For a positive integer k, we write $\psi_k^n(p) = P_p(LR([0, k \cdot 3^n] \times [0, 3^n]))$. Note that

$$\psi_{k_1+k_2}^n(p) \leq \psi_{k_1}^n(p)\psi_{k_2}^n(p) \tag{4}$$

for any k_1, k_2. For the proof of Theorem 2.7, we use the following lemma.

Lemma 4.1 *Let* $f(x) = 1 - (1-x^5)^2 + 2x^{\frac{19}{3}}(1-x)^2$*. Then*

$$\psi_3^{n+1}(p) \geq f(\psi_3^n(p)). \tag{5}$$

Proof of Lemma 4.1. We define the following events.

$$\begin{aligned}
A_n &= LR([0, 3^{n+1}] \times [0, 3^{n-1}]),\\
B_n &= LR([0, 3^{n+1}] \times [2 \cdot 3^{n-1}, 3^n]),\\
C_n &= LR([0, 4 \cdot 3^{n-1}] \times [0, 3^{n-1}]) \cap BT([3^n, 4 \cdot 3^{n-1}] \times [0, 3^n])\\
&\quad \cap LR([3^n, 3^{n+1}] \times [2 \cdot 3^{n-1}, 3^n]) \cap LR([0, 3^n] \times [2 \cdot 3^{n-1}, 3^n])^c\\
&\quad \cap LR([2 \cdot 3^n, 3^{n+1}] \times [0, 3^{n-1}])^c,\\
D_n &= LR([0, 4 \cdot 3^{n-1}] \times [2 \cdot 3^{n-1}, 3^n]) \cap BT([3^n, 4 \cdot 3^{n-1}] \times [0, 3^n])\\
&\quad \cap LR([3^n, 3^{n+1}] \times [0, 3^{n-1}]) \cap LR([0, 3^n] \times [0, 3^{n-1}])^c\\
&\quad \cap LR([2 \cdot 3^n, 3^{n+1}] \times [2 \cdot 3^{n-1}, 3^n])^c.
\end{aligned}$$

See Figure 3 for the event C_n. Then we have

$$\begin{aligned}
P_p(A_n) \ \geq\ & P_p\big(LR([0,3^n]\times[0,3^{n-1}])\cap LR([2\cdot 3^{n-1},5\cdot 3^{n-1}]\times[0,3^{n-1}])\\
&\cap LR([4\cdot 3^{n-1},7\cdot 3^{n-1}]\times[0,3^{n-1}])\cap LR([2\cdot 3^{n},3^{n+1}]\times[0,3^{n-1}])\\
&\cap BT([2\cdot 3^{n-1},3^n]\times[0,3^{n-1}])\cap BT([4\cdot 3^{n-1},5\cdot 3^{n-1}]\times[0,3^{n-1}])\\
&\cap BT([2\cdot 3^{n},7\cdot 3^{n-1}]\times[0,3^{n-1}])\big)\\
\geq\ & \{\psi_3^n(p)\}^4\{\psi_1^n(p)\}^3\\
\geq\ & \{\psi_3^n(p)\}^5
\end{aligned}$$

and

$$\begin{aligned}
P_p(C_n) \geq\ & P_p\big(LR([0,3^n]\times[0,3^{n-1}])\cap LR([2\cdot 3^{n-1},4\cdot 3^{n-1}]\times[0,3^{n-1}])\\
&\cap BT([2\cdot 3^{n-1},3^n]\times[0,3^{n-1}])\cap BT([3^n,4\cdot 3^{n-1}]\times[0,3^{n}])\\
&\cap LR([3^n,2\cdot 3^n]\times[2\cdot 3^{n-1},3^n])\cap LR([5\cdot 3^{n-1},7\cdot 3^{n-1}]\times[2\cdot 3^{n-1},3^n])\\
&\cap LR([2\cdot 3^n,3^{n+1}]\times[2\cdot 3^{n-1},3^n])\cap BT([5\cdot 3^{n-1},2\cdot 3^n]\times[2\cdot 3^{n-1},3^n])\\
&\cap BT([2\cdot 3^n,7\cdot 3^{n-1}]\times[2\cdot 3^{n-1},3^n])\cap LR([0,3^n]\times[2\cdot 3^{n-1},3^n])^c\\
&\cap LR([2\cdot 3^n,3^{n+1}]\times[0,3^{n-1}])^c\big)\\
\geq\ & \{\psi_3^n(p)\}^4\{\psi_2^n(p)\}^2\{\psi_1^n(p)\}^3\{1-\psi_3^n(p)\}^2\\
\geq\ & \{\psi_3^n(p)\}^{\frac{19}{3}}\{1-\psi_3^n(p)\}^2
\end{aligned}$$

by (4) and FKG inequality. We note that $A_n\cup B_n, C_n, D_n$ are mutually exclusive events. Combining

$$P_p(LR([0,3^{n+1}]\times[0,3^n])\geq P_p(A_n\cup B_n)+P_p(C_n)+P_p(D_n)$$

and $P_p(C_n)=P_p(D_n)$, we obtain (5). $\square$

The equation $f(x)=x$ has a solution $\alpha=0.94679\cdots$, and f is an increasing function with respect to x. If we can find N which satisfies $\psi_3^N(p)>\alpha$, then $\psi_3^{n+1}(p)>\psi_3^n(p)$ for any $n\geq N$ and we obtain $\lim_{n\to\infty}\psi_3^n(p)=1$. We shall show $\psi_3^2(7/10)>\alpha$. We consider *stiff* percolation in $R_n=[0,3^{n+1}]\times[0,3^n]$. Let

$$\tilde{\psi}^n(p)=P_p(\text{there exists an open stiff left-right crossing of } R_n).$$

Trivially $\tilde{\psi}^n(p)\leq\psi_3^n(p)$. For $0\leq i\leq 3^{n+1}$ and $0\leq j\leq 3^n$ we define a random variable $X_i^j\in\{0,1\}$ such that $X_i^j=1$ if and only if $v\rightsquigarrow(i,j)$ in R_n for some v on the left side of R_n. We write $\mathbf{X}_i=(X_i^0,X_i^1,\ldots,X_i^{3^n})$, and we regard $\{\mathbf{X}_i\}_{0\leq i\leq 3^{n+1}}$ as a Markov chain on the state space $\{0,1\}^{\{0,1,\ldots,3^n\}}$, which starts from $\mathbf{X}_0=(1,1,\ldots,1)$. Then we see

$$\tilde{\psi}^n(p)=P_p\left(\mathbf{X}_{3^{n+1}}\neq(0,0,\ldots,0)\right).$$

We can obtain $\tilde{\psi}^3(7/10)>\alpha$ by direct calculations, by using of the transition matrix of $\mathbf{X}_i$. $\square$

Next we give a proof of Theorem 3.2 in the case of $L = 4$. Set $T = \mathbf{T}_4 \setminus \{(1,1),(1,2),(2,1),(2,2)\}$. Let $G_T^{n,a,b}$ be the union of $a \times b$ copies of G_T^n. We write

$$\begin{aligned}\tilde{x}_{n,a,b}(p) &= P_p(\text{ there exists an open stiff left-right crossing of } G_T^{n,a,b}),\\ \tilde{y}_{n,a,b}(p) &= P_p(\text{ there exists an open stiff bottom-top crossing of } G_T^{n,a,b}).\end{aligned}$$

We shall show $\lim_{n\to\infty} \tilde{x}_{n,1,1}(p) = 0$ and $\lim_{n\to\infty} \tilde{y}_{n,1,1}(p) = 0$ for any $p < 1$. We use the following lemmas to prove.

Lemma 4.2 *For any $p < 1$ there exists $\varphi = \varphi(p) > 0$ such that*

$$\tilde{y}_{n,1,1}(p) \le e^{-4^n \varphi}.$$

Lemma 4.3 *Set $z_n(p) = \tilde{x}_{n,2,1}(p)$ and assume $m \ge 1$. Then we have*

$$z_{n+m}(p) \le 2^m \{z_n(p)\}^{2^m} + 2 \cdot 12^m \tilde{y}_{n,2,2}(p). \tag{6}$$

Proof of Lemma 4.2. For any $p < 1$, we can pick $k_0 = k_0(p) > 0$ and $\hat{\varphi} = \hat{\varphi}(p) > 0$ such that

$$\tilde{y}_{n,1,k_0}(p) < e^{-4^n \hat{\varphi}}$$

(See Lemma 2.1 of [S03]). We denote the event that there exists an open stiff bottom-top crossing of R by $\tilde{BT}(R)$. In stiff percolation model, if $\tilde{BT}(R)$ occurs, then $u \rightsquigarrow v$ or $v \rightsquigarrow u$ for some u on the lower side of R and some v on the upper side of R. We can see

$$\begin{aligned}\tilde{y}_{n,1,2k+1}(p) \le\ & P_p(\tilde{BT}([0,4^{n-1}] \times [0,(4k+3)\cdot 4^{n-1}]))\\ & + P_p(\tilde{BT}([3\cdot 4^{n-1},4^n] \times [(4k+1)\cdot 4^{n-1},(2k+1)\cdot 4^n]))\\ & + P_p(\tilde{BT}([0,4^{n-1}] \times [(4k+1)\cdot 4^{n-1},(2k+1)\cdot 4^n]))\\ & + P_p(\tilde{BT}([3\cdot 4^{n-1},4^n] \times [0,(4k+3)\cdot 4^{n-1}]))\\ \le\ & 4 y_{n-1,1,4k+3}(p)\end{aligned}$$

for $k \ge 0$. So there exists $l > 0$ such that

$$\tilde{y}_{n+l,1,1}(p) \le 4\tilde{y}_{n+l-1,1,3}(p) \le \cdots \le 4^l \tilde{y}_{n,1,k_0}(p) < 4^l e^{-4^n \hat{\varphi}},$$

thus we have proved the lemma. $\square$

Proof of Lemma 4.3. For $m \ge 1$ we define

$$I_m = \left\{ 1 + \sum_{k=1}^{m-1} i_k \cdot 4^k \;\middle|\; i_k \in \{1,2\} \right\}, J_m = \left\{ \sum_{k=0}^{m-1} j_k \cdot 4^k \;\middle|\; j_k \in \{0,3\} \right\},$$

and

$$\mathcal{R}^{n,m} = \left\{ \begin{array}{c} R = [(4i-1)\cdot 4^n, (4i+1)\cdot 4^n] \\ \times[(4j+1)\cdot 4^n, (4j+3)\cdot 4^n] \end{array} \;\middle|\; 0 \le i,j \le 4^{m-1}, R \cap G_T^{n+m} \ne \emptyset \right\}.$$

If there exists an open stiff left-right crossing of $[0,4^{n+m}] \times [0,4^{n+m}]$, then for some $j \in J_m$, there exist open stiff left-right crossings of $[i \cdot 4^n, (i+2) \cdot 4^n] \times [j \cdot 4^n, (j+1) \cdot 4^n]$ for all $i \in I_m$,

or

there exists an open stiff bottom-top crossing of R for some $R \in \mathcal{R}^{n,m}$.

So we have (6) because $z_{n+m}(p) \leq x_{n+m,1,1}(p)$ and $|\mathcal{R}^{n,m}| \leq 2 \cdot 12^{m-1}$. □

Proof of Theorem 3.2. Combining Lemma 4.2 and Lemma 4.3, we have

$$z_{n+m}(p) \leq 2^m \{z_n(p)\}^{2^m} + 2 \cdot 12^m e^{-4^n \varphi}.$$

Set $m = 3^n$. Clearly the second term of the right hand side goes to 0 as $n \to \infty$. For the first term we note that $z_n(p) \leq 1 - (1-p)^{2^n+1}$ by definition. We have

$$\lim_{n \to \infty} 2^{3^n} \{1 - (1-p)^{2^n+1}\}^{2^{3^n}} = 0,$$

thus we have finished the proof. □

References

[BH57] Broadbent,S.R., Hammersley,J.M. (1957) Percolation processes I. Crystals and mazes, *Proceedings of the Cambridge Philosophical Society* **53**, 629-641.

[BS96] Benjamini,I. and Schramm,O. (1996) Percolation beyond $\mathbb{Z}^d$, many questions and a few answers, *Electro. Comm. Probab.* Vol.1, No.8, 71-82.

[D84] Durrett,R. (1984) Oriented percolation in two dimensions, *Ann. Prob.* **12**, 999-1040.

[F85] Falconer, K.J. (1985) *The geometry of fractal sets*, Cambridge University Press.

[G99] Grimmett,G. (1999) *Percolation* (2nd ed.), Springer.

[H00] Häggström,O. (2000) Markov Random Fields and Percolation on General Graphs, *Advances in Applied Probability* **32**, 39-66.

[K97] Kumagai,T. (1997) Percolation on Pre-Sierpinski carpets, *New Trend in Stochastic Analysis* (Proceedings of a Taniguchi International Workshop, Eds. K.D.Elworthy et al.), World Scientific, 288-304.

[L95] Liggett,T.M. (1995) Survival of discrete time growth models, with applications to oriented percolation, *Ann. Appl. Probab.*, **5**, 613-636.

[M82] Mandelbrot,B.B. (1982) *Fractal geometry of nature*, W.H.Freeman, San Francisco.

[Os90] Osada,H. (1990) Isoperimetric constants and estimates of heat kernels of pre Sierpinski carpets, *Probab. Theory Relat. Fields*, **86**, 469-490.

[Ot12] Otobe,Y. personal communication.

[S96] Shinoda,M. (1996) Percolation on the pre-Sierpinski gasket, Osaka J. Math. **33**, 533-554.

[S02] Shinoda,M. (2002) Existence of phase transition of percolation on Sierpinski carpet lattices, *J. of Appl. Probab.* **39**, 1-10.

[S03] Shinoda,M. (2003) Non-existence of phase transition of oriented percolation on Sierpinski carpet lattices, *Probab. Theory Relat. Fields* **125**, 447-456.

MACROSCOPIC CORROSION FRONT COMPUTATIONS OF SULFATE ATTACK IN SEWER PIPES BASED ON A MICRO-MACRO REACTION-DIFFUSION MODEL

VLADIMÍR CHALUPECKÝ, TASNIM FATIMA, JENS KRUSCHWITZ, AND ADRIAN MUNTEAN

ABSTRACT. We consider a two-scale reaction diffusion system able to capture the corrosion of concrete with sulfates. Our aim here is to define and compute two macroscopic corrosion indicators: typical pH drop and gypsum profiles. Mathematically, the system is coupled, endowed with micro-macro transmission conditions, and posed on two different spatially-separated scales: one microscopic (pore scale) and one macroscopic (sewer pipe scale). We use a logarithmic expression to compute values of pH from the volume averaged concentration of sulfuric acid which is obtained by resolving numerically the two-scale system (microscopic equations with direct feedback with the macroscopic diffusion of one of the reactants). Furthermore, we also evaluate the content of the main sulfatation reaction (corrosion) product—the gypsum—and point out numerically a persistent kink in gypsum's concentration profile. Finally, we illustrate numerically the position of the free boundary separating corroded from not-yet-corroded regions.

1. INTRODUCTION

1.1. Background on sulfate corrosion.

Often in service-life predictions of concrete structures (e.g., sewer systems), the effects of chemical and biological corrosion processes are fairly neglected. In sewer systems and wastewater treatment facilities, where high concentrations of hydrogen sulfide, moisture, and oxygen are present in the atmosphere, the deterioration of concrete is caused mainly by biogenic acids. The so-called microbially-induced concrete corrosion in sewer systems has been a serious unsolved problem[1] for long time. The presence of microorganisms such as fungi, algae or bacteria can induce formation of aggressive biofilms on concrete surfaces. Particularly, the sulfuric acid that causes corrosion of sewer crowns is generated by such a complex microbial ecosystem especially in hot environments. The precise role of microorganisms in the context of sulfates attack on concrete (here we focus on sewer pipes) is quite complex and is therefore less understood from both experimental and theoretical points of view; see, e.g., the experimental studies [4] (optimum pH and growth kinetics of four relevant bacterial strains), [11] (characteristics of the crown microbial system), [12] (microbiologically influenced corrosion of natural sandstone), [16] (succession of sulfur-oxidizing bacteria in the bacterial community on corroding concrete), [17] (isolation of *Thiobacillus thiooxidans*), [21] (Hamburg sewers),[24] (air-water transfer of hydrogen sulfide). As a consequence of this, an accurate large-time forecast of the penetration of the sulfate corrosion front is very difficult to obtain.

Key words and phrases. Reaction-diffusion system, sulfate corrosion, pH, free boundary, micro-macro transmission condition, multiscale numerical methods.

[1] There are a lot of financial implications if you want to change the network of pipes in a city like Fukuoka. Our statement here is that questions like *Why changing the pipes if corrosion is not so strong yet and therefore the mechanics structure of the network can/could still hold for 5 more years?* can be addressed in a rigorous mathematical multiscale framework. Such an approach would allow a good understanding and prediction at least of extreme situations.

We want to stress the fact that concrete, in spite of its strong heterogeneity, is mechanically a well-understood material with known composition. Also, the cement (paste) chemistry is well understood. However, all cement-based materials (including concrete) involve a combination of "heterogeneous multi-phase material", "multiscale chemistry", "multiscale transport" (flow, diffusion, ionic fluxes, etc.), and "multiscale" mechanics. Having in view this complexity, such materials are *sensu stricto* very difficult to describe, to analyze mathematically, and last but not least, to deal with numerically. We expect that only after the multiscale aspects of such materials are handled properly, good predictions of the large-time behavior may be obtained. This is our path to addressing this corrosion scenario that is often referred to as *the sulfatation problem.*

Before closing these background notes, let us add some remarks [20] on a closely-related topic of acid sulphate soils[2], which might attract the attention of the multiscale research in the near future. Acid sulphate soils are an important class of soils worldwide. Particularly in coastal areas, sediments often contain a large amount of iron sulfide (FeS and/or FeS_2). When by drainage the sediment is exposed to air, this iron sulfide will oxidize to iron sulphate ($FeSO_4$). As long as the sediment still contains calcium carbonate ($CaCO_3$), the FeS will react with it, resulting in gypsum ($CaSO_4$) and iron oxide (Fe_2O_3). Gypsum, being much more soluble than calcium carbonate, will tend to leach to the ground- and surface-waters. If the Fe_SO_4 is no longer removed by reactions with $CaCO_3$ or other materials, it will tend to accumulate, resulting in a drop of the pH below 4. The problematic acid sulphate soil then will have become a reality. Acid sulphate soils were first described in 1886 by the Dutch Chemist Jacob Maarten van Bemmelen, in connection with problems arising in the Haarlemmermeer Polder. Much of the work in this direction is/was done in the tropics, including Indonesia, Vietnam, and Australia; see, e.g., [13].

1.2. **Objectives and structure of the paper.** In order to be able to tackle the biophysics of the problem at a later stage, eventually coupled with the mechanics of the concrete and the actual capturing of the macroscopic fracture initiation, we focus here on a much simpler setting modeling the multiscale transport and reaction of the active chemical species involved in the sulfatation process. Therefore, the approach and results reported here are only preliminary.

Our main objective is twofold: using a multiscale reaction-diffusion system for concrete corrosion (that allows for feedback between micro and macro scales),

- calculate pH profiles and detect the eventual presence of "sudden" pH drops;
- extract from gypsum concentration profiles the approximate position of macroscopic corrosion fronts.

In Section 2, we present the reaction mechanisms taking place in sewer pipes. In Section 3, we give a mathematical description of the problem and we set a two-scale PDE-ODE system. We briefly comment on a few mathematical properties of the model. In Section 4, we approximate a macroscopic pH numerically using a multiscale FD scheme and comment briefly on the numerical results.

2. A few notes on the involved chemistry

Our model includes two important features:

- continuous transfer of H_2S from water to air phase and vice versa;
- fast production of *gypsum* at solid-water interface.

We incorporate the Henry's law to model the transfer of H_2S from the water to the air phase and vice versa [2, 24]. The production of gypsum at the solid-water interface is modeled by a non-linear reaction rate, given by (15).

---

[2] Compared to concrete, soils are much easier to handle. Their mechanics is simpler and their chemistry is often rudimentary, if any.

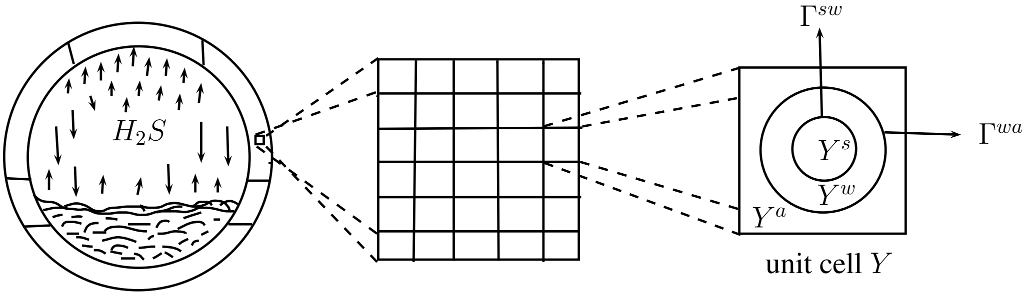

FIGURE 1. Left: Cross-section of a sewer pipe. Middle: Mesoscopic periodic approximation of a REV. Right: Our concept of pore geometry (microstructure).

There are many variants of severe attack to concrete in sewer pipes which influence the performance of concrete structure depending on the intensity of the reactions, the environment, and the turbulence of the wastewater [23]. We focus here on the most aggressive one, namely we consider the following reaction mechanisms causing sulfatation, viz.

$$10\,\mathrm{H}^+ + \mathrm{SO}_4^{2-} + \text{org. matter} \to \mathrm{H_2S(aq)} + 4\,\mathrm{H_2O} + \text{oxidized matter} \tag{1}$$

$$\mathrm{H_2S(aq)} + 2\,\mathrm{O_2} \to 2\mathrm{H}^+ + \mathrm{SO}_4^{2-} \tag{2}$$

$$\mathrm{H_2S(aq)} \rightleftharpoons \mathrm{H_2S(g)} \tag{3}$$

$$2\,\mathrm{H_2O} + \mathrm{H}^+ + \mathrm{SO}_4^{2-} + \mathrm{CaCO_3} \to \mathrm{CaSO_4}\cdot 2\,\mathrm{H_2O} + \mathrm{HCO}_{3-} \tag{4}$$

Reaction (3) is typically a surface reaction taking place as soon as water and air phases meet together. It plays an important role in transferring the H_2S from the air phase to the liquid phase where the corrosion actually takes place. For modeling details such as a Henry-like "reaction" mechanism, we refer the reader to [9, 5] and references cited therein.

3. MULTISCALE DESCRIPTION OF THE SULFATATION PROBLEM

We assume that the geometry of our concrete sample (porous medium) consists of a system of pores periodically distributed inside a three-dimensional cube $\Omega := [a,b]^3$ with $a, b \in \mathbb{R}$ and $b > a$. The exterior boundary of Ω consists of two disjoint, sufficiently smooth parts: the Neumann boundary Γ^N and the Dirichlet boundary Γ^D. We assume that the pores in concrete are made of stationary water film, air and solid parts in different ratios depending on the local porosity. The reference pore, say $Y := [0,1]^3$, has three pair-wise disjoint domains Y^s, Y^w and Y^a with smooth boundaries Γ^{sw} and Γ^{wa} as shown in Fig. 1 such that

$$Y = \bar{Y}^s \cup \bar{Y}^w \cup \bar{Y}^a.$$

We refer the reader to [9, 6] for more description of the multiscale geometry of the porous material. For a single scale (macroscopic) approach of a sulfatation scenario, we refer the reader to [1], e.g.

We consider a two-scale system of PDEs and one ODE for unknown functions $u_1 : \Omega \times (0,T) \to \mathbb{R}$, $u_k : \Omega \times Y^w \times (0,T) \to \mathbb{R}$, $k \in \{2,3\}$, and $u_4 : \Omega \times \Gamma^{sw} \times (0,T) \to \mathbb{R}$ where $(0,T)$ is the time interval. The model under consideration is derived by formal homogenization using different scalings of the diffusion coefficients in [9] (see also [14]) and is given by

$$\partial_t u_1 - d_1 \Delta u_1 = -B\left(Hu_1 - \int_{\Gamma^{wa}} u_2 \,\mathrm{d}\gamma_y\right), \quad \text{in } \Omega \times (0,T), \tag{5a}$$

$$\beta_2 \partial_t u_2 - \beta_2 d_2 \Delta_y u_2 = -\Phi_2 k_2 u_2 + \Phi_3 k_3 u_3, \quad \text{in } \Omega \times Y^w \times (0,T), \tag{5b}$$

$$\beta_3 \partial_t u_3 - \beta_3 d_3 \Delta_y u_3 = \Phi_2 k_2 u_2 - \Phi_3 k_3 u_3, \quad \text{in } \Omega \times Y^w \times (0,T), \tag{5c}$$

$$\beta_4 \partial_t u_4 = \Phi_4 k_4 \eta(u_3, u_4), \quad \text{in } \Omega \times \Gamma^{sw} \times (0,T), \tag{5d}$$

where u_1 denotes the concentration for H_2S gaseous species, u_2 for H_2S aqueous species, u_3 for H_2SO_4, and u_4 for *gypsum* at Γ^{sw}. The water film is taken here to be stationary. A detailed modeling of the role of water is still open, see, e.g., [19, 3, 22]. Δ without subscript denotes the Laplace operator with respect to macroscopic variable x and Δ_y with respect to microscopic variable y. $\mathrm{d}\gamma_y$ represents the differential over the surface Γ^{wa}. $\beta_k > 0$, $k \in \{2,3,4\}$, represents the ratio of the maximum concentration of the k-th species to the maximum concentration of H_2SO_4, $d_i > 0$, $i \in \{1,2,3\}$, are the diffusion coefficients, B is a dimensionless Biot number which gives the mass transfer rate between water and air phases, and $k_j : Y \to R$, $j \in \{2,3,4\}$, are functions modeling the reaction rate "constants". Φ_k ($k \in \{2,3,4\}$) are Damköhler numbers corresponding to three distinct chemical mechanisms (reactions). They are dimensionless numbers comparing the characteristic time of the fastest transport mechanism (here, the diffusion of H_2S in the gas phase) to the characteristic timescale of the k-th chemical reaction.

The system (5) is supplemented with initial and boundary conditions, which read as

$$u_1(x,0) = u_1^0(x), \quad \text{on } \Omega \times (0,T), \tag{6}$$

$$u_k(x,y,0) = u_k^0(x,y), \quad \text{on } \Omega \times Y^w \times (0,T),\ k \in \{2,3\}, \tag{7}$$

$$u_4(x,y,0) = u_4^0(x,y), \quad \text{on } \Omega \times \Gamma^{sw} \times (0,T), \tag{8}$$

$$u_1 = u_1^D, \quad \text{on } \Gamma^D \times (0,T), \tag{9}$$

$$n_N \cdot (d_1 \nabla u_1) = 0, \quad \text{on } \Gamma^N \times (0,T), \tag{10}$$

$$n_{wa} \cdot (d_2 \nabla_y u_2) = B\left(Hu_1 - \int_{\Gamma^{wa}} u_2 \,\mathrm{d}\gamma_y\right), \quad \text{on } \Omega \times \Gamma^{wa} \times (0,T), \tag{11}$$

$$n_{sw} \cdot (d_2 \nabla_y u_2) = 0, \quad \text{on } \Omega \times \Gamma^{sw} \times (0,T), \tag{12}$$

$$n_{wa} \cdot (d_3 \nabla_y u_3) = 0, \quad \text{on } \Omega \times \Gamma^{wa} \times (0,T), \tag{13}$$

$$n_{sw} \cdot (d_3 \nabla_y u_3) = -\Phi_3 \eta(u_3, u_4), \quad \text{on } \Omega \times \Gamma^{sw} \times (0,T), \tag{14}$$

where n_N denotes the outward unit normal vector to $\partial\Omega$ along Γ^N, and n_{wa} and n_{sw} denote the outward unit normal vectors to Y^w along Γ^{wa} and Γ^{sw}, respectively. Note that the "information" at the micro-scale is connected to the macro-scale situation via the right-hand side of (5a) and via the *micro-macro boundary condition* (11). It is also worth noticing that all involved parameters (except for H, d_3 and B) contain microscopic information. The coefficients d_3 and B are effective ones (see [9, 8] for a way of calculating them), while H can be read off from existing macroscopic experimental data.

We consider the following form of the reaction rate η at the interface Γ^{sw}

$$\eta(\alpha,\beta) = \begin{cases} \alpha^p(\bar{\beta} - \beta)^q, & \text{if } \alpha \geq 0, \beta \geq 0, \\ 0, & \text{otherwise,} \end{cases} \tag{15}$$

where $\bar{\beta}$ is a known maximum concentration of gypsum at Γ^{sw} and $p \geq 1, q \geq 1$ are partial orders of reaction. For more modeling possibilities of choosing η, see [10]. It is worth noting that production terms like

$$B\left(Hu_1(t,x) - \int_{\Gamma^{wa}} u_2(t,x,y)\,\mathrm{d}\gamma_y\right)$$

are usually referred in the literature as Henry's or Raoult's law, where $H > 0$ is known Henry's constant.

We refer the reader to [6, Theorem 3] for statements regarding the global existence and uniqueness a weak solution to problem (5)–(14) (see also [15] for the analysis on a closely related problem).

4. Simulation at a macroscopic pH scale. Capturing free boundaries

In this section the model (5) is applied to the simulation of the acid corrosion due to a microbiotical layer on a cement specimen. We focus on extracting the position of the corrosion front and on the acid reaction, which we use to obtain macro-scale profiles of pH. Both of these results can be compared to experimental data published, e.g., in [11, 16].

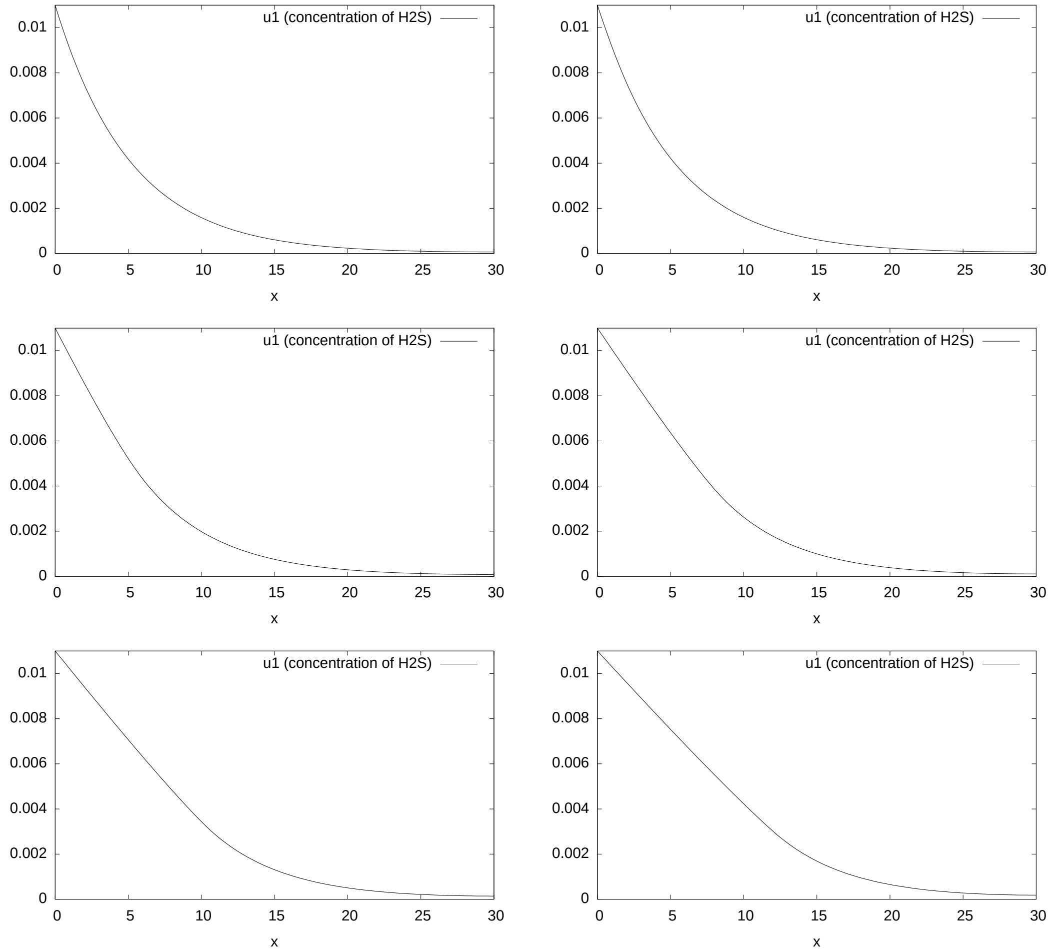

Figure 2. Time evolution of u_1 (concentration of H_2S(g)) shown at $t \in \{2000, 4000, 8000, 12000, 16000, 20000\}$ in left-right and top-bottom order.

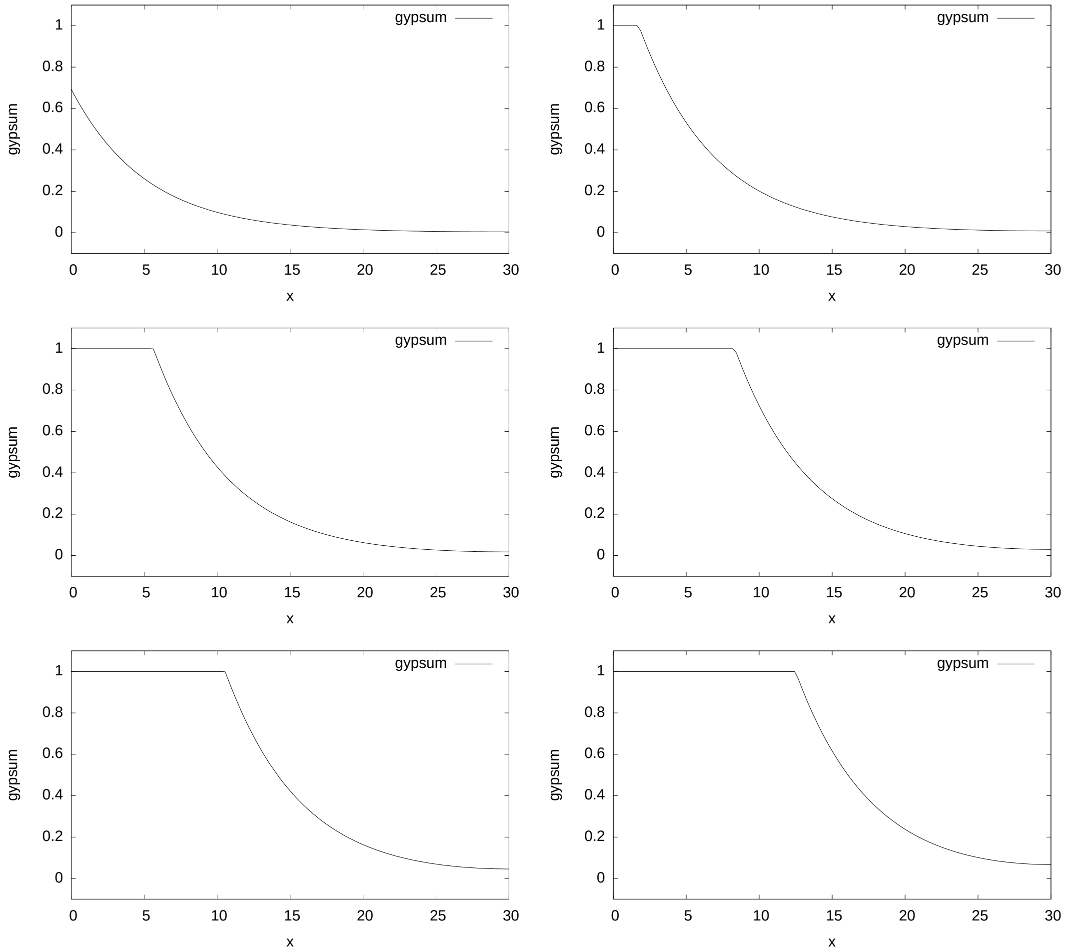

FIGURE 3. Time evolution of u_4 (gypsum) shown at $t \in \{2000, 4000, 8000, 12000, 16000, 20000\}$ in left-right and top-bottom order.

For the purpose of the simulation we employ a numerical scheme for a reduced 1D/2D version of the system (5). The reduction consists in taking $\Omega := (0, L)$ and $Y^w = (0, \ell)$ as one-dimensional intervals, which in effect corresponds to analysing the specimen in a perpendicular direction to its surface away from edges and to simplifying the micro cell geometry, respectively. The numerical scheme is based on the method of lines, where in space we use finite difference discretization and in time we employ an implicit higher-order time integrator for the solution of the non-linear ODE system. See [6, 7] for further details of the numerical scheme, its analysis with respect to convergence to the weak solutions and some basic numerical experiments. For details of a computer implementation of the numerical scheme we refer the reader to [14, Chapter 7].

In Table 1 we summarize values of the model parameters used in the simulations described below.

4.1. **Free boundaries.** Figures 2 and 3 show the evolution of $u_1(x,t)$ and $u_4(x,t)$ in time. The Dirichlet boundary condition $u_1(0,t) = u_1^D$ models a constant inflow of $H_2S(g)$ at $x = 0$, i.e., at the surface of the specimen. As the gas diffuses through the porous structure, it enters the

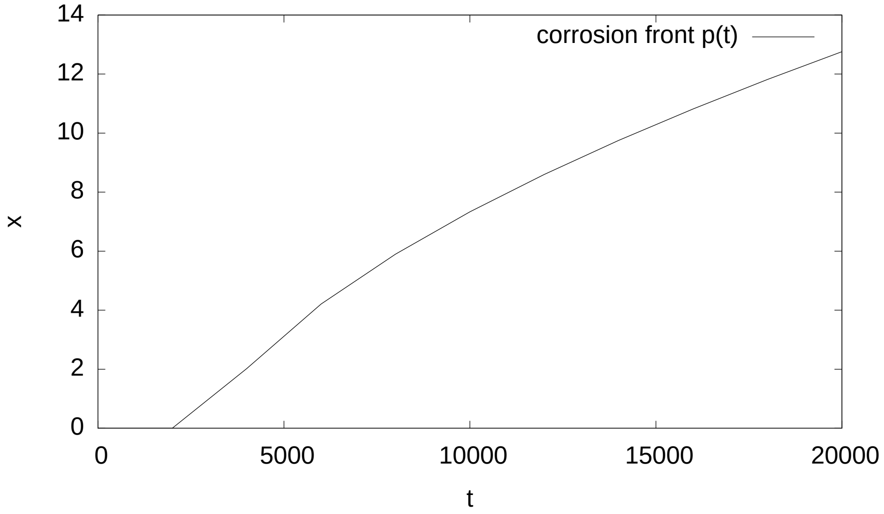

Figure 4. Position of the corrosion front.

d_1	$d_{2,3}$	k_2	k_3	k_4	$\Phi_{2,3,4}$	B	H	$\bar{\beta}$	p	q	u_1^D	L	ℓ
0.864	0.00864	1.48	0.0084	10	1	86.4	0.3	1	1	1	0.011	30	1

Table 1. Parameter values used in the numerical simulation.

water film in the pores due to the reaction (3), where it undergoes biogenic oxidation to sulfuric acid. Consequently, its concentration decreases with increasing depth. As the system becomes saturated and as the sulfatation reaction (4) converts available cement into gypsum, the total concentration of H_2S(g) starts to increase (Fig. 2).

Sulfuric acid that arises from the oxidation of H_2S(aq) then reacts at $y = \ell$ with the cement paste and converts it into gypsum (u_4) whose concentration profile is shown in Fig. 3. Interestingly, although the behavior of u_1 is as expected (i.e., purely diffusive), we notice that a *macroscopic* gypsum layer (region where u_4 is produced) is formed around $t = 1500$ and grows in time. The figure clearly indicates that there are two distinct regions separated by a slowly moving intermediate layer: the left region—the place where the gypsum production reached saturation (a threshold), and the right region—the place of the ongoing sulfatation reaction (4) (the gypsum production has not yet reached here the natural threshold).

We use u_4 to extract an approximate position of the corrosion front $p(t)$ which we define as (in our scenario, we expect u_4 to be decreasing)

$$p(t) := \{x \in (0, L) \mid u_4(x, t) = \bar{\beta} - \varepsilon\},$$

where ε is a small parameter. Figure 4 shows a graph of $p(t)$ arising from our numerical experiment. We notice that as the corroding front advances further into the concrete specimen, its rate of growth decreases. This is in agreement with experimental data since the hydrogen sulfide gas supplied from the outside environment has to be transported (by diffusion) over ever larger distance. It is important to note that the precise position of the separating layer is *a priori unknown* and to capture it simultaneously with the computation of the concentration profile would require a moving-boundary formulation similar to the one reported in [5].

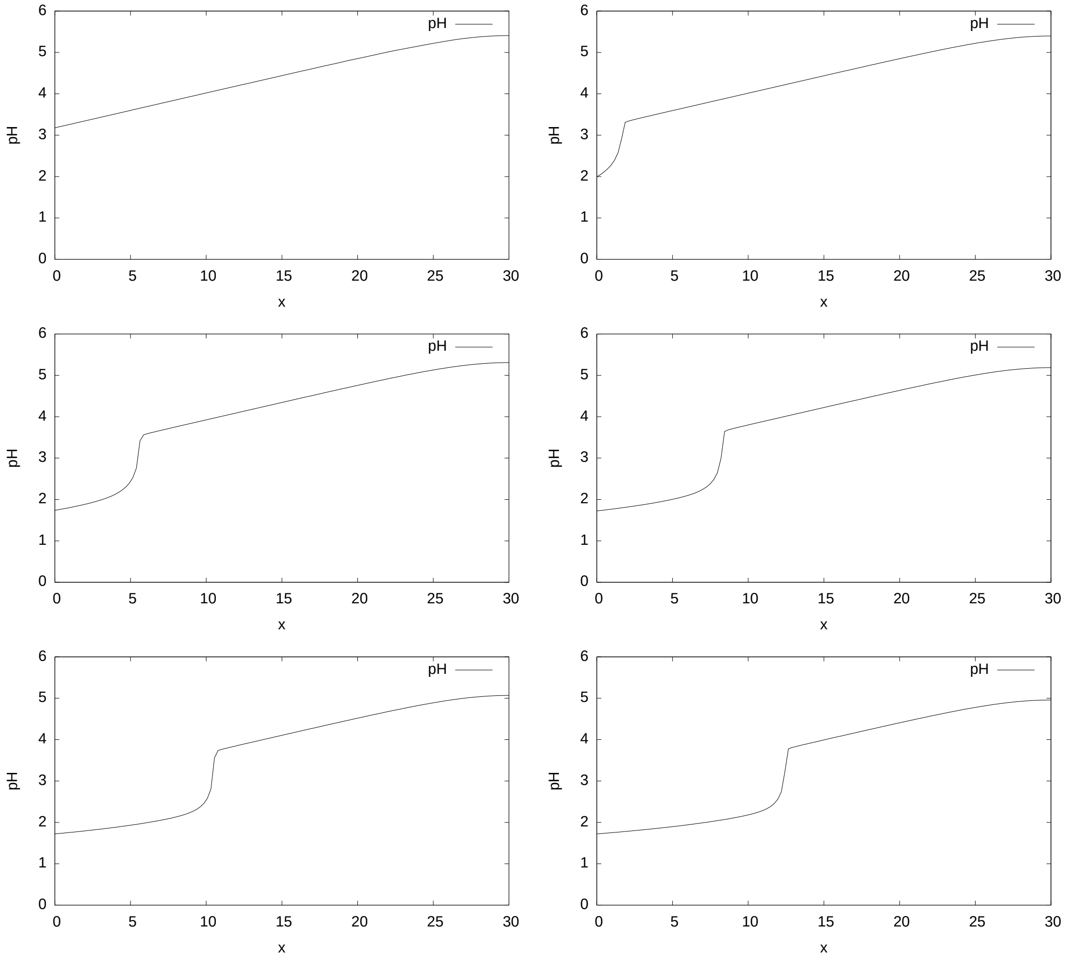

FIGURE 5. Time evolution of macro-scale pH profiles computed from micro-scale information shown at $t \in \{2000, 4000, 8000, 12000, 16000, 20000\}$ in left-right and top-bottom order.

4.2. **Drop in pH.** Emission of hydrogen sulfide from the wastewater to the air space of sewer pipe is an important process because the problems of hydrogen sulfide in sewer pipes are associated with gaseous hydrogen sulfide. Hydrogen sulfide is a weak acid with a dissociation constant of 7.0 (at 20°C) and only the non-dissociated form is emitted in the air space sewer pipe. The pH of the wastewater is therefore of importance when evaluating the potential hydrogen sulfide emission. After the hydrogen sulfide arrives at and diffuses into the concrete, the oxidation of hydrogen sulfide is biological once the pH of the solid matrix has dropped below approximately 8–9 [18]. This represents the tendency of hydronium ions to interact with other components of the solution, which affects among other things the electrical potential read using a pH meter. The concentration of hydrogen ions is expressed as pH scale and pH is defined as a negative decimal logarithm of the concentration of hydronium ions dissolved in a solution.

As the model considered in this paper contains information both from micro (pore) scale and macro-scale, we need a way of computing macro-scale values of pH from the available micro-scale data. Such information is not readily available in the system (5). However, sulfuric acid is a diprotic acid with two stages of dissociation, where the first stage occurs fully and the dissociation in the second stage can be neglected. Therefore, the concentration of hydronium ions is proportional to the concentration of sulfuric acid, which is represented by u_3 in our model. We extract the macro-scale concentration of sulfuric acid at each x by taking a volume average of u_3 over Y^w. Thus, we use the following expression for computing macroscopic pH:

$$\mathrm{pH}_{\mathrm{macro}}(x,t) = -\log_{10}\left(\frac{k_a}{|Y^w|}\int_{Y^w} u_3(x,y,t)\,\mathrm{d}y\right), \tag{16}$$

where k_a is the activity of hydronium ions.

The macro-scale pH profile computed using the formula (16) is shown in Figure 5. We can see that at the beginning of the simulation (first graph) with increasing depth the pH also increases from acid to more basic values as expected. Once all the available cement is consumed and converted into gypsum (this happens for the first time at $x = 0$ between the first and second graph in Figure 5 around $t = 1500$), the pH drops rapidly across the corrosion front. This is due to the fact that behind the corrosion front the sulfuric acid is no longer neutralised by the sulfatation reaction (4).

Note that our pH profiles are not in the experimental range. We expect the size of the drop will become comparable to the one seen in experiments as soon as effects of nonlinear moisture transport and bacteria motility and chemical activity are taken into account in the model equations. The main message that we want to draw is that we are able to detect and compute a macroscopic pH drop, once the needed micro-information is available.

Acknowledgments

We thank Peter Raats (Wageningen), Hans Kuipers (Eindhoven) and Varvara Kouznetsova (Eindhoven) for useful discussions on this topic during a multiscale symposium that took place in Eindhoven in September 2011.

References

1. D. Agreba-Driolett, F. Diele, and R. Natalini, *A mathematical model for the* SO_2 *aggression to calcium carbonate stones: Numerical approximation and asymptotic analysis*, SIAM J. Appl. Math. **64** (2004), no. 5, 1636–1667.
2. P. W. Balls and P. S. Liss, *Exchange of* H_2S *between water and air*, Atmospheric Environment **17** (1983), no. 4, 735–742.
3. R. E. Beddoe and H. W. Dorner, *Modelling acid attack on concrete: Part 1. The essential mechanisms*, Cement and Concrete Research **35** (2005), 2333–2339.
4. A. Bielefeldt, Ma. Guadalupe D. Gutierrez-Padilla, S. Ovtchinnikov, J. Silverstein, and M. Hernandez, *Bacterial kinetics of sulfur oxidizing bacteria and their biodeterioration rates of concrete sewer pipe samples*, Journal of Environmental Engineering **136** (2010), no. 7, 731–738.
5. M. Böhm, F. Jahani, J. Devinny, and G. Rosen, *A moving-boundary system modeling corrosion of sewer pipes*, Appl. Math. Comput. **92** (1998), 247–269.
6. V. Chalupecký, T. Fatima, and A. Muntean, *Multiscale sulfate attack on sewer pipes: Numerical study of a fast micro-macro mass transfer limit*, Journal of Math-for-Industry **2** (2010), no. 2010B–7, 171–181.
7. V. Chalupecký and A. Muntean, *Semi-discrete finite difference multiscale scheme for a concrete corrosion model: approximation estimates and convergence*, Japan J. Indust. Appl. Math. (2012), accepted.
8. C. Eck, *Homogenization of a phase field model for binary mixtures*, Multiscale Model. Simul. **3** (2004), no. 1, 1–27.
9. T. Fatima, N. Arab, E. P. Zemskov, and A. Muntean, *Homogenization of a reaction-diffusion system modeling sulfate corrosion in locally-periodic perforated domains*, J. Engng. Math. **69** (2010), no. 2–3, 261–276.
10. T. Fatima and A. Muntean, *Sulfate attack in sewer pipes: Derivation of a concrete corrosion model via two-scale convergence*, Non-linear Analysis: Real World Applications (2012), submitted/in press.

11. R.L. Islander, J.S. Devinny, F. Mansfeld, A. Postyn, and H. Shih, *Microbial ecology of crown corrosion in sewers.*, J. Environ. Eng. **117** (1991), no. 6, 751–770.
12. R. Mansch and E. Bock, *Untersuchung der Beständigkeit von keramischen Werkstoffen.*, Werkstoffe und Korrosion **45** (1994), 96–104.
13. R. Miller, R. Correll, J. Vanderzalm, and P. Dillon, *Modeling of movement of contaminants from sewer leaks and public open space through the unsaturated zone to the watertable*, CSIRO Report CMIS 05/41, CSIRO, Australia, 2005.
14. A. Muntean and V. Chalupecký, *Homogenization method and multiscale modeling*, MI Lecture Note Series, vol. 34, Kyushu University, GCOE Program, 2011.
15. A. Muntean and M. Neuss-Radu, *A multiscale Galerkin approach for a class of nonlinear coupled reaction–diffusion systems in complex media*, Journal of Mathematical Analysis and Applications **371** (2010), no. 2, 705–718.
16. S. Okabe, M. Odagiri, T. Ito, and H. Satoh, *Succession of sulfur-oxidizing bacteria in the microbial community on corroding concrete in sewer systems*, Appl. Env. Microb. **73** (2007), no. 3, 971–980.
17. C. D. Parker, *The corrosion of concrete. 1. Isolation of a species of bacterium associated with the corrosion of concrete exposed to atmospheres containing hydrogen sulphide.*, The Australian Journal of Experimental Biology and Medical Science **23** (1945), no. 3, 81–90.
18. ———, *Species of sulphur bacteria associated with the corrosion of concrete*, Nature **159** (1947), no. 4039, 439–440.
19. P. A. C. Raats, *Accumulation and transport of water and solutes in saturated and unsaturated zones.*, Hydrochemical balances of freshwater systems. Proc. of the Uppsala Symposium (E. Eriksson, ed.), IAHS Publ. No 150, 1984, pp. 343–357.
20. ———, Personal communication, 2011.
21. W. Sand and E. Bock, *Concrete corrosion in the Hamburg sewer systems.*, Environ. Technol. Lett. **5** (1984), 517–528.
22. R. Tixier, B. Mobasher, and M. Asce, *Modeling of damage in cement-based materials subjected to external sulfate attack. i: Formulation*, J. of Materials in Civil Engineering **15** (2003), 305–313.
23. C. Yongsiri, J. Vollertsen ans M. Rasmussen, and T. Hvitved-Jacobsen, *Air-water transfer of hydrogen sulfide: An approach for application in sewer networks*, Water Envir. Research **76** (2004), no. 81, 81–88.
24. C. Yongsiri, J. Vollertsen, and T. Hvitved-Jacobsen, *Effect of temperature on air-water transfer of hydrogen sulfide*, Journal of Environmental Engineering **130** (2004), no. 1, 104–109.

Institute of Mathematics for Industry, Kyushu University, Japan
E-mail address: `chalupecky@imi.kyushu-u.ac.jp`

Centre for Analysis, Scientific Computing, and Applications, Department of Mathematics and Computer Science, Eindhoven University of Technology, The Netherlands
E-mail address: `t.fatima@tue.nl`

Strassen.NRW, Gelsenkirchen, Germany
E-mail address: `jens.kruschwitz@strassen.nrw.de`

Centre for Analysis, Scientific Computing, and Applications, Department of Mathematics and Computer Science, Institute for Complex Molecular Systems, Eindhoven University of Technology, The Netherlands
E-mail address: `a.muntean@tue.nl`

Surfactant effect on the multiscale structure of bubbly flows

Shu TAKAGI,
Department of Mechanical Engineering,
The University of Tokyo

Abstract

Small amounts of surfactant can drastically change bubble behavior. For example, a bubble in aqueous surfactant solution rises much slower than one in purified water. This phenomenon is explained by the so-called Marangoni effect caused by a nonuniform concentration distribution of surfactant along the bubble surface. In other words, a tangential shear stress appears on the bubble surface due to the surface tension variation caused by the surface concentration distribution, which results in the reduction of the rising velocity of the bubble. More interestingly, this Marangoni effect influences not only the rising velocity, but also the lateral migration in the presence of mean shear. Furthermore, these phenomena influence the multiscale nature of bubbly flows and cause a drastic change in the bubbly flow structure. In this article, we review the recent studies related to these interesting behaviors of bubbles caused by the surfactant adsorption/desorption on the bubble surface.

Introduction

Bubbly flows are encountered in many industrial and environmental processes, such as chemical reactors, heat exchangers and aeration systems for water purification, They are also utilized to reduce the frictional drag of a moving body in water by injecting bubbles in the turbulent boundary layer, which has recently attracted much attention from many researchers (see Sugiyama et al. 2008 and Ceccio 2010 for a comprehensive review). In these bubbly flows, small amounts of surfactant can cause dramatic changes in the flow structures through the multiscale effects of the flows. Figure 1 represents the idea of the multiscale structure of bubbly flows in aqueous surfactant solutions. Small amounts of surfactant dissolved in the water adsorb onto the bubble surface, greatly affecting the bubble rising motion. Likewise affected are bubble-bubble interactions; the coalescence of small bubbles hardly occurs in the presence of surfactant. These factors are coupled and can dramatically change the whole bubbly flow structure. For example, because of this structural change of bubbly flow and also the influence of the adsorbed surfactant on mass transfer, the total mass transfer through a bubbly plume in an aeration tank can be quite different with and without surfactant.

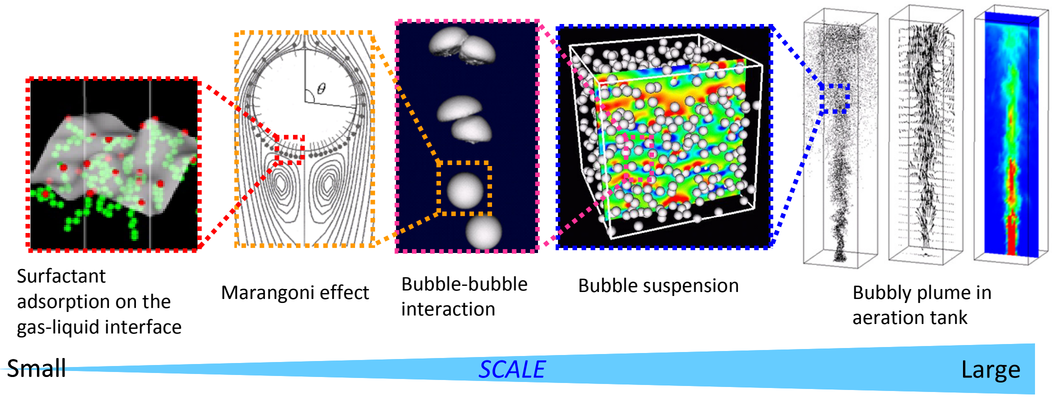

Fig. 1 Multiscale structure of bubbly flows in aqueous surfactant solution

Surfactant has at least three well-known influences on bubble motion: the reduction of rising velocity, the prevention of coalescence, and the reduction of mass transfer. The first of these is explained by the so-called Marangoni effect. As a bubble rises in aqueous surfactant solution, surfactant is swept off the front part and accumulates in the rear part. This leads to a variation of surface tension along the bubble surface, which causes tangential shear stress on the surface. This is known as the Marangoni effect due to surfactant adsorption on a bubble surface. This shear stress results in an increase of drag, which causes the reduction of the rising velocity. In many cases, the bubble surface becomes sufficiently contaminated by a small amount of dissolved surfactant so that a nearly no-slip surface is attained (Clift et al. 1978). The rising speed of the contaminated bubble decreases with increasing surfactant concentration until the same drag coefficient as a rigid sphere is reached. Thus, a fully contaminated bubble is often regarded as behaving like a rigid sphere in water.This phenomenological explanation was first given by Frumkin & Levich (1947), since which a considerable number of studies have been conducted on this subject. Comprehensive review is given in Takagi and Matsumoto(2011).

The early studies on the measurement of bubbly flows were conducted by Serizawa *et al.* (1975) and Theofanous and Sullivan (1982), in which local measurements of turbulent flow structure in pipe were made using a hot-film anemometer and Laser Doppler Anemometer (LDA or LDV), respectively. Following these studies, Wang *et al.* (1987), Lance and Bataille (1991), Serizawa *et al.* (1991) and Liu and Bankoff (1993a, 1993b) provided experimental information on: the local void fraction profile and its dependence on bubble size; the effect of initial bubble size and the bubble-induced turbulence. However, there is a dearth of information about the effect of surfactant on the global structure of bubbly flow.

In our previous studies on upward bubbly channel flow, bubbles strongly migrate toward the wall and form the crescent-like shape bubble cluster near the wall (So *et al.* (2002)). The factor of this bubble migration is thought to be a shear-induced lift force. Recently, there are some numerical approaches about the shear-induced lift force on clean bubble and rigid sphere (Legendre and Magnaudet (1998), Kurose and Komori (1999), Bagchi and Balachandar (2002)). Through the comparison of their studies, it is shown that there are large discrepancy between the case of clean bubble and that of rigid sphere. From this result, it is suggested that the contamination of water will influence bubble migration. In this study, the motion of bubbles in upward turbulent channel flow is observed. Especially, bubble clustering phenomenon near the wall is analysed. Furthermore, surfactant effect on the spatial distribution of the bubbles is investigated by changing the concentration and the species of surfactant.

Nomenclature

G	Gravitational constant (ms^{-1})
P	pressure (Nm^{-2})
A	Bubble radius
C	Concentration of surfactant, Coefficient
D	Diffusion coefficient
F	Force
U	Velocity
U	Rising velocity of a bubble

Ma	Marangoni number
La	Langmuir number
Pe	Pecret Number
Ha	Hatta number
K	dimensionless adsorption length
K	rate constant
R_G	Gas constant
Sr	dimensionless shear rate
T	absolute temperature

Greek letters

α	shear rate
μ	Viscosity
ν	kinematic viscosity
ρ	Density
σ	surface tension
Γ	surface concentration
θ_c	cap angle

Subsripts

S	Surface
∞	Value in the far-field
Max	maximum or saturated velue
D	Drag
L	Lift
P	Pressure contribution
V	Viscous contribution
Ad	Adsorption
Des	Desorption

Experimental Setup

Experimental Apparatus

The experimental apparatus is shown in Fig.2. The experiments were conducted in a vertical circulating water tunnel, which was operated in the upward direction in the test section. The height of 1600mm (x-direction) from the bubble generator to the test section is large enough for the void fraction profiles to be sufficiently developed in the case of bubbly flow and for single-phase turbulent channel flow to be fully developed. The test section has a thickness of 40mm (y-direction) and a width of 400mm (z-direction) with an aspect ratio of 10. The channel width is chosen in such a way that the flow in the centre of the channel is nearly two-dimensional.

The bubble generator was constructed with 474 stainless steel pipes of 0.07mm inner diameter and 24mm length. It is installed above the inlet nozzle of the channel, which is located at x/H=80 downward from the test section. The coordinate x denotes the stream-wise direction; y the perpendicular direction from the wall and z span-wise direction. The bubble-clustering phenomena were analysed using image-processing technique. For recording the image of bubbles accumulating near the wall, we use high-speed digital camera (Motion Pro 10000, Redlake MASD, Inc.) with 1,280 x 1,024 pixels and 8-bit resolution.

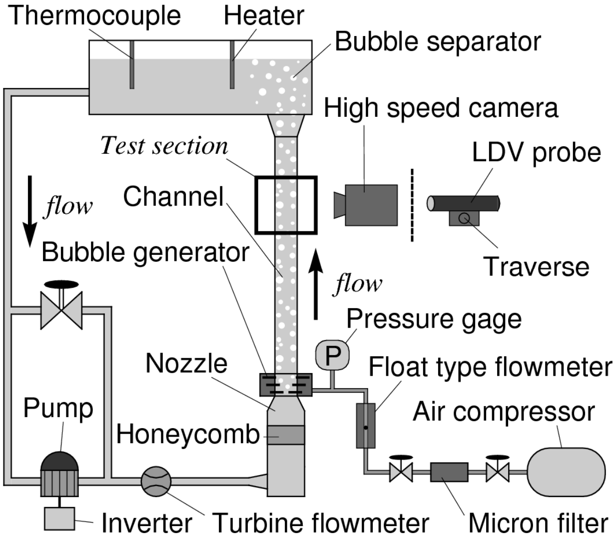

Fig. 2 Schematic of experimental apparatus

Experimental Conditions

The bulk Reynolds numbers ($Re_b=U_b\cdot 2H/\nu$), based on the characteristic length of the channel width ($2H$=40mm) and the mean bulk velocity of liquid phase (U_b), are 8200 for the present results.. Here, the bulk velocity of the liquid phase can be estimated in two different ways. One method is from the locally measured velocity profile by integrating the profiles across half of the channel and dividing by half of the channel width. The other method is from the globally measured liquid volumetric flux and dividing it by the cross-sectional area. There is a small difference of less than a few percentages between the values estimated using these two methods. This difference is caused by several factors, such as the effect of the sidewall, the accuracy of the measurement, two-dimensionality at the test section etc. In the present study, we employed the method using the locally measured velocity profile, because the bulk velocity calculated from the liquid volumetric flux is not very reliable due to the effect of the sidewall. Two types of surfactant, 3-Pentanol and Triton-X100 are used. The bulk concentration of 3-Pentanol and Triton-X100 are from 20ppm to 120ppm and 2ppm, respectively.

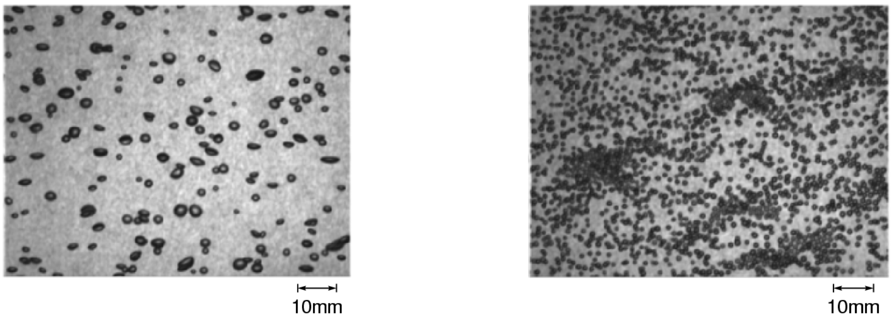

(a) without surfactant, (b) with 3-Pentanol (20ppm)

Fig.3 Photographs of bubbly flow. Re_b=8200, f_g=0.6%

Surfactant Effect

Fig.3 shows the typical snapshots of bubbly channel flow at the bulk Reynolds number (Re_b) of 8200 and the average void fraction (f_g) of 0.6%. We can prevent bubbles from coalescing by the addition of small amount of surfactant into the liquid phase (see next section 'Bubble size profiles'). 3-pentanol and Triton-X100 are used for surfactant. It is clearly observed that the bubble size and the size distribution are drastically changed by the addition of surfactant. In fig.3 (a), "without surfactant", there are larger deformed bubbles. These bubbles rise with a zigzag leaping motion against the perpendicular wall and are distributed throughout the cross section of the channel. It is also observed that this kind of leaping motion of a bubble enhances the mixing of the fluid and seems to produce the large fluctuations in the flow. Furthermore, once the small amount of surfactant is added, the whole aspect of the flow field is changed. The bubbles start accumulating near the wall and sliding along it. It is also interesting to see that the accumulated bubbles in the vicinity of the wall formed horizontal bubble clusters of 10-40mm length in some cases with 3-Pntanol, that rise and oscillate like moving waves as shown in Fig.3 (b). These changes produce a dramatic change in the whole bubbly flow structure (So *et al.*, 2002).

There are two well-known methods to avoid bubble coalescence. One is the addition of surfactant, and the other is that of salt. Zenit *et al.* (2001) added salt to the liquid phase to avoid the coalescence. In their study, in order to compare the experimental results with potential flow theories applied for bubble suspension (Sanagni and Didwania(1993), Smereka(1993)), they use salt which does not give Marangoni effects. They are trying to capture the horizontal bubble clustering which was predicted by the theory. On the other hand, in the present experiment, the liquid phase is upward flow which has a strong shear and it is also a slightly contaminated by surfactant to obtain mono-dispersed spherical bubbles by preventing the bubble coalescence. Under this condition with surfactant, the tangential stress at the gas-liquid interface resulted from Marangoni effect is not negligible and the boundary condition on the interface can be treated like intermediate state between rigid particle and clean bubble. This effect gives the smaller rising velocity and end up with more spherical shape even if the bubble size is nearly the same as that of clean bubble. Therefore, there are differences between our experiment and experiment conducted by Zenit *et al.* and our experimental system will not be used for the comparison with the potential flow theory.

To investigate the effect of added 3-pentanol on the fully developed turbulent channel flow, the streamwise mean velocity and turbulent fluctuations were measured for the single-phase flow by the LDV system. The mean velocity profiles in single-phase flow at Re_τ=147, which corresponds to Re_b=4100, both with and without 20ppm of 3-pentanol are compared. The results are also compared with the law of the wall and that of DNS (Direct Numerical Simulation) at nearly the same Reynolds number based on the wall friction velocity, which is Re_τ=150 (Kasagi *et al.*, 1992). Regardless of the addition of 3-pentanol, the present results show an excellent agreement with the law of the wall and the DNS result. The turbulent fluctuations normalized by the wall friction velocity are also in good agreement with DNS result in both x- and y-directions, regardless of the addition of 3-pentanol. Thus, the comparison with DNS data confirms that the measuring system is reliable. And through the comparison of the results with and without 3-pentanol, the effect of the added 3-pentanol to the single phase turbulence flow is negligibly small.

Numerical Method

Numrerical simulations were also conducted to investigate the effect of adsorption / desorption kinetics of surfactant to the lift force acting on bubbles.

The physical model is the same as Cuenot et al.(2005). Their simulations are for axisymmetric flow. We have employed the same model for the three dimensional flows, which is the flow around a spherical bubble in a simple shear flow. Governing equations are given as follows.

Equation of continuity for incompressible Newtonian fluid,

$$\nabla \cdot \mathbf{u} = 0, \tag{1}$$

The incompressible Navier-Stokes equations,

$$\mathbf{u} \cdot \nabla \mathbf{u} = -\frac{1}{\rho} \nabla p + \nu \nabla^2 \mathbf{u} \tag{2}$$

The concentration balance equation in liquid phase,

$$\mathbf{u} \cdot \nabla c = D \nabla^2 c, \tag{3}$$

and that on bubble surface,

$$\nabla_s \cdot \left(\mathbf{u}_s \varGamma \right) = D_s \nabla^2 \varGamma - D \left(\nabla c \right)_s \cdot \mathbf{n}, \tag{4}$$

where, **n** represents the normal unit vector on surface. The second term of the right-hand side of equation (4) represents the mass flux from the liquid phase to surface. When the ad/desorption kinetics is assumed to obey the Langmuir-Hinshelwood (L-H) kinetics (Chang, & Franses 1995), the mass flux at the bubble surface can be estimated by the following L-H equation,

$$D \left(\nabla c \right)_s \cdot \mathbf{n} = -k_{ad} c_s \left(1 - \frac{\varGamma}{\varGamma_{max}} \right) - k_{des} \varGamma. \tag{5}$$

Then the reduction of surface tension by the surfactant adsorption is given by the Frumkin equation,

$$\sigma = \sigma_0 + R_G T \varGamma \ln \left(1 - \frac{\varGamma}{\varGamma_{max}} \right), \tag{6}$$

and the Marangoni stress on surface is given by,

$$\mathbf{t} \cdot \boldsymbol{\tau} = \mathbf{t} \cdot \nabla_s \sigma = -\frac{R_G T \varGamma}{\varGamma_{max} - \varGamma} \mathbf{t} \cdot \nabla_s \varGamma, \tag{7}$$

where **t** is the unit vector in the tangential direction. Equation (7) means that the gradient of surface concentration gives the shear stress (Marangoni stress) on bubble surface, and it yields the decrease of surface velocity. The flow far from a bubble ($r = R_\infty$) converges to a simple shear flow as shown in Figure 4,

$$\mathbf{u}_\infty = -\left(U_0 + \alpha\, y \right) \mathbf{e}_x. \tag{8}$$

The dimensionless form of equations (2)-(5), (7) and (8) are written as follows using the characteristic scales U_0, $2a$, c_∞ and $\varGamma_{max}$.

$$\mathbf{u}^* \cdot \nabla^* \mathbf{u}^* = -\nabla^* p^* + \frac{1}{Re} \nabla^{*2} \mathbf{u}^*, \tag{9}$$

$$\mathbf{u}^* \cdot \nabla^* c^* = \frac{1}{Pe} \nabla^{*2} c^*, \tag{10}$$

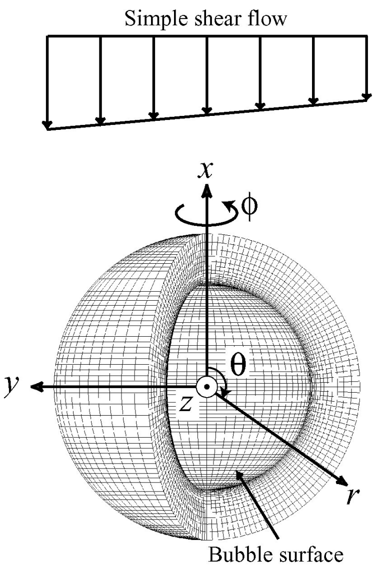

Fig. 4 Computational grids around a spherical bubble and coordinate system. Velocity field far from a bubble converges to a simple shear flow

$$\nabla^*_s \cdot \left(\mathbf{u}^*_s \Gamma^*\right) = \frac{1}{Pe_s}\nabla^{*2}\Gamma^* - \frac{1}{K\,Pe}\left(\nabla^* c^*\right)_s \cdot \mathbf{n}, \tag{11}$$

$$\left(\nabla^* c^*\right)_s \cdot \mathbf{n} = -Ha\,K\,Pe\left\{c_s^{\,*}\left(1-\Gamma^*\right) - \frac{1}{La}\Gamma^*\right\}, \tag{12}$$

$$\mathbf{t}\cdot\boldsymbol{\tau}^* = -\frac{Ma}{1-\Gamma^*}\,\mathbf{t}\cdot\nabla^*_s\Gamma^*, \tag{13}$$

$$\mathbf{u}_\infty^{\;*} = -\left(1+Sr\,y^*\right)\,\mathbf{e}_x, \tag{14}$$

where the superscript * indicates the dimensionless quantities. $Pe = 2aU_0/D$ and $Pe_s = 2aU_0/D_s$ denote the Peclet number for mass transfer in liquid phase and on surface, respectively. In this paper, D_s is assumed to be the almost same value as D, and $Pe_s = Pe$. $Sr = 2a\alpha/U_0$ is the dimensionless shear rate. The dimensionless adsorption length K, the Hatta number Ha, the Langmuir number La and the Marangoni number Ma are determined as follows.

$$K = \frac{\Gamma_{max}}{2ac_\infty}, \quad Ha = \frac{2ac_\infty k_{ad}}{U_0\Gamma_{max}}, \quad La = \frac{c_\infty k_{ad}}{\Gamma_{max}k_{des}}, \quad Ma = \frac{R_G T\Gamma_{max}}{\rho\nu\, U_0}. \tag{15}$$

The governing equations described above were calculated numerically with the finite volume method on the three-dimensional boundary-fitted grid shown in figure 3. The outer boundary of the computational domain R_∞ was fixed at $80a$, which is large enough to remove the domain size dependence of the solution for the bubble Reynolds number of 100. The computational domain was divided into 86, 87 and 32 grids in r ($a \sim R_\infty$), θ ($0 \sim \pi$) and ϕ ($0 \sim \pi$) directions, respectively. Here, the flow around a spherical bubble is symmetric with respect to the (x - y) plane, thus the domain was set for ϕ direction in $0 \le \phi \le \pi$.

Results and Discussion

Bubble Size Distribution

The diameter of the bubbles injected from the bubble generator is measured by means of a high speed digital camera at the test section. In the case without surfactant, shown as “tap water”, the average diameter is about 1.5mm and the standard deviation is about 0.7mm that was not good enough for our ‘mono-dispersed’ requirement. To investigate the reason why the bubble size has a large standard deviation, we observe the size history of a bubble released from the needle. It is found that bubbles coalesce several times before they reach the test section. In the cases with low 3-Pentanol concentration (21ppm ~ 32ppm), the bubble size profiles have double peaks around 0.9mm and 1.1mm. The second peak reflects coalscent bubbles and disappears in the case with high concentration (63ppm). A number of coalescent bubble is not so much in each 3-pentanol solution, the average diameter is about 0.9mm with a standard deviation of 0.1mm. In 2ppm Triton X-100 solution, generated bubble size becomes a little bit bigger compared with the case of 3-Pentanol solution and its average diameter is about 1mm with a standard deviation of 0.1mm. In this case, bubbles do not coalesce. From this result, the bubble size profile satisfies our ‘mono-dispersed’ requirement quite well by the addition of small amount of surfactant.

Surfactant Effect on Bubble Clustering Behaviour

Through the experiments, it is found that there is a relationship between the spatial distribution of the bubbles and the bulk concentration and the species of the surfactant. Fig.5 shows the bubbly flow without surfactant and Fig.6 shows the dependence of the surfactant concentration. The bulk Reynolds number is 8200 and the air flux rate is fixed at 1.4 l/min (the void fraction is about 0.6%, but it differs in each case). 3-Pentanol is used as a surfactant and its volumetric concentration changes from 21ppm to 168ppm to the whole volume of the liquid-phase. The photographs on the left side are the ‘front view’ of the channel (*x-z* plane) and the right side are the ‘side view’ (*x-y* plane).

In all cases, 3-pentanol injection avoids the coalescence of bubbles and ‘mono-dispersed’ 1mm bubbles are obtained. Although, two characteristic changes can be seen with the increase of the 3-pentanol concentration. One is a change of the tendency of the bubble migration toward the wall. Under the condition of the low concentration (21ppm and 42ppm), the bubbles strongly accumulate near the wall (Fig.6 (a) (b), side view). However, further increase of the concentration made this accumulation disappear as shown in the side view of Fig.6 (c). That is to say, the tendency of the bubble migration toward the wall becomes weaker with the increase of the concentration of 3-pentanol beyond certain concentration. The other change arises on a number density of the bubbles. The number density of the bubbles gradually rises with the increase of the concentration of 3-Pentanol. This is because the rising velocity of the bubble becomes smaller due to the increase of the drag on each bubble originated in so called Marangoni effect. More details on this Marangoni effect to the bubble motion is discussed in the next section.

The relation between the bubble cluster in the vicinity of the wall and the concentration of the 3-pentanol is shown in the ‘front view’ photos. In the present study, the most notable bubble clusters are observed in the case of 42ppm. (Fig.6 (b)). Fig.7 shows the bubbly flow in 2ppm Triton-X100 solution. Triton-X100 is the surfactant

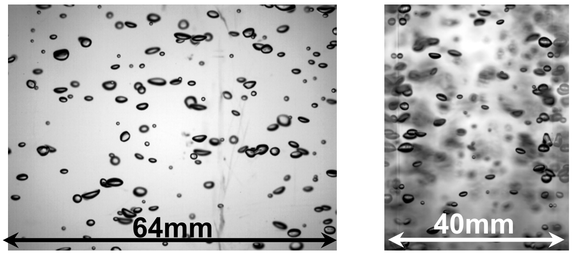

Fig.5 Photographs of bubbly flow without surfactant (Re_b=8200, the average void fraction of about 0.6%). Left; front view, Right; side view.

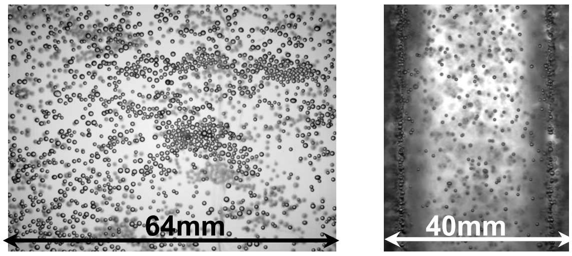

(a) 21ppm 3-Pentanol

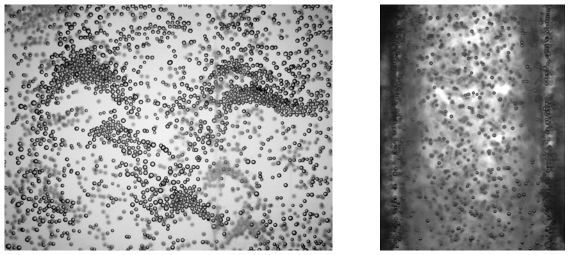

(b) 42ppm 3-Pentanol

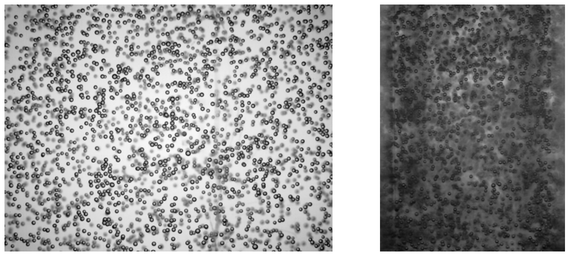

(c) 168ppm 3-Pentanol

Fig.6 Photographs of bubbly flow with a variation of the surfactant concentrations (3-Pentanol, Re_b=8200, air injection with the constant flux rate and the average void fraction of about 0.6%). Left; front view, Right; side view.

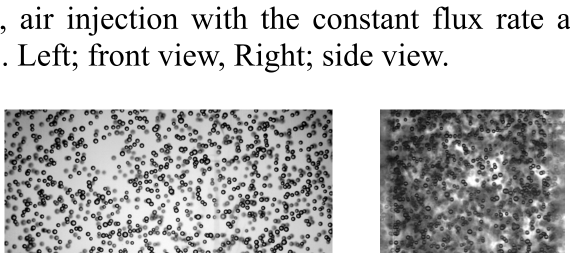

Fig.7 Photographs of bubbly flow with 2ppm Triton-X100. (The other conditions are the same as in the case of Fig.4 and Fig.5.) Left; front view, Right; side view.

which has heavier molecular weight compared with 3-Pentanol. It can cause a stronger Marangoni effect with the small amount of solution. It is shown that the bubbles distribute uniformly across the channel. There is no bubble cluster appeared in this case because the bubbles do not migrate and accumulate near the wall.

Surfactant Effect on Bubble Motions

One of the most important surfactant effects on a bubble motion is Marangoni effect (levich1962), that is, the shear stress on the bubble surface is produced by the non-uniform surfactant adsorption. Regarding to this phenomenon from a continuum scale point of view, a surface velocity becomes lower and the drag on the bubble increases. That is to say, the Marangoni effect changes the boundary condition on the bubble surface from free-slip to no-slip. Fig.8 shows experimental results for the drag coefficient($C_D = F_D \Big/ \left(\frac{1}{2} \rho U^2 \pi a^2 \right)$) of a nearly spherical bubble in quiescent liquid. Re_b is a bubble Reynolds number and is defined using the bubble diameter and the relative velocity of a bubble. In 3-pentanol solution, the bubble takes the intermediate value of C_D between the clean bubble and the rigid sphere. Increasing the concentration of 3-pentanol, drag coefficient increases from that of free-slip to no-slip. In the case of Triton X-100 solution of 2ppm, C_D is almost the same as that of rigid sphere. Takagi *et al.* (2004) conducted experiment and numerical simulation of single bubble and evaluated quantitatively the surface velocity of the rising bubble in quiescent liquid with surfactant solution. It was shown that, in 3-Pentanol of 4-150 ppm solutions, the surface velocity takes an intermediate value between in the case of free-slip condition and no-slip condition. On the other hand, in Triton-X100 of only 0.9ppm solution, it was shown that the surface becomes totally no-slip and can be regarded as that of rigid particle. From these results, it is expected that the bubbles in 3-Pentanol solutions have half-slip surface and the bubble in Triton X-100 solution has almost no-slip surface in the present experiment.

Next, we discuss how this Marangoni effect can affect the lateral migration toward the wall. It is explained as follows. Numerical studies on the lift force on a spherical bubble (Legendre and Magnaudet (1998)) and on a rigid sphere (Kurose and Komori(1999)and Bagchi and Balachandar (2002)) in a viscous linear shear flow was conducted. Those results are shown in Fig.9. C_L is calculated as $C_L = F_L \Big/ \left(\frac{4}{3} \pi a^3 \rho U \alpha \right)$, following Auton's expression. *Sr* denotes non-dimensional shear rate which is the ratio between the velocity difference across the bubble and the relative velocity.

In the present experimental conditions, bubble Reynolds number(Re_b) is about 100, and the fully contaminated bubble such as the one in Triton X-100 solution can be regarded as a rigid sphere. In this condition of Re_b=100, the lift force on a spherical bubble is more than 10 times larger than that on a rigid sphere. And, the lift force coefficient for rigid sphere can be a slightly negative value, which corresponds to the effect of the lateral migration toward the center. Therefore, under this condition, the lift coefficient of the rigid sphere is considerably less than that of the clean bubble. In the case of 21ppm 3-pentanol solution, it might be expected that the lift coefficient takes an intermediate value and it decreases as the surface condition approaches to the no-slip condition due to the increase of the concentration. In the case of 2ppm Triton X-100 solution, the lift coefficient may become the same as that of rigid sphere.

Related to this point, Fukuta et al.(2005) simulated the shear-induced lift force with stagnant cap model of a bubble moving in a simple shear flow. They assume the stagnant cap θ_c, below which free-slip (tangential stress free) condition is imposed on the bubble surface and beyond which no-slip condition is imposed. Their results are shown in Fig.10 for the drag coefficient and also for lift coefficient. It is shown that, with the decrease of cap angle (free-slip region on a bubble surface), C_D increases and C_L decreases. This decrease of the lift coefficient seems to be the main reason why the tendency of the lateral migration of bubbles toward the wall disappears with the stronger Marangoni effect.

Here, we further investigate the more detail analysis with the adsorption/desorption kinetics of surfactant taken into account. Using the numerical method explained in the previous sections, we have conducted the numerical simulations of a bubble rising in a simple shear flow of surfactant aqueous solution. Fig.11 and 12 shows the result of Langmuir number dependence of C_D and C_L, respectively. It has been shown by Takagi et al.(2004), that the Marangoni effect is strongly related to Langmuir number. That is, if the surfactant is not easy to desorb from bubble surface, they take a larger Langmuir number and shows a stronger Marangoni effect.

From Fig. 11, it is found that C_D becomes larger from the value for a clean bubble (Legendre & Magnaudet 1998) to that for a rigid sphere (Mei 1993) with the increase of *La*. This gives the reduction of rising speed of bubbles in surfactant solutions confirmed by previous experimental studies (Zhang & Finch 2001, Takagi et al. 2003). When *La* is so large ($= 1.12\text{x}10^{-1}$) that the bubble surface is contaminated sufficiently, C_D of bubble reaches the value for the rigid particle. On the other hand, C_L decreases from the value for a clean bubble calculated by Legendre & Magnaudet (1998) when *La* increases as shown in Fig. 8. At the numerical condition of this study, the dependency of C_L on *La* began appearing at the region of $La \sim O(10^{-3})$, and C_L reached almost zero at $La = 4.48\text{x}10^{-2}$. When we set larger *La*, C_L became negative value, $C_L < 0$, which was already discussed in Fig.9. To analyze these changes of forces on bubbles, the contributions of pressure to the drag coefficient C_{DP}, to the lift coefficient C_{LP}, normal viscous stress to the drag coefficient C_{DV}, to the lift coefficient C_{LV} are plotted in Fig.11 and 12. Note that $C_{DP} + C_{DV}$ equals C_D and $C_{LP} + C_{LV}$ equals C_L. For the drag force on bubbles shown in Fig.11, C_{DP} and C_{DV} contribute comparably at each *La* number and show the similar dependency on *La*. Thus it is found that both the pressure and viscous contribution become important to the drag force. However, for the lift force shown in Fig.12, C_{LP} contributes more significantly than C_{LV} at low *La*, where the large lift force acts on the bubble. This means that the lift force on bubble is dominated by the inertia effect in the condition of this calculation. In the case of a clean bubble, Legendre & Magnaudet (1998) showed that C_{LP} contributes to C_L dominantly and the inertia effects affect significantly to the lift force in the range of $Re > 50$. For the viscous contribution to the lift force on a clean bubble, they displayed that C_{LV} takes small negative value, and it contributes only a few percent to C_L at high Reynolds number. In contrast, for a contaminated bubble, C_{LP} decreases while C_{LV} changes little with the increase of *La* and the contamination of the bubble surface. At high *La* number, where the negative lift force acts on a contaminated bubble, C_{LP} reaches almost zero and the viscous contribution to the lift force becomes dominant at $Re = 100$ and $Sr = 0.2$.

The lift force is greatly affected by the slip velocity of the gas-liquid interface, depending on the surfactant species and their amount. That is, as the free-slip condition approaches to the no-slip condition by the addition of the surfactant, the lift force acting on the bubble decreases and approaches to that on a rigid sphere which has much smaller lift coefficient. This is one of the reason why the tendency of bubble migration weaken with the increase of concentration of 3-Pentanol or in Triton-X100 solution. Otherwise, factors, such as an effect of the wall and turbulence, should be taken into consideration, it is certain that shear-induced lift force plays important role about bubble migration.

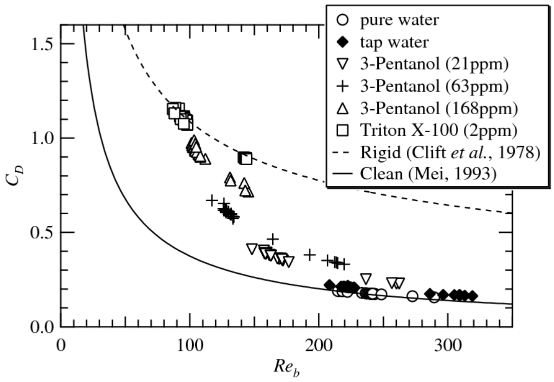

Fig.8 Surfactant dependence on the drag coefficient C_D as a function of bubble Reynolds number Re_b.

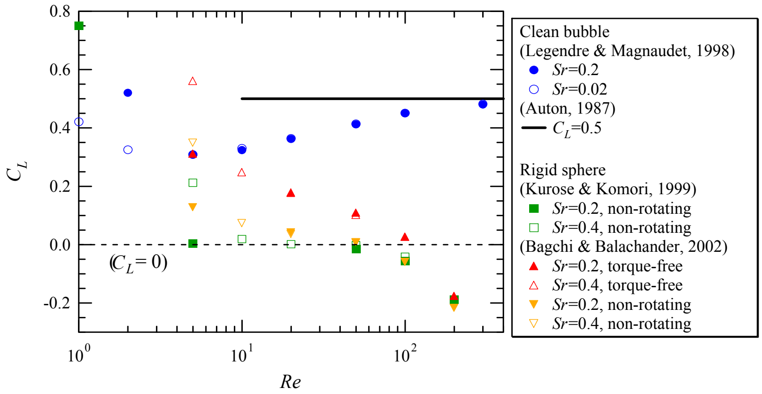

Fig.9 Lift coefficient C_L for a rigid sphere (Kurose & Komori 1999, Bagchi & Balachandar 2002) and clean bubble (Legendre & Magnaudet 1998).

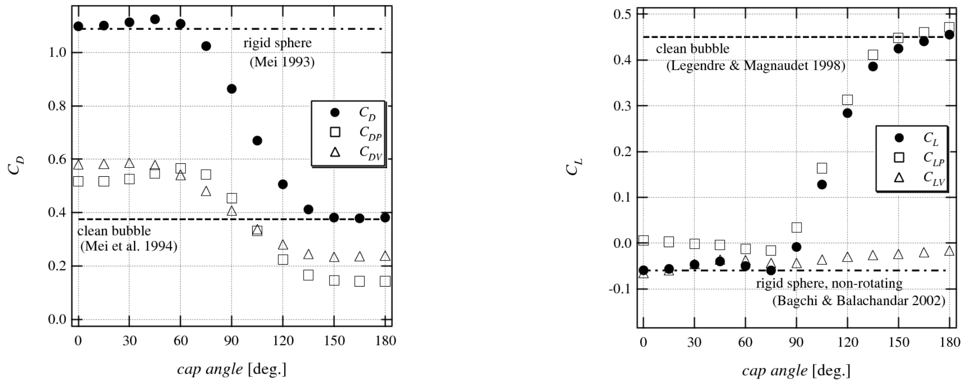

Fig. 10**:** Drag coefficient C_D (left) and lift coefficient C_L (right) for stagnant cap bubble in simple shear flow at Re_b=100. (Fukuta et al.(2005))

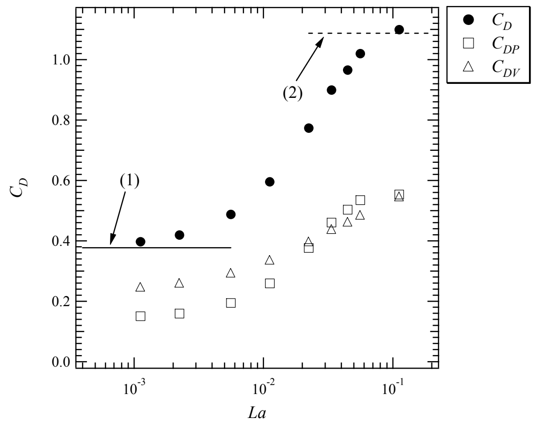

Fig.11 The plot of C_D of a bubble versus *La*.
(Line(1): clean bubble (Legendre & Magnaudet 1998), Line(2): rigid sphere (Mei 1993).)

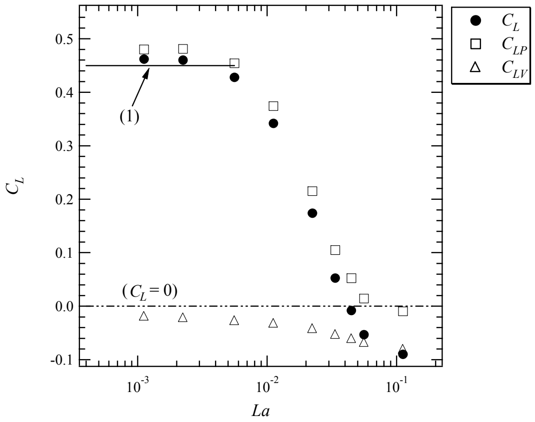

Fig. 12 The plot of C_L of a bubble versus *La*.
(Line(1): clean bubble (Legendre & Magnaudet 1998).)

Conclusions

The effect of surfactants to the upward bubbly channel flow has been introduced. By adding a small amount of 3-pentanol or Triton-X100 as surfactant, small spherical bubbles of mono-dispersed 1mm diameter were successfully obtained. The experiments were conducted under the condition of bulk Reynolds number of 8200 and average void fraction of less than 1%. It was found that the addition of the surfactant affects the whole bubbly flow structure. And the structure was drastically changed by changing the bulk concentration or the species of surfactant.

Under the condition of about 10-100 ppm concentration of 3-pentanol, small bubbles tend to accumulate near the wall and slide up along the wall. These accumulated bubbles near the wall form the horizontal bubble clusters of about 10-40mm in size in spanwise direction, which has a thin crescent-like shape. The average cluster size is much bigger than well-known coherent vortical structure in turbulent boundary layer. This fact indicated the drastic modification of turbulent flow structure. Interestingly, the increase of 3-pentanol concentration or the change of surfactant to small amount(2ppm) of Triton X-100 drastically change the whole bubbly flow structures. Under these conditions, bubble clusters are totally disappeared and lateral migration of bubbles toward the wall is no longer observed.

Numerical analysis was also conducted related to the effect of surfactant on a single bubble motion in a simple shear flow. It was shown that Marangoni effect due to the surfactant adsorption on bubble surface gives the drastic change of the lift force acting on 1mm size bubbles. This change of lift force gives the different tendency on the lateral migration of bubbles toward the wall. That is, slightly contaminated bubbles can feel the Auton's-like lift force and migrate toward the wall. This end up with the formation of bubble clusters near the wall. On the other hand, fully contaminated bubble cannot feel the lift force and they disperse uniformly across the channel without forming bubble clusters.

As is shown here, small amount of surfactant gives a drastic effect to the mutiscale structure bubbly flows. That is, surfactant affects the small scale behaviour of each bubble and then this change of bubble behaviour ends up with the large scale change of whole bubbly flow structures.

References

Auton, T. R. (1987), *J. Fluid Mech.* **183**, 199-218.

Bagchi, P. and Balachander, S. (2002), *Phys. Fluids* **14**-8, 2719-2737.

Ceccio SL. (2010), *Annu. Rev. Fluid Mech.* **42**, 183--203

Cuenot, B., Magnaudet, J. and Spennato, B. (1997), *J. Fluid Mech.* **339**, 25-53.

Fdhila, R. B. and Duineveld, P. C. (1996), *Phys. Fluids* **8**, 310-320.

Frumkin, A. and Levich (1947), V. G., *Zh. Fiz. Khim.* **21**, 1183-1204.

Fukuta M, et al. (2005), *Theo. Appl. Mech. Japan*, **54**, 227-234.

Kasagi, N., et al. (1992), A., *Trans. ASME: J. Heat Transfer* **114**-3, 598-606.

Kuruse, R. and Komori (1999), S., *J. Fluid Mech.* **384**, 183-206.

Lance, M. and Bataille, J. (1991), *J. Fluid Mech.* **222**, 95-118.

Legendre, D. and Magnaudet (1998), J., *J. Fluid Mech.* **368**, 81-126.

Levich, V. G. (1962), *Physicochemical Hydrodynamics*, Prentice- Hall,.

Liu, T. J. and Bankoff, S. G. (1993a), *Int. J. Heat Mass Transfer* **36**-4, 1049-1060.

Liu, T. J. and Bankoff, S. G. (1993b), *Int. J. Heat Mass Transfer* **36**-4, 1061-1072.

Mazzitelli, I. M., Lohse, D. and Toschi, F. (2003), *J. Fluid Mech.* **488**, 283-313.

McLaughlin, J. B. (1996), *J. Colloid Interface Sci.* **184**, 614-625.

Mei, R. (1993), *Int. J. Multiphase Flow*, **19**, 509-525.

Sangani, A.S. and Didwania A.K. (1993), *J. Fluid Mech.* **250**, 307-337.

Serizawa, A. et al. (1975), *Int. J. Multiphase Flow* **2**, 235-246.

Smereka, P. (1993), *J. Fluid Mech.* **254**, 79-112.

So, S-H., Morikita, H., Takagi, S. and Matsumoto, Y. (2002), *Exp. in Fluids* **33**, 135-142.

Sugiyama K, Calzavarini E, Lohse D. (2008), *J. Fluid Mech.* **608**, 21--41

Takagi, S., Uda, T., Watanabe, Y. and Matsumoto, Y. (2004), *Trans. JSME*: B **69**-686, 2192-2199, in Japanese.

Takagi, S. and Matsumoto, Y., (2011), *Annu. Rev. Fluid Mech.*, **43**, 615-636.

Theofanous, T. G. and Sullivan, J. (1982), *J. Fluid Mech.* **116**, 343-362.

Wang, S. K., Lee, S. J., Jones Jr., O. C. and Lathey Jr., R. T. (1987), *Int. J. Multiphase Flow* **13**-3, 327-343.

Zenit, R., Koch, D. L. and Sangani, A. S. (2001), *J. Fluid Mech.* **429**, 307-342.

Zhang, Y. and Finch, J. A. (2001) , *J. Fluid Mech.* **429**, 63-66.

Multiscale Simulation for Polymer Material Design

Takeshi Aoyagi
Analysis and Simulation Center, Asahi Kasei Corporation
e-mail:aoyagi.tb@om.asahi-kasei.co.jp

Abstract

In this article, we introduce recent activities of multiscale polymer modeling aimed for material design in industry. To design the polymer material with expected properties, we need to predict polymer structure, and study the relation between the structure and properties. However, polymer structure is hierarchical, and has a wide range of length scale and time scale. Thus, multiscale and hierarchical modeling are necessary to apply computational simulation to polymer material design. OCTA had been developed for such a hierarchical polymer modeling. OCTA includes several simulation programs, which are based on different physical model, and focus on different length scale and time scale. Some studies of hierarchical modeling of polymer have been conducted using OCTA. We describe an overview of OCTA, and an example of the study of the structure and mechanical properties of the interface of polymer blends.

1. Introduction

Polymer materials such as plastics, rubber, film and fiber are widely used for industrial products. Not only conventional bulk materials, polymer materials are also used in many high-tech materials such as electric devices, battery and artificial organ. Various kinds of function are required for such polymer products. For example, mechanical properties such as modulus and strength are important for construction materials, and electrical and optical properties such as dielectric constant and reflective index are important for electric devices and optical films. Since such functions and properties are controlled by the structure of polymers, main objective of polymer material design is to design the structure of polymers and to predict the properties of the materials from the structure.

However, the structure of polymers includes very wide range of length scale and time scale. Figure 1 shows examples of various polymer structures. Chemical structure of monomer unit is a finest structure of polymers. The topological structure of polymer chain is not simple. Not only linear chains, some polymer molecules have branched structure, and the length of chains corresponding molecular weight is not the same, and has a distribution even in same polymer products such as polyethylene, polystyrene and so on. In addition to the molecular structure, crystalline structure and phase separated structure are examples of higher order structure. Furthermore, crystal structure itself has a hierarchical structure, i.e. atomic coordinate in crystalline lattice is the finest crystal structure, and lamella, shish kebab and spherulite structure are higher order crystal structure. Since the polymer structure includes such a wide range of scale, multi scale and multi physics modeling is necessary to design polymer materials.

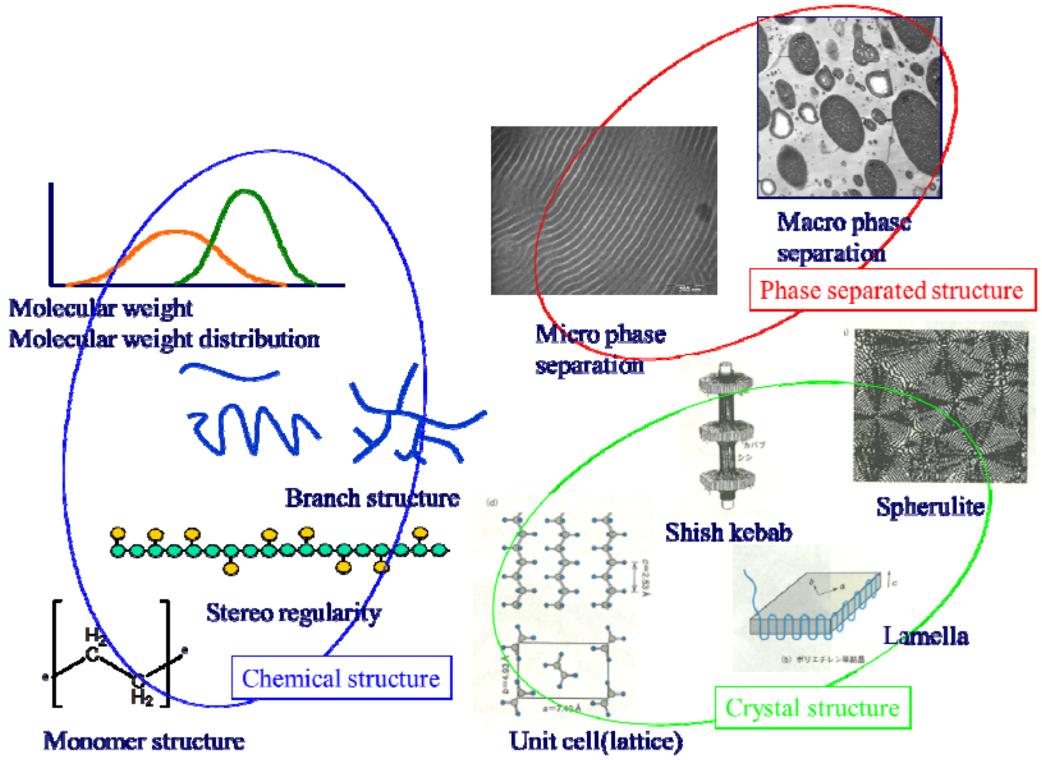

Figure 1 Example of polymer structure

Furthermore, various simulation methods are necessary to study such a hierarchical structure and many kinds of functions and properties of polymer materials. For examples, quantum physics and chemistry are needed to study electrical and optical properties. Molecular dynamics simulation will be applied to study bulk structure of polymer. However, since polymer chain has a large molecular weight and long time scale of dynamics, it is hard to apply conventional molecular dynamics simulation to realistic polymer system even though using powerful computational hardware. Thus coarse-grained models are also needed to study higher order polymer structures.

OCTA (Open Computational Tool for Advanced material technology)[1] is a simulation platform aimed for covering such a wide range of polymer structure. The OCTA was developed in a national project of Japan, and then the OCTA was opened for the public after the project finished. From the release of the first version of OCTA in April 2002, it has been maintained by many collaborators, and the researchers in more than 1000 sites have become the users.

We will introduce the overview of OCTA in the following section and an example of hierarchical modeling to study of structure and mechanical properties of the interface of polymer blends.

2. Overview of OCTA

The concept of OCTA is shown in Figure 2. The OCTA contains several simulation programs (engine) and user interface (platform). Each engine is based on different physical models, and covers different length scale and time scale. Furthermore, collaborative operations between engines are conducted to obtain realistic structures and properties of soft materials.

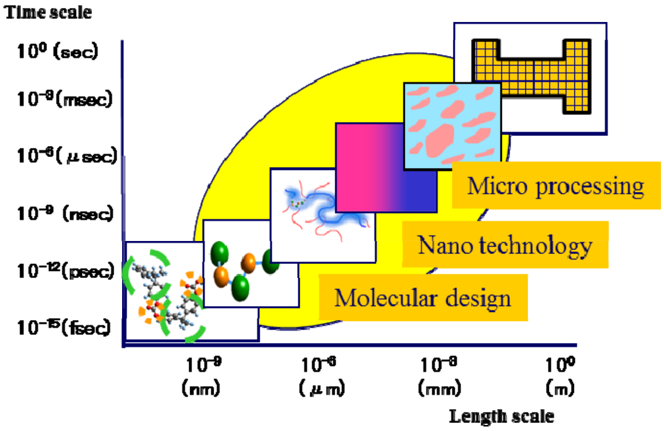

Figure 2. The concept of OCTA

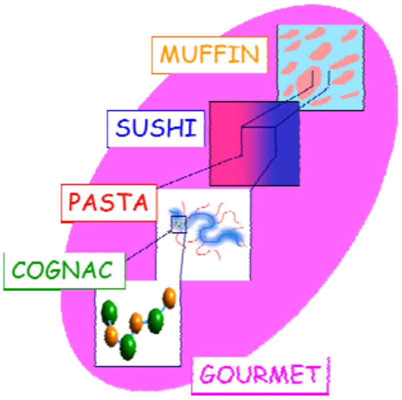

Figure 3. Computational programs in OCTA

Figure 3 shows computational programs in OCTA. OCTA originally contains four engines, COGNAC, PASTA, SUSHI and MUFFIN, and a graphical user interface, GOURMET. The overview of each engine is shown in the following.

2.1. COGNAC (COarse Grained molecular dynamics program by NAgoya Cooperation)[2]

COGNAC is a general purpose coarse-grained molecular dynamics (MD) program, which focus on the structure and dynamics of polymer chains. Using coarse-grained model, realistic length of polymer chains can be put into the simulation system, and some multiphase structures such as nano-composites and micro phase separated structure of block copolymers can be studied. Figure 4 shows example of multiphase structures studied by COGNAC.

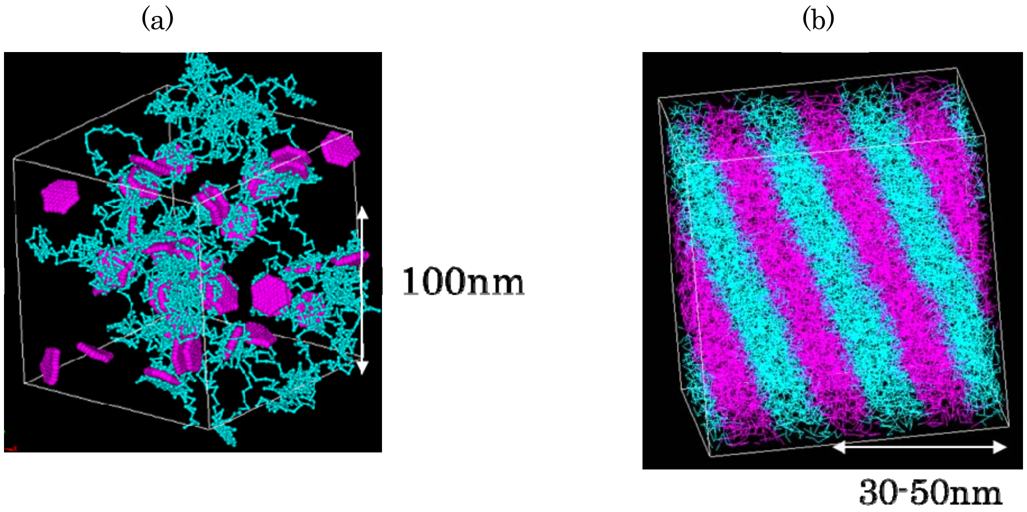

Figure 4. Examples of multiphase structures studied by COGNAC, (a) polymer-clay nano composite (b) micro phase separated structure of diblock copolymer. Scales in figures show typical values, and depend on the coarse-graining method.

2.2. PASTA (Polymer rheology Analyzer with Slip-link model of enTAnglement)[3]

PASTA is based on slip-link model, and predicts the viscoelastic properties of polymer melts. A unit of length scale of coarse-graining is entanglement length, which typically have molecular weight from 1,000 to 10,000. With this highly coarse-grained model, we can predict viscoelastic properties, such as storage modulus G', loss modules G" and steady state viscosity η, of realistic molecular weight and molecular weight distribution.

2.3. SUSHI (Simulation Utilities for Soft and Hard Interfaces)[4]

SUSHI is a tool for predicting self-assembly structures such as micro phase separation of block copolymers, interfacial structures of polymer blends and structures of micelles. SUSHI is based on mean field theory and topology of polymer chain is described by path integral. SUSHI output equilibrated fields of polymer segment density by iterative calculation of self-consistent filed (SCF). Dynamics of density field also can be obtained by solving diffusion equation. Figure 5 show examples of the output of SUSHI.

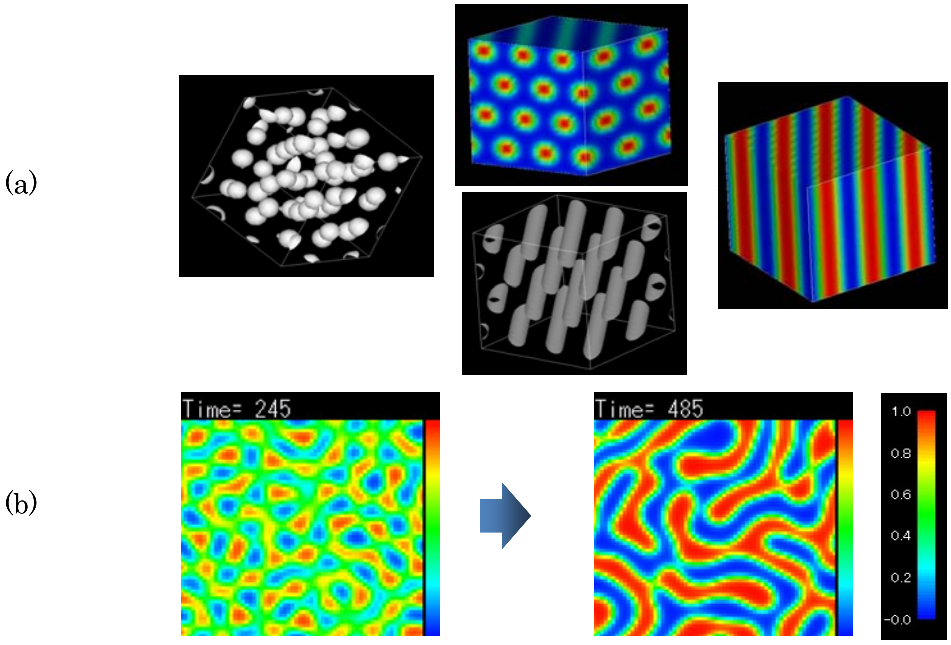

Figure 5 Examples of the output of SUSHI, (a) equilibrated morphology of diblock copolymers at various ratio of block length, (b) dynamics of the phase separation of polymer blend.

2.4. MUFFIN (MultiFarious FIeld simulator for Non-equilibrium system)

MUFFIN is a tool for multi-phase structure such as phase separation of polymer blends, suspensions and emulsions. MUFFIN has modules both for fluids and solids. Fluid modules of MUFFIN can handle phase separation of polymer blends, dynamic of droplet in fluids with taking fluid dynamics and electrostatic interaction into account. Solid modules calculate linear elastic behavior of complex multi-phase morphology using finite element method.

3. Example of hierarchical modeling[5,6]

An example of hierarchical modeling is shown in this section. Coarse-grained MD simulation and SCF calculation has been conducted to examine the structure and strength of a polymer interface reinforced with block copolymers. We studied the interface of A-homo/AB-diblock/B-homo polymer systems. Since the time scale of polymer chain dynamics is very long, it's difficult to obtain the equilibrated interfacial structure even by the coarse-grained simulation. Thus, we developed original algorithm, the density-biased Monte Carlo method[2], in which equilibrated morphologies are obtained by the SCF calculation, then the initial configurations of polymer chains for coarse-grained MD are generated from the obtained density distribution of each segments. Figure 6 shows density profile of A100/B100 blend and A100/A50B50/B100 blend (numbers after bead type A and B correspond to a number of beads in a chain) obtained from the SCF calculation, and Figure 7 shows snapshot structures of coarse-grained MD which correspond to the results of SCF calculation.

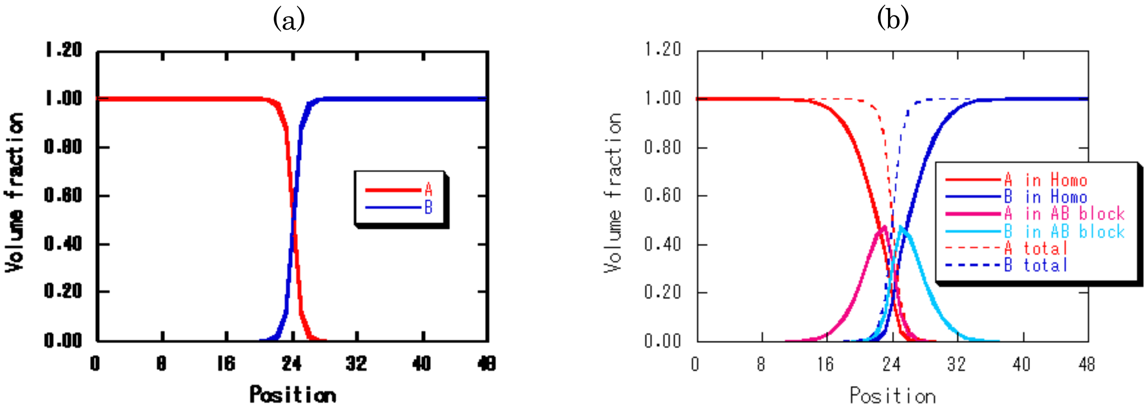

Figure 6 Density profile of each segment type, (a) A100/B100, (b) A100/A50B50/B100.

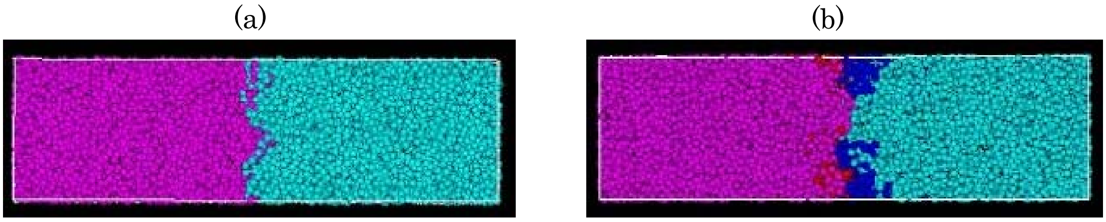

Figure 7 Snapshot structure of the interface of polymer blends, (a) A100/B100, (b) A100/A50B50/B100.

Stress-strain behavior was studied by elongating the unit cell during the coarse-grained MD simulation. Figure 8 shows an example of stress-strain curve and snapshot structure at specified strain. In this system, the fracture of interfaces was observed at around 4% strain.

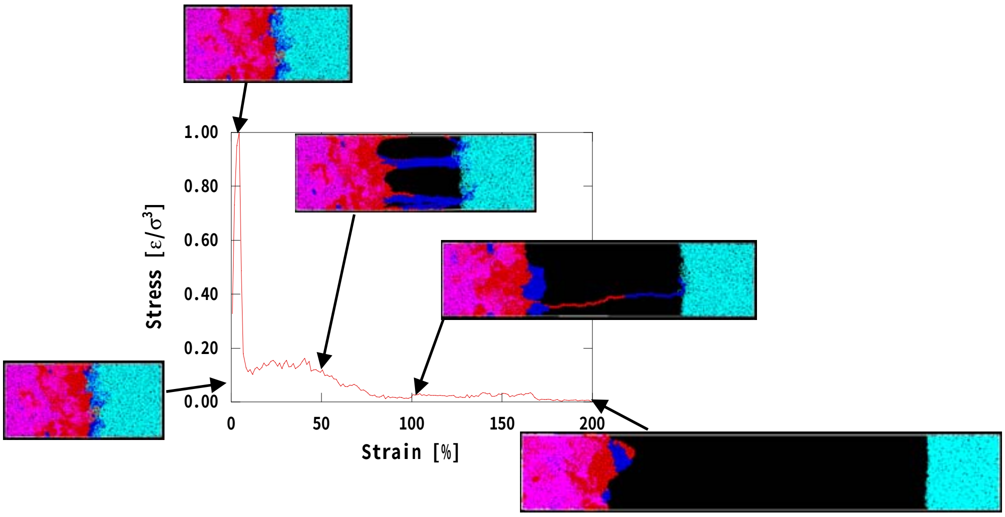

Figure 8 Stress-strain curve of the interface of polymer blend with diblock copolymer (A120/A120B30/B120) system. Inserted picture is snapshots at specified strain.

The fracture energy was calculated by integrating the stress during elongation until the interfaces were completely separated. Figure 9 shows the fracture energy as a function of surface density of block copolymers.

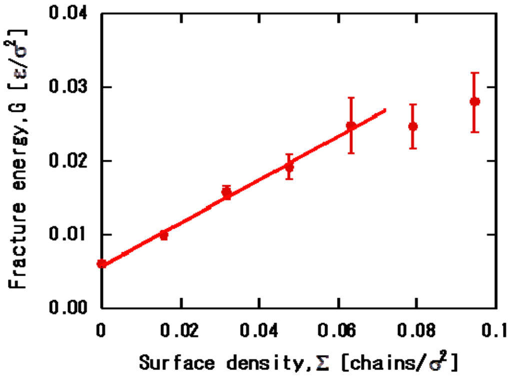

Figure 9 Fracture energy as a function of surface density of diblock copolymer.

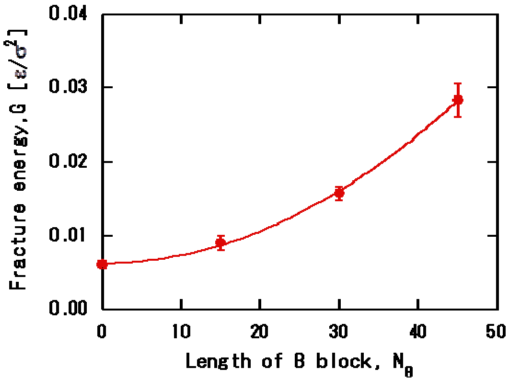

Figure 10 Fracture energy as a function of the length of shorter block.

We found that the fracture energy was proportional to the volume fraction of block copolymer until the interface was saturated with block copolymers. Figure 10 shows the interfacial energy as a function of the length of shorter block of copolymers, which is pulled out from the homopolymer phase. The fracture energy was proportional to the square of the length of the shorter block of the copolymer. These results were consistent with experimental results[7] and theoretical predictions concerning the "pull-out" region[8], where one block of diblock copolymers was short enough not to become entangled.

4. Summary and current problems to be solved

The OCTA project was thought to be succeeded as a first step of multiscale modeling of polymer materials. However, we still need to enhance the science and technology to conduct multiscale modeling, which truly contributes the polymer material design in industry. We show some examples, which are current problems to be solved in the field of polymer modeling in the following;

(1) Large scale computing

Even though we use coarse-grained model, we still need large scale computing to handle the realistic length scale and time scale. In addition to hardware, we need effective software such as massively parallelized code running on high performance hardware.

(2) Effective coarse-graining

Coarse-graining usually loses the chemical details. However, the industrial researches often require the detail of chemical structure for material design. Thus we need more general and quantitative coarse-graining method to reproduce the structure and properties of materials originated from chemical structures.

(3) Quantitative analysis of complex morphology

Self-assembly structure shows complex morphology especially in the case of complex and non-equilibrated system. We need quantitative analysis for such a complex morphology to study the relation between structures and properties.

(4) Boundary conditions for multi scale modeling

When we try to connect two computational model of different length scale, it's always problem how to transfer the boundary condition of small system to large system especially in the case of particle model. Periodic boundary condition is a simple boundary condition. However, we can't directory put small systems with periodic boundary condition into large system, which has gradient of fields in a large scale.

We belieave that many of the problems are not pecific for polymer materials, but also for general computatioal simulation and mathematical science. Thus, we hope that we would make progress to overcome the peoblems with the collobaration of physics, chemistry and mathematical science.

References:

---

[1] See web page http://octa.jp/. The package is also available from the web site.

[2] T.Aoyagi, F.Sawa, T.Shoji, H.Fukunaga, J.Takimoto, M.Doi, *Comput. Phys. Commun.*, **145**, 267 (2002).

[3] J.Takimoto, H.Tasaki, M.Doi, Proceedings of the XIIIth International Congress on Rheology, **2**, 97 (2000).

[4] T.Honda, S.Urashita, H.Morita, R.Hasegawa, T.Kawakatsu, M.Doi, *Kobunshi ronbunsyu*, **56**, 762 (1999).

[5] T.Aoyagi J.Takimoto, M.Doi, *Proceeding of International Conference on Advanced Polymers and Processing,* 217 (2001).

[6] T.Aoyagi, *Nihon Reoroji Gakkaishi*, **37**, 69 (2009).

[7] C.Creton, E.J.Kramer, C-Y Hu, H.R.Brown, *Macromolecules*, **25**, 3075 (1992).

[8] D-B.Xu, C-Y Hui, E.J.Kremar, C.Creton, *Mech. Mater.*, **11**,257 (1991).

Multiscale Simulations of Nonlinear Phenomena of Plasmas

R. Numata*

Graduate School of Simulation Studies, University of Hyogo,
7-1-28 Minatojima Minami-machi, Chuo-ku, Kobe, Hyogo 650-0047, Japan

Abstract

Multiscale hierarchy is intrinsic in collsionless plasmas, where various kinetic effects having their own scales play important roles. Gyrokinetics and the gyrokinetic code `AstroGK` are introduced to study multiscale phenomena in plasmas. An application of the gyrokinetic simulation using `AstroGK` to magnetic reconnection as an example of multiscale phenomenon is discussed.

1 Introduction

Plasmas observed in fusion experiments or in wide varieties of astrophysical situations such as the galaxy clusters, the interstellar medium, the solar corona, solar winds, the Earth's magnetosphere are typically in high temperature or in low density. Since collisions can be rare in such plasmas, deviations from thermal equilibrium can be maintained relatively long times. In thermally non-equilibrium plasmas, effects due to particle pictures of plasmas called kinetic effects play crucial roles on plasma dynamics. Examples of the kinetic effects include inertia of ions and electrons having intrinsic scales of inertial skin depths, and finite Larmor radius (FLR) effects of ions and electrons. These effects usually generate fine structures in velocity space, therefore enhance dissipations due to collisions even though collisionality is considered to be low.

Nonlinear phenomena in kinetic plasmas usually exhibit multiscale structures where various kinetic effects working at their intrinsic spatial scales are inter-related. The gyrokinetic approach is well-suited to study kinetic dynamics of plasmas. Gyrokinetics is a limit of kinetic model that describes the low-frequency dynamics of weakly collisional plasmas. It is derived by averaging the kinetic Vlasov-Landau equation and Maxwell's equation over the fast cyclotron motion, thus it omits the fast MHD waves, the cyclotron resonance, but retains FLR effects, and collisionless wave-particle interactions via the Landau resonance.

The theoretical foundation of gyrokinetics has been developed extensively over the past four decades, and gyrokinetics is now broadly employed for numerical studies of turbulence driven by microinstabilities in laboratory plasmas. It has also been recently recognized that the gyrokinetic approach is appropriate for the study of astrophysical plasmas. Taking

---

*E-mail: numata@sim.u-hyogo.ac.jp.

advantage of the knowledge and computational techniques developed in the simulation of turbulence in fusion plasmas, we have developed a gyrokinetic simulation code, `AstroGK` [1], specifically for the study of astrophysical problems and basic properties of plasmas.

In this paper, we first present our approach to study multiscale phenomena in plasmas: gyrokinetics and gyrokinetic simulation using `AstroGK`. `AstroGK` has already proven its usefullness in a number of studies. Among others, we show our recent result on the tearing instability as a typical example of multiscale phenomena in plasmas even though the result is still in preliminary linear stage.

2 Gyrokinetics and `AstroGK`

In this section, we present the gyrokinetic-Maxwell (GK-M) system of equations solved in `AstroGK`, and brief overview of the code.

We first assume that scale separations in space and time are well satisfied such that small fluctuations are locally embedded in a background plasma which is slowly varying spatially and temporally. We consider a temporally constant mean magnetic field $\boldsymbol{B}_0 = B_0\hat{\boldsymbol{b}}_0$. In the presence of a mean magnetic field, we can adopt the gyrokinetic ordering and average over the fast cyclotron motion to reduce the Vlasov–Maxwell equations to the GK-M equations; see Howes et al. [2] and Schekochihin et al. [3] for derivations of these equations expressly intended for the study of astrophysical plasmas. We also assume spatially uniform background for the sake of simplicity.

Under the gyrokinetic ordering, the distribution function of particles up to the first order is given by

$$f_s = \left(1 - \frac{q_s\phi}{T_{0s}}\right) f_{0s} + h_s, \tag{1}$$

where $s = \mathrm{i}, \mathrm{e}$ (stands for ions and electrons) is the species label, $f_{0s} = n_{0s}/(\sqrt{\pi}v_{\mathrm{th},s})^3 \exp(-v^2/v_{\mathrm{th},s}^2)$ is the zeroth-order, equilibrium Maxwellian distribution function. The first-order part of the distribution function is composed of the Boltzmann response term, and the gyro-center distribution function h_s defined in the gyro-center coordinate $(\boldsymbol{R}_s, \boldsymbol{V}_s)$ where the coordinate transform is given by

$$\boldsymbol{R}_s = \boldsymbol{r} + \frac{\boldsymbol{v}\times\hat{\boldsymbol{z}}}{\Omega_s}, \qquad \boldsymbol{V}_s = \boldsymbol{v}. \tag{2}$$

Upon averaging over the gyro-phase, the gyrokinetic equation evolves $h_s = h_s(X_s, Y_s, Z_s, V_{\parallel,s}, V_{\perp,s}, t)$:

$$\frac{\partial h_s}{\partial t} + V_{\parallel,s}\frac{\partial h_s}{\partial Z_s} + \frac{1}{B_0}\left\{\langle\chi\rangle_{\boldsymbol{R}_s}, h_s\right\} = \frac{q_s f_{0s}}{T_{0s}}\frac{\partial\langle\chi\rangle_{\boldsymbol{R}_s}}{\partial t} + C(h_s), \tag{3}$$

where parallel and perpendicular subscripts refer to directions with respect to the mean magnetic field. The gyrokinetic potential is given by $\chi = \phi - \boldsymbol{v}\cdot\boldsymbol{A}$, and the linear collision term is represented by $C(h_s)$. The angle bracket $\langle\,\cdot\,\rangle_{\boldsymbol{R}_s}$ denotes the gyro-average at fixed gyro-center coordinate $\boldsymbol{R}_s$:

$$\langle F(\boldsymbol{r})\rangle_{\boldsymbol{R}_s} = \frac{1}{2\pi}\oint F\left(\boldsymbol{R}_s + \frac{\boldsymbol{V}_s\times\hat{\boldsymbol{Z}}}{\Omega_s}\right)\mathrm{d}\Theta_s, \tag{4}$$

where $\boldsymbol{V}_s = (V_{\perp,s}, V_{\parallel,s}, \Theta_s)$. (The gyro-average at fixed particle coordinate $\langle\,\cdot\,\rangle_{\boldsymbol{r}}$ can also be defined by switching roles of $\boldsymbol{r}$ and $\boldsymbol{R}_s$.)

In the GK-M system, the electromagnetic fields are specified by the three scalar functions $\phi(\boldsymbol{r},t)$, $A_\parallel(\boldsymbol{r},t)$, and $\delta B_\parallel(\boldsymbol{r},t)$ [1] according to:

$$\boldsymbol{B} = \nabla_\perp A_\parallel \times \hat{\boldsymbol{z}} + \delta B_\parallel \hat{\boldsymbol{z}}, \qquad \boldsymbol{E} = -\nabla\phi - \frac{\partial \boldsymbol{A}}{\partial t}. \tag{5}$$

Maxwell's equations in the gyrokinetic limit reduce to the quasi-neutrality condition, and the parallel and perpendicular components of Ampère's law:

$$\sum_s \left[-\frac{q_s^2 n_{0s}}{T_{0s}} \phi + q_s \int \langle h_s \rangle_{\boldsymbol{r}} \mathrm{d}\boldsymbol{v} \right] = 0, \tag{6}$$

$$-\nabla_\perp^2 A_\parallel = \mu_0 \sum_s q_s \int \langle V_{\parallel,s} h_s \rangle_{\boldsymbol{r}} \mathrm{d}\boldsymbol{v}, \tag{7}$$

$$B_0 \nabla_\perp \delta B_\parallel = -\mu_0 \nabla_\perp \cdot \sum_s \int \langle m \boldsymbol{V}_{\perp,s} \boldsymbol{V}_{\perp,s} h_s \rangle_{\boldsymbol{r}} \mathrm{d}\boldsymbol{v}. \tag{8}$$

We refer the reader to [4] for the explicit form of the collision operator used in the code, as it has a rather cumbersome form. We mention here the basic properties of the operator. The operator is based on the linearized Landau collision operator transformed into the gyro-center coordinate. It has second-order velocity derivatives providing diffusion in velocity space and *conserving terms* which include integrations over velocity space. It is constructed to satisfy Boltzmann's *H*-theorem and the conservation of particles, momentum, and energy. It contains both like-species collisions and inter-species collisions, but the inter-species collisions account only for the collisions of electrons with one species of ions with large mass. Note that the linearized collision operator for a given species can be made independent of the first-order evolution of any other species. The theoretical basis of the collision operator is discussed in detail in [5].

`AstroGK` is a Eulerian initial value solver for the GK equation in five-dimensional phase space. It employs a pseudo-spectral algorithm to discretize the gyrokinetic equation in the spatial coordinates (x, y), an upwind finite-difference scheme in the z direction. Velocity space integrals in two dimensional velocity space are calculated using Gaussian quadrature rules. Time integration is made using the 3rd-order Adams-Bashforth for the nonlinear term. The linearized collision operator is treated by the first-order implicit Euler scheme with Sherman-Morrison formula for the moment-conserving corrections.

`AstroGK` is parallelized using MPI, and shows good parallel performance on various cutting edge supercomputers. Parallel performance is measured by taking the weak and strong scalings. The weak scaling is probed by holding the computational work per processing core constant while the number of cores, thus the total problem size, is increased. On the other hand, the strong scaling is probed by holding the problem size constant while the number of processing core is increased. Boths tests are performed on `Kraken` Cray XT5 system at the National Institute for Computational Sciences at the University of Tennessee. `Kraken`

---

[1] $\delta B_\parallel = (\nabla_\perp \times \boldsymbol{A}_\perp)_z$. We use the Coulomb gauge, which leads to $\nabla_\perp \cdot \boldsymbol{A}_\perp = 0$ with the ordering. Then, we can write $\boldsymbol{A}_\perp = \nabla_\perp \varsigma \times \hat{\boldsymbol{z}}$, and $\delta B_\parallel = -\nabla_\perp^2 \varsigma$ in terms of a single scalar function ς.

consists of 8256 computer nodes each having 12 processing cores, resulting in 99,072 compute cores in total.

Figure 1 shows the weak and strong scalings. From the weak scaling result, we observe that `AstroGK` follows the ideal scaling until the number of processors ($N_{\rm proc}$) equals to 12,288 with slight degradation of performance due to the increase of communication for $N_{\rm proc} > 1000$. From the strong scaling, we also observe the ideal scaling up to $N_{\rm proc} = 24,576$. Significant performance loss occurs only at $N_{\rm proc} = 49,152$.

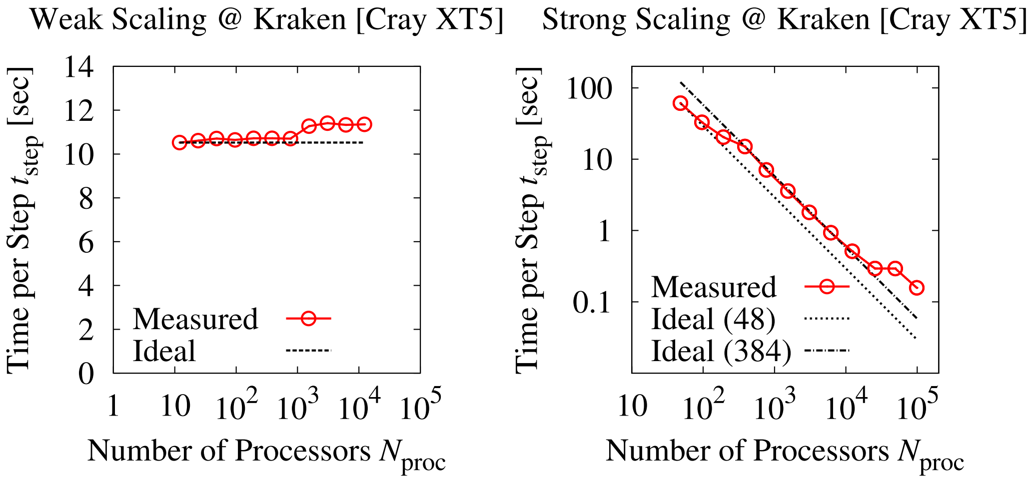

Figure 1: Parallel performance scaling of `AstroGK` on `Kraken` Cray XT5 system at NICS, the University of Tennessee. The left panel shows the weak scaling, and the right panel shows the strong scaling. Nearly ideal scalings are observed up to $10,000 \sim 20,000$ processors.

3 Magnetic reconnection as an example of multiscale phenomena

The tearing instability is important in magnetic fusion devices, where it drives the formation of magnetic islands that can significantly degrade heat and particle confinement. Solar flares and substorms in the Earth's magnetosphere are some of the many other contexts where tearing plays a crucial role, includeing magnetic reconncetion, explosive energy release, and large-scale reconfiguration of the magnetic field.

The evolusion of the tearing instability critically depends on the relationship between the width of the current layer, δ, where the frozen-flux condition breaks down and reconnection takes place, and the length scales characteristic of kinetic or non-magnetohydrodynamic (MHD) effects, such as the ion and electron skin-depth, $d_{\rm i}$ and $d_{\rm e}$, the ion sound Larmor radious, $\rho_{\rm Se}$, and the ion and electron Larmor radii, $\rho_{\rm i}$ and $\rho_{\rm e}$. For, sufficiently large electron-ion collision frequency, $\nu_{\rm e}$, the width of the reconnection layer well exceeds all of these non-MHD scales and the mode is expected to be well described by resistive MHD theory [6]. In many plasmas of interest, however, this is not the case: a decrease in the collisionality of the plasma leads to a decrease in the resistivity, causing the current layer width to shrink until it reaches or falls below the largest relevant non-MHD scale.

3.1 Problem setup

We set up an initial sheared magnetic field

$$\boldsymbol{B} = B_0\hat{\boldsymbol{z}} + B_y^{\mathrm{eq}}(x)\hat{\boldsymbol{y}} \tag{9}$$

where B_0 is the background magnetic guide field and B_y^{eq} is the in-plane, reconnecting component. A super-imposed perturbation onto the equilibrium magnetic field will grow because of the tearing instability.

We scan in collisionality and use the Sptizer's formula to calculate the plasma resistivity η, recast in terms of the Lundquist number, $S = \mu_0 a V_{\mathrm{A}}/\eta = 2.63(\nu_{\mathrm{e}}\tau_{\mathrm{A}})^{-1}(d_{\mathrm{e}}/a)^{-2}$, where V_{A} is the Alfvén velocity corresponding to the peak value of B_y^{eq} and $\tau_{\mathrm{A}} \equiv a/V_{\mathrm{A}}$ is the Alfvén time. Other relevant quantities are:

$$\begin{aligned} \rho_{\mathrm{i}} &= \tau^{1/2}\rho_{\mathrm{Se}}\sqrt{2}, \quad d_{\mathrm{i}} = \beta_{\mathrm{e}}^{-1/2}\rho_{\mathrm{Se}}\sqrt{2}, \\ \rho_{\mathrm{e}} &= \sigma^{1/2}\rho_{\mathrm{Se}}\sqrt{2}, \quad d_{\mathrm{e}} = \beta_{\mathrm{e}}^{-1/2}\sigma^{1/2}\rho_{\mathrm{Se}}\sqrt{2}. \end{aligned} \tag{10}$$

$\sigma \equiv m_{\mathrm{e}}/m_{\mathrm{i}}$, $\tau \equiv T_{0\mathrm{i}}/T_{0\mathrm{e}}$, $\beta_{\mathrm{e}} \equiv n_0 T_{0\mathrm{e}}/(B_0^2/2\mu_0)$, $\rho_{\mathrm{Se}} \equiv c_{\mathrm{Se}}/\Omega_{\mathrm{ci}}$, $c_{\mathrm{Se}} = \sqrt{T_{0\mathrm{e}}/m_{\mathrm{i}}}$, $\Omega_{\mathrm{ci}} = eB_0/m_{\mathrm{i}}$. In addition to ν_{e}, the adjustable parameters considered here include the mass ratio σ, the electron beta β_{e}, ρ_{Se}/a, and τ, although the latter is held fixed at $\tau = 1$.

We study the collisional–collisionless transition by scanning in collisionality. As ν_e is decreased, the different ion and electron kinetic scales become important. Given the challenge of clearly separating all the relevant spatial scales in a kinetic simulation, we split our study into two sets of runs: a smaller-ρ_{Se} series ($\rho_{\mathrm{Se}}/a = 0.02/\sqrt{2} \simeq 0.014$) and a larger-$\rho_{\mathrm{Se}}$ series ($\rho_{\mathrm{Se}}/a = 0.2/\sqrt{2} \simeq 0.14$). Since $\tau = 1$ is held fixed, these two sets of runs also typically correspond to $\rho_{\mathrm{i}}/a = 0.02$ and $\rho_{\mathrm{i}}/a = 0.2$, respectively.

In the former set $\rho_{\mathrm{e}},\ d_{\mathrm{e}} \ll \rho_{\mathrm{Se}} \lesssim \delta \ll a$; in this case the frozen-flux condition is broken by collisions alone, and since δ well exceeds the collisionless electron scales $\rho_{\mathrm{e}},\ d_{\mathrm{e}}$, such scales need not be resolved in the simulations. The ion response, on the other hand, is predominantly collisional ($\delta > \rho_{\mathrm{Se}}$) at the smallest considered values of $S \sim 500$ but kinetic ($\delta \lesssim \rho_{\mathrm{Se}}$) at the largest values, $S \sim 10^5$. Thus resistive MHD would be expected, at least marginally, to be valid in this case at the smaller S values. In the set of runs with larger-ρ_{Se} ($\rho_{\mathrm{Se}}/a \simeq 0.14$), we again consider $\rho_{\mathrm{e}},\ d_{\mathrm{e}} \ll \rho_{\mathrm{Se}} \lesssim a$, but since ρ_{Se}/a is ten times larger than in the previous set of runs, the ions in this second set are predominantly kinetic ($\delta \lesssim \rho_{\mathrm{Se}}$) over the entire considered range of $S \sim 100 - 10^6$. Indeed, at the highest values of S, δ reaches collisionless electron scales (d_{e} at $\beta_{\mathrm{e}} \ll 1$ and ρ_{e} at $\beta_{\mathrm{e}} \sim 1$), and the instability dynamics become essentially collisionless.

In both sets of runs, we vary S over the ranges mentioned above for three different sets of β_{e} and $\sigma = m_e/m_i$: [(β_{e}, σ)=(0.3,0.01), (0.075,0.0025), (0.01875,0.000625)]. These parameters are such that $\rho_{\mathrm{Se}}/d_{\mathrm{e}} \equiv \sqrt{\beta_{\mathrm{e}}/(2\sigma)} = \sqrt{15} \simeq 3.9$ is held fixed and thus, since ρ_{Se}/a is also held fixed (at either 0.014 or 0.14), d_{e}/a is also held fixed (at either 0.0037 or 0.037, respectively). Given the parameter dependences of d_{i} and ρ_{e} noted in (10), however, it is seen that the values of d_{i}/a and ρ_{e}/a both change as β_{e} and σ are varied in this manner: for $\rho_{\mathrm{Se}} = 0.014$, $d_{\mathrm{i}} = 0.02/\sqrt{\beta_{\mathrm{e}}}$ and $\rho_{\mathrm{e}}/a = 0.02\sqrt{\sigma}$, while for $\rho_{\mathrm{Se}}/a = 0.14$ they are ten times larger.

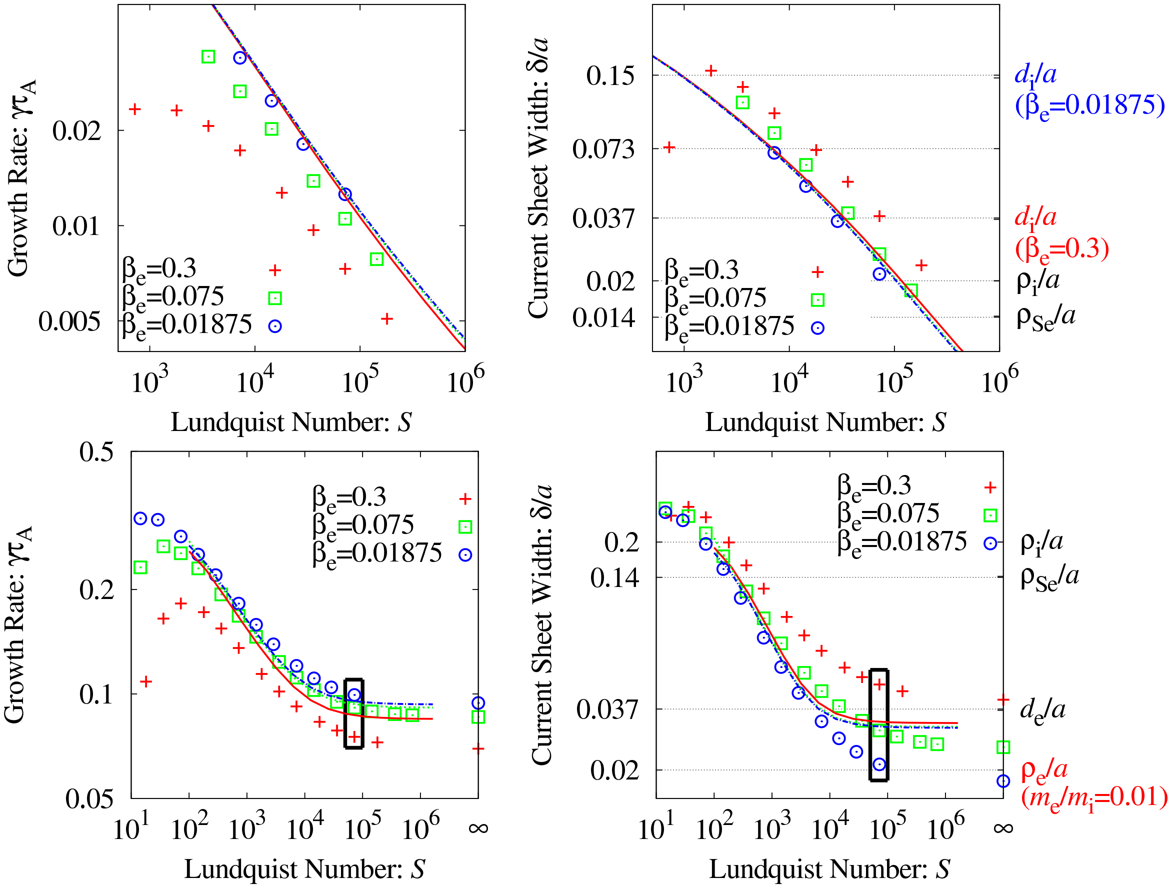

Figure 2: Growth rate and current sheet width versus the Lundquist number for $\rho_{\mathrm{Se}}/a = 0.02/\sqrt{2}$ (upper figures), and $\rho_{\mathrm{Se}}/a = 0.2/\sqrt{2}$ (lower figures). Red crosses, green squares, and blue circles show gyrokinetic results for $(\beta_{\mathrm{e}}, \sigma) = (0.3, 0.01), (0.075, 0.0025), (0.01875, 0.000625)$, respectively. Red solid, green dashed and blue dot-dashed lines are the corresponding two-fluid [7] scalings. The relevant scale lengths are identified on the right axis of the right panel.

3.2 Simulation results

Figure 2 shows the tearing mode growth rate ($\gamma = d \log A_{\parallel}/dt$ evaluated at the X-point) and current layer width (full-width at half-maximum) as functions of the Lundquist number (symbols) for $\tau = 1$. The upper panels correspond to $\rho_{\mathrm{Se}}/a = 0.014$, and the lower panels correspond to $\rho_{\mathrm{Se}}/a = 0.14$. Also plotted (lines) are the results obtained from a reduced two fluid model [7] with an isothermal electron equation of state. This model is derived under the assumption of low-β_{e}, but exactly how low β_{e} must be for the validity of this model depends on how the various quantities in the model are ordered and is thus problem-dependent. For the ordering assumed in [7], it is argued that $\beta_{\mathrm{e}} \ll \sqrt{\sigma}$ is required — a condition that is marginally satisfied here only for the lowest β_{e} case, $(\beta_{\mathrm{e}}, \sigma) = (0.01875, 0.000625)$. The two fluid model is also derived under the assumption of cold ions, but the difference between the gyrokinetic results at $\tau = 0$ and $\tau = 1$ is small.

For the largest value of the collisionality, the gyrokinetic growth rates roll-over because the current layer width is too wide to satisfy the asymptotic scale separation, $\delta \ll a$, assumed in the two-fluid model tearing mode dispersion relation that is plotted in the figure. The deviation between the gyrokinetic and two-fluid results at the lowest S values should therefore be disregarded.

It is seen from the upper right panel that, as noted earlier, $\delta > \rho_{\mathrm{Se}}$ for all but the largest S values. In this case, as expected, the two-fluid model, at least at low-β_{e}, recovers the well-known single-fluid resistive-MHD scalings [6] and is thus independent of β_{e}. The over-estimation of the growth rates by the two fluid model at higher $\beta_{\mathrm{e}} \sim 0.3$ is possibly due to either a breakdown in the low-β_{e} ordering of the fluid model or a gradual onset of kinetic effects (e.g., the invalidity of a simple isothermal equation of state).

For the lower panels, we set $\rho_{\mathrm{Se}}/a = 0.14$, and adjust ν_{e} such that $\delta \lesssim \rho_{\mathrm{Se}}$, thus focusing on the regime where ion kinetic effects are important. As in the previous case, we observe better agreement between the GK and two fluid results for lower values of β_{e}. As S increases, the growth rate and the current layer width are less dependent on the collisionality. In this regime, electron kinetic effects (Landau damping and even finite electron orbits: note that for $\beta_{\mathrm{e}} = 0.3$, $\delta/\rho_{\mathrm{e}} \approx 2$) play an role to break the frozen-flux condition instead of collisions, thus called the collisionless regime. Since these effects are absent in the two fluid model, the scalings do not agree for any values of β_{e} in this regime.

4 Summary

Multiscale hierarchy is intrinsic in plasmas, and is observed in many situations of interest. In collisionless plasmas, various kinetic effects play important roles. Our approach to such multiscale phenomena is a gyrokinetic simulation. With the help of scale separation of dynamics under the mean magnetic field, we can reduce the phase space dimension from six to five using the gyrokinetic ordering, thus an accurate kinetic simulation becomes possible though it is still computational demanding.

We have briefly discussed the gyrokinetic model and the gyrokinetic simulation code, `AstroGK`, intended for studies of astrophysical plasmas and basic properties of plasmas. Then, we have shown the recent application of the gyrokinetic simulation to magnetic reconnection as a typical example of multiscale phenomema in plasmas. Starting from a collisional case, we gradually introduced various kinetic effect into the phenomena and observed transition from the collisional fluid-like case to the collisionless kinetic case by changing the collisionality parameter.

We have only shown one attempt of understanding multiscale phenomena in plasmas by the gyrokinetic simulation. However, there have been many studies of nonlinear gyrokinetic simulations using `AstroGK` published recent years. For example, the first kinetic simulations of turbulence describing the transition from Alfvén to kinetic Alfvén wave turbulence at the scale of the ion Larmor radius in an attempt to understand solar wind turbulence [8, 9], nonlinear phase-mixing properties of turbulence [10], the study of the statistical properties of phase-space structures of plasma turbulence [11], the Alfvén wave dynamics in the LAPD experiment [12]. We refer the readers to the listed publications for more detailed discussions.

Acknowlegement

The author would like to thank M. Barnes, W. Dorland, G. G. Howes, N. Loureiro, B. Rogers, and T. Tatsuno for fruitful collaborations.

References

[1] R. Numata, G. G. Howes, T. Tatsuno, M. Barnes, and W. Dorland, `AstroGK`: Astrophysical gryokinetics code, *J. Comput. Phys.* **229**, 9347 (2010).

[2] G. G. Howes, S. C. Cowley, W. Dorland, G. W. Hammett, E. Quataert, and A. A. Schekochihin, Astrophysical gyrokinetics: Basic equations and linear theory, *Astrophys. J.* **651**, 590 (2006).

[3] A. A. Schekochihin, S. C. Cowley, W. Dorland, G. W. Hammett, G. G. Howes, E. Quataert, and T. Tatsuno, Astrophysical gyrokinetics: Kinetic and fluid turbulent cascades in magnetized weakly collisional plasmas, *Astrophys. J. Suppl. Series* **182**, 310 (2009).

[4] M. Barnes, I. G. Abel, W. Dorland, D. R. Ernst, G. W. Hammett, P. Ricci, B. N. Rogers, A. A. Schekochihin, and T. Tatsuno, Linearized model Fokker-Planck collision operators for gyrokinetic simulations II. numerical implementation and tests, *Phys. Plasmas* **16**, 072107 (2009).

[5] I. G. Abel, M. Barnes, S. C. Cowley, W. Dorland, and A. A. Schekochihin, Linearized model Fokker-Planck collision operators for gyrokinetic simulations I. theory, *Phys. Plasmas* **15**, 122509 (2008).

[6] H. P. Furth, J. Killeen, and M. N. Rosenbluth, Finite-resistivity instabilities of a sheet pinch, *Phys. Fluids* **6**, 459 (1963).

[7] R. Fitzpatrick, Magnetic reconnection in weekly collisional highly magnetized electron-ion plasmas, *Phys. Plasmas* **17**, 042101 (2010).

[8] G. G. Howes, W. Dorland, S. C. Cowley, G. W. Hammett, E. Quataert, A. A. Schekochihin, and T. Tatsuno, Kinetic simulations of magnetized turbulence in astrophysical plasmas, *Phys. Rev. Lett.* **100**, 065004 (2008).

[9] G. G. Howes, J. M. TenBarge, W. Dorland, E. Quataert, A. A. Schekochihin, R. Numata, and T. Tatsuno, Gyrokinetic simulations of solar wind turbulence from ion to electron scales, *Phys. Rev. Lett.* **107**, 035004 (2011).

[10] T. Tatsuno, W. Dorland, A. A. Schekochihin, G. G. Plunk, M. Barnes, S. C. Cowley, and G. G. Howes, Nonlinear phase mixing and phase-space cascade of entropy in gyrokinetic plasma turbulence, *Phys. Rev. Lett.* **103**, 015003 (2009).

[11] T. Tatsuno, M. Barnes, S. C. Cowley, W. Dorland, G. G. Howes, R. Numata, G. G. Plunk, and A. A. Schekochihin, Gyrokinetic simulation of entropy cascade in two-dimensional electrostatic turbulence, *J. Plasma Fusion Res. SERIES* **9**, 509 (2010).

[12] K. D. Nielson, G. G. Howes, T. Tatsuno, R. Numata, and W. Dorland, Numerical modeling of Large Plasma Device Alfvén wave experiments using AstroGK, *Phys. Plasmas* **17**, 022105 (2010).

On the Hamilton-Jacobi Variational Formulation of the Vlasov Equation

P. J. Morrison*

Department of Physics and Institute for Fusion Studies,
University of Texas, Austin, Texas 78712-1060, USA.

(Dated: January 27, 2012)

The Hamilton-Jacobi formulation of Vlasov-like systems and associated action principles, developed by the author and D. Pfirsch in a series of papers since the mid 1980s, are briefly reviewed and suggestions for their use are given.

I. INTRODUCTION

In this note we briefly review the Hamilton-Jacobi (HJ) formulation of Vlasov-like systems. This is a general formulation that applies to the Maxwell-Vlasov system and various guiding center and gyrokinetic theories with any number of species. It applies to both nonrelativistic and relativistic versions of these theories and even to the Vlasov-Einstein system. Indeed, it is quite general and applies to any Vlasov-like theory, but we will review it in its simplest context of the Vlasov-Poisson system.

The formulation evolved out of early work of Pfirsch [1], but the general formulation was first given in [2]. The HJ formulation is variational – it has in fact two action principles, and so it provides a natural method via Noether's theorem for obtaining unambiguous energy-momentum tensors for general kinetic theories. These were obtained and discussed in a sequence of papers [2–4] and this work was continued in [5, 6], where errors in the literature were pointed out.

This note is organized as follows. In Sec. II we review the HJ theory in the context of classical mechanics. Then in Sec. III the action principle of [2] for the general theory is described along with a reduced version given in [7]. Finally, in Sec. IV we conclude.

---

* email: morrison@physics.utexas.edu

II. CLASSICAL HAMILTON-JACOBI THEORY

Hamilton-Jacobi theory arises in the context of classical mechanics where it is proposed as a means of solving Hamilton systems:

$$\dot{q} = \frac{\partial H}{\partial p} \qquad \text{and} \qquad \dot{p} = -\frac{\partial H}{\partial q} \tag{1}$$

where $z := (q, p)$ denotes coordinates for a $2n$ dimensional manifold $\mathcal{Z}$ and $H(q, p)$ is the Hamiltonian function that defines the system. Equations (1) can be compactly written in coordinates as follows:

$$\dot{z}^i = J_c^{ij} \frac{\partial H}{\partial z^j} \tag{2}$$

where $i, j = 1 \ldots 2n$, the repeated index is to be summed, and the matrix

$$J_c := \begin{pmatrix} 0_n & I_n \\ -I_n & 0_n \end{pmatrix} . \tag{3}$$

is the the cosymplectic form. Equations (1) can also be written as

$$\dot{z} = [z, H] , \tag{4}$$

where $[\ ,\ ]$ is the Poisson bracket defined on phase space functions by

$$[f, g] = \frac{\partial f}{\partial z^i} J_c^{ij} \frac{\partial g}{\partial z^j} . \tag{5}$$

The basic idea underlying Hamilton-Jacobi theory is to solve Hamilton's equations by changing coordinates. Under a coordinate change $z \leftrightarrow \bar{z}$, Eqs. (2) become

$$\dot{\bar{z}}^i = \bar{J}^{ij} \frac{\partial \bar{H}}{\partial \bar{z}^j} \tag{6}$$

where the Hamiltonian transforms as a scalar, $H(z) - \bar{H}(\bar{z})$ and the cosymplectic form as a second order contravariant tensor

$$\bar{J}^{mn} = \frac{\partial \bar{z}^m}{\partial z^i} J_c^{ij} \frac{\partial \bar{z}^n}{\partial z^j} . \tag{7}$$

Canonical transformations or symplectomorphisms, as they are commonly referred to now when the global geometry of $\mathcal{Z}$ is under consideration, are those for which

$$\bar{J}^{mn} \equiv J_c^{mn} . \tag{8}$$

Two commonly used methods for generating canonical transformations are the Lie transform and the mixed variable generating function (MVGF). In recent times in plasma physics the Lie transform has been widely used, but each has their advantage. The Lie transform is a series representation that comes from exponentiating a Poisson bracket and when this series is truncated the canonical property is generally lost. However, the mixed variable generating function approach does not suffer from this defect, but it succeeds at the expense of giving an implicit form for canonical transformations, which for our purposes will be generated as follows:

$$p = \frac{\partial S}{\partial Q} \qquad \text{and} \qquad Q = \frac{\partial S}{\partial P} \qquad \text{with} \qquad \left\| \frac{\partial^2 S}{\partial q \partial P} \right\| \neq 0\,. \tag{9}$$

Here $\bar{z} = (Q, P)$ are the new canonical variables, $S(q, P, t)$ is the MVGF, $\| \, \|$ denotes determinant and the nonvanishing of $\|\partial^2 S/\partial q \partial P\|$ is a necessary condition, by the implicit function theorem, for the transformation $z \leftrightarrow \bar{z}$ to exist. If the transformation has explicit time dependence then the new Hamiltonian does not transform as a scalar, energy not being a covariant quantity, but is given by

$$\bar{H}(Q, P, t) = H(q, p, t) + \frac{\partial S}{\partial t}\,. \tag{10}$$

The strategy of HJ theory is to make $\bar{H}$ so simple that trajectories in terms of (Q, P) can be obtained, and then the complication in the orbits is embodied in the transformation back to (q, p). The transformation back is obtained by solving the HJ equation obtained by inserting (9) into (10), giving

$$\frac{\partial S}{\partial t} + H\left(q, \frac{\partial S}{\partial q}, t\right) = \bar{H}\,. \tag{11}$$

This is the HJ equation for the *generating function* S.

Various choices for $\bar{H}$ can be considered. For example $\bar{H} \equiv 0$ would mean all of the dynamics is in the transformation back. This amounts to the use of initial conditions as coordinates which, except in the most trivial cases, are not good coordinates because of serious branching issues. Basically, these coordinates are not isolating, i.e., they do not define good surfaces in $\mathcal{Z}$. A more realistic choice is to choose $\bar{H}(P)$, where all the configuration space coordinates are ignorable. This amounts to seeking a transformation to action-angle variables. It is now known that only for integrable systems do such coordinates exist, and if the system is not nearly integrable, i.e., not near to the case where $\mathcal{Z}$ is foliated by n-tori, then such coordinates do not even approximately exist. But, near to integrability,

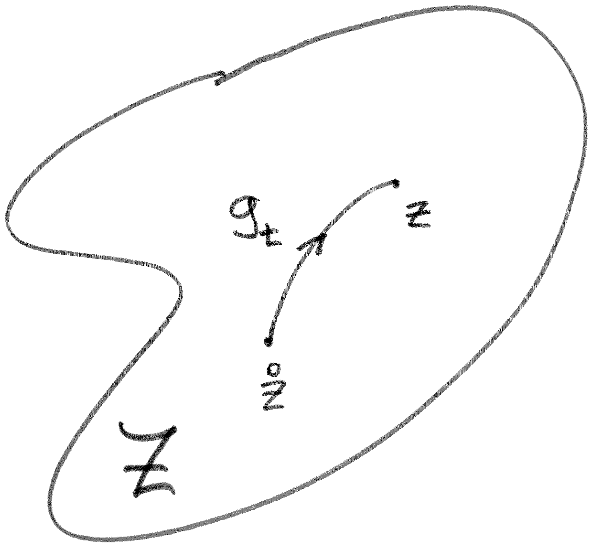

FIG. 1: Canonical transformation of phase space.

perturbation theory makes sense, as has been shown by KAM theory, which incidentally was first proven in the HJ context. Thus, there are various issues with classical existence theory of the HJ equation, tied up with small divisors, the existence of caustics, etc., which we will not pursue.

Before proceeding to how HJ theory arises in the context of Vlasov, we mention one more fact from mechanics that we will need, viz., Hamilton dynamics itself is a canonical transformation. This means that if we could integrate Hamilton's equations for all initial conditions $\mathring{z}$, then this would define a map from $\mathcal{Z}$ to itself as depicted in Fig. 1. The map $\mathring{z} \mapsto z(t)$, denoted by g_t in the figure, is a canonical transformation. The set $G = \{g_t | t \in \mathbb{R}\}$ is the Lie group of one-parameter family of canonical transformations, where $g_t : \mathcal{Z} \to \mathcal{Z}$ for all times.

III. HAMILTON-JACOBI ACTION PRINCIPLES FOR VLASOV-POISSON

Here we first consider the Vlasov-Poisson system, then proceed to construct two action principles.

A. The Vlasov-Poisson system

Global existence theories for this system were proven in the early 1990s by Pfaffelmoser, Perthame, Schaeffer and others; but, since our presentation will be formal, these theorems will not concern us. We will consider the simplest case of one spatial dimension with a single dynamical variable, the phase space density $f(q,p,t)$, that only depends on (q,p,t) and $f : U \times \mathbb{R}^2 \to \mathbb{R}^+$, where the set $U \in \mathbb{R}$ is often the circle or all of $\mathbb{R}$. Let $D := U \times \mathbb{R}$ be the phase spatial domain. The Vlasov equation of interest here is

$$\frac{\partial f}{\partial t} + p\frac{\partial f}{\partial q} - E\frac{\partial f}{\partial p} = 0 \qquad \Longleftrightarrow \qquad \frac{\partial f}{\partial t} + [f,H] = 0 \tag{12}$$

which is the equation a single electron species, which we wish to solve for a given initial condition $\mathring{f}(q,p) = f(q,p,0)$. The equality of (12) follows from the definitions

$$H := \frac{p^2}{2} - \phi, \qquad E =: -\frac{\partial \phi}{\partial q}, \qquad \text{and} \qquad [f,g] := \frac{\partial f}{\partial q}\frac{\partial g}{\partial p} - \frac{\partial f}{\partial p}\frac{\partial g}{\partial q}\,. \tag{13}$$

Here, unlike in Sec. II, (q,p) denote independent variables. From context is should be clear when we mean dependent and when we mean independent variable for these quantities.

It remains to determine the electrostatic potential $\phi(q,t)$ through Poisson's equation

$$\frac{\partial^2 \phi}{\partial q^2} = \int_{\mathbb{R}} dp\, f \qquad \longleftrightarrow \qquad \phi(q,t) = \int_D dq' dp'\, K(q|q') f(q',p',t) \tag{14}$$

where $K(q,q')$ denotes the "Green's" function. For convenience we have included charge neutrality in the definition of f.

There are two essential components of Vlasov theory that we will exploit:

CE: The characteristic equations of (12), given by

$$\dot{q} = [q,H] \qquad \text{and} \qquad \dot{p} = [p,H]\,, \tag{15}$$

which exist because of the hyperbolic nature of (12).

SR: The rule for constructing f from its initial condition $\mathring{f}$ given the solution to (15), i.e.,

$$f(q,p,t) = \mathring{f}\left(\mathring{q}(q,p,t), \mathring{p}(q,p,t)\right) = \mathring{f} \circ g_{-t}\, \mathring{z} =: z\#\mathring{f}\,. \tag{16}$$

In the first equality of (16) we have first written the solution in the usual way of plasma physics, in the second in terms of the one-parameter group discussed in Sec. II, and lastly in terms of a compact notation. Because the characteristic equations (15) are Hamiltonian we know g_t, which is the inverse of the map $\mathring{z} \mapsto z(t)$, denotes a canonical transformation. Thus, we say that the solution f is a *symplectic rearrangement* (SR) of $\mathring{f}$.

B. HJ Vlasov Formulation and the First Action Principle

The HJ formulation alters both of the essential components of Vlasov theory as follows:

CE: The characteristic equations are replaced by the generating function $S(q,P,t)$, knowledge of which is completely equivalent to the trajectories $(q(\mathring{q},\mathring{p},t),p(\mathring{q},\mathring{p}))$.

SR: The rule for constructing f is replaced by a new equivalent rule given in terms of a new variable defined by

$$\Phi(q,P,t) := \left\| \frac{\partial^2 S}{\partial q \partial P} \right\| \, f\left(q, \frac{\partial S}{\partial q}, t\right) \, . \tag{17}$$

The quantity $\|\partial^2 S/\partial q \partial P\|$ was investigated in quantum mechanical contexts by Van Vleck, Pauli, and DeWitt-Morette, and is often referred to as the Van Vleck determinant.

To complete the formulation one needs equations for the pair of functions (Φ, S), such that these equations and the rule give solutions equivalent to the Vlasov equation, which can be written as

$$f\left(q, \frac{\partial S}{\partial q}, t\right) = \mathring{f}\left(\frac{\partial S}{\partial P}, P\right) \, . \tag{18}$$

It is evident that the HJ equation for S cannot be an ordinary HJ equation since, like the usual Vlasov equation, it must be global in nature. This arises in (12) through the electric field E that is determined by Poisson's equation. Thus, the HJ equation will be, like Vlasov, an integro-differential equation. With this in mind we rewrite the solution of Poisson's equation of (14) in a few different ways:

$$\begin{aligned}
\phi(q,t) &= \int_D dq'dp' \, K(q|q') \, f(q',p',t) \\
&= \int_D dq'dP' \, K(q|q') \, f(q',p',t) \left\| \frac{\partial^2 S}{\partial q' \partial P'} \right\| \\
&= \int_D dq'dP' \, K(q|q') \, \Phi(q',P',t) \, ,
\end{aligned} \tag{19}$$

where the last expression shows a clean linear relationship between ϕ and Φ.

To obtain the equations for S and Φ we appeal to the phase space action principle, the principle of mechanics that yields Hamilton's equations upon variation. This action principle is given by

$$\mathcal{A}[q,p] = \int_{t_0}^{t_1} dt \; (p \cdot \dot{q} - H) \; , \tag{20}$$

which is defined on phase space paths that begin at q_0 at time t_0 and end at q_1 at time t_1. The functional derivative $\delta\mathcal{A}/\delta q = 0$ and $\delta\mathcal{A}/\delta p = 0$ imply Hamilton's equations (1); boundary conditions on p are not specified. In analogy to (20) we suppose Φ and S are like conjugate variables and write the following action for them:

$$\mathcal{A}[S,\Phi] = -\int_{t_0}^{t_1} dt \int_D dqdP\,\Phi\left(\frac{\partial S}{\partial t} + \frac{1}{2}\left|\frac{\partial S}{\partial q}\right|^2 - \frac{\phi}{2} - \bar{H}\right) \tag{21}$$

where ϕ is to be viewed as a shorthand for the expression defined by (19) and H_0 is a reference Hamiltonian analogous to the $\bar{H}$ of classical HJ theory and we are free to tailor this to the problem at hand. This amounts to a kind of gauge freedom. Variation of (21) with respect to Φ gives

$$\frac{\partial S}{\partial t} + \frac{1}{2}\left|\frac{\partial S}{\partial q}\right|^2 - \phi - \bar{H} = 0\,, \tag{22}$$

while variation with respect to S gives

$$\frac{\partial \Phi}{\partial t} + \frac{\partial}{\partial q}\cdot\left(\Phi\,\frac{\partial H}{\partial P}\right) - \frac{\partial}{\partial P}\cdot\left(\Phi\,\frac{\partial \bar{H}}{\partial Q}\right) = 0\,. \tag{23}$$

Thus we arrive at the following

Theorem *If S satisfies (22) and Φ satisfies (23), then if f is constructed according to (17) it satisfies the Vlasov-Poisson system of (12) with (14).*

Proof The proof is mainly a chain rule exercise. For the details we refer the reader to [2, 3]. ∎

At first impression one might wonder if progress has been made since we began with one equation and now have two to solve – albeit now we have equations derivable from a variational principle. It turns out that (23) has special properties that make it easy to solve. Instead of pursing this here, in the next section we will eliminate this variable all together.

C. Reduced HJ Vlasov Formulation and the Second Action Principle

Before proceeding to our reduced action principle we describe a cartoon of the Vlasov phase space, as depicted in Fig. 2. Solutions of the Vlasov equation lie in some function space that we will denote by $\mathcal{F}$. We will not be specific about $\mathcal{F}$, but only discuss properties in a formal manner with intuition coming from finite-dimensional noncanonical Hamiltonian

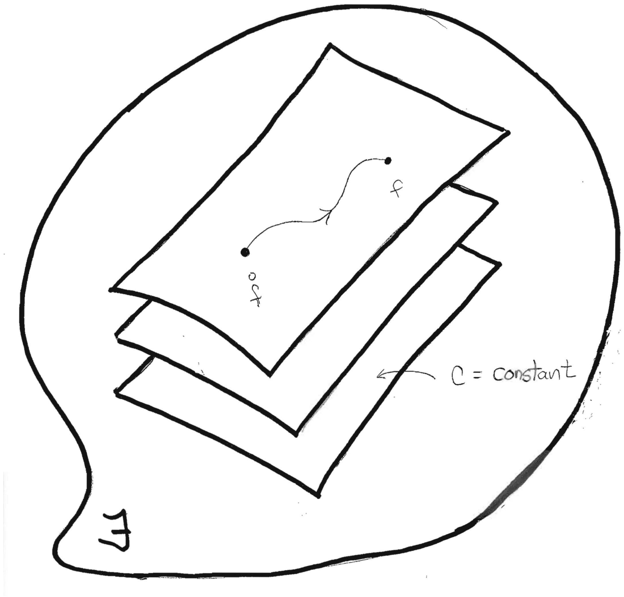

FIG. 2: Depiction of Poisson manifold foliated by constant Casimir symplectic leaves.

systems (see e.g. [8]) for which phase space is a Poisson manifold. Because $f = z\#\mathring{f}$, i.e. f is a SR of $\mathring{f}$, not all functions f are accessible from a given $\mathring{f}$. Under mild continuity conditions, the rule $f = z\#\mathring{f}$ implies certain properties of f and $\mathring{f}$ must coincide for all time, viz., the number of extrema and their values, the level set topologies, and the area between any two level sets. The SR property defines an equivalence relation $\sim$, where a phase space function $\mathring{f} \sim f$ if $\exists$ any canononical transformation z, i.e. any trajectory functions that can be generated by any Hamiltonian, such that $f = z\#\mathring{f}$. Thus, the dynamics takes place on a constraint set or, equivalently, motion lies entirely within an equivalence class. In this way the function state space $\mathcal{F}$ is foliated by leaves, each of which is labeled by an initial condition $\mathring{f}$. In [4, 9] states $f \sim \mathring{f}$ were called *dynamically accessible.*

The space $\mathcal{F}/\sim$ is formally an infinite-dimensional symplectic manifold and an explicit nondegenerate Poisson bracket on it was given in [10]. Thus we refer to the leaves as symplectic leaves. On such a leaf in the vicinity of an equilibrium $\mathring{f}$, a linear canonical form for the Poisson bracket was explicitly obtained in [11–13] and structural stability in the manner of Krein's theorem was considered in [14]. All this suggests a variational principle in terms of the single function S with a fixed symplectic leaf label. This principle is given by the following:

$$\mathcal{A}[S, \mathring{f}] = -\int_{t_0}^{t_1} dt \int_D dq dP\, \mathring{f}\left(\frac{\partial S}{\partial P}, P\right) \left\| \frac{\partial^2 S}{\partial q \partial P} \right\| \left(\frac{\partial S}{\partial t} + \frac{1}{2}\left|\frac{\partial S}{\partial q}\right|^2 - \frac{\phi}{2} \right) , \tag{24}$$

where we have explicitly displayed the dependence on $\mathring{f}$, but this quantity is not to be varied.

Since in (24) the potential ϕ is now a shorthand for

$$\phi(q,t) = \int_D dq' dP'\, K(q|q')\, \mathring{f}\left(\frac{\partial S}{\partial P'}, P'\right) \left\| \frac{\partial^2 S}{\partial q' \partial P'} \right\| , \tag{25}$$

it is clear that variation with respect to S is an onerous task with contributions from $\mathring{f}$, the Van Vleck determinant, and the other dependence on S. After some effort, one can show $\delta\mathcal{A}[S, \mathring{f}]/\delta S = 0$ implies

$$\frac{\partial S}{\partial t} + \frac{1}{2}\left|\frac{\partial S}{\partial q}\right|^2 - \phi - \bar{H}\left(\frac{\partial S}{\partial P}, P, t\right) = 0\,, \tag{26}$$

where $\bar{H}$ is any function that satisfies

$$[\mathring{f}(Q,P), \bar{H}(Q,P,t)] = 0\,. \tag{27}$$

We refer the reader to [7] for more details of this calculation. In priciple, if we are given $\mathring{f}$ and we solve (26) for S, then we can use (18) to construct f, which can be shown to be a solution to the Vlasov-Poisson system.

IV. CONCLUSIONS

There are many comments that can be made about the above HJ formulations and variational principles, but we will consider only two.

First, it is clear that the nonlinearity that occurs in the term $E\partial f/\partial p$ in the Vlasov equation has been redistributed in both formulations. For example, from the action principle of (24) nonlinearity is manifest in the choice of $\mathring{f}$. Thus it might be worthwhile to reinvestigate existence proofs in this setting, particularly in light of the activity on viscosity solutions for HJ and the current studies of weak KAM theory. Through the HJ equation we have a natural place where pde and ode methods meet, and it seems that techniques from Hamiltonian dynamical systems theory may prove useful here.

Second, if one obtains an approximate solution to the HJ equation (26) by any means, numerical or otherwise, then the solution constructed will be a SR. It may not be a good solution, but it will satisify $f = z\#\overset{\circ}{f}$ and all the constraints this relation implies. Thus, one might think this kind of approximation would be superior.

In closing, we reiterate that everything done here for the Vlasov-Poisson system can be done for any Vlasov-like system, including the coupling to field equations like Maxwell's or Einstein's.

Acknowledgment

Supported by U.S. Dept. of Energy Contract # DE-FG05-80ET-53088.

---

[1] D. Pfirsch. New variational formulation of Maxwell-Vlasov and guiding-center theories local charge and energy conservation laws. *Z. Naturforsch.*, 39a:1–8, 1984.

[2] D. Pfirsch and P. J. Morrison. The energy-momentum tensor for the linearized Maxwell-Vlasov and kinetic guiding center theories. *Phys. Fluids*, 3B:271–283, 1991.

[3] D. Pfirsch and P. J. Morrison. Local conservation laws for the Maxwell-Vlasov and collisionless guiding-center theories. *Phys. Rev.*, 32A:1714–1721, 1985.

[4] P. J. Morrison and D. Pfirsch. Free-energy expressions for Vlasov equilibria. *Phys. Rev.*, 40A:3898–3906, 1989.

[5] D. Pfirsch and D. Correa-Restrepo. New method of deriving local energy- and momentum-conserving Maxwell-collisionless drift-kinetic and gyrokinetic theories: basic theory. *J. Plasma Phys.*, 70:719–755, 2004.

[6] D. Correa-Restrepo and D. Pfirsch. The electromagnetic gauge in the variational formulation of kinetic and other theories. *J. Plasma Phys.*, 71:503–517, 2005.

[7] H. Ye and P. J. Morrison. Action principles for the Vlasov equation. *Phys. Fluids*, 4B:771–776, 1992.

[8] P. J. Morrison. Hamiltonian description of the ideal fluid. *Rev. Mod. Phys.*, 70:467–521, 1998.

[9] P. J. Morrison and D. Pfirsch. The free energy of Maxwell-Vlasov equilibria. *Phys. Fluids*, 2B:1105–1113, 1990.

[10] H. Ye, P. J. Morrison, and J. D. Crawford. Poisson bracket for the Vlasov equation on a symplectic leaf. *Phys. Lett.*, 156A:96–100, 1991.

[11] P. J. Morrison and B. A. Shadwick. Canonization and diagonalization of an infinite dimensional Hamiltonian system: Linear Vlasov theory. *Acta Physica Polonica*, 85A:759–769, 1994.

[12] P. J. Morrison and D. Pfirsch. Dielectric energy versus plasma energy, and Hamiltonian action-angle variables for the Vlasov equation. *Phys. Fluids*, 4B:3038–3057, 1992.

[13] P. J. Morrison. Hamiltonian description of Vlasov dynamics: Action-angle variables for the continuous spectrum. *Trans. Theory and Stat. Phys.*, 29:397–414, 2000.

[14] G. I. Hagstrom and P. J. Morrison. On Krein-like theorems for noncanonical Hamiltonian systems with continuous spectra: Application to Vlasov-Poisson. *Trans. Theory and Stat. Phys.*, 39:466–501, 2011.

A new solution method for singular perturbation problems in magnetized plasmas

M. Furukawa [1]

Grad. Sch. Frontier Sci., Univ. Tokyo, Kashiwa-shi, Chiba 277-8561, Japan

This proceeding is a summary of recently published papers on a new solution method for singular perturbation problems in magnetized plasmas. The new method enables us to fully avoid inherent difficulties of the traditional matched asymptotic expansion. The important ingredients are the utilization of a finite-width inner layer, and the ordering scheme in the outer region. Explanations on how these ingredients work, and some discussions are given.

1 Background

1.1 General introduction

Singular perturbation problems often appear when we model phenomena in nature. Suppose the model is described by a set of differential equations, and it includes a small parameter ϵ. A solution by a naive expansion in ϵ can give essentially different behavior compared with the exact solution, which characterizes the singular perturbation problem. If the highest-order derivative term in the governing equation is multiplied by ϵ, the model is a typical singular perturbation problem. For example, if a solid body is placed in a high Reynolds number fluid flow, a thin boundary layer is formed around it. Viscosity plays an important role only in the boundary layer, where the viscous term is the highest-order derivative term in the governing equation multiplied by a small parameter or the inverse of the Reynolds number. In this proceeding, we consider resistive magnetohydrodynamics (MHD) linear stability of a magnetized plasma. The resistivity term has the highest-order derivative in the governing equation. The normalized resistivity or the inverse of the Lundquist number serves as the small parameter in this case. An internal boundary layer or a resistive layer can be formed inside the plasma. These are both boundary-layer problems, that are typical and classical multi-scale phenomena.

MHD linear stability analysis of magnetically confined plasmas has been one of the important issues in nuclear fusion development. If the plasma becomes unstable against various MHD modes, the confinement is lost completely or is degraded significantly at least. The loss of confinement leads to release of energy which was confined, that can seriously damage the experimental device. Therefore the accurate calculation of the stability boundary in parameters' space of the experiment has been strongly required.

---

[1] E-mail: furukawa@k.u-tokyo.ac.jp

This work has been done in collaboration with

Dr. S. Tokuda, International Fusion Energy Research Center, Japan Atomic Energy Agency, Japan, and

Dr. L.-J. Zheng, Institute for Fusion Studies, University of Texas at Austin, USA.

Finite plasma resistivity introduces several types of resistive MHD instability such as tearing modes[1]. If the tearing mode becomes unstable, magnetic reconnection occurs and magnetic islands form in the plasma. Since large-scale magnetic islands degrade the plasma confinement significantly and even cause complete loss of the confinement, control and suppression of the islands are one of the urgent issues. To understand physics of them, accurate calculation of the resistive MHD stability is indispensable.

1.2 Problem setting and governing equations

In order to study the singular perturbation problem in magnetized plasmas, we adopt a high-beta reduced MHD model[2, 3]. This model describes vortical motions of a plasma with long wave length along a strong ambient magnetic field in the shear Alfvén time scale. We assume a cylinderical plasma with its minor radius a and length $2\pi R_0$, with the inverse aspect ratio $\varepsilon := a/R_0 \ll 1$. Note that this ε is different from a small parameter defining the singular perturbation problem. The cylindrical coordinate system (r, θ, z) is used. Linearizing the equations and assuming the spacio-temporal dependence of perturbed quantities $Q_1(r, \theta, z, t)$ as $Q(r)\mathrm{e}^{\mathrm{i}\,(m\theta + nz/R_0)+\gamma t}$, we obtain

$$\gamma \nabla_\perp^2 \varphi = -\mathrm{i}\, F \nabla_\perp^2 \psi - \frac{\mathrm{i}\, m J_0'}{r}\psi + \frac{\mathrm{i}\, m \kappa_{0r}}{r} p, \tag{1}$$

$$\gamma \psi = -\mathrm{i}\, F \varphi + \eta \nabla_\perp^2 \psi, \tag{2}$$

$$\gamma p = \frac{\mathrm{i}\, m \beta'}{r}\varphi, \tag{3}$$

where Eqs. (1), (2) and (3) are the vorticity equation, the Ohm's law along magnetic field, and pressure equation, respectively. We assumed that the equilibrium plasma rotation does not exist for simplicity. If $\Re\gamma > 0$, the plasma is unstable. All the quantities are normalized by the strong ambiend magnetic field B_0, the minor radius a, the Alfvén velocity $v_\mathrm{A} := B_0/\sqrt{\mu_0 \rho_0}$ with ρ_0 being the equilibrium mass density and μ_0 the vacuum permeability, the Alfvén time $\tau_\mathrm{A} := a/v_\mathrm{A}$, and the magnetic pressure $B_0^2/2\mu_0$. The fluid velocity is $\mathbf{v} := \hat{\mathbf{z}} \times \nabla_\perp \varphi$ with $\hat{\mathbf{z}}$ the unit vector in the z direction, $\nabla_\perp$ the gradient operator in the r–z plane and $\nabla_\perp^2 := \partial^2/\partial r^2 + (1/r)\partial/\partial r - (m/r)^2$, the magnetic field is $\mathbf{B} = \hat{\mathbf{z}} + \nabla_\perp \psi \times \hat{\mathbf{z}}$, the equilibrium current in the negative z direction is J_0, the prime denotes $\mathrm{d}/\mathrm{d}r$, β is the equilibrium pressure, κ_{0r} is the curvature of equilibrium magnetic field, the parallel wave number is written as $F := \varepsilon m(n/m + 1/q)$ with $q := -\varepsilon r/\psi_0'$ being the safety factor, ψ_0 is the equilibrium component of ψ, and η is the resistivity or the inverse of Lundquist number. We also use the following notation for later convenience:

$$\gamma \mathsf{M} \cdot \mathbf{u} = \mathsf{R} \cdot \mathbf{u}, \tag{4}$$

where $\mathbf{u} := (\varphi, \psi, p)^\mathrm{T}$, and M and R are defined appropriately.

Equations (1), (2) and (3) are fourth-order system. Note that Eq. (3) does not include radial derivative. As noted above, this is the singular perturbation problem because of the η term. If we assume a high-temperature plasma aimed at fusion, η can be 10^{-9} – 10^{-11}.

1.3 Brief introduction of matched asymptotic expansion

A magnetic flux surface satisfying $q = m/n$ is called a rational surface, where the parallel wave number F becomes zero. For a marginally stable wave with $\gamma = 0$, the rational surface is also a resonant surface on which the wave frequency coincides with the Alfvén frequency. Note that the resonant surface and the rational surface does not coincide generally if the finite equilibrium plasma rotation and/or the finite real frequency of the wave exist. Even if we focus on a slow resistive instabilities caused by $\eta \ll 1$, small effects such as inertia and resistivity are comparable to the effect of magnetic-field-line tension related to F, since F vanishes on the rational surface. Then a thin resistive layer is formed around the resonant surface. We have traditionally applied the matched asymptotic expansion by using η as a small parameter[1, 4, 5]. The resistive layer is the inner layer of the matched asymptotic expantion. In the inner layer, although we take into account the inertia and resistivity, we can simplify the governing equation by using that the layer is very thin. To focus on the inside of the thin layer and on the slow dynamics, we re-scale the radial coordinate and the frequency by using the resistivity as a small parameter. This leads to the so-called inner-layer equation. The inner-layer equation is the fourth-order system.

A set of the complementary regions of the inner layer is the outer region. Since the resistivity and the inertia terms can be neglected in the outer region, we solve the inertia-less, ideal MHD equation or the so-called Newcomb equation[6], which is given by

$$\mathcal{N}\psi = 0, \tag{5}$$

$$\mathcal{N} := \nabla_\perp^2 + \frac{m}{rF}\left(J_0' + \frac{m}{rF}\kappa_{0r}\beta'\right). \tag{6}$$

The Newcomb equation is the second-order system, which has two independent solutions. The rational surface is the regular singular point of the Newcomb equation if F' or q' does not vanish there. Then we can construct the Frobenius series solution around the resonant surface. One of the independent solutions is non-square-integrable, which is called large solution. The other one is square-integrable, called small solution. The ratio of the small solution to the large solution, called matching data, plays crucial role in the asymptotic matching.

Since we have four independent solutions in the inner layer, we need to select two of the four which asymptotically match onto the outer solution. The successful matching then gives us the dispersion relation.

1.4 Difficulties of matched asymptotic expansion

Although the matched asymptotic expansion is well established mathematically, it has some difficulties in practice:

(i) Although the resistivity and the inertia are neglected in the outer region, they can be important there if the plasma is close to marginal stability against ideal MHD. A plasma close to its ideal MHD marginal stability may be preferable to improve efficiency of a fusion reactor. Such a situation may be simulated by a cylindrical plasma with $q = 1$ surface inside the plasma, since the $m/n = 1/1$ internal kink mode is marginally stable against ideal MHD.

(ii) The method cannot be applied in the first place if the resonant surface becomes an irregular singular point of the Newcomb equation. The Frobenius series solution and also the matching data cannot be obtained around the resonant surface. An important type of discharge in fusion development has non-monotonic q profile, and the minimum-q position can be such irregular singularity.

(iii) Accurate numerical computation of the matching data is still difficult in toroidal plasmas even though some sophisticated theory have been developed for cylindrical[7, 8] and toroidal geometries[9, 10, 11, 12].

(iv) In the plasma close to marginal stability against ideal MHD, the matching data diverges. Although a numerical scheme to calculate huge matching data was developed[13], it is reported that the accuracy of the matching data strongly depend on the local equilibrium accuracy and grid arrangement[14].

(v) Careful treatment is required in solving the inner equation numerically since the radial coordinate is re-scaled into unbounded space[10]. The norm of the inner solution then diverges.

2 Ingredients of new matching method

We have developed a new matching method for removing the difficulties raised above[15, 16]. The key ingredients of the new method are an utilization of an inner region with a *finite width*, and an ordering scheme for the outer region. These are briefly explained below. More detailed descriptions of the formulation, as well as numerical results are found in Refs. [15, 16].

2.1 Finite-width inner region

In our new method, we adopt a finite-width inner region, instead of infinitely thin inner layer. Neither the radial coordinate nor the frequency are re-scaled via small resistivity.

Here we use "inner region" since it is different from the so-called inner layer which is infinitely thin. Figure 1 shows the geometry. Suppose there is a resonant surface at $r = r_\mathrm{s}$. We set an inner region at $r_\mathrm{L} < r < r_\mathrm{R}$. The outer regions are at $0 \leq r < r_\mathrm{L}$ and at $r_\mathrm{R} < r \leq 1$. The solutions in the inner and outer regions are then matched *directly, not asymptotically*, by imposing continuity of perturbed magnetic field at the matching points r_L and r_R.

The matching points are taken to be reasonably apart from r_s. Our numerical results showed that the growth rate γ can be accurately calculated if the width of the inner region is five times the resistive layer width $x_\mathrm{r} := |r/nB_\theta q'|^{1/3}\eta^{1/3}$ with B_θ the equilibrium poloidal magnetic field. For high-temperature plasmas, the resistivity is so small, x_r and thus the required inner-region width becomes very thin.

Since the matching points are apart from the singular point, we can fully avoid the difficulties in the numerical computation. Accurate computation of the matching data, including the divergent case, and the careful treatment of the unbounded space are unnecessary. Furthermore, our method is applicable to the irregular singularity case, since the method does not rely on the Frobenius series solution.

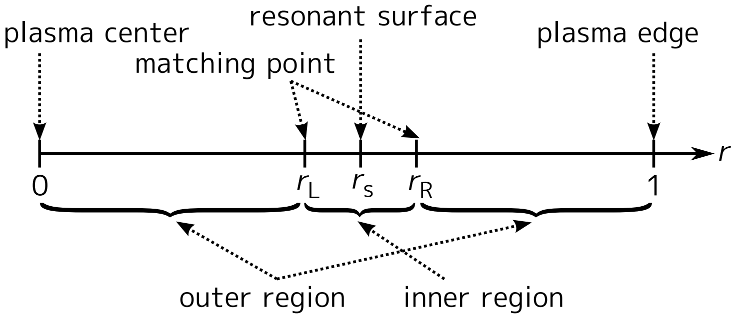

Figure 1: Geometry.

Note that the finite-width inner region was originally introduced for ideal MHD modes[17], and extended to resistive wall modes in rotating cylindrical plasmas[18]. The important difference from these studies is that the resistivity term increases the order of spatial derivative. We then need to select two of the four independent solutions in the inner region, that can match onto the outer solution. A natural idea for the selection is to impose smooth disappearance of parallel electric field $E_\parallel$ as approaching the matching points from the inner side[15], which can be implemented by imposing a boundary condition of the third kind is imposed on φ:

$$\varphi' = \quad \frac{\psi'}{\psi} - \frac{F'}{F} \quad \varphi. \tag{7}$$

This is obtained from the linearized ideal Ohm's law

$$E_\parallel = -\gamma\psi - \mathrm{i}\,F\varphi = 0 \tag{8}$$

and its radial derivative $E'_\parallel = 0$. Note that $E_\parallel = 0$ and $E'_\parallel = 0$ lead to Eq. (7), but Eq. (7) does not necessarily lead to $E_\parallel = 0$ and $E'_\parallel = 0$. If we assume that Eq. (7) is given, $E'_\parallel$ can be expressed as

$$E'_\parallel = E_\parallel \frac{\psi'}{\psi}. \tag{9}$$

Therefore, when Eq. (7) is imposed, $E'_\parallel$ approaches zero if $E_\parallel$ approaches zero as long as ψ'/ψ is finite. This boundary condition is consistent with that applied in the traditional matched asymptotic expansion[15].

2.2 Ordering scheme in outer region

Our numerical results by using the finite-width inner region were mostly satisfactory, although we had one exceptional situation; it is the $m/n = 1/1$ internal kink mode[15]. Figure 2 shows $E_\parallel$ as a function of r for the $m/n = 1/1$ internal kink mode. This is obtained by solving Eqs. (1) – (3) numerically as an eigenvalue problem in the whole domain without matching procedure. The resonant surface $q = 1$ exists at $r = 0.5$. We observe that $E_\parallel$ remains considerably in the $q < 1$ region. Note that the amplitude is normalized so that the maximum absolute value becomes unity for all η, in order to show the relative amplitude of $E_\parallel$ in the $q < 1$ region. The relative amplitude of $E_\parallel$ increases as η is increased. In the traditional method, we assume an inner layer around $q = 1$ surface, and the $q < 1$ region is treated by ideal MHD where $E_\parallel$ must be zero. This can degrade the accuracy of the approximation of asymptotic matching.

Note that this $m/n = 1/1$ internal kink mode is not just an example where the approximation becomes less accurate. We consider that the situation for the $m/n = 1/1$ internal kink mode in a cylindrical plasma is similar to resistive MHD modes in a toroidal plasma close to ideal MHD marginal stability. This is because the $m/n = 1/1$ internal kink mode in a cylindrical plasma is marginally stable against ideal MHD. In a tokamak operation for example, we try to raise plasma beta (a ration of plasma pressure to magnetic pressure) to obtain high fusion gain, up to close to the ideal MHD marginal stability. Thus resistive MHD modes in such a plasma should have similar character as the $m/n = 1/1$ internal kink mode, i.e. the small inertia and resistivity play important roles even in outer regions apart from resonant surfaces.

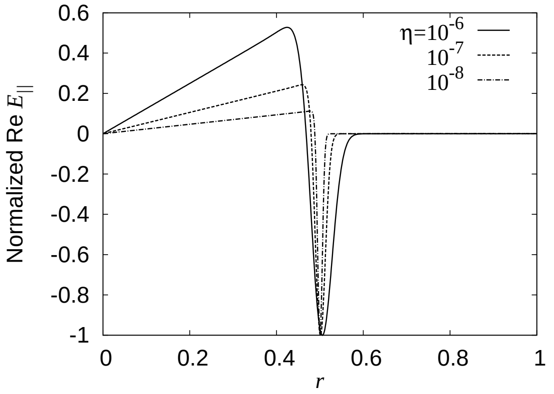

Figure 2: (This is Fig. 21 of Ref. [15]) $E_\parallel$ for $m/n = 1/1$ internal kink mode. The $q = 1$ surface exists at $r = 0.5$.

The remaining $E_\parallel$ indicate the relative importance of the resistivity and the inertia in the $q < 1$ region. We have therefore developed an ordering scheme for the outer region to include those effects perturbatively. We found that the appropriate ordering, by using small parameter $\delta \ll 1$, is given by

$$\begin{aligned}
&\eta \sim \mathcal{O}(\delta^3), && \gamma = \delta\gamma_{(1)} + \delta^2\gamma_{(2)} + \cdots, \\
&\varphi = \delta\varphi_{(1)} + \delta^2\varphi_{(2)} + \cdots, && \psi = \psi_{(0)} + \delta\psi_{(1)} + \cdots, \\
&p = p_{(0)} + \delta p_{(1)} + \cdots,
\end{aligned}$$

and

$$\frac{\partial}{\partial r} \sim \mathcal{O}(1). \tag{10}$$

This ordering scheme looks similar to the one adopted for the inner layer in the asymptotic matching method, however, Eq. (10) makes essential difference. Equation (10), i.e. that we regard the radial derivative of perturbed quantities to be of order unity, is validated because the gradient can be very large only inside the inner layer. Note that the subscripts such as $_{(0)}$ have different meaning from the subscript $_0$ expressing equilibrium quantities.

The ordering scheme then gives us a hierarchy of generalized Newcomb equations. The lowest- and the first-order equations agree with the conventional one as $\mathcal{N}\psi_{(0)} = \mathcal{N}\psi_{(1)} = 0$, and the second-order equation is obtained as

$$\mathcal{N}\psi_{(2)} = -\frac{\gamma_{(1)}^2}{F}\nabla_\perp^2 \frac{\psi_{(0)}}{F} + \frac{\eta}{\gamma_{(1)}}\left(\frac{m}{rF}\right)^2 \kappa_{0r}\beta'\nabla_\perp^2\psi_{(0)}. \tag{11}$$

Although it has an inhomogeneous terms on the right-hand side, Eq. (11) is also the Newcomb equation. The effects of plasma inertia and resistivity manifest themselves in the inhomogeneous terms, which can be calculated by the lower-order solutions. When we obtain $\psi_{(j)}$, we can express $\varphi_{(j+1)}$ and $p_{(j)}$ in the outer region by using the parallel Ohm's law and the pressure equation. The higher-order terms modifies the outer solution to include effects of inertia and resistivity.

In the inner region, we solve Eqs. (1) – (3) by imposing appropriate boundary conditions at each order. For example, we solve

$$\gamma_{(1)}\mathsf{M}\cdot\mathbf{u}_{(0)} = \mathsf{R}\cdot\mathbf{u}_{(0)} \tag{12}$$

in the lowest order. An important point is that $\mathbf{u}_{(0)}$ is solved so that it matches onto $\varphi_{(1)}$, $\psi_{(0)}$ and $p_{(0)}$ in the outer region. The subscripts of $\mathbf{u}_{(j)}$ does not necessarily express the order of the solution in the inner region, since the adopted ordering scheme, especially Eq. (10), breaks down in the inner region.

We solve the inner-region equation as a boundary-value problem by assuming a guess $\gamma_{(j)}$. The boundary conditions are given so that the amplitude of $\mathbf{u}_{(j)}$ coincides with those of the outer solution. Then, the radial derivatives of those quantities cannot be coninuous across the matching points for an arbitrary $\gamma_{(j)}$. We therefore seek $\gamma_{(j)}$ which makes the radial derivative of the perturbation, here we use $\psi'_{(j)}$, continuous across the matching points by the Newton–Raphson method for example, In other words, the the continuity of $\psi'_{(j)}$ across the matching points gives us the dispersion relation.

3 Discussion and Conclusions

So far we have briefly explained the newly developed matching method. One thing we should point out is that the required width of the inner region becomes smaller as η is decreased. We solve the 3×3 matrix system only in the inner region. In the outer region, we solve the Newcomb equation, which is an ordinary differential equation for only one scalar variable ψ. Then the computational cost is reduced significantly if we consider high-temperature plasmas. This feature of our method may become more attractive in toroidal geometry, since multiple poloidal Fourier modes couple, making the matrix size bigger.

However, the required inner-region width was just estimated from the numerical results. Although this estimate seems to be reasonable because we can expect satisfactory results if the matching points are well outside the resistive layer, we would also need a mathematical theory on how the results, the growth rate for example, should scale on the inner-region width. This is an open question.

Another point is the relation between our matching method and the matched asymptotic expansion. The accuracy of the numerical results improves if the inner-region width is increased in our method. On the contrary, the approximation of matched asymptotic expansion becomes better for smaller resistivity and thus the thinner inner layer. This difference is of course because our method connects the solutions directly, not asymptotically, across the matching points, which is essentially different from the matched asymptotic expansion. However, in developing the mathematical theory on the scaling pointed out above, the relation would become clearer.

Now let us give conclusions. We have developed a new matching method for resistive MHD stability analysis, which is one of the typical example of singular perturbation problems. Contrary to the traditional matched asymptotic expansion, we adopt an inner region with a finite width. The inner and outer solutions are matched directly, not asymptotically, across the matching points. This enables us to fully avoid to treat singularity, because the matching points are chosen to be reasonably apart from the singular point. The new method is also applicable to the case with irregular singularity. The other important ingredient is the ordering scheme in the outer region. This leads to the hierarchy of the generalized Newcomb equation. Then we can take into account the effects of inertia and resistivity perturbatively in the outer region. We have applied the new method to well-known examples such as $m/n = 2/1$ tearing, resistive interchange, double tearing, $m/n = 1/1$ internal kink modes. The results showed that the new method can accurately calculate the stability of thoes modes. Computational time is also significantly reduced.

Acknowledgments

This work was supported by KAKENHI 19760595 and KAKENHI 23760805.

References

[1] H. P. Furth, J. Killeen and M. N. Rosenbluth, Phys. Fluids **6**, 459 (1963).

[2] H. R. Strauss, Phys. Fluids **20**, 1354 (1977).

[3] R. D. Hazeltine, J. D. Meiss, *"Plasma Confinement"* (Dover Publications, Inc., Mineola, New York, 2003).

[4] B. Coppi, J. M. Greene, and J. L. Johnson, Nucl. Fusion **6**, 101 (1966).

[5] A. H. Glasser, J. M. Greene, and J. L. Johnson, Phys. Fluids **18**, 875 (1975).

[6] W. A. Newcomb, Ann. Phys. **10**, 232 (1960).

[7] A. Pletzer and R. L. Dewar, J. Plasma Phys. **45**, 427 (1991).

[8] S. Tokuda and T. Watanabe, J. Plasma Fusion Res. **73**, 1141 (1997).

[9] A. Pletzer, A. Bondeson, and R. L. Dewar, J. Comput. Phys. **115**, 530 (1994).

[10] S. Tokuda, Nucl. Fusion **41**, 1037 (2001).

[11] S. Tokuda and T. Watanabe, Phys. Plasmas **6**, 3012 (1999).

[12] L. -J. Zheng, M. Kotschenreuther, J. Comput. Phys. **211**, 748 (2006).

[13] R. L. Dewar and M. Persson, Phys. Fluids B **5**, 4273 (1993).

[14] D. P. Brennan *et al.*, Phys. Plasmas **9**, 2998 (2002).

[15] M. Furukawa, S. Tokuda and L. -J. Zheng, Phys. Plasmas **17**, 052502 (2010).

[16] M. Furukawa and S. Tokuda, Phys. Plasmas **18**, 062502 (2011).

[17] Y. Kagei and S. Tokuda, Plasma Fusion Res. **3**, 039 (2008).

[18] J. Shiraishi, S. Tokuda, and N. Aiba, Phys. Plasmas **17**, 012504 (2010).

Multi-scale modeling in heterogeneous material properties : An application to porous piezoelectric material

Mitsuteru Asai[1]

[1]Department of Civil Engineering, Kyushu University, 744 moto-oka, Nishi-ku Fukuoka, 819-0395, Japan

E-mail: asai@doc.kyushu-u.ac.jp

Abstract. Many engineering problems involve different scale in space or time. The main interest for engineering designer is to find an optimum macroscopic response of structure, although the macroscopic response is strongly dependent on the microscopic material properties. The material itself has an individual microstructure, and the optimum material is fabricated by controlling the microstructure. Usually, the macroscopic material properties are measured by the experimental material tests. The asymptotic homogenization collaborated with the finite element method has been successfully proposed to find an averaging macroscopic material properties. In this paper, an application of the homogenization method to porous piezoelectric material has been described. (The detail has been published in the reference [1].)

1. Introduction

Piezoelectric materials have the physical properties of a transducer, which converts electrical energy to mechanical energy and vice versa. $Pb(Zr,Ti)O_3$ (PZT) ceramic is one of the most prominent piezoelectric materials with outstanding properties, and it is widely used for ultrasonic transducers and highly sensitive sensors. Particularly in the field of micro-electro-mechanical systems (MEMS), PZT ceramic is expected to be used in system requiring precise positioning control and considerable actuation force with low electric power.

Porous PZT ceramics have been proposed to obtain a remarkable electromechanical coupling factor and Q-factor. The properties and effects of porous PZT ceramics have been investigated [2,3]. However, the mechanism of these improvements of porous PZT is unclear. Moreover, there are no reports discussing the 3D morphology of its microstructures. If piezoelectric materials is composed of simple microstructures, theoretical approaches, such as Eshelby's tensors [4] and the upper and lower bounds generalizing the Hashin-Strukman variational principle [5], can estimate the macroscopic material properties. There is an alternative computational approach based on the homogenization method [6-8] for mechanical properties. The advantage is robustness in application to periodic heterogeneous materials composed of complex microstrucures. The homogenization method has been developed to solve nonlinear problems [9-11], solid-fluid coupling problems [12,13] and piezoelectric problems [14,15].

In this context, automatic finite element (FE) mesh generation of complex microstructures is essential for practical use. The digital image-based modeling [16] with cross-sectional images has been employed for an automation process. Although accurate cross-sectional images were captured by sectioning and polishing [17], it is too time consuming way. Thus, nondestructive observation by the X-ray computer tomography (CT) is strongly requested for practical use in industries.

In this study, a multi-scale analysis based on the homogenization method is utilized to evaluate material property of real porous PZT ceramics. In the FE modeling of 3D micrographs, the accuracy of the X-ray CT images is validated with several direct cross-sectional images by scanning electron microscope (SEM). A semi-automatic process provides reasonable 3D micrographs with information of the SEM images.

2. Multi-scale modeling for porous piezoelectric materials

2.1 Outline of the homogenization method for the evaluation of macroscopic properties

In this study, the homogenization method incorporated with FEM is used to evaluate the effective material properties of porous PZT. The details of the formulation can be found in the references [14,15], and are summarized here.

First, we assume that the porous piezoelectric material may have an averaged properties in a macroscale $\boldsymbol{x}$. The materials properties depend on the morphology of the microstructure that can be realized in a microscale $\boldsymbol{y}$. In addition, it is assumed that the microstructure has periodicity. The representative volume element (RVE) is indicated as Y. These two scales are related by a positive small number $\lambda = \boldsymbol{x}/\boldsymbol{y}$.

Here, we choose $\boldsymbol{u}^{\lambda}(\boldsymbol{x})$, $\phi^{\lambda}(\boldsymbol{x})$ as independent variables for two field coupled problems, and we assume that these independent variables can be expressed by the asymptotic expansion,

$$\begin{aligned}\boldsymbol{u}^{\lambda}(\boldsymbol{x}) &= \boldsymbol{u}^{0}(\boldsymbol{x}) + \lambda\boldsymbol{u}^{1}(\boldsymbol{x},\boldsymbol{y}) + \lambda^{2}\boldsymbol{u}^{2}(\boldsymbol{x},\boldsymbol{y}) + \cdots \\ \phi^{\lambda}(\boldsymbol{x}) &= \phi^{0}(\boldsymbol{x}) + \lambda\phi^{1}(\boldsymbol{x},\boldsymbol{y}) + \lambda^{2}\phi^{2}(\boldsymbol{x},\boldsymbol{y}) + \cdots\end{aligned} \tag{1}$$

The other dependent variables can be derived with the above assumptions in a similar expansion form. Strain $\boldsymbol{\varepsilon}^{\lambda}$ and electric field vector $\boldsymbol{E}^{\lambda}$ are obtained by taking the derivative of independents.

$$\begin{aligned}\boldsymbol{\varepsilon}^{\lambda}(\boldsymbol{x}) &= \left\{\frac{1}{2}\left[\boldsymbol{u}^{0}\otimes\nabla_{x}+\left(\boldsymbol{u}^{0}\otimes\nabla_{x}\right)^{T}\right]+\frac{1}{2}\left[\boldsymbol{u}^{1}\otimes\nabla_{y}+\left(\boldsymbol{u}^{1}\otimes\nabla_{y}\right)^{T}\right]\right\}\\ &\quad +\lambda\left\{\frac{1}{2}\left[\boldsymbol{u}^{1}\otimes\nabla_{x}+\left(\boldsymbol{u}^{1}\otimes\nabla_{x}\right)^{T}\right]+\frac{1}{2}\left[\boldsymbol{u}^{2}\otimes\nabla_{y}+\left(\boldsymbol{u}^{2}\otimes\nabla_{y}\right)^{T}\right]\right\}+\cdots\\ &= \boldsymbol{\varepsilon}^{0}(\boldsymbol{x},\boldsymbol{y})+\lambda\,\boldsymbol{\varepsilon}^{1}(\boldsymbol{x},\boldsymbol{y})+\cdots\\ \boldsymbol{E}^{\lambda}(\boldsymbol{x}) &= -\left(\nabla_{x}\phi^{0}+\nabla_{y}\phi^{1}\right)-\lambda\left(\nabla_{x}\phi^{1}+\nabla_{y}\phi^{2}\right)+\cdots\\ &= \boldsymbol{E}^{0}(\boldsymbol{x},\boldsymbol{y})+\lambda\,\boldsymbol{E}^{1}(\boldsymbol{x},\boldsymbol{y})+\cdots\end{aligned}\tag{2}$$

where the chain rule on the derivative operator ($\nabla^{\lambda}=\nabla_{x}+\nabla_{y}/\lambda$) is used. Stress $\boldsymbol{\sigma}^{\lambda}$ and electric displacement $\boldsymbol{D}^{\lambda}$ can be evaluated by applying the constitutive equations as follows:

$$\begin{aligned}\boldsymbol{\sigma}^{\lambda} &= \boldsymbol{C}(\boldsymbol{y}):\boldsymbol{\varepsilon}^{\lambda}-\boldsymbol{e}^{T}(\boldsymbol{y})\cdot\boldsymbol{E}^{\lambda}\\ &= \left\{\boldsymbol{C}(\boldsymbol{y}):\boldsymbol{\varepsilon}^{0}-\boldsymbol{e}^{T}(\boldsymbol{y})\cdot\boldsymbol{E}^{0}\right\}+\lambda\left\{\boldsymbol{C}(\boldsymbol{y}):\boldsymbol{\varepsilon}^{1}-\boldsymbol{e}^{T}(\boldsymbol{y})\cdot\boldsymbol{E}^{1}\right\}+\cdots\\ &= \boldsymbol{\sigma}^{0}+\lambda\,\boldsymbol{\sigma}^{1}+\cdots\\ \boldsymbol{D}^{\lambda} &= \boldsymbol{e}(\boldsymbol{y}):\boldsymbol{\varepsilon}^{\lambda}+\Xi(\boldsymbol{y})\,\boldsymbol{E}^{\lambda}\\ &= \left\{\boldsymbol{e}(\boldsymbol{y}):\boldsymbol{\varepsilon}^{0}+\Xi(\boldsymbol{y})\,\boldsymbol{E}^{0}\right\}+\lambda\left\{\boldsymbol{e}(\boldsymbol{y}):\boldsymbol{\varepsilon}^{1}+\Xi(\boldsymbol{y})\,\boldsymbol{E}^{1}\right\}+\cdots\\ &= \boldsymbol{D}^{0}+\lambda\,\boldsymbol{D}^{1}+\cdots\end{aligned}\tag{3}$$

Note that each material constant should be distributed in a microscale $\boldsymbol{y}$. For the case of porous materials, some regions have material parameters as bulk material and other regions are assigned to pores, which are not discretized into finite elements. By substituting these equations into governing equations in the weak form, several sets of equations in each order of λ can be derived. Consequently, microscopic and macroscopic governing equations are obtained as

$$\begin{aligned}&\int_{Y}\partial_{y}\delta\boldsymbol{u}^{1}:\boldsymbol{\sigma}^{0}\,dy=\boldsymbol{0}\\ &\int_{Y}\partial_{y}\delta\phi^{1}\cdot\boldsymbol{D}^{0}\,dy=0\end{aligned}\tag{4}$$

$$\begin{aligned}&\int_{\Omega}\partial_{x}\delta\boldsymbol{u}^{0}:\left(\boldsymbol{C}^{H}:\boldsymbol{\varepsilon}^{H}-\boldsymbol{e}^{H^{T}}\cdot\boldsymbol{E}^{H}\right)d\Omega=\int_{\Omega}\rho^{H}\delta\boldsymbol{u}^{0}\cdot\boldsymbol{b}\,d\Omega+\int_{\Gamma_{\sigma}}\delta\boldsymbol{u}^{0}\cdot\bar{\boldsymbol{t}}\,d\Gamma\\ &\int_{\Omega}\nabla_{x}\delta\phi^{0}\cdot\left(\boldsymbol{e}^{H}:\boldsymbol{\varepsilon}^{H}+\boldsymbol{\Xi}^{H}\cdot\boldsymbol{E}^{H}\right)d\Omega=\int_{\Gamma_{D}}\delta\phi^{0}\bar{q}\,d\Gamma\end{aligned}\tag{5}$$

Eqn. (4) means self-equilibrium in the RVE indicated as Y, and (5) is a similar equation to the conventional governing equations except for the use of the homogenized material properties.

A macroscopic strain and a macroscopic electric field vector are defined by volume averaging in the RVE.

$$\boldsymbol{\varepsilon}^H(\boldsymbol{x}) = \left\langle \boldsymbol{\varepsilon}^0 \right\rangle = \frac{1}{|Y|}\int_Y \boldsymbol{\varepsilon}^0 \, dy$$
$$\boldsymbol{E}^H(\boldsymbol{x}) = \left\langle \boldsymbol{E}^0 \right\rangle = \frac{1}{|Y|}\int_Y \boldsymbol{E}^0 \, dy \tag{6}$$

In addition, macroscopic material tensors, which can be used as conventional material tensors for the macroscopic boundary problem, are obtained from the characteristic functions.

$$C^H_{ijkl}(\boldsymbol{x},\boldsymbol{y}) = \frac{1}{|Y|}\int_Y C_{ijkl} + C_{ijpq}\frac{\partial \chi^{kl}_p(\boldsymbol{x},\boldsymbol{y})}{\partial y_q} + e_{rij}\frac{\partial \varphi^{kl}(\boldsymbol{x},\boldsymbol{y})}{\partial y_r} dY$$
$$e^H_{mij}(\boldsymbol{x},\boldsymbol{y}) = \frac{1}{|Y|}\int_Y e_{mij} + e_{pij}\frac{\partial R^m(\boldsymbol{x},\boldsymbol{y})}{\partial y_p} + C_{ijpq}\frac{\partial \Phi^m_p(\boldsymbol{x},\boldsymbol{y})}{\partial y_q} dY \tag{7}$$
$$\Xi^H_{im}(\boldsymbol{x},\boldsymbol{y}) = \frac{1}{|Y|}\int_Y \Xi^H_{im} + \Xi^H_{ip}\frac{\partial R^m(\boldsymbol{x},\boldsymbol{y})}{\partial y_p} - e_{ipq}\frac{\partial \Phi^m_p(\boldsymbol{x},\boldsymbol{y})}{\partial y_q} dY$$

Note that characteristic functions should satisfy the periodic boundary conditions in the RVE because of an assumption in the derivation of homogenized material tensors. These functions should be calculated to solve microscopic governing equations (4) using FEM in general.

$$\int_Y \partial_y \delta\boldsymbol{u}^1 : (\boldsymbol{C} : \partial_y \boldsymbol{\chi}^{kl} + \boldsymbol{e}^T \cdot \nabla_y \varphi^{kl}) dy = -\int_Y \partial_y \delta\boldsymbol{u}^1 : \boldsymbol{C} : \boldsymbol{I}^{kl} dy$$
$$\int_Y \nabla_y \delta\phi^1 \cdot (\boldsymbol{e} : \partial_y \boldsymbol{\chi}^{kl} - \boldsymbol{\Xi} \cdot \nabla_y \varphi^{kl}) dy = -\int_Y \nabla_y \delta\phi^1 \cdot \boldsymbol{e} : \boldsymbol{I}^{kl} dy \tag{8}$$

$$\int_Y \partial_y \delta\boldsymbol{u}^1 : (\boldsymbol{C} : \partial_y \boldsymbol{\Phi}^m + \boldsymbol{e}^T \cdot \nabla_y R^m) dy = -\int_Y \partial_y \delta\boldsymbol{u}^1 : \boldsymbol{e}^T \cdot \boldsymbol{I}^m dy$$
$$\int_Y \nabla_y \delta\phi^1 \cdot (\boldsymbol{e} : \partial_y \boldsymbol{\Phi}^m - \boldsymbol{\Xi} \cdot \nabla_y R^m) dy = \int_Y \nabla_y \delta\phi^1 \cdot \boldsymbol{\Xi} \cdot \boldsymbol{I}^m dy \tag{9}$$

where $\boldsymbol{\chi}^{kl}$ and φ^{kl} have nine components associated with the free index k,l and these are reduced to six individual components for their symmetry. $\boldsymbol{\Phi}^m$ and R^m also have three components. In total, nine sets of equations should be solved for the evaluation of homogenized materials tensors.

2.2 Semi-automatic process to generate 3D micrographs for porous PZT

As mentioned in the Introduction, the image scanning by X-ray CT is essential for automatic FE mesh generation of microstructure for heterogeneous materials. Here, a semi-automatic process is employed to ensure the accurate porosity ratio. First, conventional image-based modeling with X-ray CT images is summarized as follows.

STEP 1. Capture the cross-sectional images in gray scale by X-ray CT

STEP 2. Estimate the porosity ratio

STEP 3. Automatic binarization of X-ray CT images with reference to the estimated porosity ratio

STEP 4. Automatic 3D FE Modeling with binarized X-ray CT images

In the classical rule of mixture, macroscopic material properties are basically functions of the porosity ratio. In addition, the shape and the size of pores strongly depend on the estimated porosity ratio in the above-mentioned process. Therefore, the porosity ratio is a significant factor in the design of porous materials. The mercury penetration method has been widely used, but the reliability of this measurement is not guaranteed for samples involving closed micropores. Thus, an image-based measurement technique that counts the area of pores in each cross-section has been adopted in STEP 2.

In STEP 3, rectangular specimens with the size 1.5mm×1.5mm×5mm are used for the observation by X-ray CT. Then, the direct cross-sectional images of the same specimen are captured by SEM with sectioning and polishing. The gray-scale SEM images are binarized manually, and black areas corresponding to pores are measured. The manual binarization is implemented with only a cross-sectional SEM image composed of six images taken differently. This area (=$1470\times1470\ \mu m^2$) is 30 times larger than the cross-section area of the RVE (=$260\times260\ \mu m^2$) defined in the next capter. It should be noted that the porosity ratios in all cross-sectional X-ray CT images are measured, and the difference among others is small. Therefore, area of the SEM image is sufficiently large enough to estimate the porosity ratio.

As shown in Fig. 3(c), resolution of the X-ray CT images in the peripheral area is lacking. Therefore, only the central region(=$650\times650\ \mu m^2$) of the original X-ray CT images(=$1170\times1170\ \mu m^2$) was used for the 3D microstructure reconstruction in STEP 3.

The above mentioned semi-automatic process to generate FE model is illustrated in Fig. 1. The key points of this process are 1) the estimation of the porosity ratio using manually binarized SEM images and 2) the limited use of X-ray CT images.

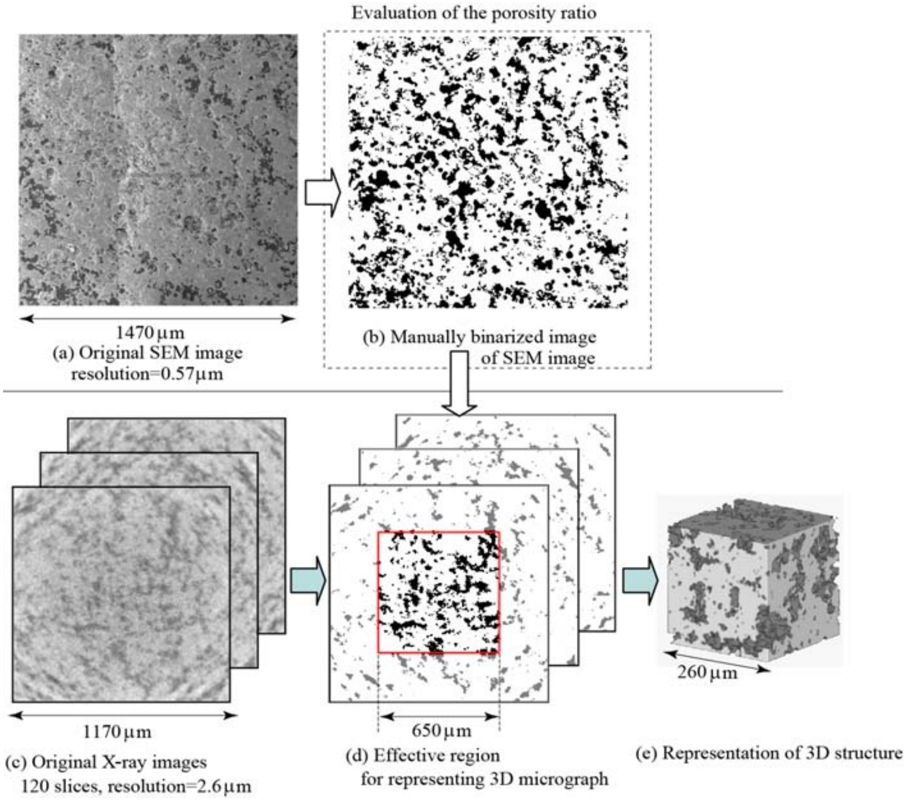

Figure 1. Semi-automatic process to generate FEM model for porous PZT ceramics.

3. Application to porous PZT materials

3.1 X-ray CT and SEM observation for 3D microstructure

Macroscopic material properties of two porous PZT samples with different porosity ratio were evaluated by the homogenization method. Figure 2 shows the X-ray CT images for these samples. The resolution is 2.6 μm for each sample. After capturing 120 X-ray CT images, the direct cross-sectional images are captured by SEM with the fine resolution (=0.57 μm). The estimated porosity ratios of samples A and B are 7.1% and 25.5 %, respectively. The estimation is implemented with manually binarized SEM images as mentioned.

For sample B with 25.5% porosity ratio, the sizes of pores were measured by the binarized SEM and X-ray CT images. While the resolution of X-ray CT images is sufficiently high for sample B, sample A has many micropores beyond the resolution of the X-ray CT.

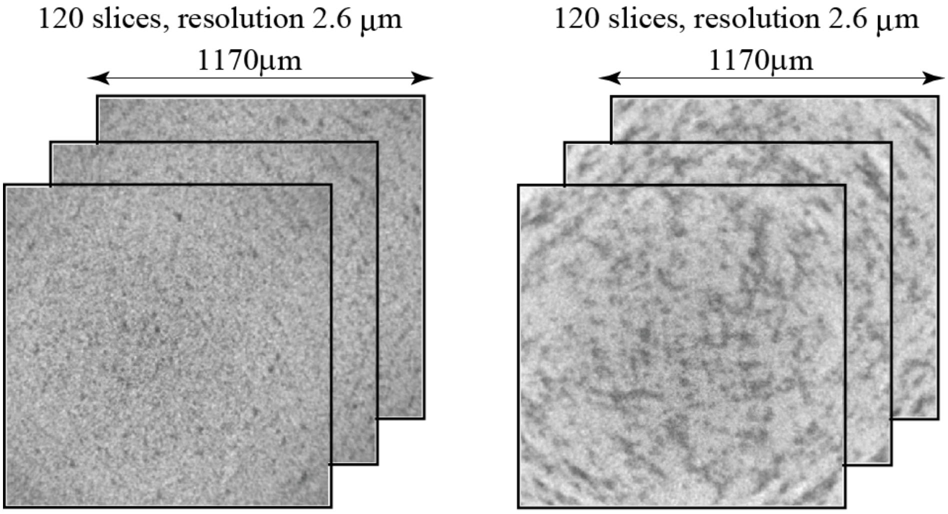

(a) Original X-ray CT images for sample A

(b) Original X-ray CT images for sample B

Figure 2. X-ray CT images for two different samples.

3.2 Modification for unresolved micropores in binarization process

Here, a treatment for unresolved micropores is described. After the elimination of unresolved micropores, the porosity ratio is counted as 4.4% in the SEM image. The threshold of X-ray CT images in the automatic binarization is readjusted to this ratio.

The remaining porosity ratio (2.7% in volume) is recovered by randomly distributed cubic pores that are fixed by 2^3 in the voxel model as shown in Fig. 3. During the compensating process for the remaining porosity ratio, overlapping and/or adjoining pore is removed and located in other free space. Note that effect of the distribution of micropores is predictable by the classical rule of mixture, and it is vanishingly small. Figures 3 and 4 show the result of 3D reconstruction by labeling each collar of closed pores. These observations in 3D morphology reveal that sample A has many closed pores and sample B has an open pore percolating huge small pores.

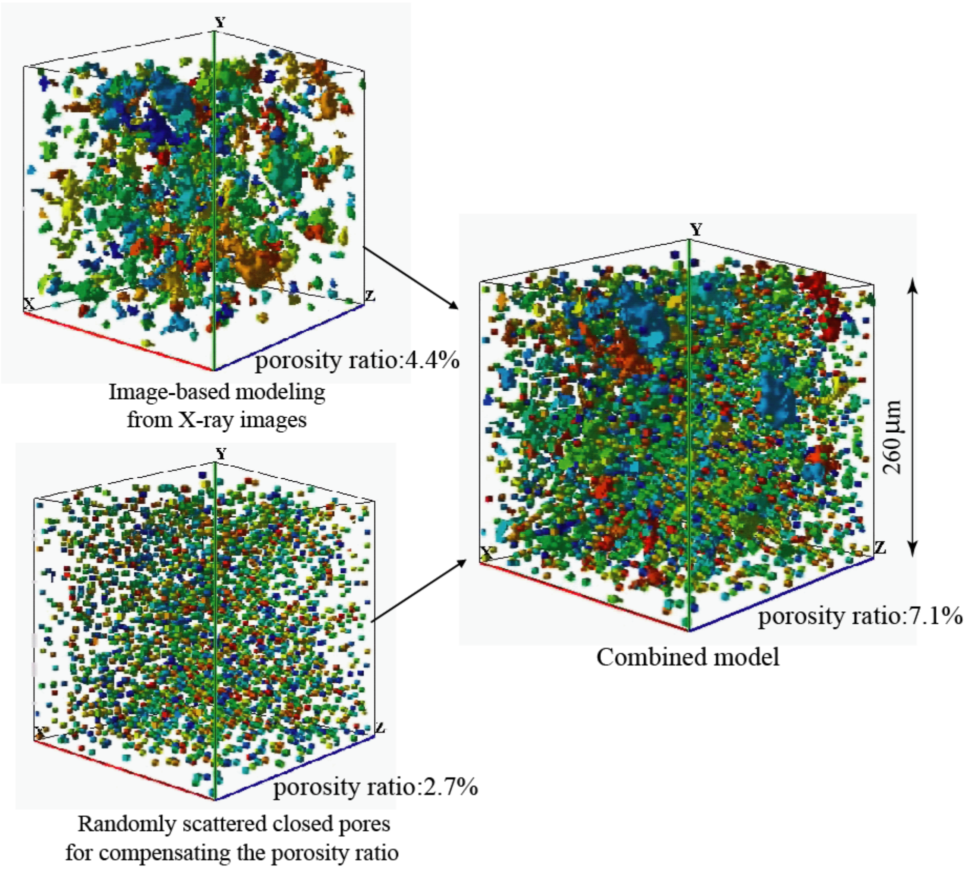

Image-based modeling
from X-ray images

Randomly scattered closed pores
for compensating the porosity ratio

Combined model

Figure 3. Labeling image of pores in sample A.

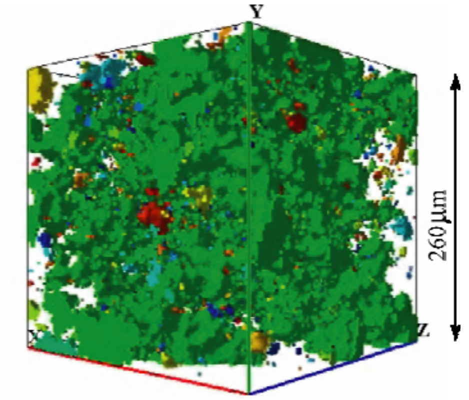

Figure 4. Labeling image of pores in sample B.

Table 1. Bulk material coefficients

	Notation in vector-matrix format	Values
Elastic constants (GPa)	C_{11}	125.2
	C_{33}	116.8
	C_{12}	80.99
	C_{13}	80.61
	C_{44}	22.50
	C_{66}	26.25
Piezoelectric constants (C/m^2)	e_{31}	-10.8
	e_{33}	18.72
	e_{15}	15.99
Dielectric constants (C^2/Nm^2)	${}^{e}\Xi_{11}$	26.78
	${}^{e}\Xi_{33}$	31.87

4.4 Discussion of the macroscopic material parameters

Figure 5 shows the homogenized material parameters for these two samples. These numerical results are compared with results of a series, in which a spherical pore is located in the center of the RVE as shown in Fig. 5(a). In the series of spherical pore, the porosity ratios vary according to its radius. Figure 5(d) shows the component of the piezoelectric strain tensor $\boldsymbol{d}^{H}$ in the following "d-form" constitutive equations:

$$\begin{aligned} \boldsymbol{\varepsilon}^{H} &= \boldsymbol{S}^{H} : \boldsymbol{\sigma}^{H} + \boldsymbol{d}^{H^{T}} \cdot \boldsymbol{D}^{H} \quad (\varepsilon_{ij}^{H} = C_{ijkl}^{H}\sigma_{kl}^{H} + d_{mij}^{H} D_{m}^{H}) \\ \boldsymbol{E}^{H} &= \boldsymbol{d}^{H} : \boldsymbol{\sigma}^{H} + {}^{d}\boldsymbol{\Xi}^{H} \cdot \boldsymbol{D}^{H} \quad (E_{i}^{H} = d_{ikl}^{H}\sigma_{kl}^{H} + {}^{d}\Xi_{ij}^{H} D_{j}^{H}) \end{aligned} \tag{10}$$

The above equations are called homogenized "d-form" constitutive equations. Each component in the e-form constitutive equations in Fig. 5(a)–11(c) shows a monotonic decrease in porosity ratio, but the slopes are different. As the porosity ratio increases, the absolute values in d_{ij}^{H} also show a monotonic decrease as shown in Fig. 5(d) for d_{31}^{H} and d_{33}^{H}.

Using these homogenized values, a macroscopic electromechanical coupling factor can be evaluated as,

$$k_{h}^{H} = \sqrt{\frac{{d_{h}^{H}}^{2}}{{}^{d}\Xi_{33}^{H}\hat{S}^{H}}}\ , \ d_{h}^{H} \equiv \mathrm{d}_{31}^{H} + \mathrm{d}_{32}^{H} + \mathrm{d}_{33}^{H},\ \hat{S}^{H} \equiv \mathrm{S}_{11}^{H} + \mathrm{S}_{22}^{H} + \mathrm{S}_{33}^{H} + 2\mathrm{S}_{23}^{H} + 2\mathrm{S}_{31}^{H} + 2\mathrm{S}_{12}^{H} \tag{11}$$

where roman style in the material tensor means the vector matrix notation. These results for each model are plotted in Fig. 6(d). The constituents in k_{h} are also plotted in Fig. 6. Two characteristic microstructures, labeled as model A and model B in Fig 6(a), have been evaluated to discuss the effect of the morphology.

These results are summarized below,

1. Comparisons between sample A and a virtual model containing a spherical pore with the same porosity ratio reveal that a change in each material parameters for the case of randomly distributed closed pores modeled as a function of porosity ratio.
2. Each component in material tensors shows monotonic changes with reference to the porosity ratio: however, this is strongly dependent on the morphology of its microstructure. In particular, for the electromechanical coupling factor at 25% porosity ratio, the value in model A is almost double the value in model B.
3. The percolation of pores plays a significant role to improve the electromechanical coupling factor. The effect of the percolation is also discussed from a microstructural viewpoint by Roncari et al.[18].
4. The d_{33}^{H} (d_{333}^{H} in tensor description) is a positive value, and the other component of the piezoelectric strain tensor d_{31}^{H} (d_{311}^{H}) and d_{32}^{H} (d_{322}^{H}) have negative values. The slope of change in d_{33}^{H} is lower than that in the absolute values in the other directions d_{31}^{H} and d_{32}^{H}. Consequently, these changes cause the monotonic increase in d_h. Experimental results [2,3] support our numerical results qualitatively.

In future work, we have to verify the accuracy of the homogenization method by comparing with experimental data. In general, PZT materials are used after polarization as a precondition for piezoelectric properties. The polar directions are strongly dependent on the initial orientation of the crystal and on the distribution of stress and electrical displacement vector in the polarization process at high voltage. Therefore, we have to carefully consider the crystallographic orientation and nonlinear material behaviors.

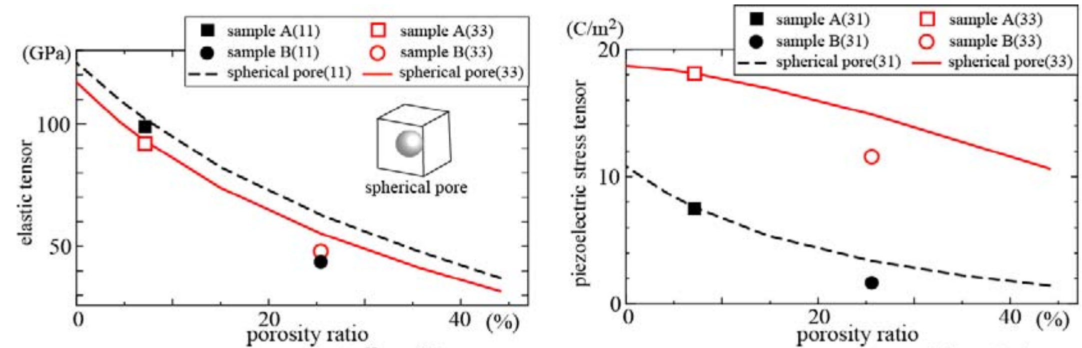

(a) elastic tensor (C_{11}^H , C_{33}^H) (b) piezoelectric stress tensor ($|e_{31}^H|$, e_{33}^H)

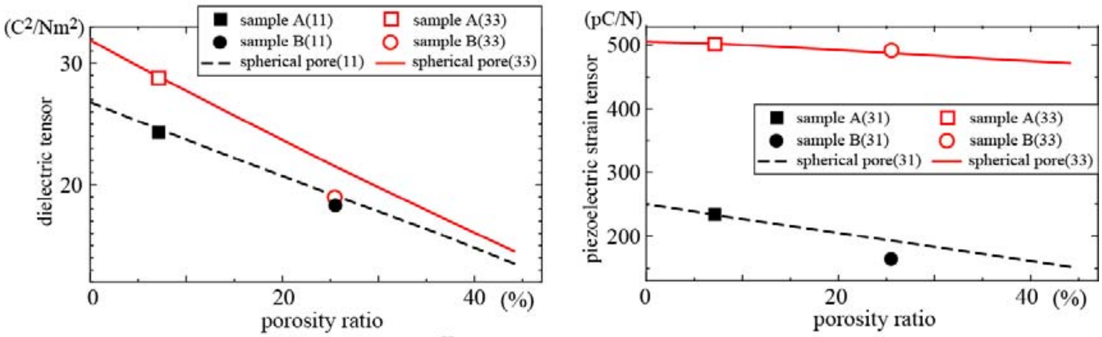

(c) dielectric tensor (${}^e\Xi_{11}^H$, ${}^e\Xi_{33}^H$) (d) piezoelectric strain tensor ($|d_{31}^H|$, d_{33}^H)

Figure 5. Homogenized material properties of image-based models and fictitious models with a closed spherical pore. The round bracket in figures indicates the components of tensor in vector-matrix notation.

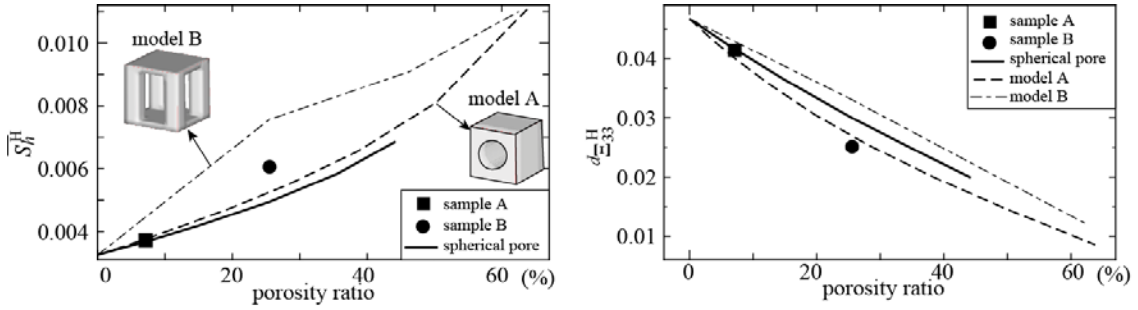

(a) elastic compliance (S_h^H) (b) dielectric property (${}^d\Xi_{33}^H$)

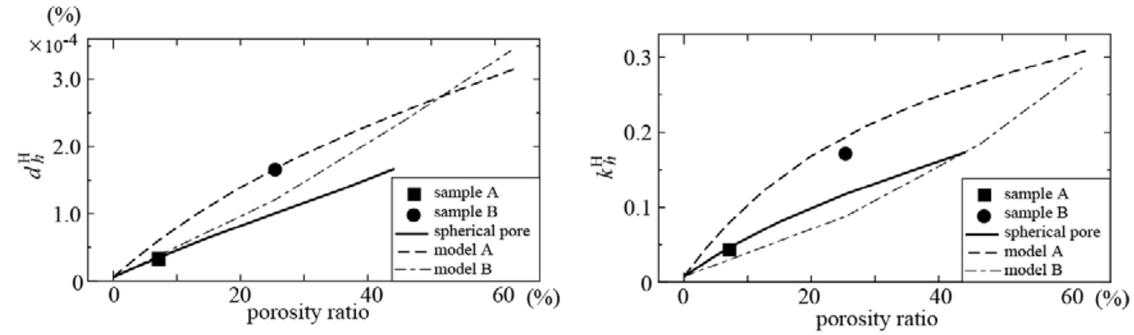

(c) piezoelectric strain property (d_h^H) (d) electromechanical coupling factor (k_h^H)

Figure 6. Comparison of the effect of microstructures in macroscopic material properties.

5. Conclusions

In this paper, we discussed the mechanisms of outstanding properties of porous PZT with several numerical results by the homogenization method.

A major problem in the homogenization method is the application to the nonlinear problem including material and geometrical nonlinearities. The asymptotic homogenization is one of the convergence theories. That is, when the spatial scale in material differs vastly from the spatial scale in structure, the theory gives a reasonable approximation. However, the engineering material, especially in the nonlinear region, shows the ‘scale effect’. If the nonlinear homogenization theory, which can predict the scale effect in the material response, is proposed, many engineers may use the design of structure and material.

References

[1] Asai M, Takano N, Uetsuji Y and Taki K 2007 *Modeling and Simulation in Metarial Science and Engineering* **15** 597-617

[2] Kumar B P, Kumar H H and Kharat D K 2006 *Materials Science and Engineering* B **127** 130-133

[3] Dunn M L and Taya M 1993 *J. Am. Ceram. Soc.* **76** 1697-1706

[4] Benveniste Y 1992 *J. Appl. Phys.* **72**(3) 1086-1095

[5] Hori M and Nemat-Nasser S 1998 *Mech. Mater.* **30** 1-19

[6] Lions J L 1979 *Variational Method in Mechanics of Solids* New York Pergman Press 3-19

[7] Guedes J M and Kikuchi N 1990 *Comput. Methods Appl. Mech. Engrg.* **83** 143-198

[8] Takano N, Ohnishi Y, Zako M and Nishiyabu K 2001 *Int. J. Solids Struct.* **38** 36-37

[9] Ghosh S and Moorthy S 1995 *Comput. Methods Appl. Mech. Engrg.* **121** pp.373-409

[10] Takano N, Ohnishi Y and Zako M 2000 *Int. J. Solids Struct.* **37** 6515-6535

[11] Terada K and Kikuchi N 2001 *Comput. Methods Appl. Mech. Engrg.* **190** 5427-5464

[12] Terada K, Ito T and Kikuchi N 1998 *Comput. Methods Appl. Mech. Engrg.* **153** 223-257

[13] Takano N, Zako M, Okazaki T and Terada K 2002 *Compos. Sci. Technol.* **62** 1347-1356

[14] Silva C N, Fonseca J S O, Espinosa F M, Crum A T, Brady G A, Halloran J W and Kikuchi N 1999 *Archives of computational methods in engineering* **6** 117-182

[15] Uetsuji Y, Nakamra Y, Ueda S and Nakamachi E 2004 *Modeling Simul. Mater. Sci. Eng.* **12** 303-317

[16] Hollister S and Kikuchi N 1994 *Biotechnol. Bioeng.* **43** 586-596

[17] Takano N, Zako M, Kubo F and Kimura K 2003 *Int. J. Solids Struct.* **40**(5) 1225-1242

[18] Roncari E, Galassi C, Craciun C, Capiani C and Piancastelli 2001 *J. Eur. Ceram. Soc.* **21** 409-417

Efficient numerical computations on large scale electromagnetic field problems using an iterative domain decomposition method

TAGAMI, Daisuke

Institute of Mathematics for Industry, Kyushu University
tagami@imi.kyushu-u.ac.jp

Abstract

An iterative domain decomposition method is applied to magnetostatic problems. In our previous methods the gauge condition is neglected, then the magnetic vector potential is only one unknown function. On the other hand, it has been well-known that some theoretical results has been introduced, where a mixed formulation with the Lagrange multiplier is introduced in order to impose the gauge condition. Therefore, in this paper, we formulate again an iterative domain decomposition method based on a mixed formulation of magnetostatic problem, and discuss relations with the previous one.

Keywords: *magnetostatic problem, mixed formulation, iterative domain decomposition method*

1 Introduction

We have introduced an iterative domain decomposition method to solve quite large scale electromagnetic field problems; see, for example, Kanayama *et al.* [8]. In our previous methods the gauge condition is neglected, then the magnetic vector potential is only one unknown function. These previous results focus themselves on the engineering points of view: the previous formulation enables us to reduce computational consts in practical large scale simulations. However this formulation yields an indeterminate linear system, it is difficult to mathematically justify numerical results, for example unique solvability of the problems and convergency of the approximate solution.

On the other hand, some theoretical results has been introduced by, for example, Kikuchi [6], [7], where a mixed formulation with the Lagrange multiplier is introduced in order to impose the gauge condition. These results focus themselves on the mathematical point of view: owing to the introduction of the Lagrange multiplier, their mixed formulation enable us to prove unique solvability of the problems and convergency of the approximate solution. However this formulation yields an indefinite linear system, it is difficult to find an appropriate iterative solver, which is efficient enough to reduce computational costs for practical large scale problems.

At first in this paper, we formulate again an iterative domain decomposition method based on a mixed formulation of magnetostatic problem introduced in Kikuchi [6], [7], which enable us to prove unique solvability of the problems and convergency of the approximate solution. Seconed, to reduce computational costs, we simplify our iterative domain decomposition method into another one, and we discuss relations between the reduced formulation and the previous one.

2 Formulation of magnetostatic problems

Let Ω be a polyhedoral domain with its boundary Γ, and $\boldsymbol{n}$ the outward unit normal of Ω. Let $\boldsymbol{u}$ denote the magnetic vector potential, $\boldsymbol{f}$ an excitation current density, and ν the magnetic reluctivity. Then, we consider the magnetostatic equation with the Coulomb gauge condition:

$$\begin{cases} \operatorname{rot}(\nu \operatorname{rot} \boldsymbol{u}) = \boldsymbol{f} & \text{in } \Omega, & \text{(1a)} \\ \operatorname{div} \boldsymbol{u} = 0 & \text{in } \Omega, & \text{(1b)} \\ \boldsymbol{u} \times \boldsymbol{n} = \boldsymbol{0} & \text{on } \Gamma; & \text{(1c)} \end{cases}$$

for example, see Kikuchi [6].

As usual, let $L^2(\Omega)$ be the space of real functions defined in Ω and 2nd power summable in Ω, let $\|\,.\,\|$ be its norm, and let $(\,.\,,\,.\,)$ be its inner product; let $H^1(\Omega)$ be the space of functions in $L^2(\Omega)$ with derivatives up to the 1st order, and let $\|\,.\,\|_1$ and $|\,.\,|_1$ be its norm and seminorm, respectively; and set functional spaces X, M, V, and Q by

$$\begin{aligned} X &:= \{\boldsymbol{v} \in (L^2(\Omega))^3;\ \operatorname{rot} \boldsymbol{v} \in (L^2(\Omega))^3\}, & M &:= H^1(\Omega), \\ V &:= \{\boldsymbol{v} \in X;\ \boldsymbol{v} \times \boldsymbol{n} = \boldsymbol{0} \ \text{on } \Gamma\}, & Q &:= \{q \in M;\ q = 0 \ \text{on } \Gamma\}, \end{aligned}$$

respectively; set bilinear forms $a(\,.\,,\,.\,)$ and $b(\,.\,,\,.\,)$ by

$$\begin{aligned} a(\boldsymbol{u}, \boldsymbol{v}) &:= \int_\Omega \nu \operatorname{rot} \boldsymbol{u} \operatorname{rot} \boldsymbol{v}\, dx, & &\forall (\boldsymbol{u}, \boldsymbol{v}) \in X \times X, \\ b(\boldsymbol{v}, q) &:= \int_\Omega \boldsymbol{v} \operatorname{grad} q\, dx, & &\forall (\boldsymbol{v}, q) \in (L^2(\Omega))^3 \times M, \end{aligned}$$

respectively.

Now, by introducing the Lagrange multiplier p, we obtain a mixed weak formulation of (1) as follows: given $\boldsymbol{f} \in (L^2(\Omega))^3$, find $(\boldsymbol{u}, p) \in V \times Q$ such that

$$\begin{cases} a(\boldsymbol{u}, \boldsymbol{v}) + b(\boldsymbol{v}, p) = (\boldsymbol{f}, \boldsymbol{v}), & & \text{(2a)} \\ b(\boldsymbol{u}, q) = 0, & \forall (\boldsymbol{v}, q) \in V \times Q. & \text{(2b)} \end{cases}$$

Some theoretical results of (2) such as the unique solvability have been proved in Kikuchi [6].

Remark 1 *As in mentioned in Kikuchi [6], if* $\boldsymbol{f}$ *satisfies that* $\operatorname{div} \boldsymbol{f} = 0$ *in* Ω*, then* $p = 0$*. This property plays a key role in the forthcoming section.*

3 Domain decomposition method

For simplicity, the domain Ω is assumed to be decomposed into two non-overlapping subdomains $\Omega^{(1)}$ and $\Omega^{(2)}$ with their boundaries $\partial\Omega^{(1)}$ and $\partial\Omega^{(2)}$, respectively:

$$\Omega^{(i)} \neq \emptyset \quad (i = 1, 2), \qquad \bar{\Omega} = \bar{\Omega}^{(1)} \cup \bar{\Omega}^{(2)}, \qquad \Omega^{(1)} \cap \Omega^{(2)} = \emptyset;$$

and let γ_{12} be the interface between $\Omega^{(1)}$ and $\Omega^{(2)}$ defined by $\gamma_{12} := \bar{\Omega}^{(1)} \cap \bar{\Omega}^{(2)}$; see Fig. 1. For $i = 1, 2$, the outward unit normal of $\Omega^{(i)}$ is denoted by $\boldsymbol{n}^{(i)}$, and set $\boldsymbol{n} = \boldsymbol{n}^{(1)} (= -\boldsymbol{n}^{(2)})$ on the interface γ_{12}.

Instead of the real functions defined in Ω, we associate this decomposition to function spaces, bilinear forms, and inner product: let $L^2(\Omega^{(i)})$ and $H^1(\Omega^{(i)})$ be the space of real functions defined in $\Omega^{(i)}$, which are corresponding to $L^2(\Omega)$ and $H^1(\Omega)$; set function spaces $X^{(i)}$, $M^{(i)}$, $V^{(i)}_{\gamma_{12}}$, $Q^{(i)}_{\gamma_{12}}$, $V^{(i)}$, and $Q^{(i)}$ by

$$\begin{aligned} X^{(i)} &:= \{\boldsymbol{v} \in (L^2(\Omega^{(i)}))^3;\ \operatorname{rot} \boldsymbol{v} \in (L^2(\Omega^{(i)}))^3\}, & M^{(i)} &:= H^1(\Omega^{(i)}), \\ V^{(i)}_{\gamma_{12}} &:= \left\{\boldsymbol{v} \in X^{(i)};\ \boldsymbol{v} \times \boldsymbol{n} = \boldsymbol{0} \ \text{on } \partial\Omega^{(i)} \backslash \gamma_{12}\right\}, & Q^{(i)}_{\gamma_{12}} &:= \left\{q \in M^{(i)};\ q = 0 \ \text{on } \partial\Omega^{(i)} \backslash \gamma_{12}\right\}, \\ V^{(i)} &:= \left\{\boldsymbol{v} \in X^{(i)};\ \boldsymbol{v} \times \boldsymbol{n} = \boldsymbol{0} \ \text{on } \partial\Omega^{(i)}\right\}, & Q^{(i)} &:= \left\{q \in M^{(i)};\ q = 0 \ \text{on } \partial\Omega^{(i)}\right\}, \end{aligned}$$

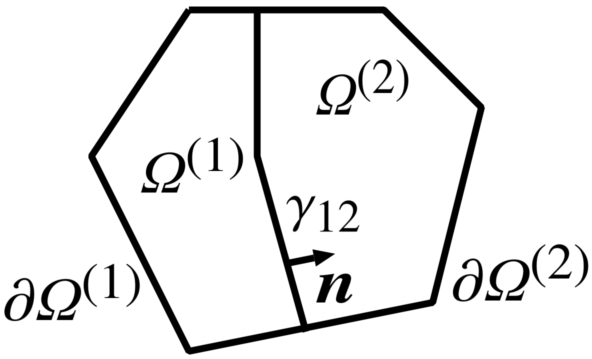

Fig. 1: Two non-overlapping subdomains of Ω.

respectively; and set bilinear forms and inner product $a^{(i)}(\,.\,,\,.\,)$, $b^{(i)}(\,.\,,\,.\,)$, and $(\,.\,,\,.\,)_{\Omega^{(i)}}$ by

$$
\begin{aligned}
a^{(i)}(\boldsymbol{u}^{(i)},\, \boldsymbol{v}^{(i)}) &:= \int_{\Omega^{(i)}} \nu \operatorname{rot} \boldsymbol{u}^{(i)} \operatorname{rot} \boldsymbol{v}^{(i)}\, dx, && \forall(\boldsymbol{u}^{(i)}, \boldsymbol{v}^{(i)}) \in X^{(i)} \times X^{(i)},\\
b^{(i)}(\boldsymbol{v}^{(i)},\, p^{(i)}) &:= \int_{\Omega^{(i)}} \boldsymbol{v}^{(i)} \operatorname{grad} p^{(i)}\, dx, && \forall(\boldsymbol{v}^{(i)}, p^{(i)}) \in (L^2(\Omega^{(i)}))^3 \times M^{(i)},\\
(\boldsymbol{u}^{(i)},\, \boldsymbol{v}^{(i)})_{\Omega^{(i)}} &:= \int_{\Omega^{(i)}} \boldsymbol{u}^{(i)}\, \boldsymbol{v}^{(i)}\, dx, && \forall(\boldsymbol{u}^{(i)}, \boldsymbol{v}^{(i)}) \in (L^2(\Omega^{(i)}))^3 \times (L^2(\Omega^{(i)}))^3,
\end{aligned}
$$

respectively. Moreover, set function spaces Λ and Ξ by

$$
\Lambda := \Big\{\boldsymbol{\lambda} : \gamma_{12} \to \mathbb{R}^3;\ \boldsymbol{\lambda} = (\boldsymbol{v} \times \boldsymbol{n})|_{\gamma_{12}},\ \boldsymbol{v} \in V\Big\}, \qquad \Xi := \Big\{\xi : \gamma_{12} \to \mathbb{R};\ \xi = q|_{\gamma_{12}},\ q \in Q\Big\};
$$

and set $\overline{\boldsymbol{u}}^{(i)}(\boldsymbol{\eta})$ by any extension operator from Λ to $V^{(i)}_{\gamma_{12}}$ such that $\boldsymbol{\eta} = (\overline{\boldsymbol{u}}^{(i)}(\boldsymbol{\eta}) \times \boldsymbol{n})|_{\gamma_{12}}$, and $\bar{p}^{(i)}(\zeta)$ by any extension operator from Ξ to $Q^{(i)}_{\gamma_{12}}$ such that $\zeta = p(\zeta)|_{\gamma_{12}}$. A characterization of *tangential trace* spaces Λ and an *tangential extension* operator on $\overline{\boldsymbol{u}}^{(i)}(\boldsymbol{\eta})$ has been given in Alonso–Valli [1], Buffa–Ciarlet [2], [3], Buffa, *et al.* [4], and Quarteroni–Valli [9].

Now, a two-subdomain problem is introduced by the followings: for $i = 1, 2$, find $(\boldsymbol{u}^{(i)}, p^{(i)}) \in V^{(i)}_{\gamma_{12}} \times Q^{(i)}_{\gamma_{12}}$ such that

$$
\begin{cases}
a^{(i)}(\boldsymbol{u}^{(i)},\, \boldsymbol{v}^{(i)}) + b^{(i)}(\boldsymbol{v}^{(i)},\, p^{(i)}) = (\boldsymbol{f}^{(i)},\, \boldsymbol{v}^{(i)})_{\Omega^{(i)}}, & \text{(3a)}\\
b^{(i)}(\boldsymbol{u}^{(i)},\, q^{(i)}) = 0, \qquad \forall(\boldsymbol{v}^{(i)},\, q^{(i)}) \in V^{(i)} \times Q^{(i)} & \text{(3b)}\\
\boldsymbol{u}^{(1)} \times \boldsymbol{n} = \boldsymbol{u}^{(2)} \times \boldsymbol{n} \qquad \text{on } \gamma_{12}, & \text{(3c)}\\
p^{(1)} = p^{(2)} \qquad \text{on } \gamma_{12}, & \text{(3d)}\\
a^{(2)}(\boldsymbol{u}^{(2)},\, \overline{\boldsymbol{u}}^{(2)}(\boldsymbol{\eta})) + b^{(2)}(\overline{\boldsymbol{u}}^{(2)}(\boldsymbol{\eta}),\, p^{(2)}) & \\
\quad = (\boldsymbol{f}^{(1)},\, \overline{\boldsymbol{u}}^{(1)}(\boldsymbol{\eta}))_{\Omega^{(1)}} + (\boldsymbol{f}^{(2)},\, \overline{\boldsymbol{u}}^{(2)}(\boldsymbol{\eta}))_{\Omega^{(2)}} - a^{(1)}(\boldsymbol{u}^{(1)},\, \overline{\boldsymbol{u}}^{(1)}(\boldsymbol{\eta})) - b^{(1)}(\overline{\boldsymbol{u}}^{(1)}(\boldsymbol{\eta}),\, p^{(1)}), & \text{(3e)}\\
b^{(2)}(\boldsymbol{u}^{(2)},\, \bar{p}^{(2)}(\zeta)) = b^{(1)}(\boldsymbol{u}^{(1)},\, \bar{p}^{(1)}(\zeta)), \qquad \forall(\boldsymbol{\eta},\, \zeta) \in \Lambda \times \Xi. & \text{(3f)}
\end{cases}
$$

If $\{(\boldsymbol{u}^{(1)},\, p^{(1)}), (\boldsymbol{u}^{(2)},\, p^{(2)})\}$ is a pair of the solutions of two-subdomain problem (3), then the solution of the one-domain problem (2) could be constructed by

$$
(\boldsymbol{u}, p) := \begin{cases}
(\boldsymbol{u}^{(1)},\, p^{(1)}) \qquad \text{in } \Omega^{(1)}, & \text{(4a)}\\
(\boldsymbol{u}^{(2)},\, p^{(2)}) \qquad \text{in } \Omega^{(2)}. & \text{(4b)}
\end{cases}
$$

On the other hand, if $(\boldsymbol{u}, p)$ is a solution of the one-domain problem (2), then a pair of the solutions $\{(\boldsymbol{u}^{(1)},\, p^{(1)}), (\boldsymbol{u}^{(2)},\, p^{(2)})\}$ of the two-subdomain problem (3) could be constructed by

$$
(\boldsymbol{u}^{(i)}, p^{(i)}) := (\boldsymbol{u}|_{\Omega^{(i)}}, p|_{\Omega^{(i)}}) \quad \text{in } \Omega^{(i)}. \tag{5}
$$

Moreover, as mentioned in Sec 2, the one-domain problem (2) is uniquely solvable. Then two-subdomain problem (3) is also uniquely solvable. Therefore, the equivalency between both formulations and unique solvability could be obtained as follows:

Theorem 1 *There exists a unique solution* $(\boldsymbol{u}, p) \in V \times Q$ *of the two-subdomain problem* (3). *Moreover, the one-domain problem* (2) *and the two-subdomain problem* (3) *are equivalent.*

For $i = 1, 2$, let $\mathscr{E}^{(i)}(\boldsymbol{f}, \boldsymbol{\lambda}, \xi)$ an extention operator from $(L^2(\Omega))^3 \times \Lambda \times \Xi$ to $V^{(i)}_{\gamma_{12}} \times Q^{(i)}_{\gamma_{12}}$ defined by $\mathscr{E}^{(i)}(\boldsymbol{f}, \boldsymbol{\lambda}, \xi) := (\boldsymbol{u}^{(i)}, p^{(i)})$, where $(\boldsymbol{u}^{(i)}, p^{(i)})$ is the solution of the following magnetostatic problem:

$$\begin{cases} a^{(i)}(\boldsymbol{u}^{(i)}, \boldsymbol{v}^{(i)}) + b^{(i)}(\boldsymbol{v}^{(i)}, p^{(i)}) = (\boldsymbol{f}^{(i)}, \boldsymbol{v}^{(i)})_{\Omega^{(i)}}, & & \text{(6a)} \\ b^{(i)}(\boldsymbol{u}^{(i)}, q^{(i)}) = 0, & \forall(\boldsymbol{v}^{(i)}, q^{(i)}) \in V^{(i)} \times Q^{(i)}, & \text{(6b)} \\ \boldsymbol{u}^{(i)} \times \boldsymbol{n} = \boldsymbol{\lambda} & \text{on } \gamma_{12}, & \text{(6c)} \\ p^{(i)} = \xi & \text{on } \gamma_{12}. & \text{(6d)} \end{cases}$$

Then, a *Steklov–Poincaré* operator $\mathscr{A}$ from $\Lambda \times \Xi$ to $(\Lambda \times \Xi)'$ is set by

$$\langle \mathscr{A}(\boldsymbol{\lambda}, \xi), (\boldsymbol{\eta}, \zeta) \rangle_{\gamma_{12}} := \sum_{i=1}^{2} \{ a^{(i)}(\overline{\boldsymbol{u}}^{(i)}, \overline{\boldsymbol{v}}^{(i)}) + b^{(i)}(\overline{\boldsymbol{v}}^{(i)}, \bar{p}^{(i)}) + b^{(i)}(\overline{\boldsymbol{u}}^{(i)}, \bar{q}^{(i)}) \}, \quad \forall \boldsymbol{\lambda}, \boldsymbol{\eta} \in \Lambda, \ \forall \xi, \zeta \in \Xi \tag{7}$$

where $(\overline{\boldsymbol{u}}^{(i)}, \bar{p}^{(i)}) := \mathscr{E}^{(i)}(0, \boldsymbol{\lambda}, \xi)$ and $(\overline{\boldsymbol{v}}^{(i)}, \bar{q}^{(i)}) := \mathscr{E}^{(i)}(0, \boldsymbol{\eta}, \zeta)$; and an *interface source* $\boldsymbol{\chi} \in (\Lambda \times \Xi)'$ is set by

$$\langle \boldsymbol{\chi}, (\boldsymbol{\eta}, \zeta) \rangle_{\gamma_{12}} := \sum_{i=1}^{2} \{ (\boldsymbol{f}^{(i)}, \overline{\boldsymbol{v}}^{(i)})_{\Omega^{(i)}} - a^{(i)}(\widehat{\boldsymbol{u}}^{(i)}, \overline{\boldsymbol{v}}^{(i)}) - b^{(i)}(\overline{\boldsymbol{v}}^{(i)}, \widehat{p}^{(i)}) - b^{(i)}(\widehat{\boldsymbol{u}}^{(i)}, \bar{q}^{(i)}) \}, \quad \forall \xi, \zeta \in \Xi \tag{8}$$

where $(\widehat{\boldsymbol{u}}^{(i)}, \widehat{p}^{(i)}) := \mathscr{E}^{(i)}(\boldsymbol{f}^{(i)}, \boldsymbol{0}, 0)$ and $(\overline{\boldsymbol{v}}^{(i)}, \bar{q}^{(i)}) := \mathscr{E}^{(i)}(\boldsymbol{0}, \boldsymbol{\eta}, \zeta)$. Now we introduce the following *interface problem* on γ_{12}:

$$\langle \mathscr{A}(\boldsymbol{\lambda}, \xi), (\boldsymbol{\eta}, \zeta) \rangle_{\gamma_{12}} = \langle \boldsymbol{\chi}, (\boldsymbol{\eta}, \zeta) \rangle_{\gamma_{12}}, \qquad \forall (\boldsymbol{\eta}, \zeta) \in \Lambda \times \Xi. \tag{9}$$

By using the solution $(\boldsymbol{u}^{(i)}, p^{(i)})$ of two-subdomain problem (3), let us set $(\boldsymbol{\lambda}, \xi)$ by $\boldsymbol{\lambda} := \boldsymbol{u}^{(1)} \times \boldsymbol{n}$ $(= \boldsymbol{u}^{(2)} \times \boldsymbol{n})$ and $\xi := p^{(1)} (= p^{(2)})$. Then, because of (3c)–(3f), $(\boldsymbol{\lambda}, \xi)$ satisfies the *interface problem* (9). On the other hand, once the solution $(\boldsymbol{\lambda}, \xi)$ is obtained by solving the *interface problem* (9), for $i = 1, 2$, each pair $(\boldsymbol{u}^{(i)}, p^{(i)}) \in V^{(i)}_{\gamma_{12}} \times Q^{(i)}_{\gamma_{12}}$ could be found from the problem (3a) and (3b) in the corresponding subdomain $\Omega^{(i)}$, where the solution $(\boldsymbol{\lambda}, \xi)$ is regarded as the Dirichlet boundary on the interface: $\boldsymbol{u}^{(i)} \times \boldsymbol{n} = \boldsymbol{\lambda}$ and $p^{(i)} = \xi$ on γ_{12}. Finally, from (4), we can obtain the solution $(\boldsymbol{u}, p)$ of the one-domain problem (2).

Therefore, error analysis of the approximate solution of the problem (3) could be reduced into error analysis of the one of each subdomain problem; For example, when magnetic vector potential $\boldsymbol{u}$ is approximated by the Nedelec element of the first order and the Lagrange multiplier p is approximated by the conventional $P1$-element; see Kikuchi [7].

The *interface problem* (9) is symmetric, and not positive definite. Then, by following Glowinski *et al.* [5], the following conjugate gradient algorithm could be obatined (at least formally):

```
Choose $(\boldsymbol{\lambda}_0, \xi_0)$;
Compute $(\boldsymbol{g}_0, \delta_0)$ by (10);
$(\boldsymbol{w}_0, \omega_0) := (\boldsymbol{g}_0, \delta_0)$;
for $k = 0, 1, \ldots$;
    Compute $\mathscr{A}(\boldsymbol{w}_k, \omega_k)$ by (11);
    $\alpha_k := ((\boldsymbol{g}_k, \delta_k), (\boldsymbol{g}_k, \delta_k)) / (\mathscr{A}(\boldsymbol{w}_k, \omega_k), (\boldsymbol{w}_k, \omega_k))$;
    $(\boldsymbol{\lambda}_{k+1}, \xi_{k+1}) := (\boldsymbol{\lambda}_k, \xi_k) - \alpha_k (\boldsymbol{w}_k, \omega_k)$;
    $(\boldsymbol{g}_{k+1}, \delta_{k+1}) := (\boldsymbol{g}_k, \delta_k) - \alpha_k \mathscr{A}(\boldsymbol{w}_k, \omega_k)$;
```

```
    $\beta_k := ((\boldsymbol{g}_{k+1}, \delta_{k+1}), (\boldsymbol{g}_{k+1}, \delta_{k+1}))/((\boldsymbol{g}_k, \delta_k), (\boldsymbol{g}_k, \delta_k))$;
    If $((\boldsymbol{g}_{k+1}, \delta_{k+1}), (\boldsymbol{g}_{k+1}, \delta_{k+1}))/((\boldsymbol{g}_0, \delta_0), (\boldsymbol{g}_0, \delta_0)) < \varepsilon$, break;
    $(\boldsymbol{w}_{k+1}, \omega_{k+1}) := (\boldsymbol{g}_{k+1}, \delta_{k+1}) + \beta_k\,(\boldsymbol{w}_k, \omega_k)$;
end;
```

where ε is a positive constant for the criterion of the convergence. In the above conjugate gradient algorythm, $(\boldsymbol{g}_0, \delta_0)$ could be computed by the extentions $(\widetilde{\boldsymbol{u}}_0^{(i)}, \widetilde{p}_0^{(i)})$ and $(\bar{\boldsymbol{v}}^{(i)}, \bar{q}^{(i)})$ as follow:

$$\begin{aligned}&\langle(\boldsymbol{g}_0, \delta_0),\ (\boldsymbol{\eta}, \zeta)\rangle_{\gamma_{12}}\\ &\quad = \sum_{i=1}^{2}\{a^{(i)}(\widetilde{\boldsymbol{u}}_0^{(i)},\ \bar{\boldsymbol{v}}^{(i)}) + b^{(i)}(\bar{\boldsymbol{v}}^{(i)},\ \widetilde{p}_0^{(i)}) - (\boldsymbol{f}^{(i)},\ \bar{\boldsymbol{v}}^{(i)})_{\Omega^{(i)}} + b^{(i)}(\widetilde{\boldsymbol{u}}_0^{(i)},\ \bar{q}^{(i)})\}, \qquad \forall(\boldsymbol{\eta},\ \zeta) \in \Lambda \times \Xi, \qquad (10)\end{aligned}$$

where $(\widetilde{\boldsymbol{u}}_0^{(i)}, \widetilde{p}_0^{(i)}) := \mathscr{E}^{(i)}(\boldsymbol{f}^{(i)}, \boldsymbol{\lambda}_0, \xi_0)$; and $\mathscr{A}(\boldsymbol{w}_k, \omega_k)$ could be computed by the extentions $(\widehat{\boldsymbol{u}}_0^{(i)}, \widehat{p}_0^{(i)})$ and $(\bar{\boldsymbol{v}}^{(i)}, \bar{q}^{(i)})$ as follow:

$$\langle\mathscr{A}(\boldsymbol{w}_k, \omega_k),\ (\boldsymbol{\eta}, \zeta)\rangle_{\gamma_{12}} = \sum_{i=1}^{2}\{a^{(i)}(\widehat{\boldsymbol{u}}_k^{(i)},\ \bar{\boldsymbol{v}}^{(i)}) + b^{(i)}(\bar{\boldsymbol{v}}^{(i)},\ \widehat{p}_k^{(i)}) + b^{(i)}(\widehat{\boldsymbol{u}}_k^{(i)},\ \bar{q}^{(i)})\}, \qquad \forall(\boldsymbol{\eta},\ \zeta) \in \Lambda \times \Xi, \qquad (11)$$

where $(\widehat{\boldsymbol{u}}_k^{(i)}, \widehat{p}_k^{(i)}) := \mathscr{E}^{(i)}(\boldsymbol{0}, \boldsymbol{w}_k, \omega_k)$. The extentions $(\widetilde{\boldsymbol{u}}_0^{(i)}, \widetilde{p}_0^{(i)})$, $(\widehat{\boldsymbol{u}}_0^{(i)}, \widehat{p}_0^{(i)})$, and $(\bar{\boldsymbol{v}}^{(i)}, \bar{q}^{(i)})$ in (10) and (11) could be computed in $\Omega^{(1)}$ and $\Omega^{(2)}$ independently. Therefore, the above conjugate gradient algorythm is familiar with parallel computations.

Moreover, as mentioned in Remark 1, if $\boldsymbol{f}^{(i)}$ satisfies that $\operatorname{div} \boldsymbol{f}^{(i)} = 0$ in $\Omega^{(i)}$, then $p^{(i)}$ vanishes. This implies that we can neglect the components corresponding to the Lagrange multiplier in the conjugate gradient algorythm. Therefore we can get the reduced conjugate gradient algorythm as follows:

```
Choose $\boldsymbol{\lambda}_0$;
Compute $\boldsymbol{g}_0$ by (12);
$\boldsymbol{w}_0 := \boldsymbol{g}_0$;
for $k = 0, 1, \ldots$;
    Compute $\mathscr{A}_1(\boldsymbol{w}_k, 0)$ by (13);
    $\alpha_k := (\boldsymbol{g}_k, \boldsymbol{g}_k)/(\mathscr{A}_1(\boldsymbol{w}_k, 0), \boldsymbol{w}_k,)$;
    $\boldsymbol{\lambda}_{k+1} := \boldsymbol{\lambda}_k - \alpha_k\,\boldsymbol{w}_k$;
    $\boldsymbol{g}_{k+1} := \boldsymbol{g}_k - \alpha_k\,\mathscr{A}_1(\boldsymbol{w}_k, 0)$;
    $\beta_k := (\boldsymbol{g}_{k+1}, \boldsymbol{g}_{k+1})/(\boldsymbol{g}_k, \boldsymbol{g}_k)$;
    If $(\boldsymbol{g}_{k+1}, \boldsymbol{g}_{k+1})/(\boldsymbol{g}_0, \boldsymbol{g}_0) < \varepsilon$, break;
    $\boldsymbol{w}_{k+1} := \boldsymbol{g}_{k+1} + \beta_k\,\boldsymbol{w}_k$;
end;
```

In the reduced conjugate gradient algorythm, $\boldsymbol{g}_0$ could be computed by the first component of the following equation:

$$\begin{aligned}&\langle(\boldsymbol{g}_0, \delta_0),\ (\boldsymbol{\eta}, \zeta)\rangle_{\gamma_{12}}\\ &\quad = \sum_{i=1}^{2}\{a^{(i)}(\widetilde{\boldsymbol{u}}_0^{(i)},\ \bar{\boldsymbol{v}}^{(i)}) + b^{(i)}(\bar{\boldsymbol{v}}^{(i)},\ \widetilde{p}_0^{(i)}) - (\boldsymbol{f}^{(i)},\ \bar{\boldsymbol{v}}^{(i)})_{\Omega^{(i)}} + b^{(i)}(\widetilde{\boldsymbol{u}}_0^{(i)},\ \bar{q}^{(i)})\}, \qquad \forall(\boldsymbol{\eta},\ \zeta) \in \Lambda \times \Xi, \qquad (12)\end{aligned}$$

where $(\widetilde{\boldsymbol{u}}_0^{(i)}, \widetilde{p}_0^{(i)}) := \mathscr{E}^{(i)}(\boldsymbol{f}^{(i)}, \boldsymbol{\lambda}_0, 0)$; and $\mathscr{A}_1(\boldsymbol{w}_k, 0)$ could be computed by the first component of the following equation:

$$\langle\mathscr{A}(\boldsymbol{w}_k, 0),\ (\boldsymbol{\eta}, \zeta)\rangle_{\gamma_{12}} = \sum_{i=1}^{2}\{a^{(i)}(\widehat{\boldsymbol{u}}_k^{(i)},\ \bar{\boldsymbol{v}}^{(i)}) + b^{(i)}(\bar{\boldsymbol{v}}^{(i)},\ \widehat{p}_k^{(i)}) + b^{(i)}(\widehat{\boldsymbol{u}}_k^{(i)},\ \bar{q}^{(i)})\}, \qquad \forall(\boldsymbol{\eta},\ \zeta) \in \Lambda \times \Xi, \qquad (13)$$

where $(\widehat{\boldsymbol{u}}_k^{(i)}, \widehat{p}_k^{(i)}) := \mathscr{E}^{(i)}(\mathbf{0}, \boldsymbol{w}_k, 0)$.

References

[1] Alonso, A. and Valli, A., Some remarks on the characterization of the space of tangential traces of $H(\mathrm{rot}; \Omega)$ and the construction of an extension operator, *Manuscripta Math.*, 89 (1996), pp.159–178.

[2] Buffa, A. and Ciarlet, P.-G., On traces for functional spaces related to Maxwell's equations. I, An integration by parts formula in Lipschitz polyhedra, *Math. Methods Appl. Sci.*, 24 (2001), pp.9–30.

[3] Buffa, A. and Ciarlet, P.-G., On traces for functional spaces related to Maxwell's equations. II, Hodge decompositions on the boundary of Lipschitz polyhedra and applications, *Math. Methods Appl. Sci.*, 24 (2001), pp.31–48.

[4] Buffa, A., Costabel, M., and Sheen, D., On traces for $\mathbf{H}(\mathbf{curl}, \Omega)$ in Lipschitz domains, *J. Math. Anal. Appl.*, 276 (2002), pp.845–867.

[5] Glowinski, R., Dinh, Q.V., and Periaux, J., Domain decomposition methods for nonlinear problems in fluid dynamics, *Compt. Meths. Appl. Mech. Engrg.*, 40 (1983), pp.27–109.

[6] Kikuchi, F., Mixed formulations for finite element analysis of magnetostatic and electrostatic problems, *Japan J. Appl. Math.*, 6 (1989), pp.209–221.

[7] Kikuchi, F., On a discrete compactness property for the Nedelec finite elements, *J. Fac. Sci. Univ. Tokyo, Sect. IA Math.*, 36 (1989), pp.479–490.

[8] Kanayama, H., Shioya, R., Tagami, D., and Matsumoto, S., 3-D Eddy Current Computation for a Transformer Tank, *COMPEL*, 21 (2002), pp.554–562.

[9] Quarteroni, A. and Valli, A., Domain Decomposition Methods for Partial Differential Equations, Oxford, 1999.

Variational approach to multi-scale dynamical system
$\sim$ an application to collisionless magnetic reconnection $\sim$

Makoto Hirota, Philip J. Morrison[a)]

Japan Atomic Energy Agency, Naka, Ibaraki, 311-0193, Japan and

[a)] *University of Texas at Austin, Austin, Texas 78712, USA*

I. INTRODUCTION

In mathematical models that describe multi-scale physics, microscopic effect often acts as singular perturbation; a higher derivative term is brought into macroscopic governing equations. Instead of directly solving such multi-scale problem (which is usually difficult even with the help of numerical computation), it is mathematically tractable and physically informative to solve it approximately with some techniques such as the renormalized perturbation method and the asymptotic matching method. In this work, we present another approach that utilizes the variational principle. This powerful approach is basically applicable to problems which can be regarded as a multi-scale *Hamiltonian* system.

Two typical examples of multi-scale problems are shown in FIG. 1. The parameters $\nu, \alpha \in \mathbb{R}$ are usually small in physical context and, hence, the higher-order derivative works only inside thin boundary layer. While these two examples are known to be integrable, it is generally difficult to solve nonlinear behavior of more complicated multi-scale problems. Note that, in the case of the KdV equation, the singular perturbation does not leads to energy dissipation but modifies conservation law of the dynamical system. For such *conservative* singular perturbations, we can take advantage of Hamiltonian structure of the systems to find constants of motion [1, 2]. Even when the system is not integrable, variational principle allows us to predict behavior of solution in a heuristic manner. If we makes a good choice of test function, we can obtain an approximate solution without solving higher-order differential equations directly or perturbatively. Accuracy of the result depends on how good the test function mimics the true solution.

In order to demonstrate the variational approach, we argue a problem of magnetic reconnection in collisionless (i.e., dissipationless) plasma. Although this approach is not all-purpose, we expect a lot of applications to other multi-scale Hamiltonian systems.

Dissipative	Conservative
Burgers equation: $\dfrac{\partial u}{\partial t} + u\dfrac{\partial u}{\partial x} = \nu\dfrac{\partial^2 u}{\partial x^2}$	KdV equation: $\dfrac{\partial u}{\partial t} + u\dfrac{\partial u}{\partial x} + \alpha\dfrac{\partial^3 u}{\partial x^3} = 0$
Time-irreversible	Time-reversible
Shock	Soliton

($\Uparrow$ multi-scale Hamiltonian system)

FIG. 1: Two kinds of singular perturbation

II. MODEL OF COLLISIONLESS MAGNETIC RECONNECTION

In perfect fluid, the topology of vortex field line will not change according to the well-known Kelvin's circulation theorem. This vorticity conservation law is violated in the presence of small viscosity (which is a singular perturbation leading to the Navier-Stokes equation), where reconnection of vortex field lines occurs on a small scale. Analogous phenomenon is also present in magnetohydrodynamics (MHD), in which the topology of magnetic field is preserved in ideal limit. Again, one can show that magnetic field lines reconnect by adding resistivity into the ideal MHD equations. Magnetic reconnection is naturally observed in various plasmas (ionized gases) residing in magnetosphere, solar flare and magnetic confinement experiments. In these circumstances, however, ions and electrons are almost collisionless, which implies that the resistivity is very small (magnetic Raynolds number is $R_m \sim 10^{9-13}$). It is pointed out that the analysis and simulation of the resistive MHD equations cannot fully explain the reconnection speed of observations. Therefore, we need to take account of other microscopic effects (i.e., singular perturbations) that seem to cause fast magnetic reconnections in collisionless plasmas.

Instead of resistivity, the effect of "electron inertia" (which is also neglected in the ideal MHD model) is a major candidate of singular perturbation that triggers collisionless reconnection. As simplest analytical model, we consider the following equations for 2D velocity field $\boldsymbol{v} = \nabla\phi(x,y,t) \times \boldsymbol{e}_z$ and magnetic field $\boldsymbol{B} = \nabla\psi(x,y,t) \times \boldsymbol{e}_z$,

$$\frac{\partial \nabla^2\phi}{\partial t} - [\phi, \nabla^2\phi] - [\nabla^2\psi, \psi] = 0, \tag{1}$$

$$\frac{\partial(\psi - d_e^2\nabla^2\psi)}{\partial t} - [\phi, \psi - d_e^2\nabla^2\psi] = 0, \tag{2}$$

where $[f,g] = (\nabla f \times \nabla g)\cdot\boldsymbol{e}_z$. In comparison to the 2D Euler equation, the vorticity equation (1) includes the electromagnetic force, $[\nabla^2\psi, \psi]$, where $J = -\nabla^2\psi$ corresponds to (electric) current. The small scale parameter $d_e \ll 1$ (called the electron skin depth) plays a role of singular perturbation. When $d_e = 0$, the (collisionless) Ohm's law (2) conserves the magnetic flux ψ and hence the field line of $\boldsymbol{B}$ never changes its topology. On the other hand, for $d_e \neq 0$, the modified flux $\psi_e = \psi - d_e^2\nabla^2\psi$ is still conserved, but the magnetic reconnection is allowed to occur within a thin layer of the width $\sim d_e$ [3]. Since the electron inertia does not cause energy dissipation, (1) and (2) are known to be a Hamiltonian system [4]; $\partial_t F = \{F, H\}$ for $\forall F(\phi,\psi)$, where

$$\text{Hamiltonian: } H = \frac{1}{2}\int d^2x \left[|\nabla\phi|^2 + |\nabla\psi|^2 + d_e^2(\nabla^2\psi)^2\right] \tag{3}$$

$$\text{Casimir invariants: } C_1 = \int d^2x \mathcal{F}_1(\psi_e)\nabla^2\phi, \quad C_2 = \int d^2x \mathcal{F}_2(\psi_e) \tag{4}$$

for $\forall\mathcal{F}_{1,2} : \mathbb{R} \to \mathbb{R}$.

In this work, we consider a 1D static equilibrium state which is periodic in both x and y directions,

$$\phi \equiv 0, \quad \psi(x) = \cos x \quad \text{on} \quad x \in [-\pi, \pi]. \tag{5}$$

The corresponding magnetic field $\boldsymbol{B}$ is antiparallel as shown in FIG. 2. This magnetic shear will serve as the free energy source for instability.

Asymptotic matching analysis of the linearized system [5, 6] shows that the reconnection is indeed triggered by a linearly unstable mode, leading to the energy conversion from magnetic energy $\frac{1}{2}\int |\nabla\psi|^2 d^2x$ to kinetic energy $\frac{1}{2}\int |\nabla\phi|^2 d^2x$ and also current energy $\frac{1}{2}\int d_e^2 J^2 d^2x$. However, it seems that such the perturbation analysis fails to converge even before the mode amplitude reaches the scale of d_e. Nonlinear regime of the reconnection process is investigated to some extend [7] but remains mostly unclear.

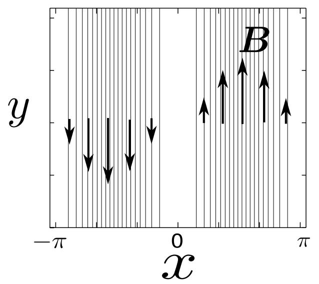

FIG. 2: Equilibrium magnetic field (=initial state)

III. VARIATIONAL PRINCIPLE ∼ LAGRANGIAN FORMULATION ∼

To study the above mentioned reconnection process, we first formulate the variational principle for (1) and (2), where displacement field of fluid elements is the dynamical variable to be varied. By translating the (noncanonical) Hamiltonian system, (1) and (2), in the language of (canonical) Lagrangian mechanics, we can distinguish free energy source of the instability in explicit form.

From now on, let us simply denote the equilibrium state by (ϕ, ψ_e) and the perturbed state by $(\tilde{\phi}, \tilde{\psi}_e)$, where $\phi = 0$ and $\psi_e = (1 + d_e^2)\cos x$. The conservation law (2) restricts the perturbation $\psi_e \to \tilde{\psi}_e$ such that the dynamics is constrained on the constant Casimir surface, $C_2 = \text{const}$. In the same manner as Newcomb's Lagrangian theory [8], we can formally solve (2) by introducing displacement field. Since the fluid is 2D and incompressible, the perturbed state $(\tilde{\phi}, \tilde{\psi}_e)$ is generated by a gauge function $G(x, y, t)$ such that

$$\tilde{\phi}(x + \partial_y G(x,y,t), y, t) = \partial_t G(x,y,t), \tag{6}$$

$$\tilde{\psi}_e(x + \partial_y G(x,y,t), y, t) = \psi_e(x). \tag{7}$$

One can directly confirm that this perturbation is a solution of (2) for any G. Here, $\Xi(x, y, t) = \partial_y G(x, y, t)$ corresponds to the displacement of fluid in x direction. For these constrained perturbations, we define the Lagrangian as

$$L[G] = L(\tilde{\phi}, \tilde{\psi}_e) = \frac{1}{2}\int d^2x \quad |\nabla\tilde{\phi}|^2 - |\nabla\tilde{\psi}|^2 - d_e^2|\nabla^2\tilde{\psi}|^2 \quad . \tag{8}$$

By invoking the variational principle,

$$\delta \int L[G]dt = 0 \quad \text{w.r.t.} \quad \forall\delta G, \tag{9}$$

we find that the Euler-Lagrange equation corresponds to the vorticity equation (1). Therefore, we can analyze nonlinear behavior of perturbation $(\tilde{\phi}, \tilde{\psi})$ using the canonical coordinate G. By comparison with the Hamiltonian (3), one can find that $W = \frac{1}{2}\int \quad |\nabla\tilde{\psi}|^2 + d_e^2|\nabla^2\tilde{\psi}|^2 \quad d^2x$ plays a role of potential energy of this dynamics. If the potential energy decreases ($\delta W < 0$) for some function G (i.e., some displacement of fluid), then such a perturbation will grow with the release of free energy [9].

We will show that a rather simple fluid motion is enough to prove the occurrence of spontaneous magnetic reconnection which, moreover, accelerates in the nonlinear phase.

IV. LINEAR STABILITY ANALYSIS

Let us perform small-amplitude expansion of the Lagrangian (8) around the equilibrium state. In this work, we measure the amplitude of perturbation by $\epsilon = \max|\Xi| = \max|\partial_y G|$.

From (6) and (7), we get

$$\tilde{\phi} = G_t - \Xi G_t' + \frac{1}{2}(\Xi^2 G_t')' - \frac{1}{6}(\Xi^3 G_t')'' + \frac{1}{24}(\Xi^4 G_t')''' + O(\epsilon^6), \tag{10}$$

$$\tilde{\psi}_e = \psi_e - \Xi\psi_e' + \frac{1}{2}(\Xi^2\psi_e')' - \frac{1}{6}(\Xi^3\psi_e')'' + \frac{1}{24}(\Xi^4\psi_e')''' + O(\epsilon^5). \tag{11}$$

where $G_t = \partial_t G$ and the prime ($'$) denotes the x derivative. Substitution of these expressions into the Lagrangian gives

$$L(\tilde{\phi}, \tilde{\psi}_e) = L(\psi_e) + L^{(1)}\,(\psi_e; G) + \frac{1}{2}L^{(2)}(\psi_e; G, G) + \frac{1}{6}L^{(3)}(\psi_e; G, G, G) + \ldots \tag{12}$$

Since the equilibrium state is already an extremum of the Lagrangian, one can show that the first-order term vanishes, $L^{(1)}\,(\psi_e; G) = 0$, for any G.

Then, the second-order Lagrangian $L^{(2)}$ governs the linearized dynamics. By assuming $\Xi(x, y, t) = \epsilon\mathrm{Re}[\hat{\xi}(x)e^{ik(y-ct)}]$ with a wavenumber $k \in \mathbb{R}$ and an eigenvalue $c \in \mathbb{C}$, we can write the eigenvalue problem in the form of

$$\{[c^2 - (\psi_e')^2]\hat{\xi}'\}' - k^2[c^2 - (\psi_e')^2]\hat{\xi} = d_e^2\psi_e' J'''\hat{\xi} + \psi_e' d_e^2\nabla^2(1 - d_e^2\nabla^2)^{-1}\nabla^2(\psi_e'\hat{\xi}), \tag{13}$$

where ∇^2 should be interpreted as $\nabla^2 = \partial_x^2 - k^2$. Note that this is essentially a fourth order ordinary differential equation (unless $d_e = 0$) because there is an integral operator $(1 - d_e^2\nabla^2)^{-1}$ on the right hand side. This integrodifferential form (13) is nonetheless very informative, for it comes from the extremum condition of the symmetric quadratic Lagrangian $L^{(2)}$. Multiplying $\hat{\xi}^*$ on the both sides of (13) and integrating over the x domain $[-\pi, \pi]$, we get $c^2 I^{(2)} = W^{(2)}$ where

$$I^{(2)} = \int dx \quad |\hat{\xi}'|^2 + k^2|\hat{\xi}|^2 \quad > 0, \tag{14}$$

$$W^{(2)} = \int dx \Big[\underset{\text{(i)}}{\underline{|\nabla(\psi_e'\hat{\xi})|^2}} + \underset{\text{(ii)}}{\underline{\psi_e'\psi'''|\hat{\xi}|^2}} - \underset{\text{(iii)}}{\underline{\nabla^2(\psi_e'\hat{\xi}^*) d_e^2(1 - d_e^2\nabla^2)^{-1}\nabla^2(\psi_e'\hat{\xi})}} \Big]. \tag{15}$$

The functionals, $c^2 I^{(2)}$ and $W^{(2)}$, respectively represent the kinetic and potential energies for linear perturbation, which are obviously symmetric. Now, we can apply the Rayleigh-Ritz method to this problem. Namely, if $W^{(2)}/I^{(2)}$ takes a minimum value for some $\hat{\xi}$, then such a $\hat{\xi}$ is the eigenfunction of the eigenvalue $c^2 = \min[W^{(2)}/I^{(2)}]$, which actually provides the lower bound of c^2, that is, the most unstable mode ($\mathrm{Im}\, c > 0$) when $W^{(2)} < 0$. Even though analytical form for the true solution of (13) is intractable, we can estimate $\min[W^{(2)}/I^{(2)}]$ by substituting a test function $\hat{\xi}$ that is composed of elementary functions.

As indicated in (15), there are three terms in the potential energy, which have definite signs, (i)> 0, (ii)< 0 and (iii)< 0. In the ideal MHD limit ($d_e = 0$), we can easily prove (i)+(ii) > 0, which implies that there is no instability triggering reconnection. We remark that, if there was no magnetic shear $\psi'' \equiv 0$ in the equilibrium state, we could again prove linear stability (i)+(iii) > 0. The effect of electron inertia (iii) merely weakens the magnetic field tension (i) on small scale $\sim d_e$. Thus, magnetic reconnection ($W^{(2)} < 0$) will be triggered in the presence of both magnetic shear (ii) and electron inertia (iii).

Let us temporarily suppose that $d_e = 0$ and introduce $\hat{\psi} = -\psi'\hat{\xi}$. When $k^2 < 1$, we can show that $\hat{\psi} = \cos\kappa(|x| - \pi/2)$ formally makes $W^{(2)}$ negative, where $\kappa = \sqrt{1 - k^2}$. However, this perturbation cannot be unstable because the corresponding $\hat{\xi} = -\hat{\psi}/\psi'$ becomes discontinuous at $x = 0, \pm\pi$ and $I^{(2)} = \infty$. The role of the singular perturbation

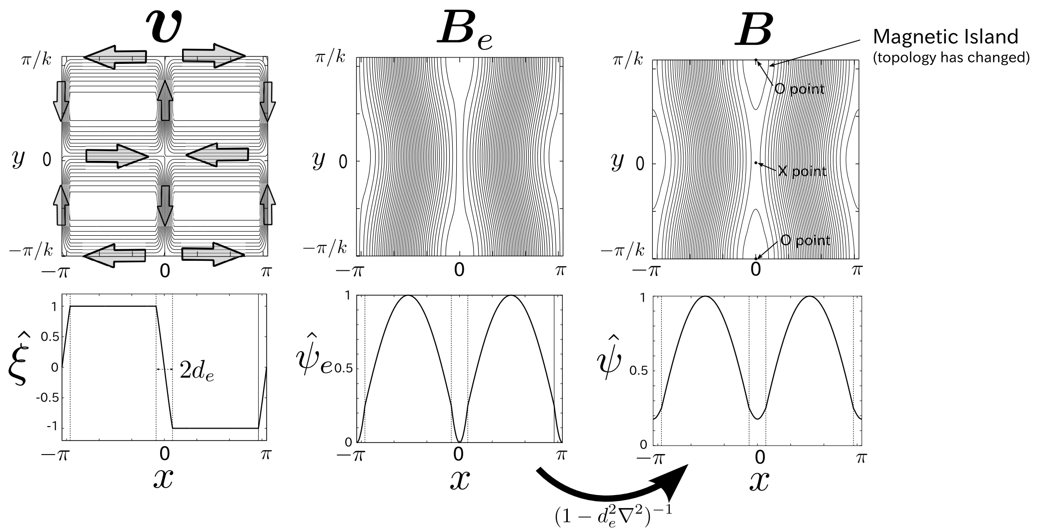

FIG. 3: Trial eigenfunctions $\hat{\xi}, \hat{\psi}_e, \hat{\psi}$ chosen by this work. Corresponding field lines are respectively shown above, where $\boldsymbol{B}_e = \nabla\psi_e \times \boldsymbol{e}_z$. (Note: amplitudes of linear perturbations are exaggerated to display the island structure. For such island size, the nonlinear effect is important in reality.)

$d_e \ll 1$ is to *smooth out* these discontinuities by establishing thin boundary layers around them. For simplicity, we assume the ordering, $\pi k^2/4 \ll d_e^2 \ll 1$, and choose the following structure of eigenfunction.

$$\hat{\xi}(x) = \begin{cases} 1 & -\pi + d_e < x < -d_e \\ -x/d_e & -d_e < x < d_e \\ -1 & d_e < x < \pi - d_e \end{cases} \tag{16}$$

where the boundary layers at $x = \pm\pi$ are basically equivalent to the one at $x = 0$ (see FIG. 3). We can directly show that this piecewise linear function indeed makes $W^{(2)}$ negative and keeps $I^{(2)}$ finite as follows.

Since k^2 is assumed to be small, the most part of the kinetic energy (14) stems from the boundary layers,

$$I^{(2)} \simeq \frac{4}{d_e}. \tag{17}$$

In order to estimate $W^{(2)}$, we needs to calculate $\hat{\psi} = (1-d_e^2\nabla^2)^{-1}\hat{\psi}_e$ for given $\hat{\psi}_e = -\psi_e'\hat{\xi}$. By noting that $(1-d_e^2\nabla^2)^{-1} \simeq \int e^{-|x-s|/d_e} \circ ds$, we can derive $\hat{\psi}$ which is not so spiky as $\hat{\psi}_e$ in the boundary layers (as shown in FIG. 3). After some lengthy but straightforward calculation, we obtain, to leading order,

$$W^{(2)} \simeq -\frac{4}{6}(1 + 27e^{-2})d_e = -4 \times 0.776 d_e. \tag{18}$$

The linear growth rate $\gamma = \mathrm{Im}(kc)$ is therefore evaluated as

$$\gamma = \sqrt{0.776}kd_e = 0.881kd_e. \tag{19}$$

In FIG. 3, we also exhibit field lines of $\boldsymbol{v}$, $\boldsymbol{B}_e$ and $\boldsymbol{B}$ perturbed by this unstable mode. Via reconnection of magnetic field lines, the potential energy (or mostly the magnetic energy) decreases, $W^{(2)} < 0$, and in turn the kinetic energy increases $c^2 I^{(2)} > 0$ by generating convection cells. The so-called magnetic island is observed in $\boldsymbol{B}$ as evidence of topological

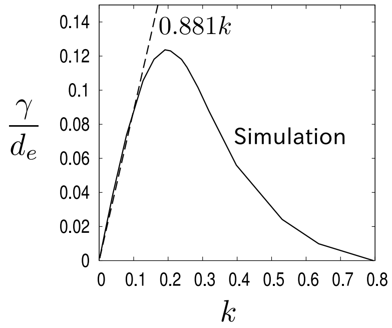

FIG. 4: Linear growth rate of the tearing mode

change. Unstable mode which triggers magnetic reconnection is generally called the tearing mode.

In FIG. 4, the analytical estimate of the growth rate is compared with a numerical simulation with parameters $k = 0.5/2\pi$ and $d_e/2\pi = 0.01$. For smaller k, we observe a good agreement since the piecewise linear function agrees well with the true eigenfunction. We remark that we can also reproduce the maximum growth rate at $k \simeq 0.2$ by improving the test function in an appropriate manner.

V. NONLINEAR STABILITY ANALYSIS

At the beginning of studying nonlinear stage of the above linear instability, one may try to continue the perturbation analysis of the Lagrangian (12) (i.e., weakly nonlinear analysis). However, we have already seen that the linearly unstable mode $\Xi = \epsilon\hat{\xi}\cos[k(y-ct)]$ has a steep gradient $\Xi' \sim \Xi/d_e$ in the boundary layers. This fact means that the perturbation expansion, (10) and (11), will not converge when ϵ reaches d_e. Actually, we will find that ϵ exceeds d_e without saturation and a fully nonlinear analysis is required around the boundary layers.

To avoid this difficulty of perturbation analysis, let us again exploit the variational method. Namely, if a trial fluid motion (parameterized by the amplitude ϵ) continues to decrease the potential energy W, such a motion is expected to be nonlinearly unstable. As a natural extension of linearly unstable motion, we choose a nonlinear displacement $\Xi(x, y, \epsilon) = \partial_y G(x, y, \epsilon)$ that is generated by the infinitesimal displacement field $\hat{\xi}(x)\cos ky = \partial_y \hat{g}(x, y)$ prescribed by (16). Mathematically, we should integrate the following evolution equation for G,

$$\partial_\epsilon G(x, y, \epsilon) = \hat{g}(x + \partial_y G(x, y, \epsilon), y), \quad G(x, y, 0) \equiv 0. \tag{20}$$

The resulting function G generates nonlinear perturbations $\tilde{\phi}$ and $\tilde{\psi}$ according to (6) and (7), where only the amplitude ϵ is regarded as a function of t. For this fluid motion, a simple relation holds,

$$\tilde{\phi}(x, y, t) = \hat{g}(x, y)\frac{d\epsilon}{dt}. \tag{21}$$

Therefore, the estimate of the kinetic energy K is almost the same as the one for linear perturbation,

$$K = \frac{1}{2}\int\int |\nabla\tilde{\phi}|^2 dxdy \simeq \frac{2\pi}{k}\frac{1}{k^2 d_e}\left(\frac{d\epsilon}{dt}\right)^2 \tag{22}$$

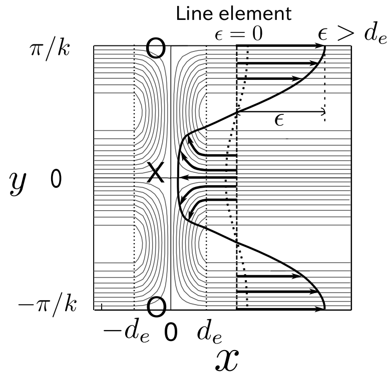

FIG. 5: Nonlinear displacement

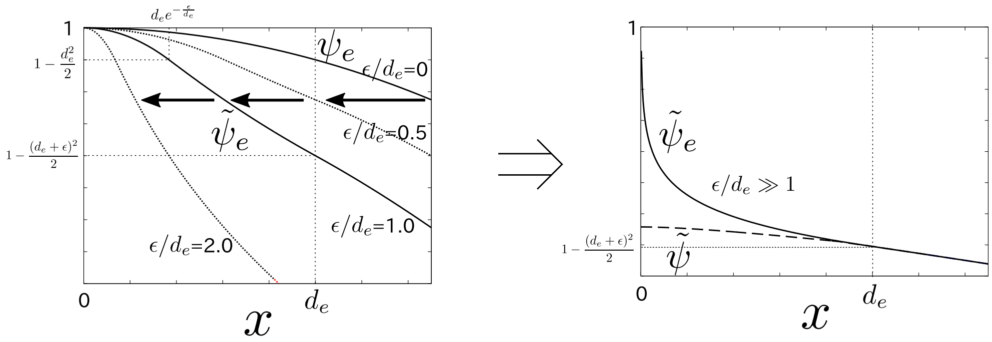

FIG. 6: Development of $\tilde{\psi}_e$ at the X point, $(x, y) = (0, 0)$.

Since the x component of the velocity is given by $\tilde{v}_x = \hat{\xi}(x)\cos ky \times d\epsilon/dt$, the amplitude $\epsilon(t)$ is equal to the maximum displacement along the x direction and, hence, measures the half width of the magnetic island. We have seen in the previous section that the exponential growth $\epsilon(t) \propto e^{\gamma t}$ occurs in the linear regime $0 \leq \epsilon \ll d_e$. Now, we are interested in what happens in the nonlinear regime $\epsilon > d_e$.

When $\epsilon > d_e$, a line element of fluid is distorted by convection as illustrated in FIG. 5. The displacement is no longer sinusoidal along the y direction and the asymmetry between the X point ($y = 0$) and the O point ($y = \pm\pi/k$) is more emphasized.

At the X point, the equilibrium flux $\psi_e \simeq \cos x$ will be compressed by flow along the x direction, which is analytically expressed by

$$\tilde{\psi}_e|_{y=0} = 1 + \begin{cases} -\frac{1}{2}e^{2\epsilon/d_e}x^2 & 0 < x < d_e e^{-\epsilon/d_e} \\ -\frac{1}{2}\quad d_e \log\frac{x}{d_e} + d_e + \epsilon \quad ^2 & d_e e^{-\epsilon/d_e} < x < d_e \\ -\frac{(x+\epsilon)^2}{2} & d_e < x \end{cases} \tag{23}$$

As the fluid motion evolves ($\epsilon \nearrow$), $\tilde{\psi}_e$ will concentrate on the X point (see FIG. 6). For large $\epsilon/d_e \gg 1$, the spike of $\tilde{\psi}_e$ looks like a logarithmic function $\sim -\epsilon \log|x/d_e|$. By solving $\tilde{\psi} = (1 - d_e^2\partial_x^2)^{-1}\tilde{\psi}_e$ for $\tilde{\psi}$, we obtain the current profile $\tilde{J} = (\tilde{\psi}_e - \tilde{\psi})/d_e^2$ as

$$\tilde{J}|_{y=0} \simeq 1 - \epsilon\frac{e^{x/d_e}\mathrm{Ei}(-x/d_e) + e^{-x/d_e}\mathrm{Ei}(x/d_e)}{2d_e}, \tag{24}$$

where $\mathrm{Ei}(x) = \int_{-\infty}^{x}(e^s/s)ds$ is the exponential integral. Although a strong current spike develops $\tilde{J} \to (\epsilon/d_e)\log|x/d_e|$ at the X point, note that it remains square-integrable.

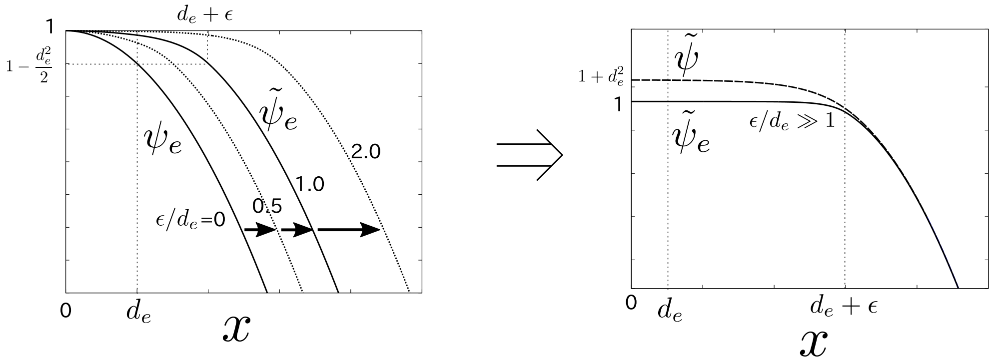

FIG. 7: Development of $\tilde{\psi}_e$ at the O point, $(x,y)=(0,\pi/k)$.

Therefore, we estimate the potential energy change around X point ($x=0, y=0$) as follows,

$$\int_0^{d_e} d_e^2(|\tilde{J}|^2-|J|^2)dx = 1.35\epsilon^2 d_e + O(\epsilon d_e^2) \tag{25}$$

$$\int_0^{d_e} |\tilde{\psi}'|^2 dx - \int_0^{d_e+\epsilon} |\psi'|^2 dx = -\frac{\epsilon^3}{3} - 0.78\epsilon^2 d_e + O(\epsilon d_e^2) \tag{26}$$

in nonlinear regime $\epsilon/d_e \gg 1$, where decrease of magnetic energy (due to the reconnection) is more dominant than increase of current energy.

On the other hand, at the O point ($x=0, y=\pm\pi/k$), the flux $\tilde{\psi}_e$ will be expanded by convection,

$$\tilde{\psi}_e|_{y=\pi/k} = 1 + \begin{cases} -\frac{1}{2}e^{-2\epsilon/d_e}x^2 & 0<x<d_e \\ -\frac{d_e^2}{2}e^{2\frac{x-d_e-\epsilon}{d_e}} & d_e<x<d_e+\epsilon \\ -\frac{(x-\epsilon)^2}{2} & d_e+\epsilon<x \end{cases} \tag{27}$$

As shown in FIG. 7, the subsequent $\tilde{\psi}_e$ becomes flat-topped and the generated current is very small,

$$\tilde{J}|_{y=\pi/k} \simeq \begin{cases} -1-\frac{2}{3}e^{2\frac{x-d_e-\epsilon}{d_e}}+\frac{3}{2}e^{\frac{x-d_e-\epsilon}{d_e}} & 0<x<d_e+\epsilon \\ -\frac{1}{6}e^{-\frac{x-d_e-\epsilon}{d_e}} & d_e+\epsilon<x \end{cases}. \tag{28}$$

Therefore, in the nonlinear regime $\epsilon/d_e \gg 1$, no significant change in the potential energy occurs around the O point;

$$\int_0^{\infty} d_e^2(|\tilde{J}|^2-|J|^2)dx = -\epsilon d_e^2 + O(d_e^3) \tag{29}$$

$$\int_0^{d_e+\epsilon} |\tilde{\psi}'|^2 dx - \int_0^{d_e} |\psi'|^2 dx = O(d_e^3) \tag{30}$$

which are negligible in comparison to the changes at the X point.

Although we have only investigated the two extremal situations, i.e., the X and O points, we can expect that the potential energy continues to decrease even in the nonlinear regime $\epsilon/d_e \gg 1$. The prominence of the current spike at the X point cannot elevate the total potential energy. By contrast, the potential energy can decrease faster than the linear regime in powers of ϵ^3.

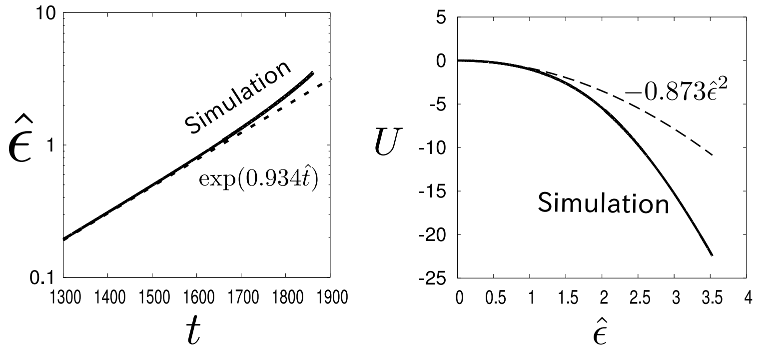

FIG. 8: Time evolution of modal amplitude (left) and potential energy (right).

In terms of normalized variables, $\hat{\epsilon} = \epsilon/d_e$ ($\hat{t} = kd_e t$), we reduce the Lagrangian to

$$L = K - W \simeq \left(\frac{d\hat{\epsilon}}{d\hat{t}}\right)^2 - U(\hat{\epsilon}), \tag{31}$$

which immediately gives the equation of motion,

$$\frac{d^2\hat{\epsilon}}{d\hat{t}^2} = -U'(\hat{\epsilon}). \tag{32}$$

We have performed nonlinear simulation of this instability (with parameters $k = 0.5/2\pi$ and $d_e/2\pi = 0.01$, again). The liner growth rate (which is numerically $\gamma = 0.934kd_e$) is indeed accelerated when $\epsilon > d_e$ in FIG. 8(left). The numerically evaluated potential $U(\hat{\epsilon})$ is plotted in FIG. 8(right), whose decrease becomes steeper than the linear regime $U(\hat{\epsilon}) = -0.873\hat{\epsilon}^2$. However, it is very difficult to survey further nonlinear evolution because numerical simulation has limitations to deal with the current spike which becomes increasingly singular. By adding a diffusion term of current (which makes the current energy dissipate), we observe that the growth of $\hat{\epsilon}$ is enhanced and the reconnection continues.

The fluid motion we considered here may not be the most unstable one, but it certainly decreases the potential energy, which implies capability to release free energy of the equilibrium state. As one can easily imagine, this nonlinear growth should be decelerated eventually before ϵ reaches the equilibrium scale size $\epsilon \to 1$ (at which the magnetic energy will start to be exhausted).

---

[1] V. I. Arnold, *Mathematical Methods of Classical Mechanics.* Springer, Berlin (1978) (see Appendix. 13).
[2] P. J. Olver, *Application of Lie Group to Differential Equations.* 2nd ed., Springer, New York (2000) (see Chap. 7).
[3] J. A. Wesson, Nucl. Fusion **30** 2545 (1990).
[4] T. J. Schep, F. Pegoraro and B. N. Kuvshinov **1**, 2843 (1994).
[5] R. D. Hazeltine and H. R. Strauss, Phys. Fluids **21**, 1007 (1978).
[6] F. Porcelli, Phys. Rev. Lett. **66**, 425 (1991).
[7] M. Ottaviani and F. Porcelli, Phys. Rev. Lett. **71**, 3802 (1993).
[8] W. A. Newcomb, Nucl. Fusion Suppl. Pt. 2, 451 (1962).
[9] I. B. Bernstein *et al.*, Proc. Roy. Soc. London **A244**, 17 (1958).

Multiscale characteristics of moist convections and heavy precipitation in the tropics

Shigeo Yoden, Shigenori Otsuka, and Nurjanna J. Trilaksono
Department of Geophysics, Kyoto University, Kyoto, Japan

Introduction

Moist convections are the main driver of the tropical circulation and a key element of the multiple scale interactions in the tropics. Such dynamical situation in the tropics is quite different from that in mid-latitudes, i.e., dry dynamics governed by the conservation law of potential vorticity [1]. In the tropics, our dynamical understanding is still limited and ability of numerical weather predictions is far from satisfactory, mainly due to the wide range of spatial and time scales of the multiple scale interactions. Numerical representation of moist convections and their organization with a finite mesh size is still one of the major defects of current global climate models too.

About a quarter of a century ago, in 1986, Hayashi and Sumi [2] made a numerical experiment with a general circulation model (GCM) of the atmosphere with an idealized lower boundary condition of an ocean covered globe ("aqua planet"). They found a long period (30-40 days) oscillation as a collective motion of cumulus ensemble activity along the equator as shown in Fig.1. The oscillation was characterized by a superposition of two different scales: the scale of precipitation patterns and the scale of the modulation of precipitation. They pointed out the resemblance of the latter structure to that of the observed intraseasonal variation of the equatorial circulation known as Madden-Julian Oscillation (MJO) found by Madden and Julian [3, 4]. Motivated by this theoretical work, Nakazawa [5] verified the existence of such multiscale characteristics in the real tropical atmosphere by analyzing the 3-hourly geostationary meteorological satellite (GMS) infrared data.

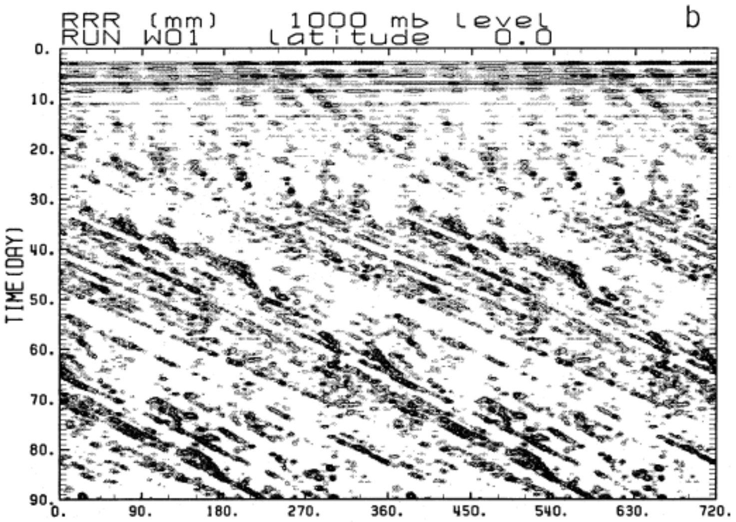

Fig. 1. Longitude-time section of precipitation per 12 hours obtained by an "aqua planet" numerical experiment [2]. The regions of precipitation greater than 1 mm/12 h are shaded.

Since then, lots of numerical and observational studies on the multiscale characteristics of moist convections in the tropics have been performed under the evolution of research environment with rapid advancement of computational powers and innovation of observational instruments. For example, Miura et al. [6] recently succeeded in simulating an MJO event by using a global cloud-resolving model with a horizontal resolution of 3.5 km. Benefits of the advancement of computational powers also enable us to use a regional atmospheric model for numerical weather predictions to investigate multiscale characteristics of moist convections and heavy precipitation in the tropics. In this lecture, some key works on multiple-scale interactions in the tropical atmosphere were reviewed and the recent results of our numerical studies were presented, which might be interesting to applied mathematicians too.

Time-lagged ensemble simulation of heavy precipitation over West Java

We have made numerical experiments on the moist convections and their organization in association with heavy precipitation during the Jakarta flood event in January-February 2007 (Trilaksono et al. [7, 8]) with a regional numerical weather prediction model, Japan Meteorological Agency – Nonhydrostatic model (JMA-NHM). In these studies, we adopted an ensemble simulation technique to obtain probabilistic information, because mesoscale convective systems in the atmosphere include some stochastic processes in space and time. The time-lagged ensemble technique that we adopted also has an advantage to reduce a systematic error associated with a diurnal cycle of spinup processes depending on the initial local time of each run; spinup of model precipitation is influenced by the strong diurnal cycle of precipitation in the tropics.

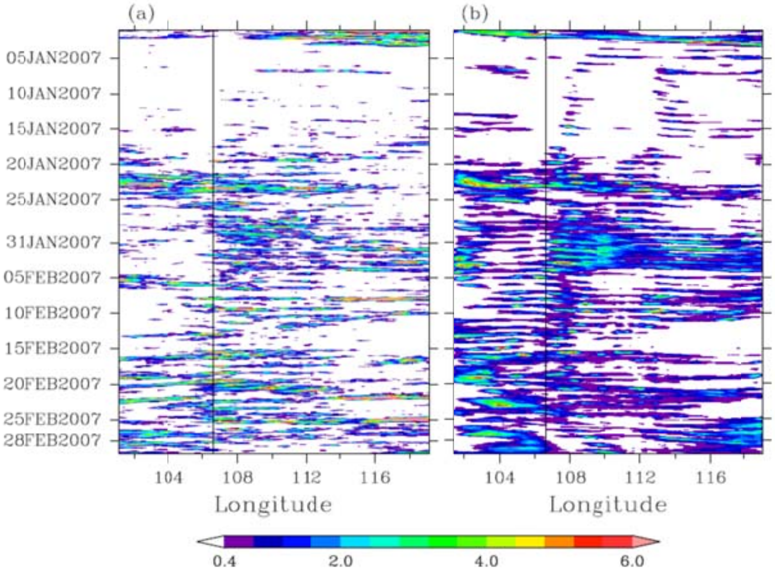

Fig. 2. Time-longitude cross sections of (a) the TRMM data and (b) the ensemble mean of the model simulated precipitation rate averaged between 5.5S − 8S [7]. The vertical lines in (a) and (b) denote the longitude of106.6E which is the longitude of Jakarta.

Figure 2 shows the time-longitude cross sections of (a) the TRMM estimated rainfall data, and (b) the ensemble mean of the model simulated precipitation rate averaged between 5.5S - 8S with a horizontal resolution of 20 km. Note that the horizontal resolution is one order smaller than that of Hayashi and Sumi (~310 km) whereas one order larger than that of Miura et al. (~3.5 km). Comparison of such plots of the real atmospheric data and those obtained by numerical simulation shows fundamental agreement on the temporal modulation of the spatial distributions of precipitation, including the enhancement of precipitation on the time scale of pentad during the period of heavy rainfall, from 31 January to 4 February, in the Jakarta Flood event. During the simulated two-month period, modulation of the monsoon circulation is observed and the Jakarta Flood event is associated with a strong cold surge event across the equator. See [7] for the details.

Statistical analysis of the numerically obtained heavy precipitation in the tropics

The numerical data obtained in the time-lagged ensemble downscaling experiments with four horizontal resolutions (2, 4, 5, and 20 km, denoted as EXP *i* km) were analyzed to study the spatial and temporal variation of precipitation distribution simulated by the model for five days of the Jakarta Flood event [8, 9]. Figure 3 shows a histogram of precipitation rate for EXP2km, EXP4km, EXP5km, and EXP20km (from left to right), and for the Java sea, the northern coast of Java Island, the mountain area, and the southern coast of Java Island (from top to bottom), for all the nine ensemble members. There is a large variation of values for different resolutions and different regions in the upper tail of the histogram. All the models show a high value of precipitation in the northern coast region regardless of their horizontal resolution, and EXP4km shows the highest value of precipitation (77 mm/hr). If we look at the slope of the frequency distributions, a higher resolution experiment tends to show a more gradual decrease of rainfall frequency as function of rainfall value.

The upper tail of cumulative distribution functions (CDFs) of the precipitation rates was analyzed in details to focus on the heavy rainfall part. In the northern coast region, the highest contribution of heavy precipitation is well reproduced in the experiments except EXP20km, indicating that the downscaling improves the statistical nature of heavy precipitation. In general, the performance of downscaling is good in the situation of Jakarta Flood event in February 2007, in which convective activities play an important role in the heavy precipitation. Finer resolution results show better performance on the precipitation over complex terrain of the mountain region.

These results of the statistical analysis of heavy precipitation are indicative of possibility to use this kind of quantities for potential forecast of heavy precipitation in future as a product of ensemble forecasts. As an extension of these studies, we are now analyzing the size distributions of rain areas. The distributions show a power low for lower rain rates while a lognormal distribution for higher rain rates in all the experiments of the four horizontal resolutions. Details of the distributions and their dependence on the model resolution would become important information to understand the nature of moist convections and their organization in the tropics.

References

[1] Hoskins, B. J., M. E. McIntyre and A. W. Robertson, 1985: On the use and significance of isentropic potential vorticity maps. *Quart. J. R. Met. Soc.*, **111**, 877-946.

[2] Hayashi, Y.-Y. and A. Sumi, 1986: The 30-40 day oscillations simulated in an "aqua planet" model. *J. Meteor. Soc. Japan*, **64**, 451-467.

[3] Madden, R. A. and P. R. Julian, 1971: Detection of a 40-50 day oscillation in the zonal wind in the tropical Pacific. *J. Atmos. Sci.*, **28**, 702-708.

[4] Madden, R. A. and P. R. Julian, 1972: Description of global-scale circulation cells in the tropics with a 40-50 day period. *J. Atmos. Sci.*, **29**, 1109-1123.

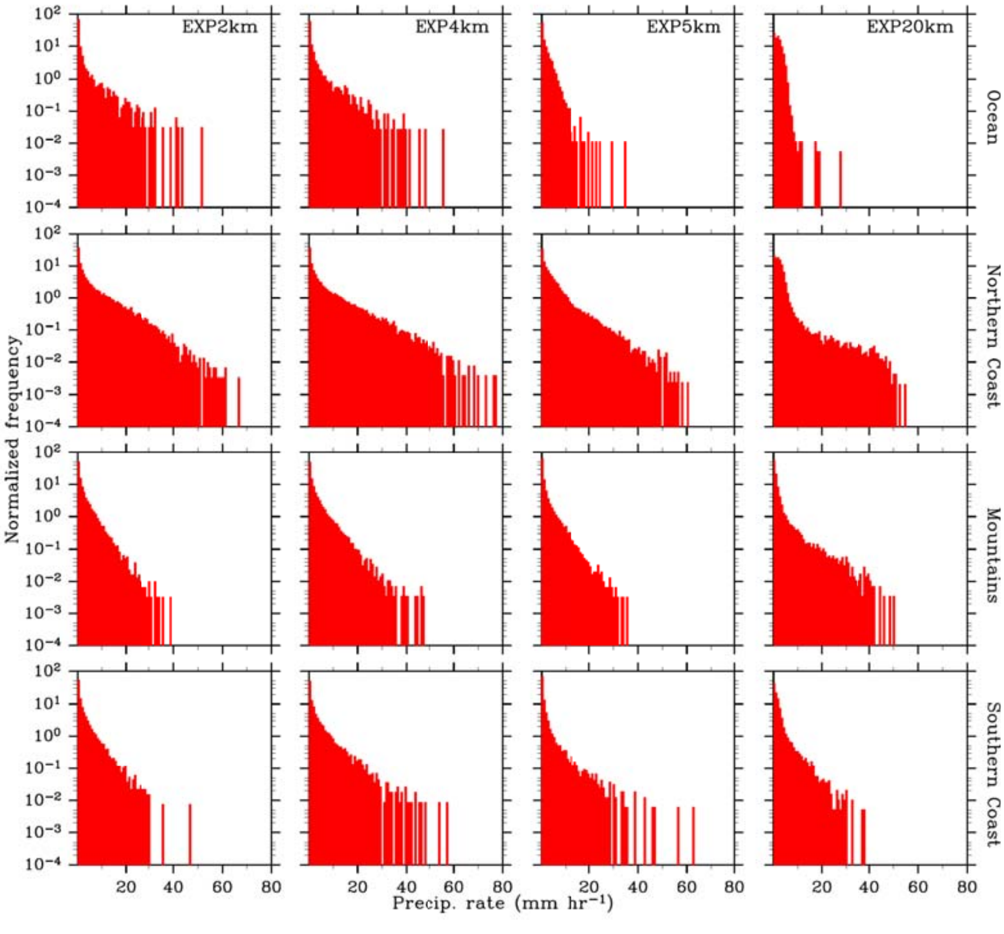

Fig. 3. A histogram of model-simulated precipitation rate for (left to right) EXP2km, EXP4km, EXP5km, and EXP20km, over (top to bottom) the Java sea, the northern coast of Java Island, the mountain area, and the southern coast of Java Island for all ensemble members [9].

[5] Nakazawa, T., 1988: Tropical super clusters within intraseasonal variations over the western Pacific. *J. Meteor. Soc. Japan*, **66**, 823-839.

[6] Miura, H., M. Satoh, T. Nasuno, A.T., Noda, and K. Oouchi, 2007: A Madden-Julian Oscillation event simulated using a global cloud-resolving model. *Science*, **318**, 1763-1765.

[7] Trilaksono, N.J., S. Otsuka, and S. Yoden, 2012: A Time-lagged ensemble simulation on the modulation of precipitation over west Java in January-February 2007. *Mon. Wea. Rev.*, **140**, 601-616.

[8] Trilaksono, N. J., S. Otsuka, S. Yoden, K. Saito, and S. Hayashi, 2011: Dependence of model-simulated heavy rainfall on the horizontal resolution during the Jakarta flood event in January-February 2007. *SOLA*, **7**, 193-196.

[9] Trilaksono, N.J., 2012: *Numerical Studies of Heavy Precipitation over West Java in January–February 2007*. Ph.D. thesis, Kyoto University, 106pp.

Dimension Reduction Study of Microseismic Activity in the Earth's Crust and Mantle in the Plate Boundary Region

Mitsuhiro Toriumi

Institute for Research of Earth Evolution (IFREE)
JAMSTEC, JAPAN

Abstract

Microseismic activity of the crust and mantle in the southwestern Japan was studied by means of dimension reduction method using principal component analysis. The microseismicity rates defined by the number of the microseismic events of M1-M2 were estimated in the volume of the Japanese crust and the subducting Philippine Sea Plate and of 1998-2008 from the JMA1 database. The spatial dimension of this region is 96 and total number of the microseismicity rate data reaches 120.

The data were projected effectively on hyper surface of 10 dimension, and the components of this reduced space are obtained as the eigenvectors of the cross correlation matrix of the total data. It shows that the linear combinations of the microseismicity rates can be divided mainly into three types of postseismic signals after large earthquakes, slowly changing components, and annually changing components. The last term is probably derived from solid tidal force, and the first term is responsible for the relaxation after large earthquake and the second term is due to long term strain change in the crust and subducting plate.

Key words: microseismicity, dimension reduction, deformation of the earth interior, principal component analysis

1, Introduction

Recent heavily disaster at 3.11 of 2011 in the northeastern Japan attacked severe damages to Japanese islands and aftershocks of seismic large events now continue to take place in the subducting Pacific plate and overriding crust and wedge mantle beneath Japanese islands. The seismic activity of the crust and mantle is basically governed by the mechanical states and properties of the rocks, because seismic events are thought to be the shear crack propagation. The magnitude of earthquakes can be represented by the logarithmic intensity of the product of rigidity of rocks, displacement of shear, and the area of the shear crack surface, and thus the wide variation of the earthquake magnitude is responsible for the wide range of shear crack surface area. The earthquakes of M9 reach about 500km x 200km, and those of M1 do about 1mx1m.

The earthquake events are similar to the spike signals in the time series of the mechanical states in the mantle and crust (Aoki and Scholz, 2003; Terakawa and Matsu'ura, 2010). The intensities of the spikes are represented by the logarithmic magnitude of moment generated by the single earthquake and the their time intervals between various spikes with different intensities are not always the values but not perfectly random. The spike signals show clearly the mechanical states over the critical condition where the rocks behave brittle manner of shear deformation, namely the rapid propagation of shear cracks. On the other hand, the micro-earthquake signals are generated in the condition under the large scale failure stress, and then they rise repeatedly in the same volume by the repeated stress operation.

In the experimental investigation, repeated nature of shear crack activation has been shown by many authors (Ohnaka and Mogi, 1981). Especially, the acoustic emissions in the deformation of rocks can be sharply observed as repeated signals from the micro cracks corresponding to the magnitude of strain. The rate of the generation of the signals clearly increases with increasing strain magnitude, suggesting that the rate of acoustic emission signals is potentially indicator of the local strain in the sample, and that the distribution pattern of the signal rates should display the localization of the large strain or the degree of the strain localization responsible for the large scale failure of the specimen.

The strain localization in the plate boundary and within the crust and mantle is most important problem to understand the fracture process in the earth interior (Ashby and Sammis, 1991). Considering that the fault propagation, that is the large shear crack, is not point-source process but the crack tip source process that represents peripheral region source of the shear cracks. Therefore, the coeval strain localization can reveal several long tubed regions along the large scale shear cracks in the earth interior. Thus, in order to study the mechanical coupling of the strain magnitude among the regions apart from each other, we require intensities of correlation functions of the time series of strain magnitude measured by rate of repeated micro earthquake signals among many localities in the earth interior and also we need the secure observations of many localities and narrow time intervals because of clarifying the short term strain localization.

The author intends to study the dimension reduction of the microseismicity rate defined by the micro earthquake numbers generated in the proper time intervals and volume in the earth interior to obtain the time trajectories of some combination of the microseismicity rates of many localities. Such linear combinations represent the new unit vectors in the reduced orthogonal coordinate system and they imply the intensities of mechanical coupling among all localities studied here.

2, Microseismicity rate as an indicator of the combination of strain, stress and fracture toughness

The seismic activity of the earth interior is sharply concentrated along the plate boundary zone although deep activity is restricted in the subduction zone. As stated in the earlier section, the intensity of the earthquake can be represented by logarithmic moment release generated from fault slip motion as the magnitude which ranges from 0 to 10. In the past the maximum magnitude of the plate boundary earthquake recorded reaches 9.5 at the 1960 Chile, but 3.11 Tohoku-Pacific earthquake was that of M9.0. After such giant earthquakes there are lots of showers of various magnitudes of earthquakes, and they are called as post seismic events having the intensities from M1 to M8.

Considering that the earthquake takes place by rapid slip motion of the large scale shear cracks in the earth interior, the elastic strains are to be concentrated at the crack tips around the area of that cracks. However, the displacements along on the shear crack surface are not the same distance, the shear crack propagation should make the local accumulation of strain and stress. Thus, near the large scale shear slip, coincident strain and stress localized regions must be associated with the large shear cracks.

Experimental investigations of yielding and successive fracturing of compressed rock specimens have revealed many signals of acoustic emission with very high frequencies which were generated randomly in the initial stage and in the later signals become concentrated along on the maximum shear planes post dated by conjugated faults. It seems that the change of the spatio-temporal pattern of the signal distribution in the deformed specimens should be apparently recognized before and after the large scale earthquake as an excess signal over the noisy background.

The detection of such signals must be surveyed by means of through searches of many time series of seismic activities of many neighboring volumes of the crust and mantle. Then, first, the author will intend to define the microseismicity rate as the spike density rate in the earth interior as follows.

In this paper, he introduced the microseismicity rate to be the total number of seismic spike signals between M1 to M2 per one month in the unit volume of 0.5^o x 0.5^o x thickness with 20km of the island arc crust of the Southwest Japan and subducted Philippine Sea Plate. In these regions the widths of longitude and latitude are about 50 km length, respectively. Time window of one month is selected because of available spike numbers to investigate the stochastic analyses during the high resolution periods from 1998 to 2008 for well-defined time series of seismicity over M1 have been continuously observed by means of dense observatories network by Japan Agency of Meteorogy was started at 1998.

Here, the author avoided the seismicity rates exceeding M2 because rather large earthquakes represent the large scale shear crack propagation and then those action must change irreversibly the mechanical nature but more small size shear cracks may be reversible signature of the mechanical state of the crust and mantle as seen in the experimental deformation of the rock samples before yielding (Atkinson, 1984).

The studied area is ranged from 32 to 36 ^{o} of the latitude and from 132.5 to 138.5 ^{o} of the longitude, involving the Southwest Japan Arc and trench segment from Nannkai - Tonankai - Tokai region as shown in figure 1. Therefore, 12x8 blocks of the SW Japan crust and and those of the Philippine Sea Plate are chosen for data analyses. The time interval is taken as one month from January of 1998 to 2008, and thus sample number attains 120 in the time series. Thus the total number of independent parameters is 140x12x8.

In this study, the seismicity rate is taken as the vector data in the 12x8 dimensional space and therefore samples of vector data count 120 in the studied case. Accordingly the following data sets can be assembled to infer the trajectory of the mechanical states of the crust and subducting mantle in the SW Japan as shown in figure 2;

Xj (n(1j), n(2j), n(3j), ...n(kj)) for j=1 to 140

where n and X are microseismicity rates and their vector, respectively, and k is 96.

Expermenntal results of acoustic emmision in the deformation of rocks indicate clear relations between strain and number of acoustic signals. The time study of the numbers of signals also indicated repeated generation of micro shear cracks and show the scarce hysteresis between the strain and number of acoustic emission (Ohnaka and Mogi, 1981). It leads that the shear cracks under the size of critical Griffith crack must be reversible for instantaneous slip motion: the micro shear crack may retreat the undeformed state by elastic stresses induced by the foward slip. The critical size of the shear crack is estimated about 10 m in diameter in the earth interior. Consequently the shear cracks of M1-2 are less than the critical Griffith cracks.

In the case of water-filled shear crack the surface tension should decrease because of hydration reaction between mineral surface and water. According to critical size proportional to surface tension, the critical Griffith crack size becomes small. On the other hand, higher temperature condition yield enhancement of ductile behavior, suggesting an increase of fracture toughness.

Therefore, the shear cracks can be divided into two types by the length: the crack under the critical size is reversible type and that over the critical size is to be irreversible one. The shear cracks of M1-2 may be the reversible type. In this paper, the author intends to reveal the mechanical coupling among every reference volumes in the studied region with special reference to microseismicity rate time series as previously shown in figure 2.

2, Dimension reduction of microseismicity rate

The microseismicity rate vectors have apparently dependent parameters n(i,j) of given j and also, the time series of every n(i,j) of given i shows the tranjectories of local microseismicity rate. As shown in figure 3, the trajectories of the microseismicity rates are considered to be the unique attractor in the space of n(i) for i=1 to 96, because every components of Xj for j=1 to 140 are mutually as a function of them and the time. In other words, we can consider the following dynamical differential equations of n(i),

$$d\, n(i)/dt = f_i(n(j))$$

Thus, if we think of the strong dependency as exemplified by the perfectly continuous elastic mass applied by the external force through the boundary, every n(i) are approximatedly the same and the its trajectory in the high dimension space is uniquely governed by the external force change. On the other hand, the slider block system in which every blocks are connected by spring and frictional stresses operate between the block and the basement floor have strongly random slip motions of each block. In this system, the available linear comibinations of positions of every blocks display the clear attractor in the new low dimensional space. This space must be constructed by the dimension reduction method by using the principal component anaysis concerning the displacements of every blocks and their time series as shown in the plate boundary along the Japan trench by Toriumi (2009).

The actual dimension of the hyper space made by n(i) is to be determined by the hyper surface which contains almost always the trajectories of X as shown in figure 3 and then it is obtained by the transformed coordinates by made by rotation matrix W as follows;

$$Z = W X + g$$

in which g is the Gaussian noise term derived from projection onto the hyper surface.

In order to determine the unique rotation matrix W, the optimization of the distance from the newly obtained Cartesian coordinates Z with smaller dimension should be performed, leading to obtain the eigenvector of the cross correlation matrix composed with large number of time collection samples (Jollife, 2002). Consequently, we estimate the principal component vectors Z1, Z2, Z3, …and Zl (l is less than 96 in this study) in the decreasing order of the eigen value. Following the normal principal component analysis method, we choose the number of available number of new dimensions as the dispersion of the samples data becomes 90%. Actually, the dispersion curve against the number of new dimensions displays rapid decrease and then changes to be flat near the 90% of the value, suggesting the minimum Akaike information criterion at that point.

In this study, we use the projected hyper surface of 10 dimension for the necessary of the redundant number of dimensions. Later, it shows that the projected hyper surface changes during the time because of successive change of mechanical coupling modes among the studied blocks of the crust and mantle as sharply shown by localization of large earthquake and its following post seismic activity.

3, Results

The microseismicity rates are estimated from JMA1 database in the ERI of university of Tokyo. The time range studied here are from 1998 Jan.31 to 2008 Jan.31. The microseismicity rate of the earthquakes with magnitude ranging from 1 to 2 is to be number of event in the one month within the volume of 0.5^o x 0.5^o of latitude and longitude and depth range of 20km in the crust and of 50km in the Philippine Sea Plate.

Total number of micro earthquake events reaches about 60,000. The data processing has been carried out using the R-language open source. The visualization of the eigenvectors of the cross correlation matrix was performed by pseudo coloring in the map as shown in figures 4 and 5.

First, we intend to show the case of the Philippine Sea Plate which is subducting under the SW Japan arc reaching to the mantle under the front of the Japan Sea from the Nankai trough. As seen in figure 6, the first principal component Z1 indicates sharply the microseismic activities just after the large earthquake, judging from the localization of the intensity of Z1 just at the location of the large earthquake. The decay pattern of the seismicity rate after the large earthquake is similar to the power law type one, indicating the postseismic activity shown by Ishimori-Iida relation.

The second and subsidiary components of the microseismicity rates of the subducted oceanic plate can be classified into three types: one shows the time series having slow change, the second is the time series having annual and sub annual change as shown in figure 6. The third type shows the random variation in the time series as shown in figure 6. The geometrical patterns of slowly changing components display clearly the mechanical coupling among the regions of central area beside the Nankai trough and the areas of Kii and eastern Shikoku and Kinki regions. The time series of these components appear several to several ten years periodic changes with slightly correlation to the large earthquakes. Further, their time changes contain slight fluctuation.

The most striking temporal changes of the higher components are annual to sub annual periodic patterns as shown in figure 7. The periodicity of these patterns can be also suggested by the foulier spectra of the time series of the annual changes as shown in figure 8, showing that there are several periodicities having 1 and half years, three years and more long periodicities. The geometrical patterns of the annual periodicity of the higher components are identified to the mechanical correlations among the regions of near Nankai trough and Kii and Hamanako regions.

4, Discussions and conclusions

The dimension reduction method using the principal component analysis can be available for investigation of the strength of mechanical coupling within the island arc crust and subducting oceanic plate in the southwestern Japan region. The geometrical patterns obtained by the intensity distribution of the correlation matrix of the projected hyper surface, that is the eigenvectors, show sharply the several characteristic features and time series. Firstly, it should be said that the microseismicity rates of the crust and oceanic plate can be decomposed to principal components in terms both of geometrical patterns and temporal changes. The first component is identified to the localized microseismic activity just after the large earthquakes, that is the post seismic activity. The second type is the slowly changing microseismicity rates and it contains several to several ten years periodicities and small fluctuations. In addition, the third type is revealed to show the annual periodic change, suggesting that the microseismic activity of the small scale shear cracks is strongly responsible for the solid tidal deformation of the earth interior.

The first component of the reduced dimensional space has relaxation of the Poisson type just having logarithmic decrease with time, suggesting the diffusive relaxation of elastic strain energy around the center of the earthquake. In other words, the time change of the combination microseismicity rates have the following relation with time,

$$dZ1/dt = -kZ1$$

where k is the time decay constant of the postseimicity.

The behavior of the slow processes of the higher principal components displays long-term variation of the mechanical coupling among the plate boundary regions and the oceanic plate interior, and the mechanical relationships between the large earthquake event and the slow processes can be investigated by correlation diagram between the intensity of the first component Z1 and that of the higher components. In figure 9, the correlation diagrams between Z1 and Z2, and Z6 and Z7 are shown, suggesting that the peaks of slowly changing higher components are correlated with the time of large earthquake.

On the other hand, the annual changing components are suggested to be responsible for the change of tidal strain in the earth interior, judging from the peaks of the principal components showing the combination of the microseismicity rates occur near the equinox times in the year. Considering that the the microseismic signals are generated by the rapid slip of small shear cracks and that micro shear cracks should have the peculiar orientations related with the plate motion, the critical resolved shear stress acted on the micro shear crack surfaces becomes the peak magnitude at the maximum tidal periods as suggested by Nakata et al. (2008). Thus the maximum activity of the microshear cracks should take place annually or subannually as being revealed in this study.

The dimension reduction study of the microseismicity rates in the island arc crust and the subducting oceanic plate reveals that the microseismic activity can be divided into several types of the eigenvector space of the cross correlation matrix of the time series data. One is the post seismic activity after large earthquake, the second is the slow process involving the large earthquake effect, and the third is the tidal strain – inducing microseismic activity. These components show the strong mechanical coupling in the map displaying the intensity distribution of their components.

Acknowledgements

The author thanks Y.Kaneda and T. Tsutomu of the JAMSTEC, M.Okada, Z.Yoshida and R.Kuwatani of the University of Tokyo, and K.Fukumoto of the Kyushu University for many discussions and suggestions.

References

Atkinson, B. K., Subcritical crack growth in geological materials. J.Geophys.Res., 89,4077-4114.1984.

Aoki, Y., and C.H. Scholz, Vertical deformation of the Japanese islands, 1996-1999. Jour. Gophys.Res., 108, 2257, doi:10.1029/2002JB002129, 2003.

Ashby, M.F., and C.G.Sammis, Damage mechanism of the solids in compression, Pure and Applied Geophysics, 133, 3, 489-521, 1991

Jollife, I.T., Principal Component Analysis, 530pp, Springer, 2002

Nakata, R., N.Suda, and H.Tsuruoka, Non-volcanic tremor resulting from the combined effect of earth tides and slow slip events. Nature geoscience, vol.1, Oct. 676-678, 2008.

Ohnaka, M., and K.Mogi, Frequency dependence of acoustic emission activity in rocks under incremental, uniaxial compression. Bull. Earthquake Res.Inst., 56, 67-89, 1981.

Terakawa, T., and M.Matsu’ura, The 3-D tectonic stress fields in and around Japan inverted from centroid moment tensor data of seismic events, Tectonics, 29, TC6008, doi:10.1029/2009TC002626, 2010.

Toriumi, M., Principal Component Analyses of Seismic Activity in the Plate Boundary Zone of Northeastern Japan Arc. Jour. Disaster Res., 4,2, 209-213, 2009.

Figure 1, The studied areas of dimension reduction of microseismicity rates of the Philippine Sea Plate (A) and island arc crust (B), showing the microseismic locations of M1 to M2 from 1998-2010.

Figure 2, Microseismicity rates and the microseismicity vector showing the number of micro earthquake events of the divided blocks in the oceanic plate. See text.

Figure 3, Trajectory of the microseismicity rate vector in the original space and reduced hyper surface. See text.

Figure 4, Spatial patterns of the principal components in the reduced hyper surface of the subducting Philippine Sea Plate, showing the color index of intensity of the components . Red color is positive and blue color is negative intensity, but the color contrast should be noticed.

Figure 5, Spatial patterns of principal components in the reduced hyper surface showing the strength of mechanical coupling in the island arc crust of SW Japan. The explanations are the same in the previous figure.

Figure 6, Time series of the principal components in the reduced hyper surface of the Philippine Sea Plate. See text.

Figure 7, Time series and the spatial patterns of the annually changing components of the reduced hyper surface of data from Philippine Sea Plate.

Figure 8, Fourier spectra of the annually changing principal components of the microseismicity rate vectors in the southwestern Japan crust and Philippine Sea Plate(upper).

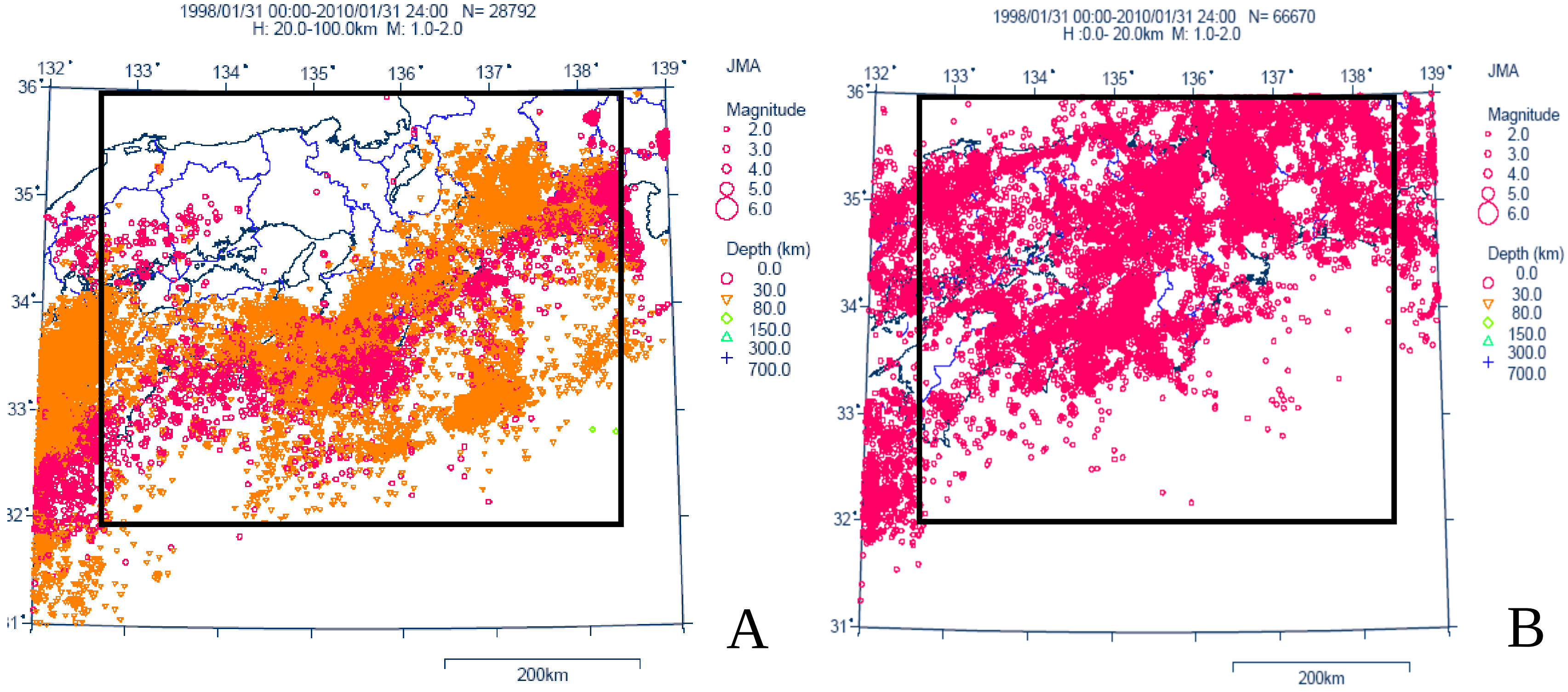

Figure 1, The studied areas of dimension reduction of microseismicity rates of the Philippine Sea Plate (A) and island arc crust (B), showing the microseismic locations of M1 to M2 from 1998-2010.

$$\mathbf{X}(t) = (n1(t), n2(t), n3(t), , , nk(t)) \quad ; \quad k\text{ - dimension}$$

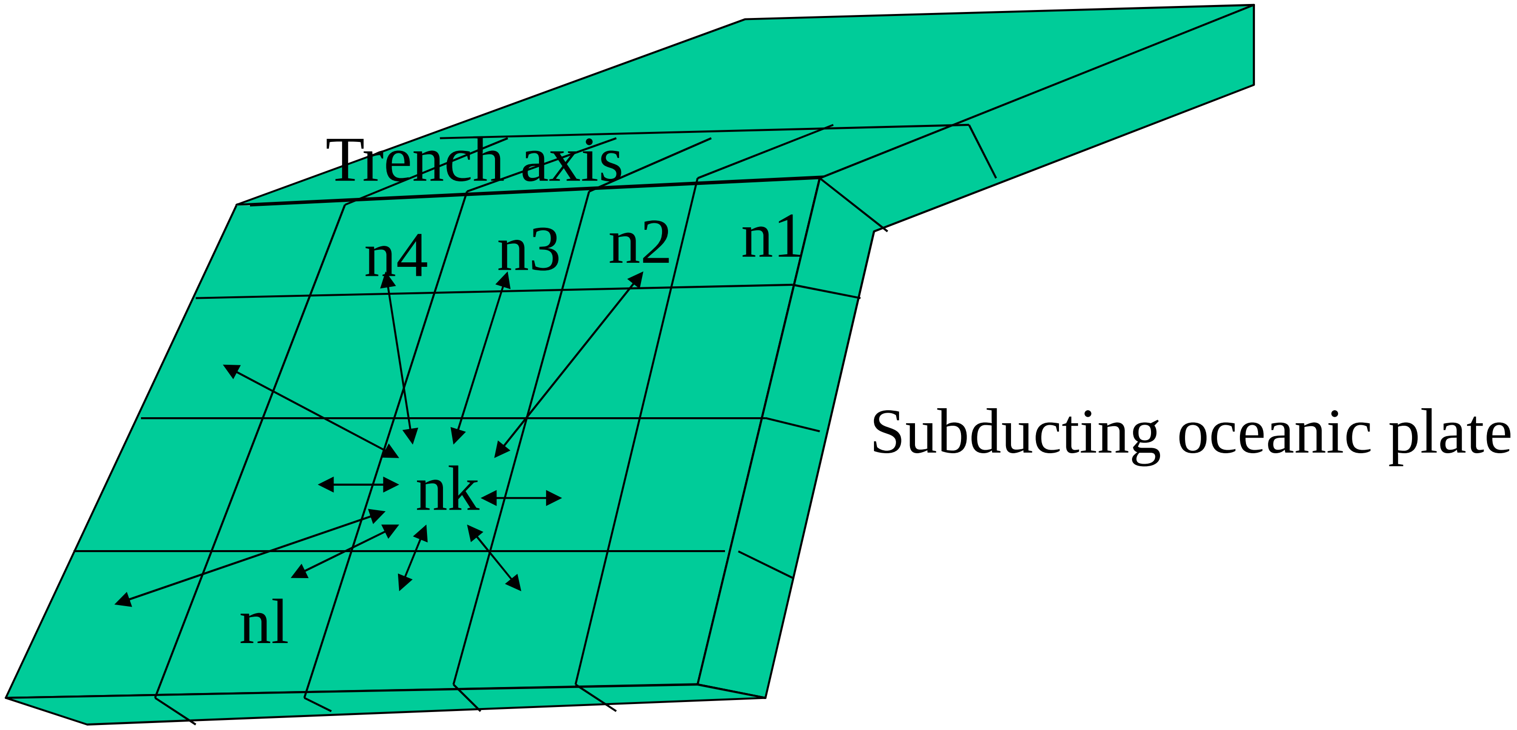

Figure 2, Microseismicity rates and the microseismicity vector showing the number of micro earthquake events of the divided blocks in the oceanic plate. See text.

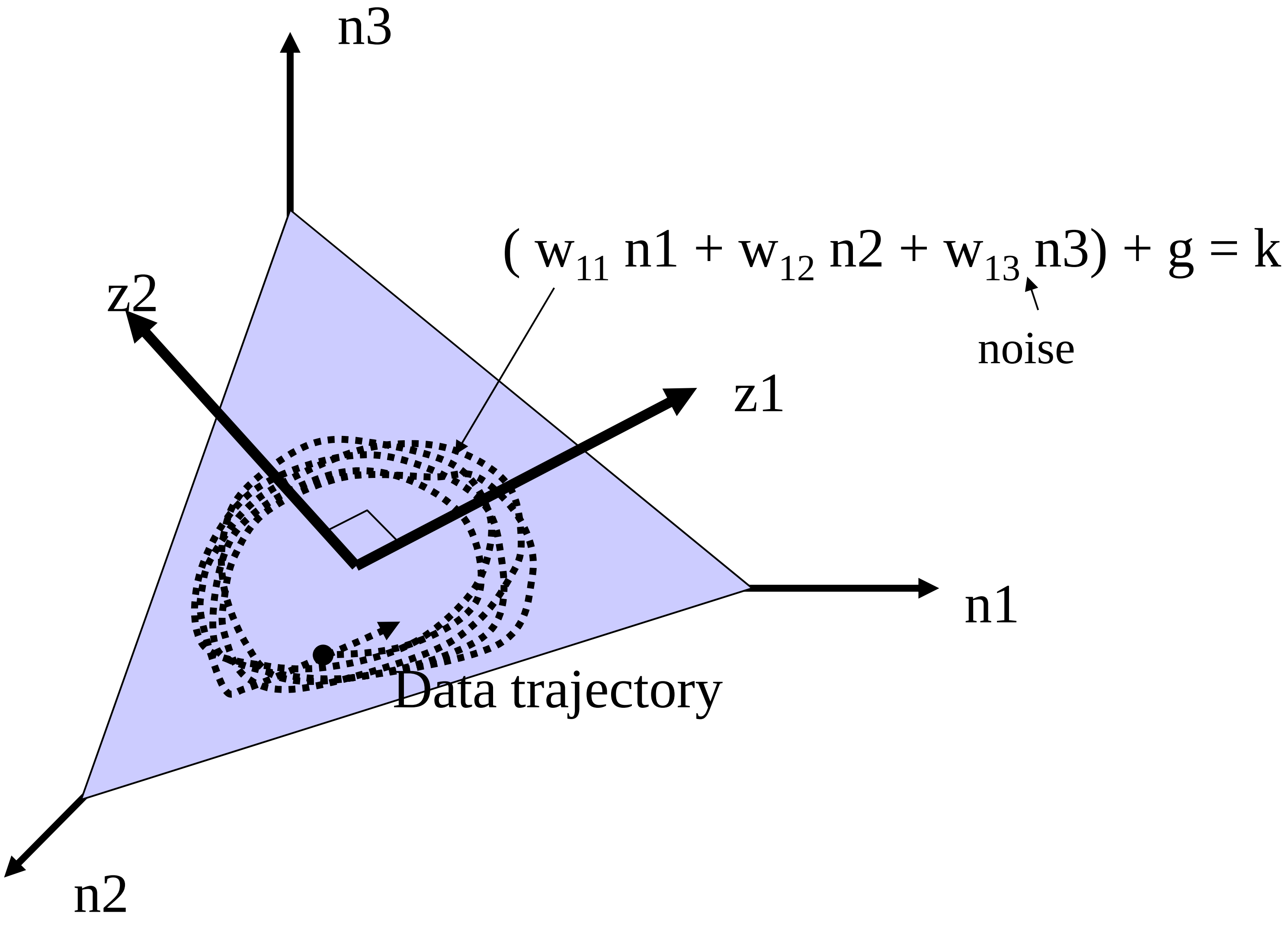

Figure 3, Trajectory of the microseismicity rate vector in the original space and reduced hyper surface. See text.

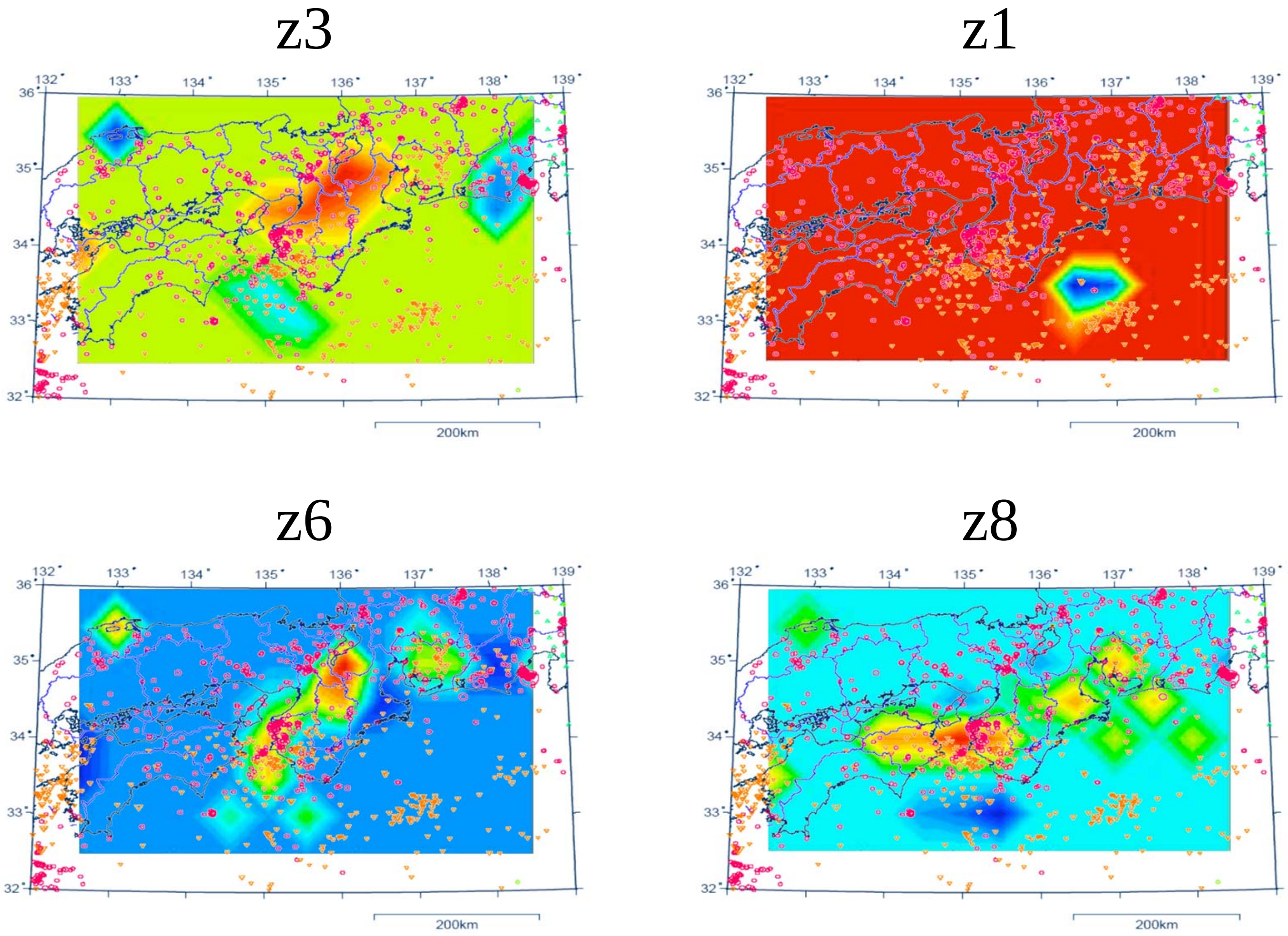

Figure 4, Spatial patterns of the principal components in the reduced hyper surface of the subducting Philippine Sea Plate, showing the color index of intensity of the components . Red color is positive and blue color is negative intensity, but the color contrast should be noticed.

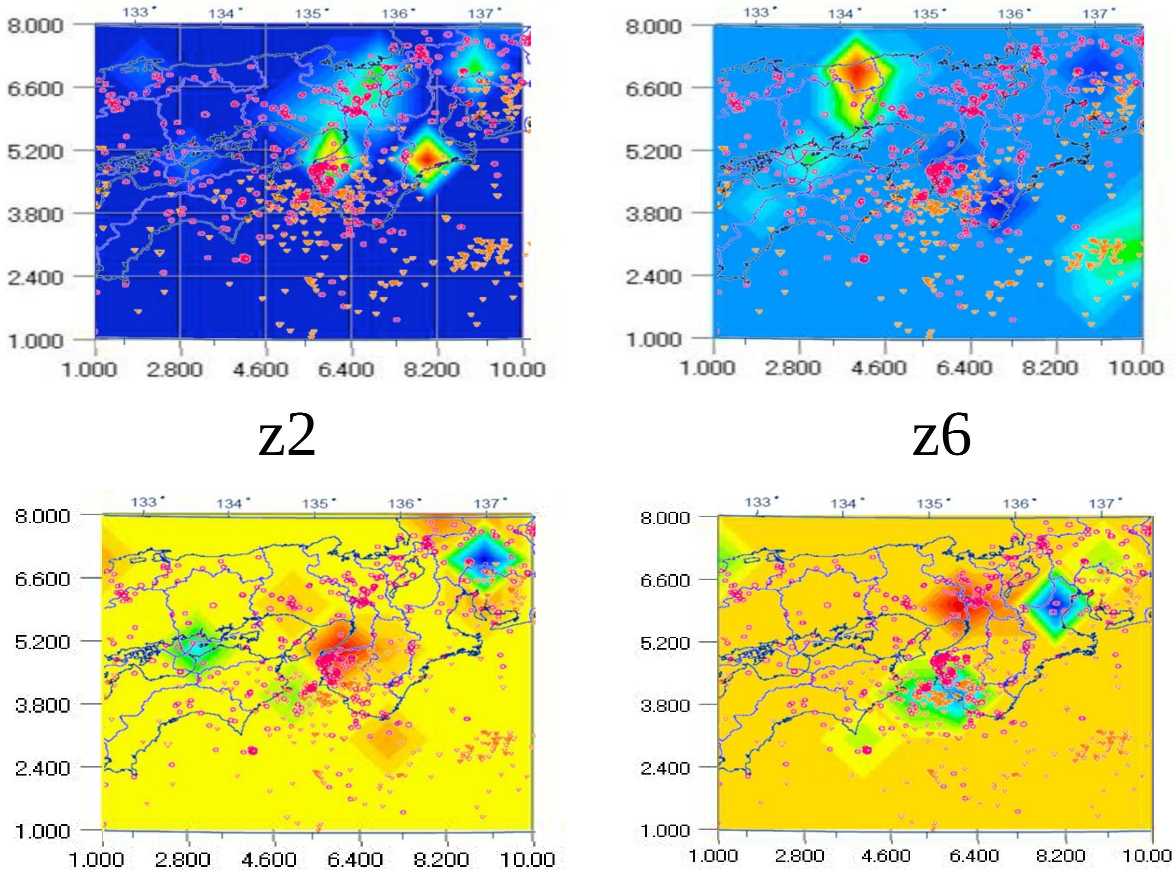

z2

z6

z4

z10

Figure 5, Spatial patterns of principal components in the reduced hyper surface showing the strength of mechanical coupling in the island arc crust of SW Japan. The explanations are the same in the previous figure.

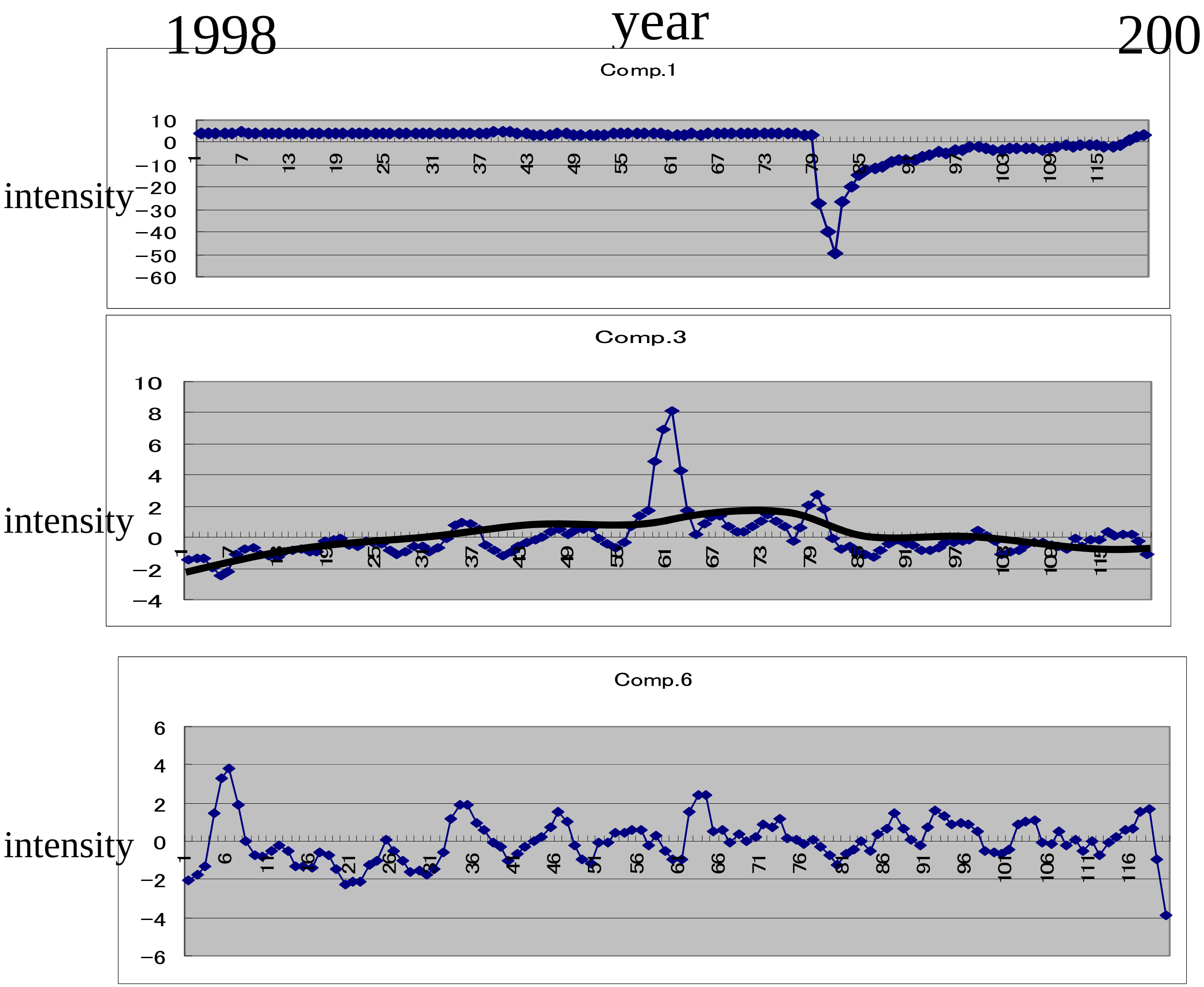

Z1

relaxation process
after large eqs.

Z3

Slow process

Z6

Annual process

Figure 6, Time series of the principal components in the reduced hyper surface of the Philippine Sea Plate. See text.

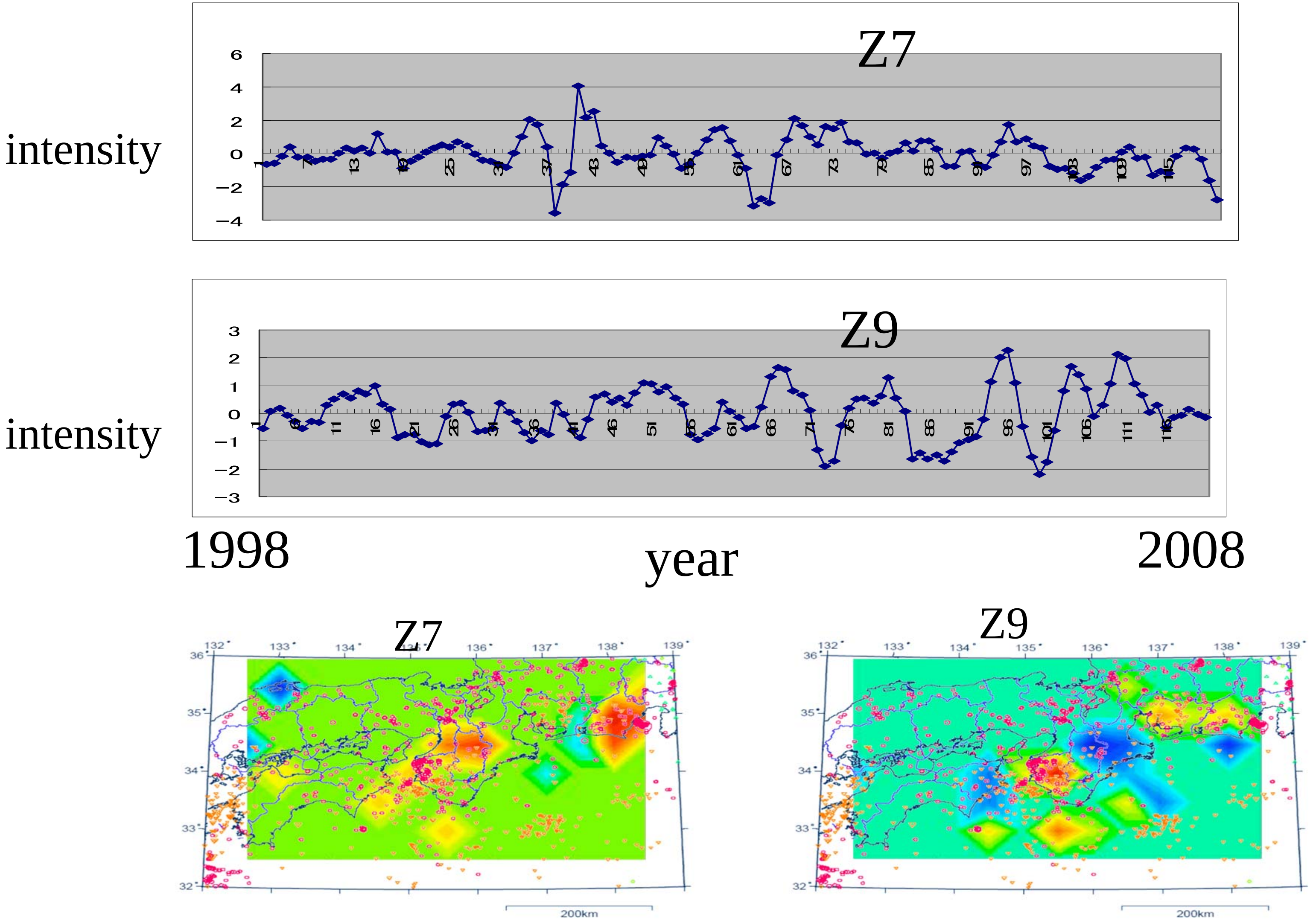

Figure 7, Time series and the spatial patterns of the annually changing components of the reduced hyper surface of data from Philippine Sea Plate.

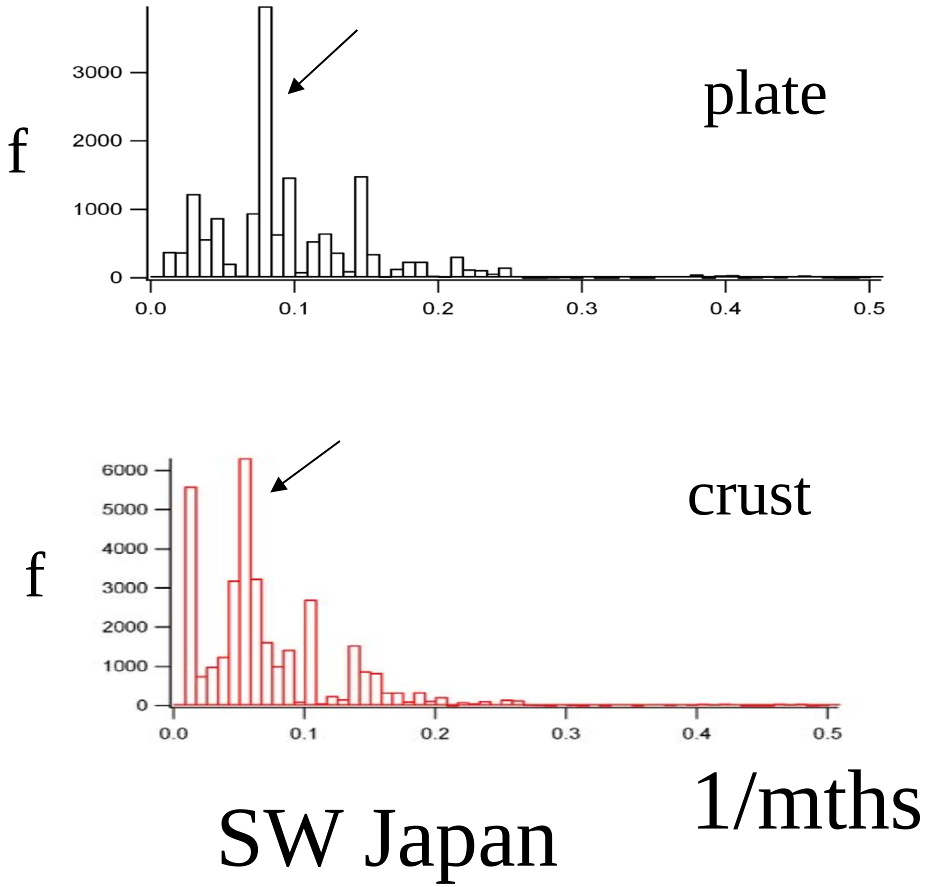

Figure 8, Fourier spectra of the annually changing principal components of the microseismicity rate vectors in the southwestern Japan crust and Philippine Sea Plate(upper).

ON THE EVOLUTION OF COPULAS

NAOYUKI ISHIMURA AND YASUKAZU YOSHIZAWA

ABSTRACT. This article reports our recent studies on the evolution of copulas. As is well known, a copula provides a flexible tool for investigating dependence relations among random variables. Except for a few cases, however, copulas are concerned mainly with the static problems, not with the time-dependent ones. On the other hand, we have introduced the concept of the evolution of copulas, which claims that a copula itself evolves according to the time variable. We review our establishments as well as drawbacks on this topic.

1. INTRODUCTION

This article reviews our recent researches on the evolution of copulas [5][6][17][18] with comments and extensions.

A copula function, or simply a copula, is well employed tool for understanding the dependence structure among random variables. Copulas make a link between multivariate joint distributions and univariate marginal distributions. The study of copulas has been developed extensively from around 1990s. Because of their flexible structure, copulas have been applied in many situations, such as risk management, financial mathematics, seismological analysis, and so on. Let us recall the definition of copula and the fundamental theorem due to A. Sklar [13] in the bivariate case.

Definition 1. A function C defined on $I^2 := [0,1] \times [0,1]$ and valued in I is called a copula if the following conditions are fulfilled.

(i) For every $(u, v) \in I^2$,

$$C(u,0) = C(0,v) = 0, \quad C(u,1) = u \quad \text{and} \quad C(1,v) = v. \tag{1}$$

(ii) For every $(u_i, v_i) \in I^2$ $(i = 1, 2)$ with $u_1 \le u_2$ and $v_1 \le v_2$,

$$C(u_1,v_1) - C(u_1,v_2) - C(u_2,v_1) + C(u_2,v_2) \ge 0. \tag{2}$$

The requirement (2) is referred to as *the* 2*-increasing condition.* We also note that a copula is continuous by its definition.

Theorem 2. (Sklar's theorem) *Let H be a bivariate joint distribution function with marginal distribution functions F and G; that is,*

$$\lim_{x\to\infty} H(x,y) = G(y), \qquad \lim_{y\to\infty} H(x,y) = F(x).$$

Then there exists a copula, which is uniquely determined on $RanF \times RanG$, such that

$$H(x,y) = C(F(x), G(y)). \tag{3}$$

Conversely, if C is a copula and F and G are distribution functions, then the function H defined by (3) is a bivariate joint distribution function with margins F and G.

2000 *Mathematics Subject Classification.* 91G80; 35K05.

Key words: evolution of copulas, heat equation, discrete process, convergence.

As its definition indicates, copulas are concerned principally with the static problems, not with the time-dependent ones. A few exceptions include the study on the copulas and the Markov processes by W.F. Darsow, B. Nguyen, and E.T. Olsen [1], and also on the dynamic copulas by A.J. Patton [12]. The former investigates the dependence relation between the Markov processes at different times. The typical procedure of the latter is as follows: Take one Archimedean copula (which is a well known class of one-parameter family of copulas) and denote it by $C(u, v; \rho)$, where ρ is a parameter whose value should belong to some interval J ($\subset \boldsymbol{R}$). The dynamic copula is then provided as

$$C(u, v; \rho_t) \qquad \text{with} \quad \rho_t = \Lambda(X_t(\rho_{t-1})),$$

where $X_t(\rho_{t-1})$ means some time-series model, say ARMA(p, q)-type process, and Λ is the transformation function which is designed to keep $\rho_t \in J$.

On the other hand, we have proposed the concept of the evolution of copulas. To be a little specific, the evolution of copulas proclaims that a copula itself evolves according to the time, where copulas satisfy the standard heat equation.

The purpose of this review is to summarize the results concerning the evolution of copulas and to make some extensions. Shortcomings of this concept are also discussed.

2. Evolution of Copulas

This section recalls the results of [5][6].

The evolution of copulas we have introduced is a time parameterized family of copulas $\{C(u, v, t)\}_{t\geq 0}$, which satisfy the heat equation:

$$\frac{\partial C}{\partial t}(u, v, t) = \Big(\frac{\partial^2}{\partial u^2} + \frac{\partial^2}{\partial v^2}\Big) C(u, v, t). \tag{4}$$

Here, by the definition of copula, we understand that $C(\cdot, \cdot, t)$ fulfills (1)(2); to be precisely, we postulate that

(i) for every $(u, v, t) \in I^2 \times (0, \infty)$,

$$C(u, 0, t) = C(0, v, t) = 0, \quad \text{and} \quad C(u, 1, t) = u \quad \text{and} \quad C(1, v, t) = v. \tag{5}$$

(ii) for every $(u_i, v_i, t) \in I^2 \times (0, \infty)$ $(i = 1, 2)$ with $u_1 \leq u_2$ and $v_1 \leq v_2$,

$$C(u_1, v_1, t) - C(u_1, v_2, t) - C(u_2, v_1, t) + C(u_2, v_2, t) \geq 0. \tag{6}$$

The stationary solution to (4), which is referred to as the harmonic copula, is uniquely determined to be $\Pi(u, v) := uv$, in view of the boundary condition (1). We note that the copula Π represents the independent structure between two respective random variables.

The main establishment of [5] is the existence proof of solutions to (4), which satisfy the copula conditions (5)(6). In particular, the solution $u = u(u, v, t)$ is expressed as

$$\begin{aligned} &C(u, v, t) \\ &\quad = uv + 4 \sum_{m,n=1}^{\infty} e^{-\pi^2(m^2+n^2)t} \sin m\pi u \sin n\pi v \iint_{I^2} \sin m\pi\xi \sin n\pi\eta (C_0(\xi, \eta) - \xi\eta) d\xi d\eta. \end{aligned}$$

The typical result is

Theorem 3. *For any bivariate copula* $C_0(u,v)$*, there exists a unique family of time-parametrized bivariate copulas* $\{C(u,v,t)\}_{t\geq 0}$ *such that*

$$\begin{aligned} &\frac{\partial C}{\partial t}(u,v,t) = \Big(\frac{\partial^2}{\partial u^2} + \frac{\partial^2}{\partial v^2}\Big)C(u,v,t) \quad \text{for } (u,v,t) \in I^2 \times (0,\infty) \\ &C(u,v,0) = C_0(u,v) \qquad\qquad \text{on } (u,v) \in I^2. \end{aligned} \tag{7}$$

Moreover we have

$$\lim_{t\to\infty} C(u,v,t) = \Pi(u,v) \quad \text{uniformly on } (u,v) \in I^2.$$

In the time-reversed version, we have

Theorem 4. *For any bivariate copula* $C_T(u,v)$*, where* T (>0) *denotes the maturity, there exists a unique family of time-parametrized bivariate copulas* $\{C(u,v,t)\}_{0\leq t\leq T}$ *such that*

$$\begin{aligned} &\frac{\partial C}{\partial t}(u,v,t) + \Big(\frac{\partial^2}{\partial u^2} + \frac{\partial^2}{\partial v^2}\Big)C(u,v,t) = 0 \quad \text{for } (u,v,t) \in I^2 \times \{t \leq T\}, \\ &C(u,v,T) = C_T(u,v) \qquad\qquad \text{on } (u,v) \in I^2. \end{aligned}$$

Here the convergence property as $t \to -\infty$ is not so relevant issue from the financial standpoint.

In addition to the above results, the convergence of the population version of Kendall's tau and Spearman's rho, which are denoted by τ and ρ, respectively, is proved. These are known quantity of the measures of association and represented in terms of copulas as follows (see [11]): Let X and Y be continuous random variables whose copula is C. Then we have

$$\begin{aligned} \tau_{X,Y} &= \tau_C = 4\iint_{I^2} C(u,v)dC(u,v) - 1 = 1 - 4\iint_{I^2} \frac{\partial C}{\partial u}(u,v)\frac{\partial C}{\partial v}(u,v)\,dudv, \\ \rho_{X,Y} &= \rho_C = 12\iint_{I^2} C(u,v)\,dudv - 3 = 12\iint_{I^2} (C(u,v) - uv)\,dudv. \end{aligned}$$

We obtain the next theorem, whose proof is given for completeness.

Theorem 5. *Let* $C_t = C(u,v,t)$ $(t \geq 0)$ *be a time-parametrized family of bivariate copulas, which satisfy (7). Then it follows that*

$$|\tau_{C_t}| + |\rho_{C_t}| \leq Ae^{-Bt} \quad \text{as } t \to \infty,$$

where A *and* B *are positive constants.*

In particular, $C_t \to \Pi$ *exponentially as* $t \to \infty$.

Proof. We employ the notation: $\|(C-\Pi)(t)\|_2^2 := \iint_{I^2} (C(u,v,t) - uv)^2\,dudv$. We compute

$$\begin{aligned} \frac{1}{2}\frac{d}{dt}\|(C-\Pi)(t)\|_2^2 &= \iint_{I^2} (C-\Pi)\cdot\triangle(C-\Pi)\,dudv = -\|\nabla(C-\Pi)(t)\|_2^2 \\ &\leq -\alpha\|(C-\Pi)(t)\|_2^2, \end{aligned} \tag{8}$$

where $\alpha > 0$ denotes a constant due to the Poincaré inequality. The use of this inequality is possible thanks to $C - \Pi = 0$ on ∂I^2. We thus deduce that

$$\|(C-\Pi)(t)\|_2^2 \leq \|C_0 - \Pi\|_2^2 e^{-2\alpha t}.$$

Taking into account of this estimate, we infer that

$$|\rho_c| \leq 12\|(C-\Pi)(t)\|_2 \leq 12\|C_0 - \Pi\|_2 e^{-\alpha t}.$$

This proves the exponential convergence of ρ.

Next we turn our attention to τ. We recall the next formula, which is derived upon direct calculation.

$$\tau_C = \frac{2}{3}\rho_C - 4\iint_{I^2} \frac{\partial}{\partial u}(C(u,v)-uv)\cdot\frac{\partial}{\partial v}(C(u,v)-uv)\,dudv.$$

It then follows that

$$\begin{aligned} e^{\alpha t}|\tau_C(t)| &\leq \frac{2}{3}e^{\alpha t}|\rho_C(t)| + 4e^{\alpha t}\iint_{I^2}\left|\frac{\partial}{\partial u}(C-\Pi)(t)\cdot\frac{\partial}{\partial v}(C-\Pi)(t)\right| dudv \\ &\leq 8\|C_0-\Pi\|_2 + 4e^{\alpha t}\|\nabla(C-\Pi)(t)\|_2^2. \end{aligned}$$

In light of the continuity of $\|\nabla(C-\Pi)(t)\|_2$ with respect to t, it suffices to show that

$$\int_t^\infty e^{\alpha s}\|\nabla(C-\Pi)(s)\|_2^2 ds < \infty,$$

which implies that $e^{\alpha t}\|\nabla(C-\Pi)(t)\|_2^2 \leq M < \infty$ for all large t with some constant M.

In view of (8), we infer that

$$\begin{aligned} \frac{1}{2}\frac{d}{dt}(e^{\alpha t}\|(C-\Pi)(t)\|_2^2) + e^{\alpha t}\|\nabla(C-\Pi)(t)\|_2^2 &= \frac{\alpha}{2}e^{\alpha t}\|(C-\Pi)(t)\|_2^2 \\ &\leq \frac{\alpha}{2}e^{-\alpha t}\|C_0-\Pi\|_2^2, \end{aligned}$$

from which we conclude that

$$\begin{aligned} 2\int_t^\infty e^{\alpha s}\|\nabla(C-\Pi)(s)\|_2^2 ds &\leq e^{\alpha t}\|(C-\Pi)(t)\|_2^2 + \int_t^\infty \alpha e^{-\alpha s}\|C_0-\Pi\|_2^2 ds \\ &\leq 2\|C_0-\Pi\|_2^2 e^{-\alpha t}. \end{aligned}$$

In summary, we have established $e^{\alpha t}|\tau_C(t)| \leq 8\|C_0-\Pi\|_2 + 4M$ and the proof of the exponential convergence of τ is thereby completed. □

3. EVOLUTION OF COPULAS IN DISCRETE PROCESSES

This section reproduces [17].

The evolution of copulas is able to be considered in discrete processes. The construction of a discretely parametrized family of copulas proceeds as follows.

Let $N \gg 1$ and $0 < h \ll 1$. We put

$$\Delta u = \Delta v := \frac{1}{N}, \qquad \Delta t := h, \qquad \lambda := \frac{\Delta t}{(\Delta u)^2} = \frac{\Delta t}{(\Delta v)^2} = hN^2,$$

and

$$u_i := i\Delta u = \frac{i}{N}, \qquad v_j := j\Delta v = \frac{j}{N} \qquad (i,j = 0,1,\cdots,N).$$

Our family of copulas $\{C^n(u,v)\}_{n=0,1,2,\cdots}$ is now defined as follows: First,

$$C^0(u,v) := C_0(u,v),$$

where C_0 denotes given initial copula.

At $\{(u_i,v_j)\}_{i,j=0,1,\cdots,N}$, the value $C^n_{i,j} := C^n(u_i,v_j)$ is defined to be governed by the system of difference equations

$$\frac{C^{n+1}_{i,j}-C^n_{i,j}}{\Delta t} = \frac{C^n_{i+1,j}-2C^n_{i,j}+C^n_{i-1,j}}{(\Delta u)^2} + \frac{C^n_{i,j+1}-2C^n_{i,j}+C^n_{i,j-1}}{(\Delta v)^2} \quad \text{for } i,j=1,2,\cdots,N-1, \tag{9}$$

combined with the boundary conditions

$$\begin{cases} C^n_{0,j} = 0 = C^n_{i,0} \\ C^n_{i,N} = u_i, \quad C^n_{N,j} = v_j \end{cases} \qquad \text{for } i,j = 0,1,\cdots,N.$$

As to the point $(u,v) \in \boldsymbol{I}^2$ other than $\{(u_i,v_j)\}_{i,j=0,1,\ldots,N}$, the value $C^n(u,v)$ is provided by interpolation. That is, if for instance

$$u_i \le u \le u_{i+1}, \quad v_j \le v \le v_{j+1},$$

then we put

$$\begin{aligned} C^n(u,v) := C^n_{i,j} &+ \frac{C^n_{i+1,j}-C^n_{i,j}}{u_{i+1}-u_i}(u-u_i) + \frac{C^n_{i,j+1}-C^n_{i,j}}{v_{j+1}-v_j}(v-v_j) \\ &+ \frac{C^n_{i+1,j+1}-C^n_{i+1,j}-C^n_{i,j+1}+C^n_{i,j}}{(u_{i+1}-u_i)(v_{j+1}-v_j)}(u-u_i)(v-v_j). \end{aligned}$$

Other parts are computed similarly. We note that if $C^n_{i,j} = u_iv_j$, $C^n_{i+1,j} = u_{i+1}v_j$, $C^n_{i,j+1} = u_iv_{j+1}$ and $C^n_{i+1,j+1} = u_{i+1}v_{j+1}$ then $C^n(u,v) = uv$ for $u_i \le u \le u_{i+1}$, $v_j \le v \le v_{j+1}$. We thus stress that the current interpolation should replace the one in [17].

It is easy to check that a sequence of copulas $\{C^n(u,v)\}_{n=0,1,2,\cdots}$ defined above verify the boundary conditions (1) as well as the 2-increasing condition (2) provided $\lambda \le 1/4$. We also note that in this range of λ, the difference scheme (9) is stable.

Next, we define $D^n(u,v) := C^n(u,v) - uv$. It follows that $\{D^n_{i,j} := C^n_{i,j} - u_iv_j\}_{n=0,1,2,\cdots}$ satisfies the system of difference equations (9) with the null boundary conditions. Thanks to the interpolation above, we infer that

$$\max_{(u,v)\in\boldsymbol{I}^2} |D^n(u,v)| \le K\theta^n, \tag{10}$$

for some constants K, θ with $0<\theta<1$, provided $\lambda < 1/4$. In particular, we have $D^n \to 0$ as $n \to \infty$ uniformly on $\boldsymbol{I}^2$. In summary, we have the next theorem.

Theorem 6. *For any initial copula C_0, there exists a sequence of copulas $\{C^n(u,v)\}_{n=0,1,2,\cdots}$, which satisfy the system of difference equations (9) at every $\{(u_i,v_j)\}_{i.j=0,1,\cdots,N}$. As $n \to \infty$, it follows that*

$$C^n(u,v) \to uv \quad \textit{uniformly on } I^2.$$

The convergence of the population version of Kendall's tau (τ) and the Spearman's rho (ρ) under this discrete processes is also shown. The formulas for τ and ρ utilize the ones for the empirical copulas (see §5.6 of [11]), which are, respectively,

$$\tau = \frac{2N}{N-1}\sum_{i,j=2}^{N}(C^n_{i,j}C^n_{i-1,j-1} - C^n_{i,j-1}C^n_{i-1,j}), \qquad \rho = \frac{12}{N^2-1}\sum_{i,j=1}^{N}(C^n_{i,j} - u_iv_j).$$

The convergence as $n \to \infty$ is then deduced directly.

Theorem 7. *For any initial copula C_0, a sequence of copulas $\{C^n(u,v)\}_{n=0,1,2,\cdots}$ proved in Theorem 6 fulfills*

$$|\tau|, |\rho| \to 0 \quad \text{exponentially as } n \to \infty.$$

Proof. In view of (10) and the uniform bound $\max_{(u,v)\in I^2} |C(u,v)| \leq 1$, we assert that

$$\max_{i,j=0,1,\cdots,N} |C^n_{i,j} - u_i v_j| \to 0$$

exponentially as $n \to \infty$. Taking into account that

$$u_i v_j u_{i-1} v_{j-1} - u_i v_{j-1} u_{i-1} v_j = 0,$$

we see immediately the desired result. □

4. GENERALIZATIONS

It is fortunate that in discrete processes we are able to deal with the evolution of copulas in higher dimensions. We recall the definition of copulas once again in the d-dimensional case.

Definition 8. A function C defined on $I^d := [0,1]^d$ and valued in I is called a copula if the following three conditions are fulfilled.

(i) $C(u_1, u_2, \cdots, u_d)$ is increasing in each component u_i.

(ii) For every $i \in \{1, 2, \cdots, d\}$, $u_i \in I$,

$$C(u_1, \cdots, u_{i-1}, 0, u_{i+1}, \cdots, u_d) = 0, \quad C(1, \cdots, 1, u_i, 1, \cdots, 1) = u_i.$$

(iii) (d-increasing condition) For every $(u_{1i}, u_{2i}, \cdots, u_{di}) \in I^d$ with $u_{1i} \leq u_{2i}$ $(i = 1, 2)$,

$$\sum_{i_1=1}^{2} \cdots \sum_{i_d=1}^{2} (-1)^{i_1+i_2+\cdots+i_d} C(u_{1i_1}, u_{2i_2}, \cdots, u_{di_d}) \geq 0.$$

The Sklar's theorem holds also in this d-dimensional version (see for instance [11]).

Theorem 9. (Sklar's theorem) *Let H be a joint distribution function with marginal distribution functions $F_1, F_2, \cdots, F_d$. Then there exists a copula $C : I^d \to I$, which is uniquely determined on $RanF_1 \times RanF_2 \times \cdots \times RanF_d$, such that, for all $x_i \in [-\infty, \infty]$ $(i = 1, 2, \cdots, d)$,*

$$H(x_1, x_2, \cdots, x_d) = C(F_1(x_1), F_2(x_2), \cdots, F_d(x_d)). \tag{11}$$

Conversely, if C is a copula and $F_1, F_2, \cdots, F_d$ are univariate distribution functions, then the function H defined by (11) is a joint distribution function with margins $F_1, F_2, \cdots, F_d$.

Hereafter we confine ourselves to the 3-dimensional case as an illustration of the idea and for simplicity. The detailed treatment together with the convergence as the mesh size tending to zero will be discussed elsewhere.

As before, let $N \gg 1$ and $0 < h \ll 1$. We put

$$\Delta u = \Delta v = \Delta w := \frac{1}{N}, \quad \Delta t := h, \quad \lambda := \frac{\Delta t}{(\Delta u)^2} = \frac{\Delta t}{(\Delta v)^2} = \frac{\Delta t}{(\Delta w)^2} = hN^2,$$

and

$$u_i := i\Delta u = \frac{i}{N}, \quad v_j := j\Delta v = \frac{j}{N}, \quad w_k := k\Delta w = \frac{k}{N} \quad (j = 0, 1, \cdots, N).$$

A family of copulas $\{C^n(u,v,w)\}_{n=0,1,2,\cdots}$ is defined similarly as in the bivariate case: The initial condition is

$$C^0(u,v,w) := C_0(u,v,w),$$

where C_0 denotes given initial copula.

At $\{(u_i, v_j, w_k)\}_{i,j,k=0,1,\cdots,N}$, the value $C^n_{i,j,k} := C^n(u_i, v_j, w_k)$ should be governed by the system of difference equations

$$\begin{aligned}\frac{C^{n+1}_{i,j,k} - C^n_{i,j,k}}{\Delta t} &= \frac{C^n_{i+1,j,k} - 2C^n_{i,j,k} + C^n_{i-1,j,k}}{(\Delta u)^2} + \frac{C^n_{i,j+1,k} - 2C^n_{i,j,k} + C^n_{i,j-1,k}}{(\Delta v)^2} \\ &\quad + \frac{C^n_{i,j,k+1} - 2C^n_{i,j,k} + C^n_{i,j,k-1}}{(\Delta w)^2} \quad \text{for } i, j.k = 1, 2, \cdots, N-1,\end{aligned} \tag{12}$$

combined with the boundary conditions

$$\begin{cases} C^n_{0,j,k} = C^n_{i,0,k} = C^n_{i,j,0} = 0 \\ C^n_{i,N,N} = u_i, \quad C^n_{N,j,N} = v_j, \quad C^n_{N,N,k} = w_k \end{cases} \quad \text{for } i, j, k = 0, 1, \cdots, N.$$

As to the point $(u, v, w) \in \boldsymbol{I}^3$ other than $\{(u_i, v_j, w_k)\}_{i,j,k=0,1,\dots,N}$, the value $C^n(u, v, w)$ is provided by interpolation. This time it is a little complicated. If for instance

$$u_i \le u \le u_{i+1}, \quad v_j \le v \le v_{j+1}, \quad w_k \le w \le w_{k+1},$$

then we define

$$\begin{aligned} C^n(u,v,w) &:= C^n_{i,j,k} \\ &+ \frac{C^n_{i+1,j,k} - C^n_{i,j,k}}{u_{i+1} - u_i}(u - u_i) + \frac{C^n_{i,j+1,k} - C^n_{i,j,k}}{v_{j+1} - v_j}(v - v_j) + \frac{C^n_{i,j,k+1} - C^n_{i,j,k}}{w_{k+1} - w_k}(w - w_k) \\ &+ \frac{C^n_{i+1,j+1,k} - C^n_{i+1,j,k} - C^n_{i,j+1,k} + C^n_{i,j,k}}{(u_{i+1} - u_i)(v_{j+1} - v_j)}(u - u_i)(v - v_j) \\ &+ \frac{C^n_{i+1,j,k+1} - C^n_{i+1,j,k} - C^n_{i,j,k+1} + C^n_{i,j,k}}{(u_{i+1} - u_i)(w_{k+1} - w_k)}(u - u_i)(w - w_k) \\ &+ \frac{C^n_{i,j+1,k+1} - C^n_{i,j,k+1} - C^n_{i,j+1,k} + C^n_{i,j,k}}{(v_{j+1} - v_j)(w_{k+1} - w_k)}(v - v_j)(w - w_k) \\ + &\frac{C^n_{i+1,j+1,k+1} - C^n_{i+1,j+1,k} - C^n_{i+1,j,k+1} - C^n_{i,j+1,k+1} + C^n_{i+1,j,k} + C^n_{i,j+1,k} + C^n_{i,j,k+1} - C^n_{i,j,k}}{(u_{i+1} - u_i)(v_{j+1} - v_j)(w_{k+1} - w_k)} \cdot \\ &\quad \cdot (u - u_i)(v - v_j)(w - w_k). \end{aligned}$$

Other parts are computed similarly. It is to be noted that the coefficients of the terms involving $u - u_i$, $v - v_j$, $w - w_k$ are all non-negative by virtue of the d-increasing condition.

It is easy to check that a sequence of copulas $\{C^n(u, v, w)\}_{n=0,1,2,\cdots}$ is well defined and the difference scheme is stable provided $\lambda \le 1/6$. The similar result as Theorem 6 holds also true.

Theorem 10. *For any initial copula C_0 of 3-dimension, there exists a sequence of copulas $\{C^n(u, v, w)\}_{n=0,1,2,\cdots}$, which satisfy the system of difference equations (12) at every $\{(u_i, v_j, w_k)\}_{i.j=0,1,\cdots,N}$. As $n \to \infty$, it follows that*

$$C^n(u, v, w) \to uvw \quad \textit{uniformly on } I^3.$$

Here we omit the details of the proof and other properties.

5. Discussions

The copula approach provides a flexible way of designing the description of the dependence structure among random environment. The copula technique is now widely employed in many multivariate risk models; we recall for instance the works of [2][3][4][7]. The book by R.B. Nelsen [11] offers an excellent introduction to this area, and a nice review by H. Tsukahara [14] should be mentioned (see also [15][16]).

The copula theory, however, is principally concerned with the static problems. To the authors' knowledge, the attempt of extending copulas to involve time variable in any sense is that of examples listed in Introduction. Indeed, T. Mikosch [10] casts a doubt about the applicability of the dynamic copula.

On the other hand, we have introduced the notion of the evolution of copulas. The idea is rather easy and we just presume that the copula itself evolves and deforms its structure according to the time-dependent partial differential equation, in our case, the standard heat equation. The existence and the convergence are proved. However, along this evolution every copula converges to the typical product copula; that is, all the nonlinear dependence structure evolves to the independence structure. This is surely not so welcome from the viewpoint of finance. We thus think that the time-reversal version like Theorem 4 may be useful in applications.

The evolution of copulas in discrete setting is another fascinating subject for further investigations; we can treat easily the case of higher dimensions. We return to this issue, possibly with the application to real data, in the future researches.

Acknowledgement. The first author (N.I.) is supported in part by the grant from the Japan Society for the Promotion of Sciences (No.21540117) as well as the research grant (2011) from the Tokio Marine Kagami Memorial Foundation.

References

[1] W.F. Darsow, B. Nguyen, and E.T. Olsen; Copulas and Markov processes, *Illinois J. Math.*, **36** (1992), 600–642.

[2] E.W. Frees and E.A. Valdez; Understanding relationships using copulas, *North American Actuarial J.*, **2** (1998), 1–25.

[3] K. Goda; Statistical modeling of joint probability distribution using copula: Application to peak and permanent displacement seismic demands, *Struct. Safety*, **32** (2010), 112–123.

[4] K. Goda and G.M. Atkinson; Interperiod dependence of ground-motion prediction equations: A copula perspective, *Bull. Seismological Soc. Amer.*, **99** (2009), 922–927.

[5] N. Ishimura and Y. Yoshizawa; On time-dependent bivariate copulas, *Theor. Appl. Mech. Japan*, **59** (2011), 303–307.

[6] N. Ishimura and Y. Yoshizawa; A note on the time evolution of bivariate copulas, to appear in the *Proceedings of FAM2011*, Sofia University.

[7] R. Lebrun and A. Dutfoy; A generalization of the Nataf transformation to distributions with elliptical copula, *Prob. Engineering Mech.*, **24** (2009), 172–178.

[8] D.X. Li; On default correlation: A copula function approach, *J. Fixed Income*, **9** (2000), 43–54.

[9] A.J. McNeil, R. Frey, and P. Embrechts, *Quantitative Risk Management*, Princeton Univ, Press, Princeton, 2005.

[10] T. Mikosch; Copulas: Tales and facts, *Extremes*, **9** (2006), 3–20.

[11] R.B. Nelsen; *An Introduction to Copulas*, 2nd edition, Springer Series in Statistics, Springer, New York, 2006.

[12] A.J. Patton; Modelling asymmetric exchange rate dependence, *International Econ. Review*, **47** (2006), 527–556.

[13] A. Sklar; Random variables, joint distribution functions, and copulas, *Kybernetika*, **9** (1973), 449–460.

[14] H. Tsukahara; Copulas and their applications, *Japanese J. Appl. Statist.*, **32** (2003), 77–88 (in Japanese).
[15] Y. Yoshizawa; Modeling for the enterprise risk management, *Sonpo-Soken Report*, **90** (2009), 1–49 (in Japanese).
[16] Y. Yoshizawa; Risk management of extremal events, *Sonpo-Soken Report*, **92** (2010), 35–90 (in Japanese).
[17] Y. Yoshizawa and N. Ishimura; Time evolution copulas and rank correlation, in the proceedings of *JCOSSAR 2011* (in Japanese).
[18] Y. Yoshizawa and N. Ishimura; Evolution of bivariate copulas in discrete processes, *JSIAM Letters*, **3** (2011), 77–80.

Naoyuki ISHIMURA: Graduate School of Economics, Hitotsubashi University, Kunitachi, Tokyo 186-8601, Japan.
E-mail address: `ishimura@econ.hit-u.ac.jp`

Yasukazu YOSHIZAWA: Graduate School of Economics, Hitotsubashi University, Kunitachi, Tokyo 186-8601, Japan.
E-mail address: `YASUKAZU.YOSHIZAWA@tmnf.jp`

Real Indeterminacy and Conservation Law in Random Matching Models with Divisible Money

Kazuya Kamiya, University of Tokyo

In this paper, I consider matching models with divisible fiat money. It is shown that there always exists a conservation law in the stationarity condition for money holdings distribution in such models and thus real indeterminacy of stationary equilibria arises. Surprisingly it has nothing to do with the other specifications, e.g., the bargaining procedures, of the models. I also introduce a policy which breaks the conservation law.

1 Introduction

Recently, real indeterminacy of stationary equilibria has been found in matching models with divisible fiat money. Kamiya and Shimizu (2006) show that there always exists a conservation law in such models and thus real indeterminacy generically arises. Surprisingly it has nothing to do with the other specifications, e.g., the bargaining procedures, of the models. Kamiya and Shimizu (2007) also present a way to break the conservation law, and to induce an efficient equilibrium. The purpose of this paper is to give a unified approach to the above two results.

A sketch of the idea is as follows. Suppose the nominal stock of money is given. When the price level is lower, there is more liquidity in the economy, the trade is more frequent, and therefore the welfare level is higher. When the price level is higher, there is less liquidity in the economy, the trade is less frequent, and therefore the welfare level is lower. If the corresponding equilibrium values of the other variables can be found, such as the money holdings distribution and the value function, as the price level continuously varies, then the real indeterminacy follows. More precisely, if the number of variables is larger than that of equations, then by applying the implicit function theorem this property holds. I can show that the stationary condition of money holdings has a conservation law and thus there is at least one more variable than the number of equations. Thus the stationary equilibria in such models are indeterminate.

In this paper, I consider the case of one fiat money. Suppose it is divisible and there is an upper bound of its holdings. I focus on the stationary equilibria in which, for some positive number p, all trades occur with its integer multiple amounts of money. I focus on stationary distributions on $\{0, \ldots, N\}$ expressed by $h = (h(0), \ldots, h(N))$, where $h(n)$ is the measure of the set of agents with np amount of money, and $N < \infty$ is the upper bound. The condition for stationarity of money holdings is $O_n = I_n$, $n = 0, 1, \ldots, N$, and $\sum_{n=0}^{N} h(n) = 1$, where O_n (I_n) is the outflow (inflow resp.) at n. Since $\sum_{n=0}^{N} O_n = \sum_{n=0}^{N} I_n$ always holds, then, at first glance, there seem to be $(N + 1)$ independent equations. Thus it seems that the numbers of independent equations and variables, $h(n), n = 0, \ldots, N$, are the same. However, it can be shown that one more equation is always redundant and that the system of equations has always at least one degree of freedom; namely, $\sum_{n=0}^{N} nO_n = \sum_{n=0}^{N} nI_n$, a conservation law, always holds. This fact is the key to the real indeterminacy of stationary equilibria.

I also show that a tax-subsidy policy can break the identity, and induce an efficient equilibrium. The identity means that the total money holding are the same before and after trades. Thus the government can break the identity by absorbing and discarding money by using tax and subsidy.

The plan of this paper is as follows. In the next section, I present a general model and discuss the case without tax-subsidy policies. Section 3 is devoted the case with the policy.

2 The Model

I first present a general model, where the private sector is a special case of Kamiya and Shimizu (2006). Hereafter, I call it KS1 simply.

There is a continuum of private agents with a mass of measure one. There are $k \geq 3$ types of agents with equal fractions and the same number of types of goods. Let κ be the reciprocal of k. A type i good is produced by a type $i - 1$ agent. A type i agent obtains some positive utility only when she consumes type i good. I make no assumption on the divisibility of goods. I assume that fiat money is durable and perfectly divisible. Time is continuous, and pairwise random matchings take place according to Poisson process with parameter $\mu > 0$.

I focus on the case that, for some positive number p, all trades occur with its integer multiple amounts of money. In what follows, I focus on a stationary distribution of economy-wide money holdings on $\{0, \ldots, N\}$ expressed by $h = (h_0, \ldots, h_N)$, where h_n is the measure of agents with np amount of money, and $N < \infty$ is the upper bound of the distribution. For simplicity, I assume that N is exogenously given. I also focus on the case of $h_n \geq 0$ and $\sum_{n=0}^{N} h_n = 1$. Let $M > 0$ be a given nominal stock of money circulating in the private sector. Since p is uniquely determined by $\sum_{n=0}^{N} pnh_n = M$ for a given h for $h_0 \neq 1$, then, deleting p from $\{0, p, \ldots, Np\}$, the set $\{0, \ldots, N\}$ can be considered as the state space.

Since I adopt a general framework, various types of bargaining procedures are allowed.[1] An agent with n, or an agent with np amount of money, chooses an action in $A_n = \{a_{n1}, \ldots, a_{ns_n}\}$. Let $A = \Pi_{n=0}^{N} A_n$. For simplicity, I focus on the stationary equilibrium in which all agents choose pure strategies. Let $S = \sum_{n=0}^{N} s_n$. Given an equilibrium action profile $a = (a_0, \ldots, a_N)$, where a_n is the action taken at np in the equilibrium, define $\alpha(a) = \{(n, j) \mid a_n = a_{nj}\}$.

The monetary transition resulted from transaction among a matched pair is described by a function f. When an agent with money holdings np and action a_{nj} meets an agent with $n'p$ and $a_{n'j'}$, the former's and the latter's states, i.e., money holdings, will be $n + f(n, j; n', j')$ and $n' - f(n, j; n', j')$, respectively. That is, f maps an ordered pair $(n, j; n', j')$ to a non-negative integer $f(n, j; n', j')$. Here "ordered" means, for example, that the former is a seller and the latter is a buyer. When N is exogenously determined, I assume

$$N \geq n + f(n, j; n', j') \quad \text{and} \quad n' - f(n, j; n', j') \geq 0.$$

Next, I introduce government agents following Aiyagari and Wallace (1997). They follow a rule which prescribes them how to collect tax from or give subsidy to the agents they are matched with. I assume that government agents can observe current money holdings of agents they are matched with. Let $G > 0$ be the measure of the government agents. Thus the total measure of agents is $1 + G$. Note that in the following arguments G can be any small positive number.

Then I describe government's policy by $(t_0, t_1, \ldots, t_N)$, where $t_n \in [-1, 1]$, $t_0 \geq 0$, and $t_N \leq 0$. Each government agent gives subsidy p to the matched agent with n with probability $|t_n|$ when $t_n > 0$, while she collects tax p with probability $|t_n|$ when $t_n < 0$. As seen in the previous section,

---

[1] See Remark 1 for the details.

the budget of the government may not be balanced out of equilibria.

Let $\theta \in \mathbb{R}^L$ be the parameters of the model besides t. Note that θ includes k, μ, and G.

Below, I adopt dynamic programming approach. Let V_n be the value of state n, $n = 0, \ldots, N$. The variables in the model are denoted by $x = (h, V, a)$. Let $W_{nj}(x; \theta, t)$ be the value of action j at state n. Thus, in equilibria, $W_{nj}(x; \theta, t) = V_n$ holds for $(n, j) \in \alpha(a)$. Note that $W_{nj}(x; \theta, t)$ includes the utility and/or the production cost of perishable goods.

2.1 Stationary Equilibria without Tax-Subsidy

First, I consider the case that $t_n = 0$ for all n.

Define

$$h_{nj} = \begin{cases} h_n & \text{if } a_{nj} = a_n, \\ 0 & \text{if } a_{nj} \neq a_n. \end{cases}$$

Then by the random matching assumption and the definition of f, the inflow I_n into state n and the outflow O_n from state n are defined as follows:

$$I_n(h, a; \theta) = \frac{\mu\kappa}{1+G}\left[\sum_{(i,j,i',j') \in X_n} h_{ij} h_{i'j'} + \sum_{(i,j,i',j') \in X'_n} h_{ij} h_{i'j'}\right],$$

$$O_n(h, a; \theta) = \frac{\mu\kappa}{1+G}\left[\sum_{(j,i',j') \in Y_n} h_{nj} h_{i'j'} + \sum_{(j,i',j') \in Y'_n} h_{nj} h_{i'j'}\right],$$

where

$$X_n = \{(i,j,i',j') \mid f(i,j;i',j') > 0,\ i + f(i,j;i',j') = n\},$$

$$X'_n = \{(i,j,i',j') \mid f(i,j,i',j') > 0,\ i' - f(i,j;i',j') = n\},$$

$$Y_n = \{(j,i',j') \mid f(n,j;i',j') > 0\},$$

$$Y'_n = \{(j,i',j') \mid f(i',j';n,j) > 0\}.$$

I denote $I_n - O_n$ by D_n. Then the condition for stationarity is $D_n = 0$ for $n = 0, \ldots, N$ and $\sum_{n=0}^{N} h_n = 1$. Clearly, $\sum_{n=0}^{N} D_n = 0$ holds as an identity, and thus at least one equation is redundant. Moreover, the following theorem prunes the above conditions of another redundant equation other than this.

Theorem 1 (Kamiya and Shimizu (2006)) For any a,

$$\sum_{n=0}^{N} nD_n(h, a; \theta) = 0, \tag{1}$$

is an identity.

The identity can be considered as a conservation law. The economic interpretation of the law is as follows. Suppose that two agents, say a buyer and a seller, meet and a monetary trade occurs. Then the amount of money the buyer pays is equal to that of the seller obtains; in other words, the sum of their money holdings before trade is equal to that after trade. Since this holds in each trade, the total amount of money before trades, expressed by $\sum_{n=0}^{N} pnO_n(h, a; \theta)$, is equal to the total amount of money after trades, expressed by $\sum_{n=0}^{N} pnI_n(h, a; \theta)$, and thus $\sum_{n=0}^{N} nD_n(h, a; \theta) = 0$ always holds.

Together with the other identity $\sum_{n=0}^{N} D_n(h, a; \theta) = 0$, the above theorem implies that h is a stationary distribution if and only if $D_n(h, a; \theta) = 0, n = 2, \ldots, N$, and $\sum_{n=0}^{N} h_n = 1$ hold. Namely, the condition for stationarity has at least one-degree of freedom. This is the main cause of the indeterminacy.

Now the equilibrium condition is expressed as follows:

Definition 1 Given θ, $x = (h, V, a) \in \mathbb{R}^{N+1} \times \mathbb{R}_{+}^{N+1} \times A$ is a (pure strategy) *stationary equilibrium without tax-subsidy* if it satisfies the following:

$$\begin{aligned} D_n(h, a; \theta) &= 0, && n = 2, \ldots, N \\ \sum_{n=0}^{N} h_n - 1 &= 0, && \\ V_n - W_{nj}(x; \theta, 0) &= 0, && (n, j) \in \alpha(a) \\ V_n - W_{nj}(x; \theta, 0) &\geq 0, && (n, j) \notin \alpha(a). \end{aligned} \tag{2}$$

(h, V) is called a stationary equilibrium for a and θ if (h, V, a) is a stationary equilibrium for θ. Let E_{θ}^{a} be the set of such (h, V)s, and $g^a : \mathbb{R}_{+}^{N+1} \times \mathbb{R}^{N+1} \times \mathbb{R}^{L} (\ni (h, V, \theta)) \to \mathbb{R}^{N-1} \times \mathbb{R} \times \mathbb{R}^{N+1} \times \mathbb{R}^{S-N-1}$ be the LHS of the above condition.

Remark 1 In addition to the above equilibrium conditions, the following conditions are typically required: (i) the existence of $p > 0$ satisfying $\sum_{n=0}^{N} pnh_n = M$, (ii) the incentive not to choose an action out of the action space, and (iii) the incentive to take the equilibrium strategy at state $\eta \notin \{0, p, \ldots, Np\}$. However, they are not very restrictive. As for (i), it immediately follows from $h_0 \neq 1$. As for (ii) and (iii), KS1 presents a sufficient condition to assure that (ii) and (iii) hold, and it is satisfied in all of the matching models with divisible money known so far, such as Zhou (1999)'s model, a divisible money version of Camera and Corbae (1999)'s model, and a divisible money version of Trejos and Wright (1995)'s model.

Let

$$C^a = \underbrace{\{0\} \times \cdots \times \{0\}}_{2N+1} \times \underbrace{\mathbb{R}_{++} \times \cdots \times \mathbb{R}_{++}}_{S-N-1},$$

and, for $(n, j) \notin \alpha(a)$,

$$C^{a(n,j)} = \underbrace{\{0\} \times \cdots \times \{0\}}_{2N+1} \times \underbrace{\mathbb{R}_{++} \times \cdots \times \mathbb{R}_{++} \times \{0\} \times \mathbb{R}_{++} \times \cdots \times \mathbb{R}_{++}}_{S-N-1},$$

where the last $\{0\}$ corresponds to $V_n - W_{nj}(x; \theta, 0)$. Moreover, for $(n, j), (n', j') \notin \alpha(a)$,

$$C^{a(n,j)(n',j')} = \underbrace{\{0\} \times \cdots \times \{0\}}_{2N+1} \times \underbrace{\mathbb{R} \times \cdots \times \mathbb{R} \times \{0\} \times \mathbb{R} \times \cdots \times \mathbb{R} \times \{0\} \times \mathbb{R} \times \cdots \times \mathbb{R}}_{S-N-1},$$

where the last two $\{0\}$s correspond to $V_n - W_{nj}(x; \theta, 0)$ and $V_n - W_{n'j'}(x; \theta, 0)$, respectively. Below, it is verified that there is the indeterminacy of the stationary equilibrium under some regularity conditions.

Assumption 1 Given a, g^a is of class C^2 and is transversal to C^a, $C^{a(n,j)}$, and $C^{a(n,j)(n',j')}$ for all $(n, j) \notin \alpha(a)$ and $(n', j') \notin \alpha(a)$.[2]

Assumption 2 Given a, there exists a C^2-manifold without boundary, $\Theta \subset \mathbb{R}^L$, such that $E^a_\theta \neq \emptyset$ holds for all $\theta \in \Theta$.

Theorem 2 (Kamiya and Shimizu (2006)) For a given a, suppose Assumptions 1 and 2 are satisfied for some Θ. Then, for almost every $\theta \in \Theta$, E^a_θ is a one-dimensional manifold with

---

[2] This assumption implies that that $D_n = 0, n = 2, \ldots, N$, are linearly independent in stationary equilibria. See KS1 for indeterminacy results of the other cases.

boundary. Moreover, at any endpoint of the manifold, only one $V_n - W_{nj}(x;\theta,0) \geq 0$, $(n,j) \notin \alpha(a)$, is binding, and at points in the relative interior of the manifold, no inequality is binding.

KS1 also shows that this indeterminacy is real. That is, the welfare are typically not the same in a connected component of the equilibrium manifold.

2.2 Stationary Equilibria with Tax-Subsidy

In this section, I investigate the case of $t \neq (0,\dots,0)$. In what follows, variables and functions with "tilde" denote the ones with nonzero t. The inflow at n, $\tilde{I}_n$, and the outflow at n, $\tilde{O}_n$, are defined as follows:

$$\begin{aligned}
\tilde{I}_n(\tilde{h},a;\theta,t) &= I_n(\tilde{h},a;\theta) + \frac{\mu G}{1+G}\left(t^+_{n-1}\tilde{h}_{n-1} + t^-_{n+1}\tilde{h}_{n+1}\right), \\
\tilde{O}_n(\tilde{h},a;\theta,t) &= O_n(\tilde{h},a;\theta) + \frac{\mu G}{1+G}|t_n|\tilde{h}_n,
\end{aligned}$$

where $t^+_n = \max\{0,t_n\}$, $t^-_n = -\min\{0,t_n\}$, and $t_{-1} = t_{N+1} = 0$. Let $\tilde{D}_n(\tilde{h},a;\theta,t) = \tilde{I}_n(\tilde{h},a;\theta,t) - \tilde{O}_n(\tilde{h},a;\theta,t)$.

Since $\sum_{n=0}^{N} n\tilde{D}_n$ is not identically zero, then I define a stationary equilibrium with tax-subsidy as follows. In other words, the tax-subsidy breaks the conservation law.

Definition 2 Given θ, $\tilde{x} = (\tilde{h},\tilde{V},a) \in \mathbb{R}^{N+1}\times\mathbb{R}^{N+1}_{+}\times A$ is a (pure strategy) *stationary equilibrium with tax-subsidy scheme* t if it satisfies the following:

$$\begin{aligned}
\tilde{D}_n(\tilde{h},a;\theta,t) &= 0, && n = 1,\dots,N \\
\sum_{n=0}^{N}\tilde{h}_n - 1 &= 0, && \\
\tilde{V}_n - W_{nj}(\tilde{x};\theta,t) &= 0, && (n,j) \in \alpha(a) \\
\tilde{V}_n - W_{nj}(\tilde{x};\theta,t) &\geq 0, && (n,j) \notin \alpha(a). \qquad (3)
\end{aligned}$$

Theorem 3 (Kamiya and Shimizu (2007)) Given a, consider the following system of the stationary condition:

$$(\tilde{D}_1,\dots,\tilde{D}_N,\sum_{n=0}^{N}\tilde{h}_n - 1)^T = (0,\dots,0)^T,$$

where T denotes transpose. If the Jacobian matrix with respect to $\tilde{h}$ of the LHS of the above system is of full rank at a stationary distribution, then the stationary distribution is locally determinate. Moreover, the budget is balanced on this stationary distribution.

Next, I discuss the existence of a locally determinate stationary equilibrium which has the following property; it is induced by a certain tax-subsidy scheme, and it exists in any given neighborhood of the stationary equilibrium which is not induced by tax-subsidy. I choose an arbitrary stationary equilibrium without tax-subsidy, denoted by $x^* = (h^*, V^*, a^*)$, which is in the relative interior of the equilibrium manifold. Thus, by Theorem 2, (2) is satisfied with strict inequalities.

First, the following vector can be found:

Lemma 1 There exists an $(N+1)$-dimensional vector τ satisfying
(a) $\tau \neq (0, \ldots, 0)$,
(b) $\left(\frac{\partial D_n(h^*, a^*; \theta)}{\partial h_i}\right)_{i=0,\ldots,N} \cdot \tau = 0$ for $n = 2, \ldots, N$,
(c) $h^* \cdot \tau = 0$.

The above lemma clearly holds, since (b) and (c) have at least one-degree of freedom.

Using this vector, a tax-subsidy scheme $t = \epsilon\tau$ is constructed. Here $\epsilon > 0$ is the size of the policy. For such a t to be a tax-subsidy scheme, I need the following assumption:

Assumption 3 It is also satisfied for τ in Lemma 1 that
(d) $\tau_N \leq 0$, and
(e) $\tau_0 \geq 0$.

Next, I make the following assumption.

Assumption 4 W_{nj} is C^2 with respect to ϵ for any (n, j).

Under the above conditions and assumptions, the government can approximately induce any stationary equilibrium.

Theorem 4 Suppose Assumptions 1, 2, 3, and 4 hold. Then, for almost every $\theta \in \Theta$, almost every $(h^*, V^*) \in E_\theta^{a^*}$, and any δ-neighborhood of (h^*, V^*), there exists a tax-subsidy scheme such that a stationary equilibrium with tax-subsidy is locally determinate and lies in the neighborhood.

References

Aiyagari, S. R. and N. Wallace, "Government Transaction Policy, the Medium of Exchange, and Welfare," *Journal of Economic Theory* 74 (1997), 1-18.

Camera, G. and D. Corbae, "Money and Price Dispersion," *International Economic Review* 40 (1999), 985-1008.

Green, E. J. and R. Zhou, "A Rudimentary Random-Matching Model with Divisible Money and Prices," *Journal of Economic Theory* 81 (1998), 252-271.

Kamiya, K. and T. Shimizu, "Real Indeterminacy of Stationary Equilibria in Matching Models with Divisible Money," *Journal of Mathematical Economics*, 42 (2006), pp. 594-617.

Kamiya, K. and T. Shimizu, "On the Role of Tax-Subsidy Scheme in Money Search Models," *International Economic Review*, 48 (2007), pp. 575-606.

Trejos, A. and R. Wright, "Search, Bargaining, Money, and Prices," *Journal of Political Economy* 103 (1995), 118-141.

Zhou, R., "Individual and Aggregate Real Balances in a Random-Matching Model,"*International Economic Review* 40 (1999), 1009-1038.

Joint Research Workshop of Institute of Mathematics for Industry, Kyushu University &
MEXT Collaborative Workshop of Mathematics and Mathematical Sciences with Various Sciences and Industrial Technologies
“Multiscale Mathematics: Hierarchy of Collective Phenomena and Interrelations between Hierarchical Structures”
December 9 (Fri) – 11 (Sun), 2011, Ito Campus, Kyushu University, Japan
http://www.imi.kyushu-u.ac.jp/eng/events/view/358

On fundamental of Rayleigh-Taylor turbulent mixing: correlations and fluctuations in statistically unsteady turbulent processes

S.I. Abarzhi
The University of Chicago, Chicago, IL, USA
Email: snezha@uchicago.edu

Content

III. Correlations and fluctuations in turbulent processes.

Abstract

We present the physics-based theoretical analysis of the mechanisms and the properties of Rayleigh-Taylor turbulent mixing, and focus on the consideration of correlations and fluctuations of the statistically unsteady turbulent mixing dynamics. The analysis extends to non-canonical circumstances the ideas of Kolmogorov theory on symmetries of turbulent dynamics, accounts for the essentially multi-scale character of the flow evolution, and identifies the transport of momentum as a better indicator of turbulent mixing dynamics than the transport of energy. The invariance of the rate of momentum loss leads to essentially non-Kolmogorov invariant, scaling and spectral properties of turbulent mixing flow. Rayleigh-Taylor turbulent mixing exhibits more order compared to isotropic turbulence. Its viscous and dissipation scales are finite and set by the flow acceleration. We discuss the outcomes of theoretical results for practical applications and for the methods of flow mitigation and control.

Keywords

Turbulent mixing, Rayleigh-Taylor instability, invariants and scaling and symmetries, statistically unsteady process, stochastic modeling

I. Introduction

Turbulence is common to consider as the last unresolved problem of classical physics [1-16]. For years its complexity and universality assisted engineers and practitioners, nourished enthusiasm of scientists, and fascinated mathematicians [1-16]. Similarity and isotropy are fundamental hypotheses that advanced our understanding of turbulent processes. Still the problem withstands the efforts applied thus indicating a need in new concepts to better control the irregular dynamics [3,4]. Turbulent motions of realistic fluids are often characterized by non-equilibrium heat transport, sharp changes of density and pressure, and may be a subject to spatially varying and time-dependent acceleration and rotation [1-16]. Turbulent mixing induced by the Rayleigh-Taylor instability (RTI) is generic problem, which we encounter when trying to extend our knowledge of turbulent processes beyond the limit of idealized consideration [3,4].

Rayleigh-Taylor (RT) turbulent mixing is an extensive interfacial mixing process which develops when fluids of different densities are accelerated against a density gradient [1,2]. It governs a broad variety of natural phenomena spanning macroscopic to atomistic scales and high to low energy density regimes, and plays an important role in technological applications in aerodynamics and aeronautics [5-13]. Examples include instabilities of plasmas, light-material interaction, material transformation under high strain rate, atmospheric flows, shock-turbulence interaction, non-canonical wall-bounded flows, scramjet combustors, liquid atomization and free-space optical telecommunications [5-13]. Rayleigh-Taylor mixing is a multi-scale, heterogeneous, anisotropic and statistically unsteady turbulent process with non-local interactions among the many scales [3,4]. Its development is usually associated with the conditions of strong gradients of pressure and density and may also include spatially varying and time-dependent acceleration, diffusion of species, heat release, and chemical reactions [17-28,29-39]. These conditions depart from those under which canonical Kolmogorov turbulence is expected to occur [14-16,40]. Capturing the properties of Rayleigh-Taylor mixing can enable a better understanding of realistic turbulent flows and can further improve the methods of their mitigation and control [40]. Here we discuss the influence of momentum transport on fundamental properties of turbulent mixing, and outline some new ideas that may help to better control the mixing process in the applications [5-13].

Arising in a variety of diverse circumstances, RT flows exhibit some similar features of their evolution [3,4]. The mixing starts to develop when the fluid interface is slightly perturbed near its equilibrium state. The flow transitions from an initial stage, where the perturbation amplitude grows relatively quickly [e.g. exponentially in time, if the fluids are incompressible and immiscible and are to sustained acceleration or gravity $\mathbf{g}$], to a nonlinear stage, where the growth-rate slows and the interface is transformed into a composition of a large-scale coherent structure and small-scale irregular structures driven by shear, and then finally to a stage of turbulent mixing, whose dynamics is believed to be self-similar [41-58].

The large-scale coherent structure in RT flows is a periodic array of bubbles and spikes, with light (heavy) fluid with density $\rho_{l(h)}$ penetrating the heavy (light) fluid in bubbles (spikes) [3,4]. The dynamics of the structure is governed by two, in general independent, length scales: the amplitude $\tilde{h}$ in the direction of gravity and the spatial period λ in the normal plane [3,4,59-62]. The horizontal scale λ is set by the mode of fastest-growth or by the initial conditions [3,4]. It may increase, if the flow is two-dimensional and the initial perturbation is broad-band and incoherent [43-49]. The vertical scale $\tilde{h}$ grows as power-law with time, and it is believed that in the mixing regime $\tilde{h} \sim gt^2$, $|\mathbf{g}| = g$ [41-58]. This scale can be regarded as an integral scale, which represents cumulative contributions of small-scale structures in the flow dynamics [3,4,59-62]. The small-scale vortical structures are produced by the Kelvin Helmholtz instabilities at the fluid interface [17-39]. In miscible fluids, the small-scale structures diffuse from the interface into the bulk, and the mixing process is slowing down. Some other features are induced in the dynamics by compressibility, high energy density conditions and non-uniform acceleration [5-13].

To quantify RT mixing flow the observations were focused on diagnostics of the coarsest scales $\tilde{h}$ and ascertainment of dependency $\tilde{h} = \alpha A g t^2$ where α is a constant and $A = (\rho_h - \rho_l)/(\rho_h + \rho_l)$ is the Atwood number [17-39]. RT dynamics was characterized by period λ, and growth of this scale with $\lambda \sim \tilde{h} \sim gt^2$ was suggested as a primary mechanism of the mixing development [43-49]. To account for the time-dependence of the integral scale $\tilde{h} \sim gt^2$ and interpret experimental and numerical data in RTI in terms of turbulent power-laws, some modifications were applied to Kolmogorov theory, including an introduction of a virtual origin and a time-scale for transition to turbulence, a substitution of time-dependencies in Kolmogorov invariants, and a description of RTI by analogy with passive scalar mixing [50-57]. Some quantitative agreements were found between the observations data that spanned relatively short dynamic range and the models that used adjustable parameters [43-57]. Some qualitative features of the turbulent process still remain unclear, e.g. a relatively ordered character of RT flow at high Reynolds numbers [56]. To date, experiments and simulations did not provide a trustworthy guidance on whether the concepts of classical turbulence are applicable to an accelerating RT flow and whether the scaling $\tilde{h}/gt^2$ and λ/gt^2 are indeed universal.

We refer the reader to recent reviews [3,4,28,40] for a detailed discussion of the state of the art in theoretical, experimental, numerical and computational studies of Rayleigh-Taylor flows. This paper presents the physics-based analysis of the mechanisms and the properties of RT mixing suggested by the studies [3,4,59-62] and focuses on the consideration of correlations and fluctuations of the statistically unsteady turbulent dynamics. We extend to non-canonical circumstances of unsteady turbulent mixing the ideas of Kolmogorov theory [14-16] on symmetries of turbulent dynamics. Our consideration accounts for the essentially multi-scale character of RT evolution, and identifies the transport of momentum as a better indicator of RT mixing flow than the transport of energy [3,4,59-62]. The invariance of the rate of momentum loss leads to essentially non-Kolmogorov invariant, scaling and spectral properties of the turbulent mixing. The RT mixing exhibits more order compared to isotropic turbulence. Its viscous and dissipation scales are finite and set by the flow acceleration [3,59-62]. We discuss the outcomes of theoretical results for practical applications and for the methods of flow mitigation and control.

II. Mechanisms, symmetries, and invariants measures of turbulent processes.

As in any natural process, turbulent transports are governed by the conservations principles [14]. The conservations of mass and momentum have the form

$$\dot{\rho} + \nabla \cdot \rho \mathbf{V} = 0\,, \qquad \rho\left(\dot{\mathbf{V}} + (\mathbf{V} \cdot \nabla)\mathbf{V} - \mathbf{g}\right) + \nabla p + \mathbf{S} = 0\,, \tag{1}$$

where ρ, $\mathbf{V}$ and p are the fluid density, velocity and pressure, $\mathbf{S}$ denotes terms induced by viscous stress and other effects, and dot marks the partial derivative in time t. In RT flow the fluid interface is a discontinuity, and equations (1) yield also the boundary conditions at the interface which balance the transports of mass, momentum and energy of the fluids [14]. The system is spatially extended and has no mass sources.

2.1 Symmetries of turbulent processes.

A cornerstone of Kolmogorov theory is that the isotropic and homogeneous turbulent flow has a number of symmetries in statistical sense [15]. Indeed, for a homogeneous fluid with $\rho = const$, with neglected effects of gravity, viscous stress and other terms, $\mathbf{g} = \mathbf{S} = 0$, and asymptotically in time, system (1) describes canonical turbulent flow [15] that is invariant to Galilean transformation, to temporal translations, and to spatial translations, and spatial inversions and rotations. It is also scale-invariant with $L \to LK$, $t \to tK^{1-n}$ and $V \to VK^n$ for any n, where

$V = |\mathbf{V}|$, and L is a characteristic length scale [14-16]. Kolmogorov [15] found that for isotropic homogeneous turbulence $n = 1/3$, and that the measure of the scaling symmetry is the rate of change of specific kinetic energy $\varepsilon \sim V^3/L$. Later it was shown that the arbitrariness of n reflects in turbulence multi-scaling and intermittency, see Refs [16,63-67] and references therein.

Similarly to Kolmogorov turbulence, Rayleigh-Taylor turbulent mixing has a number of symmetries [3,4,59-61]. Due to the presence of gravity, $\mathbf{g} \neq 0$, and non-inertial character of the dynamics, these symmetries are distinct from those of Kolmogorov turbulence. Rayleigh-Taylor mixing flow is invariant with respect to translations, inversions and rotations in the plane normal to $\mathbf{g}$, and to scaling transformation $L \to LK$, $t \to tK^{1-n}$ and $v \to vK^n$ with $n = 1/2$. The measure of this scaling symmetry v^2/L has the same dimension as g and quantifies the rate of change of specific momentum, Table 1.

Table 1: Symmetries of turbulent processes

Kolmogorov turbulence	Kolmogorov turbulence is inertial and is invariant with respect to Galilean transformation, translations in time and 3D space, and spatial rotations and inversions. It is scale-invariant, $L \to LK$, $T \to TK^{1-n}$, $v \to vK^n$ with $n = 1/3$.
RT turbulent mixing	Rayleigh-Taylor turbulent mixing is non-inertial and is invariant with respect to translation, rotations and inversions in the plane normal to gravity $\mathbf{g}$. It is scale invariant, $L \to LK$, $T \to TK^{1-n}$, $v \to vK^n$ with $n = 1/2$.

2.2 Momentum-based consideration of turbulent mixing.

In RT mixing flow, the specific momentum is gained due to buoyancy and is lost due to dissipation. The dynamics of a parcel of fluid is governed by a balance per unit mass of the rate of momentum gain $\tilde{\mu}$ and the rate of momentum loss μ as

$$\dot{h} = v, \qquad \dot{v} = \tilde{\mu} - \mu \tag{2}$$

Here h is the vertical length scale, e.g. position of the center of mass of the fluid parcel, v is the corresponding velocity, and $\tilde{\mu}$ and μ are the absolute values of vectors pointed in opposite directions along the gravity $\mathbf{g}$ [3,4,59-62]. Eqs. (2) represent in a simplified dimensional-grounds-based form the conservation of mass and momentum (1).

The rate of momentum gain is the rate of change of specific momentum which can be gained due to buoyancy (e.g. the specific buoyant force), and $\tilde{\mu} = \tilde{\varepsilon}/v$, where $\tilde{\varepsilon}$ is the rate of energy gain (e.g. the rate of change of specific potential energy). The value $\tilde{\mu} = g\, f(A)$ with $f(A)$ being a function on the Atwood number, and it is rescaled hereafter as $g\, f(A) \to g$. The rate of momentum loss is the rate of change of specific momentum which is lost due to dissipation, and $\mu = \varepsilon/v$, where ε is the rate of change of specific kinetic energy. In the limit of vanishing viscosity on the basis of dimensional grounds $\varepsilon = C v^3/L$, where L is the characteristic length scale and $C = const$ [3,59-

62]. The ratio between $\tilde{\mu}, \tilde{\varepsilon}$ as well as μ, ε are the standard relations between the (specific) power and force [14].

As discussed in [59], asymptotic solutions for model (2) depend on whether the characteristic length scale of the flow is horizontal or vertical. If the characteristic length scale is horizontal, $L \sim \lambda$, then Eqs. (2) has steady solution with $v \sim \sqrt{g\lambda}$ and $h \sim t\sqrt{g\lambda}$, and the rates of momentum and energy are balanced: $\tilde{\mu} = \mu = g$ and $\tilde{\varepsilon} = \varepsilon = (g\lambda)^{3/2} / \lambda\sqrt{C}$. If the characteristic scale is vertical, $L \sim h$, then asymptotically in time, $h = a\,gt^2/2$ and $v = a\,gt$ with $a = (1+2C)^{-1}$. The rates of energy gain and dissipation are time-dependent, $\tilde{\varepsilon} = a\,g^2 t$ and $\varepsilon = (1-a)a\,g^2 t$, and the rates of momentum gain and loss are time- and scale-invariant, $\tilde{\mu} = g$ and $\mu = C v^2/h$ [59-62]. As found in many observations, the values of a are rather small, $a \sim 0.05 - 0.15$ [17-39]. Thus, in the mixing flow almost all energy induced by the buoyancy dissipates, $\tilde{\varepsilon} \approx \varepsilon$ with $\varepsilon/\tilde{\varepsilon} = (1-a)$, and the rates of momentum gain and loss slightly imbalance one another, $\tilde{\mu} \approx \mu$ with $(\tilde{\mu} - \mu)/\tilde{\mu} = a$. Self-similar mixing may develop when horizontal scale λ grows with time as $\lambda \sim h \sim gt^2$ [43-49], and when the vertical scale h, $h \sim \tilde{h}$, is the characteristic scale for energy dissipation that occur in the small-scale structures at the fluid interface [3,59-62].

2.3 Mechanisms of development of RT mixing.

Agreeing in certain limiting cases with principal results of the heuristic models [41-57], momentum consideration (2) identifies some new properties of the mixing flow [59-62]. It suggests that the accelerated turbulent mixing develops due the imbalance of gain and loss of specific momentum, $\mu \neq \tilde{\mu}$. This imbalance may occur when (i) the horizontal scale grows as $\lambda \sim gt^2$, and/or when (ii) the vertical scale h is a characteristic scale for energy dissipation, $\varepsilon = C v^3/L$ with $L \sim h$, and when it represents cumulative contributions of small-scale structures into the flow dynamics. Existence of two distinct mechanisms of the mixing development reconciles with one another the models [41-59]. It also agrees with results of theoretical studies [4], which found that the amplitude $\tilde{h}$ and period λ provide independent contributions to the nonlinear RT dynamics and that for highly coherent large-scale coherent structures the growth of horizontal scales may not occur.

2.4 Energy budget, transports of energy and momentum, position of the center of mass.

Turbulence is a property of dissipative systems and it decays unless it is driven [14-16,63-67]. Kolmogorov turbulence is driven by an external energy source, which supplies energy to the flow at a constant rate ε: Energy is injected at large scales by an external source, and then it is transferred without loss through the inertial interval and dissipates at small scales [14-16,63-67]. According to the momentum consideration [3,59-62], for Rayleigh-Taylor turbulent mixing an external energy source (other than gravity) is not required, and the specific momentum is gained due to buoyancy and is lost due to dissipation. In accelerated flow at any scale $\mu \neq \tilde{\mu}$ and $\varepsilon \neq \tilde{\varepsilon}$, and this imbalance indicates that the mean velocity of the center of mass of the fluid entrained in the motion is time-dependent, whereas in statistically steady turbulent flow it is invariable, Table 2.

Table 2: Energy source, transports of momentum and energy, center of mass position in the turbulent processes

Kolmogorov turbulence	Energy is injected at large scales by an external source, and is transferred without losses through the inertial interval and dissipates at small scales. Mean velocity of the center of mass of the fluid system is time-independent.
RT turbulent mixing	There is no external energy source other than gravity. Energy and momentum are gained due to buoyancy and are lost due to dissipation. In steady regime $\mu-\tilde{\mu}=0$ and $\varepsilon=\tilde{\varepsilon}=(g\lambda)^{3/2}/\lambda\sqrt{C}$. Accelerated turbulent mixing is driven by imbalance between the gain and loss of specific momentum, and at any scale $\mu\neq\tilde{\mu}$ and $\varepsilon\neq\tilde{\varepsilon}$. In accelerated mixing, the mean velocity of the center of mass of the fluid system is time-dependent.

2.5 Asymptotic states of turbulent processes in space and in time.

Statistically steady Kolmogorov turbulence is an asymptotic in time state, which is achieved when the memory of the initial conditions is completely lost, and when the boundaries of the outside domain do not influence the dynamics [15,63-67]. These conditions can be realized in a spatially extended system or in a finite-size domain, when the span of scales runs several decades from viscous to integral scale [15]. Implementation of these conditions in Rayleigh-Taylor turbulent mixing requires special attention [28]. In a finite-size domain, an asymptotic in time dynamics corresponds to a stable state with no motion at all: under the influence of gravity (directed from the top to the bottom) the system transits from an unstable configuration to a stable configuration (e.g. from an initial state with heavier fluid located at the top of the domain and lighter fluid - at the bottom to a reverse state), and the change in the system potential energy dissipates into heat. In a spatially extended system (e.g. in a large domain) the flow may accelerate, however at a certain time compressibility and stratification start to play a role and results in flow stabilization, as discussed in Ref. [14,59]. To allow for the development of Rayleigh-Taylor turbulent mixing and to enable its diagnostics over substantial span of scales, the size of the domain should be large enough yet not so large to prevent mixing stabilization by effects of compressibility and stratification.

2.6 Effective drag in the turbulent flows.

Regularization of accelerated turbulent mixing is at first glance an unusual concept. However, there is some evidence from previous studies that is does take place. For instance, re-laminarization of an accelerated flow is a well-known fluid dynamics phenomenon discovered in the works of Taylor [68] for flows in curved pipes and Sreenivasan [69] for boundary layers. Another indication of a more regular character of Rayleigh-Taylor mixing follows from the characteristic value of the flow drag. Coefficient C in the dependencies $\varepsilon=Cv^3/L$ and $\mu=Cv^2/L$ can be viewed as effective drag coefficient, which is related to the growth-rate $h=a\,gt^2/2$ via $a(1+2C)=1$ [59-62]. For $C\to 0$

(no drag) the solution is a free-fall with $a \to 1$, whereas for $C \to \infty$ (infinitely large drag) $a \to 0$ and the flow cannot accelerate. Experiments and simulations report relatively small values of $a \sim 0.05 - 0.15$ (with $\alpha \sim 0.03 - 0.07$ in the relation $h = \alpha A g t^2$ in [49]). These values correspond to drag coefficient of $C \sim 3 - 8$, indicating that flow may tend to be more laminar rather than turbulent [63-67]. In canonical Kolmogorov turbulence, the value of C is calculated from the third-order velocity structure function as $C = 5/4$ and $C \sim 1$ [15,63-67]. This may lead to $a = 2/7 \approx 0.3$ ($\alpha \sim 0.14$ in $h = \alpha A g t^2$ in [49]), which is significantly greater than the values actually observed.

2.7 Invariant measures of turbulent process.

In isotropic turbulence, the total momentum is zero because of isotropy. Time- and scale-invariance of the energy dissipation rate $\varepsilon \sim v^3/L$ implies that the energy injected at large scales, $\varepsilon \sim v^2(v/L)$, is transferred without loss through the inertial range and is dissipated at small scales, $\varepsilon \sim (vL)(v/L)^2$ [15,16,63-67]. That is, time- and scale-invariance of the energy dissipation rate $\varepsilon \sim v^3/L$ is compatible with existence of inertial interval and non-dissipative energy transfer between the scales [15,16,63-67]. In accelerated Rayleigh-Taylor turbulent mixing, the rates of change of specific energy are time-dependent, the energy dissipation rate is time-dependent, $\tilde{\varepsilon} \sim \varepsilon \sim g^2 t$, and the specific momentum is imbalanced, $\tilde{\mu} \neq \mu$. Time- and scale invariance of $\mu \sim v^2/L$ implies that at any time and length scale the specific momentum is being lost at the same constant rate, and momentum transfer between the scales is non-dissipative [61]. Enstrophy is another invariant of isotropic turbulence [63-67], whereas in Rayleigh-Taylor mixing this value decays with time (thus providing another indication of a tendency of accelerated mixing flow to re-laminarize) [61]. In Rayleigh-Taylor flow, vortical structures form helixes not vortices. In a flow dominated by the growth of horizontal scales, $\lambda \sim h \sim g t^2$, the helicity is a statistically steady value and its steadiness may serve as an indicator of achieving a merger-driven self-similarity [61], Table 3.

Table 3: Some invariant measures of the turbulent process

Kolmogorov turbulence	Dynamics is statistically steady. Invariance of energy dissipation rates $\varepsilon \sim v^3/L$ is compatible with existence of inertial interval and energy cascade. Enstrophy and helicity are other invariants.
RT turbulent mixing	Dynamics is statistically unsteady. Invariance of rate of momentum loss $\mu \sim v^2/L$ leads to non-dissipative momentum transport between the scales. Energy dissipation rate and enstrophy are time-dependent, and helicity is invariant.

III. Correlations and fluctuations in turbulent processes.

3.1 Space-time scaling properties: correlations and fluctuations in the turbulent process.

For a description of scaling properties, let the length scale L and time scale T refer to large scales and times, let the characteristic velocity be v, let the characteristic velocity be v_l at a small length scales l, and let the characteristics velocity be v_τ on a short time-scale τ.

In Kolmogorov turbulence [14-16,63-67], the invariance of the energy dissipation rate $\varepsilon \sim v^3/L \sim v_l^3/l$ yields the velocity scaling $v_l/v \sim (l/L)^{1/3}$, N-th order velocity structure function $\sim (l\,\varepsilon)^{N/3}$, and velocity scaling with time $v_\tau/v \sim (\tau/T)^{1/3}$. The relative velocity of two parcels of fluids involved in these motions is $\sim (\varepsilon\tau)^{1/2}$ on a time delay τ, and it is substantially smaller than the velocity fluctuations $v_\tau \sim (\varepsilon v \tau)^{1/3}$ induced by turbulence. This well-known result means that in Kolmogorov turbulence, the main contribution to velocity fluctuations is provided by the turbulence not by the initial conditions [15], Tables 4,5.

Table 4: Spatial scaling of the velocity in the turbulent process

	Velocity scaling	**Velocity *N*th order structure function**
Kolmogorov turbulence	$v_l/v \sim (l/L)^{1/3}$ based on ε invariance	$\sim (l\,\varepsilon)^{N/3}$ based on ε invariance
RT turbulent mixing	$v_l/v \sim (l/L)^{1/2}$ based on μ invariance	$\sim (l\,\mu)^{N/2}$ based on μ invariance

In Rayleigh-Taylor turbulent mixing, the invariance of the rate of momentum loss $\mu \sim v^2/L \sim v_l^2/l$ yields the velocity scaling $v_l/v \sim (l/L)^{1/2}$, N-th order velocity structure function $\sim (l\,\mu)^{N/2}$, and the velocity scaling with time $v_\tau/v \sim (\tau/T)$. For two parcels of fluids involved in the motion with a time delay τ, their relative velocity is $\sim (\tilde{\mu} - \mu)\tau \sim g\tau$ and it is comparable to $v_\tau \sim \mu\tau$ induced by turbulent fluctuations, whereas their own velocities grow with time as $\sim gt$ and $\sim g(t-\tau)$ [14]. We see that in accelerated mixing flow, the velocity fluctuations are 'frozen' to the level of the initial conditions, and with time the contribution of fluctuations to the mixing dynamics is reduced, Tables 4,5.

Table 5: Temporal scaling of the velocity in the turbulent process

	Velocity scaling	**Velocity fluctuations**
Kolmogorov turbulence	$v_\tau/v \sim (\tau/T)^{1/3}$ based on ε invariance	$v_\tau \sim (\varepsilon v \tau)^{1/3}$ based on ε invariance and $(\varepsilon v \tau)^{1/3} >> (\varepsilon\tau)^{1/2}$
RT turbulent mixing	$v_\tau/v \sim (\tau/T)$ based on μ invariance	$v_\tau \sim \mu\tau$ based on μ invariance and $\mu\tau \sim (\tilde{\mu} - \mu)\tau \sim g\tau$

3.2 Reynolds number, viscous scale and integral scale in turbulent processes.

In Kolmogorov turbulence, Reynolds number is finite $\mathrm{Re} = vL/\nu = const$ and local Reynolds number $\mathrm{Re}_l = v_l l/\nu$ scales as $\mathrm{Re}_l \sim \mathrm{Re}(l/L)^{4/3}$ leading to the viscous length scale $l_\nu \sim (\nu^3/\varepsilon)^{1/4}$ and time-scale $\tau_\nu \sim (\nu/\varepsilon)^{1/2}$ for $\mathrm{Re}_l \sim 1$. In accelerated turbulent mixing the Reynolds number grows with time as $\mathrm{Re} = vL/\nu \sim g^2t^3/\nu$ and the local Reynolds number $\mathrm{Re}_l = v_l l/\nu$ scales as $\mathrm{Re}_l \sim \mathrm{Re}(l/L)^{3/2}$. For $\mathrm{Re}_l \sim 1$ viscosity plays a dominant role, thus leading to viscous length-scale $l_\nu \sim (\nu^2/\mu)^{1/3}$ with the corresponding time scale $\tau_\nu \sim (\nu/\mu^2)^{1/3}$. The viscous length-scale is finite. It is set by the flow acceleration and are comparable to the wavelength of mode of fastest growth [1,2]. Thus despite in accelerated Rayleigh-Taylor mixing the Reynolds number can reach large values relatively quickly the flow viscous scale remains finite. An upper limit for Reynolds number $\mathrm{Re} \sim g^2t^3/\nu$ can be estimated at a border of validity of incompressible approximation $gt \sim c$ as $\mathrm{Re}_c \sim c^3/g\nu$, where c is the sound speed, Table 6.

Table 6: Reynolds number, viscous scale, and integral scale in the turbulent process

	Reynolds number	**Viscous and integral scales**
Kolmogorov turbulence	$\mathrm{Re} = vL/\nu = const$. Invariance of ε leads to $\mathrm{Re}_l \sim (v_l l/\nu) \sim \mathrm{Re}(l/L)^{4/3}$.	Invariance of ε leads to $l_\nu \sim (\nu^3/\varepsilon)^{1/4}$ and $\tau_\nu \sim (\nu/\varepsilon)^{1/2}$. An integral scale is the scale at which energy is gained by the flow system
RT turbulent mixing	$\mathrm{Re} = vL/\nu \sim g^2t^3/\nu$. Invariance of μ leads to $\mathrm{Re}_l \sim (v_l l/\nu) \sim \mathrm{Re}(l/L)^{3/2}$. For $gt \sim c$ upper limit is $\mathrm{Re}_c \sim c^3/g\nu$.	Invariance of μ leads to $l_\nu \sim (\nu^2/\mu)^{1/3}$ and $\tau_\nu \sim (\nu/\mu^2)^{1/3}$. An integral scale is the coarsest vertical scale representing cumulative contributions of small scale structures.

In Kolmogorov turbulence the integral scale is the scale, at which energy is gained by the flow system. For turbulent mixing this consideration may not be directly applicable. In Rayleigh-Taylor mixing, momentum and energy are gained and dissipated at any scale, and imbalance between the rate of momentum gain and loss leads to flow acceleration. The coarsest vertical scale in Rayleigh-Taylor flow can be regarded as an integral cumulative scale, which represents cumulative contributions of small-scale structures in the flow dynamics, Table 6.

3.3 Dimensional-analysis-based spectral properties of the turbulent process.

In isotropic turbulence, the invariance of energy dissipation rate leads to kinetic energy spectrum $E(k) \sim \varepsilon^{2/3}k^{-5/3}$ [15,63-67]. In Rayleigh-Taylor mixing accurate determination of spectra (and corresponding eigen-functions) is a formidable task because the dynamics is statistically unsteady. Dimensional analysis suggests that the spectrum of specific kinetic energy have the form

$E(k) \sim \mu k^{-2}$, which is steeper than Kolmogorov; similarly for the spectrum of specific momentum one obtains $M(k) \sim \mu^{1/2} k^{-3/2}$. In Kolmogorov turbulence $M(k) \equiv 0$ due to isotropy, Table 7, [61].

Table 7: Dimensional-analysis-based spectral properties of the turbulent process

	Spectrum of specific kinetic energy	**Spectrum of specific momentum**
Kolmogorov turbulence	$E(k) \sim \varepsilon^{2/3} k^{-5/3}$ set by invariance of ε.	$M(k) \equiv 0$ due to isotropy
RT turbulent mixing	$E(k) \sim \mu k^{-2}$ set by invariance of μ	$M(k) \sim \mu^{1/2} k^{-3/2}$ set by invariance of μ

3.4 Pressure fluctuations.

In Kolmogorov turbulence, pressure fluctuations are evaluated using fourth-order velocity structure function so that pressure fluctuates as $\sim \varepsilon^{4/3} l^{4/3}$ with spectrum $\sim \varepsilon^{4/3} k^{-7/3}$ [63-67]. For Rayleigh-Taylor mixing dimensional analysis suggests for pressure fluctuations $\sim \mu^2 l^2$ with spectrum $\sim \mu^2 k^{-3}$ which is steeper than in Kolmogorov turbulence, Table 8 [61].

Table 8: Dimensional-analysis-based properties of pressure fluctuations

	Scaling	**Spectrum**
Kolmogorov turbulence	$\sim \varepsilon^{4/3} l^{4/3}$ set by invariance of ε.	$\sim \varepsilon^{4/3} k^{-7/3}$ set by invariance of ε.
RT turbulent mixing	$\sim \mu^2 l^2$ set by invariance of μ	$\sim \mu^2 k^{-3}$ set by invariance of μ

3.5 Statistically steady and statistically unsteady turbulent mixing.

To conclude this section, we discuss in more details statistically steady and statistically unsteady regimes in Rayleigh-Taylor flows. In a steady regime, the flow can appear more coherent or more 'turbulent' depending on the Atwood number and the initial conditions [3,4]. For the steady flow, the rates of momentum gain and loss as well as energy gain and dissipation are balanced, $\tilde{\mu} = \mu$ and $\tilde{\varepsilon} = \varepsilon$, and the characteristic length scale of the flow λ is constant. The characteristic velocity is $v \sim \sqrt{g\lambda}$, the Reynolds number is $\mathrm{Re} = vL/\nu \sim \lambda\sqrt{g\lambda}/\nu$, and the energy dissipation rate is constant $\varepsilon \sim (g\lambda)^{3/2}/\lambda$. This formally corresponds to the viscous scale $\left(\nu^3/\varepsilon\right)^{1/4} \sim \left(\nu^3\lambda/(g\lambda)^{3/2}\right)^{1/4}$, which is smaller than the mode of fastest growth $\left(\nu^2/g\right)^{1/3}$ for $\lambda > \left(\nu^2/g\right)^{1/3}$. However, as $\lambda/\left(\nu^3\lambda/(g\lambda)^{3/2}\right)^{1/4} \sim \left(\lambda/\left(\nu^2/g\right)^{1/3}\right)^{9/8}$ and $9/8 \approx 1$, the characteristic span of scales in the steady flow is well captured by the ratio $\lambda/\left(\nu^2/g\right)^{1/3}$.

The flow acceleration increases the flow velocity, integral length scale, Reynolds numbers, and energy dissipation rate. At the first glance, this may lead to an appearance of high-Reynolds number turbulent flow with a significant span of scales [41-58]. Momentum consideration [59-62] suggests however that buoyancy-driven turbulent mixing is accelerated due to imbalance between the gain and loss of momentum and energy with $(\tilde{\mu}-\mu)/\tilde{\mu}=a$ and $(\tilde{\varepsilon}-\varepsilon)/\tilde{\varepsilon}=a$. In this flow the velocity $v \sim gt$, the length scale $h \sim gt^2$, the Reynolds number $\mathrm{Re} \sim g^2t^3/\nu$, and the span of scales $\sim gt^2/(\nu^2/g)^{1/3}$ indeed increases. Here the viscous scale is $\sim (\nu^2/g)^{1/3}$ and upper limit for the span of scales is $\sim c^2/g(\nu^2/g)^{1/3}$ for $c \sim gt$. However, compared to the case of statistically steady isotropic and homogeneous turbulence, the accelerated turbulent mixing exhibits stronger correlations, reduced contribution of fluctuations and steeper spectra and may tend to be more laminar [59-62], Table 9.

Table 9: Flow quantities in statistically steady and statistically unsteady Rayleigh-Taylor mixing

Steady RT flow	Balance of momentum and energy $\tilde{\mu}=\mu$ and $\tilde{\varepsilon}=\varepsilon$. Constant length scale λ, velocity $v \sim \sqrt{g\lambda}$, Reynolds number $\mathrm{Re} \sim \lambda\sqrt{g\lambda}/\nu$ and energy dissipation rate $\varepsilon \sim (g\lambda)^{3/2}/\lambda$ with corresponding viscous scale $\left(\nu^3\lambda/(g\lambda)^{3/2}\right)^{1/4}$ and span of scales $\left(\lambda/(\nu^2/g)^{1/3}\right)^{9/8}$.
Unsteady RT flow	Imbalance of momentum and energy $(\tilde{\mu}-\mu)/\tilde{\mu}=a$ and $(\tilde{\varepsilon}-\varepsilon)/\tilde{\varepsilon}=a$. Time-dependent length scale $h \sim gt^2$, velocity $v \sim gt$, Reynolds number $\mathrm{Re} \sim g^2t^3/\nu$ and energy dissipation rate $\varepsilon \sim g^2t$. Constant rate of momentum loss $\mu \sim g$ with corresponding viscous scale $\sim (\nu^2/g)^{1/3}$ and span of scales $\sim gt^2/(\nu^2/g)^{1/3}$ with upper limit $\sim c^2/g(\nu^2/g)^{1/3}$.

IV. Stochastic modeling of statistically unsteady turbulent mixing process

As in any turbulent process, RT mixing dynamics has a random character, which is resulted from contribution of small-scale structures and interactions of all the scales [60,63-67]. Capturing this randomness is a complex task. In Kolmogorov turbulence, random character of flow dissipation is induced by velocity fluctuations with the energy dissipation rate being a statistic invariant [63-67]. In RT mixing flow the velocity and the length scale both fluctuate and the energy dissipation rate grows with time. We account for the random character of dissipation in RT flow on the basis of idea that even in a statistically unsteady process [whose fluctuating quantities are time-dependent and non-Gaussian] there exist time- and scale-invariant values fluctuating about their means, particularly, the rate of momentum loss μ [60].

To study the effect of fluctuations on the mixing dynamics, Eqs.2 are represented in a differential form

$$dh = v dt, \qquad dv = \mathrm{d}\tilde{\mathrm{M}} - \mathrm{dM}, \tag{3a}$$

with differentials of momentum gain $\mathrm{d}\tilde{\mathrm{M}} = g\,dt$ and loss $\mathrm{dM} = C\left(v^2/h\right)dt$ and with C being a stochastic process [60]. This process is, in general, time-dependent, $C = C(t)$, and is characterized by a time-scale τ_C, showing how fast the distribution $C(t)$ approaches a stationary probability density function $p(C)$. The function $p(C)$ is non-symmetric, $C > 0$, with the mean value $\langle C\rangle$, with the mode $C_{\max}$ corresponding to the highest value of $p(C)$, and with the standard deviation σ, describing the fluctuations intensity. For stochastic processes with log-normal distribution $p(C) = e^{\left(-(\ln C - \ln C_0)^2/2\sigma^2\right)}\Big/\sqrt{2\pi}\sigma C$, the mean $\langle C\rangle = C_0 \exp\left(\sigma^2/2\right)$, the mode $C_{\max} = C_0 \exp\left(-\sigma^2\right)$, and the set of stochastic differential equations in (3a) takes the form

$$dh = v dt, \qquad dv = g dt - C\frac{v^2}{h}dt, \qquad dC = -C\left(\ln\frac{C}{\langle C\rangle} - \frac{\sigma^2}{2}\right)\frac{dt}{\tau_C} + \sigma C\sqrt{\frac{2}{\tau_C}}dW, \tag{3b}$$

with dW being a standard Weiner process.

The stochastic modeling results indicate that fluctuations do not change the asymptotic time-dependence of the dynamics, so that $h \sim gt^2/2$ as $t/\tau \to \infty$, yet they influence significantly the coefficient $a = 2h/gt^2$ [60]. Depending on the shape of the distribution $p(C)$ and on the fluctuations intensity σ, the mean value of a may vary in several folds, and, furthermore, it saturates slowly with time for $(t/\tau) >> 1$. This result explains qualitatively the several-fold scatter in the values of a in the experiments and simulations [49]. It indicates that the growth-rate parameter a is sensitive to the dissipation statistics and it is a significant parameter not because it is “deterministic” or “universal,” but because its value is rather small, $a << 1$ [50]. Found in many experiments and simulations, the small a implies that in RT flows almost all energy induced by the buoyant force dissipates, and a slight imbalance between the rates of momentum loss μ and gain $\tilde{\mu}$ is sufficient for the mixing development. We emphasize that the rate of momentum loss $\mu(t) = C v^2/h$ is relatively insensitive to the effect of fluctuations, and monitoring the momentum transport is thus has crucial importance for grasping the essentials of the mixing process.

V. Outcomes of theoretical analysis for mitigation and control of turbulent mixing process

To date, the design of experiments on RT mixing [17-39] employs the results of traditional models [41-58] suggesting the following scenarios for RT evolution. Initially, small perturbations at the interface with wavelength λ grow fast. In the nonlinear regime the velocity is $v \sim \sqrt{g\lambda}$ and amplitude is $h \sim vt \sim t\sqrt{g\lambda}$. Horizontal and vertical scales are strongly coupled, and self-similar growth of horizontal scales (e.g. bubble interaction and merge) leads to flow acceleration with $\lambda \sim h \sim gt^2$. In accelerated regime the scales grow as $h \sim gt^2$ and $\lambda \sim gt^2$, the Reynolds number and energy dissipation rate increase as $\mathrm{Re} \sim g^2t^3/\nu$ and $\varepsilon \sim v^3/h \sim g^2 t$. This may be interpreted as the development of a turbulent state of the mixing flow, which is similar to isotropic and homogeneous turbulence and is independent of the initial conditions, and whose viscous scale decays as $(\nu^3/\varepsilon)^{1/4} \sim (\nu^3/g^2 t)^{1/4}$ and span of scales increases as $h/(\nu^3/\varepsilon)^{1/4} \sim g^{3/2} t^{9/4}/\nu^{3/4}$. Therefore, according to these scenarios, RT turbulent mixing, once it appears, cannot be controlled. To proceed to mixing regime faster, the initial perturbation may contain large wavelength modes. To suppress the mixing development, the interface should be ‘finely polished’ [41-58].

As discussed in the foregoing, some of results of traditional models [41-58] can be obtained within the frames of the theoretical analysis [59-62] with the use of additional adjustable parameters. Some other results of the traditional models [41-58] are known to have severe limitations [4].

The theoretical analysis [3,4,59-62] finds that in the nonlinear regime of RTI, horizontal and vertical scales contribute independently to the dynamics, and the rates of specific momentum and energy are balanced, $\tilde{\mu} = \mu$ and $\tilde{\varepsilon} = \varepsilon$. Accelerated turbulent mixing develops due to imbalance of specific momentum and energy with $(\tilde{\mu} - \mu)/\tilde{\mu} = a$ and $(\tilde{\varepsilon} - \varepsilon)/\tilde{\varepsilon} = a$, where $h = a\, g t^2/2$ (with ‘effective’ g accounting for the density ratio). There are two distinct mechanisms for the mixing development: (i) growth of horizontal scale (period) $\lambda \sim g t^2$ and (ii) dominance of vertical scale (amplitude) $L \sim h$ or energy dissipation. Bubble merge is possible but not a necessary condition for the mixing to occur. Compared to isotropic turbulence, RT turbulent mixing exhibits more order, steeper spectra, stronger correlations, and weaker contributions of fluctuations, which are ‘frozen’ to the initial conditions. In turbulent mixing flow the viscous scale is finite and is set by flow acceleration as $(\nu^2/\mu)^{1/3} \sim (\nu^2/g)^{1/3}$. The span of scales is $h/(\nu^2/g)^{1/3} \sim g t^2/(\nu^2/g)^{1/3}$ with the upper limit $c^2/g(\nu^2/g)^{1/3}$. In the mixing flow the rates of gain and loss of specific momentum are time- and scale-independent, $\tilde{\mu} \sim \mu \sim v^2/L \sim g$, the rates of energy gain and dissipation are time-dependent, $\tilde{\varepsilon} \sim \varepsilon \sim g^2 t$, and Reynolds number increases as $\mathrm{Re} \sim g^2 t^3/\nu$. Therefore, the theoretical analysis [3,4,59-62] suggests that RT mixing flow can in principle be controlled by means of initial perturbation and acceleration. Horizontal and vertical scales can be controlled independently, and initial perturbation with large wavelengths may not induce any turbulence [4,59-62]. For better control of RT mixing, one should impose proper (e.g. highly coherent) initial conditions in order to prevent bubble merge. Furthermore, one should choose very special initial conditions to force the flow to fluctuate [3,4,59-62].

It would be beneficial for the design of experiments on RT mixing to account for that in strongly fluctuating turbulent flows the Reynolds number is high; yet not in any high Reynolds number flow the fluctuations are strong [59-62]. Implementation of turbulent flows in experiments is an extremely challenging task [28], as good experiments on turbulence are the ‘quantitative’ experiments, which require accurate interpretation of the (bias-free) experimental noise. A qualitative experiment with a binary answer ‘yes/no’ may be a good solution the case of RT turbulent mixing. Such an experiment may involve a comparative study of RT mixing dynamics with various initial conditions, e.g. involving hexagonal grid, square grid, two-mode grid, and fractal grid [70] in case of three-dimensional spatially extended flows. According to the analysis [3,4,59-62], the expected results would be the following. For accurately implemented hexagonal grid, bubble merge may not occur, and the flow is ‘regular’ and is dominated by the coherent structure. For square grid, bubble merge may occur via multi-pole interactions. For two-mode grid with small and large wavelengths, bubble merge will develop faster compared to square grid. Fractal grid [70] may be the best to induce fluctuations and a 'turbulent-like' dynamics (these fluctuations may be dominated by the few modes and may not be stochastic [70]).

VI. Conclusion

We have considered the effect of momentum transport on scaling, invariant and statistical properties of Rayleigh-Taylor mixing flow [3,4,59-62]. It is shown that the rate of momentum loss is a better indicator of the unsteady turbulent dynamics than the rate of energy dissipation. Our consideration accounts for the multi-scale character of turbulent mixing dynamics and indicates two possible mechanisms for the mixing development. The first is the traditional "merge" associated with the growth of horizontal scales. The second is associated with the production of small-scale structures and with the growth of the vertical scale, which plays the role of the integral scale for energy dissipation. Based on invariance of the rate of momentum loss, we found that the fundamental properties of statistically unsteady Rayleigh-Taylor turbulent mixing depart substantially from classical Kolmogorov scenario. In particular, turbulent mixing flow exhibits more order compared to isotropic turbulence, and its viscous scale is set by the flow acceleration. The stochastic modeling results indicate that the growth-rate parameter of the mixing zone is a sensitive to statistical properties of dissipation. The momentum-based consideration of Rayleigh-Taylor mixing suggests a principal opportunity of mitigation and control of the statistically unsteady turbulent process.

VII. Acknowledgement

The work is partially supported by the US National Science Foundation and the US Department of Energy. The author deeply thanks Drs. K.R. Sreenivasan, S.I. Anisimov, B. Alder, A. Bershadskii, R.P. Drake, S. Fedotov, B. Fryxell, Y. Fukumoto, S. Gauthier, G. Glatzmaier, G. Hazak, L.P. Kadanoff, A. Klimenko, V. Lvov, K. Nishihara, A. Pouquet, B. Remington, J. Schumacher, A.L. Velikovich, J. Werne, and V. Yakhot for discussions.

VIII. References

1. Rayleigh, Lord, 1883 Investigations of the character of the equilibrium of an incompressible heavy fluid of variable density. Proc. London Math. Soc. 14, 170.
2. Davies R M and Taylor G I 1950, The mechanics of large bubbles rising through extended liquids and through liquids in tubes. Proc. R. Soc. London, Ser. A 200, 375.
3. Abarzhi S I 2008 Review on nonlinear coherent dynamics of unstable fluid interface: conservation laws and group theory Physica Scripta T132, 297681
4. Abarzhi S I 2010, Review of theoretical modeling approaches of Rayleigh-Taylor instabilities and turbulent mixing. Philosophical Transactions of the Royal Society A 368, 1809.
5. Zel'dovich Ya B and Raizer Yu P 2002 Physics of Shock Waves and High-temperature Hydrodynamic Phenomena. 2nd Engl. edn (New York: Dover)
6. Remington B A, Drake R P, Ryutov DD 2006, Experimental astrophysics with high power lasers and Z-pinches. Rev. Mod. Phys. 78, 755
7. Drake R P 2009, Perspectives of high energy density physics. Phys. Plasmas 16, 055501
8. Hillebrandt W and Niemeyer J C 2000 Type Ia supernova explosion models. Annu. Rev. Astron. Astrophys. 38, 191
9. Spalart P R and Watmuff J H 1993 Experimental and numerical study of a turbulent boundary layer with pressure gradients. J. Fluid Mech. 249, 337
10. Gutman E J, Schadow K C and Yu K H 1995 Mixing enhancement in supersonics free shear flows. Annu. Rev. Fluids 27, 375
11. Stone J M, Hawley J F, Gammie C F and Balbus S A 1996 Three-dimensional magneto-hydrodynamical simulations of vertically stratified accretion disks Astrophys. J. 463, 656
12. Choi J P and Chan V W S 2002 Predicting and adapting satellite channels with weather-induced impairments. IEEE Trans. Aerosp. Electron. Syst. 38, 779
13. Marmottant P and Villermaux E 2004 On spray formation. J. Fluid Mech. 498, 73
14. Landau L D and Lifshitz E M 1987 Course of theoretical physics VI, Fluid mechanics. Pergamon Press, New York.
15. Kolmogorov A N 1941 Local structure of turbulence in an incompressible fluid for very large Reynolds numbers. Dokl. Akad. Nauk. SSSR 30, 299; Energy dissipation in locally isotropic turbulence. Dokl. Akad. Nauk. SSSR 32, 19.
16. Sreenivasan K R 1999 Fluid turbulence. Rev. Mod. Phys. 71, S383.
17. Read K I 1984 Experimental investigation of turbulent mixing by Rayleigh–Taylor instability. Physica D 12, 45.
18. Marinak M M, Glendinning S G, Wallace R J, Remington B A, Budil K S, Haan S W, Tipton R E and Kilkenny J D 1998 Nonlinear Rayleigh–Taylor evolution of a three-dimensional multimode perturbation. Phys. Rev. Lett. 80 4426.
19. Schneider M, Dimonte G and Remington B 1998 Large and smalls scale structures in Rayleigh–Taylor mixing. Phys. Rev. Lett. 80, 3507
20. Dalziel S B, Linden P F, Youngs D L, 1999, Self-similarity and internal structure of turbulence induced by Rayleigh–Taylor instability. J. Fluid Mech. 399, 1.

21. Dalziel S B, Patterson M D, Caulfield C P, Coomaraswamy I A 2008, Mixing efficiency in high-aspect-ratio Rayleigh-Taylor experiments, Physics of Fluids 20, 065106.
22. Waddell J T, Jacobs J W, and Niederhaus C E 2001, Experimental study of Rayleigh–Taylor instability: Low Atwood number liquid systems with single-mode initial perturbations. Phys. Fluids 13, 1263.
23. Wilson M and Andrews M J 2002, Spectral measurements of Rayleigh– Taylor mixing at small Atwood number. Phys. Fluids 14, 938.
24. Kucherenko Y A, Shestachenko O E, Balabin S I, Pylaev A P 2003 RFNC-VNIITF multi-functional shock tube for investigating the evolution of instabilities in non-stationary gas dynamic flows. Laser Part. Beams 21, 381.
25. Kucherenko Y A, Balabin S I, Ardashova R I, Kozelkov O E, Dulov A V, and Romanov I A 2003 Experimental study of the influence of the stabilizing properties of transitional layers on the turbulent mixing evolution. Laser Part. Beams 21, 369.
26. Ramaprabhu P, Andrews M J 2003 Experimental investigation of Rayleigh–Taylor mixing at small Atwood numbers. J Fluid Mech. 503, 233; Banerjee A, Kraft W N, Andrews M J 2010 Detailed measurements of a statistically steady Rayleigh-Taylor mixing layer from small to high Atwood numbers. J Fluid Mechanics 659, 127.
27. Meshkov E E 2006, Studies of Hydrodynamic Instabilities in Laboratory Experiments, (in Russian). Sarov, FGYC-VNIIEF, ISBN 5-9515-0069-9.
28. Orlov S S, Abarzhi S I, Oh S B, Barbastathis G, Sreenivasan K R 2010, High-performance holographic technologies for fluid dynamic experiments. Philosophical Transactions of the Royal Society A 368, 1705.
29. Linden P F, Redondo J M, and Youngs D L 1994, Molecular mixing in Rayleigh–Taylor instability. J. Fluid Mech. 265, 97.
30. He X Y, Zhang R Y, Chen S Y and Doolen G D 1999 On the three-dimensional Rayleigh–Taylor instability. Phys. Fluids 11, 1143.
31. Cook A W and Dimotakis P E 2001 Transition stages of Rayleigh–Taylor instability between miscible fluids. J. Fluid Mech. 443 69.
32. Calder A C, Dursi L J, Fryxell B, Plewa T, Weirs V G, Dupont T, Robey H F, Kane J O, Drake R P, Remington B A, Dimonte G, Hayes J, Stone J M, Ricker P M, Timmes F X, Zingale M, and Olson K 2002, On validating an astrophysical simulation code. Astrophys. J., Suppl. Ser. 143, 201.
33. Poujade O 2002, Rayleigh-Taylor turbulence is nothing like Kolmogorov turbulence in the self-similar regime, Phys Rev Letters 97, 085002.
34. Dimonte G, Youngs D L, Dimits A, Weber S, Marinak M, Wunsch S, Garasi C, Robinson A, Andrews M J, Ramaprabhu P, Calder A C, Fryxell B, Biello J, Dursi L, MacNeice P, Olson K, Ricker P, Rosner R, Timmes F, Tufo H, Young Y N, Zingale M, 2004 A comparative study of the turbulent Rayleigh-Taylor instability using high-resolution three-dimensional numerical simulations: The Alpha-Group collaboration. Phys. Fluids 16, 1668.
35. Cook A W, Cabot W, and Miller P 2004, The mixing transition in Rayleigh–Taylor instability. J. Fluid Mech. 511, 333.

36. Ristorcelli J R and Clark T T 2004, Rayleigh-Taylor turbulence: self-similar analysis and direct numerical simulations. J Fluid Mechanics 507, 213.
37. Milovich J L, Amendt P, Marinak M and Robey H 2004 Multi-mode shortwavelength perturbation growth studies for the National Ignition Facility double-shell ignition target design. Phys. Plasmas 11, 1552.
38. Cabot W H and Cook A W 2006, Reynolds number effects on Rayleigh-Taylor instability with possible implications for type-Ia supernovae, Nature Physics 2, 562.
39. Kadau K, Rosenblatt C, Barber J L, Germann T C, Huang Z B, Carles P and Alder B J 2007 The importance of fluctuations in fluid mixing. Proc. Natl. Acad. Sci. USA 104, 774107745; Kadau K, Barber J L, Germann T C, Holian B L, Alder B J 2010 Atomistic methods in fluid simulation. Phil. Trans. Royal Society 368, 1547.
40. Abarzhi S I and Sreenivasan K R, 2010 Introduction – Turbulent Mixing and Beyond, Phil. Trans. Royal Society A London 368, Issue 1916, 1539-1546
41. Belen'ki S Z and Fradkin E S 1965 Theory of turbulent mixing, Trudi FIAN 29, 207 (in Russian)
42. Neuvazhaev V E 1975, Theory of turbulent mixing. Doklady Akademii Nauk 222, 1053.
43. Sharp D H 1984 An overview of Rayleigh–Taylor instability. Physica D 12, 3; Glimm J and Sharp D H 1990 Chaotic mixing as a renormalization-group fixed-point. Phys. Rev. Lett. 64, 2137
44. George E, Glimm J, Li X-L, Marchese A and Xu Z-L 2002 A comparison of experimental theoretical, and numerical simulation Rayleigh–Taylor mixing rates Proc. Natl. Acad. Sci., USA 99, 2587
45. Youngs D L 1984 Numerical simulations of turbulent mixing by Rayleigh–Taylor instability Physica D 12 32
46. Youngs D L 1991 Three-dimensional numerical simulations of turbulent mixing by Rayleigh–Taylor instability. Phys. Fluids A 3 1312
47. Alon U, Hecht J, Mukamel D and Shvarts D 1994 Scale-invariant mixing rate of hydrodynamically unstable interfaces. Phys. Rev. Lett. 72, 2867
48. Alon U, Hecht J, Offer D and Shvarts D 1995 Power-laws and similarity of Rayleigh–Taylor and Richtmyer–Meshkov mixing fronts at all density ratios. Phys. Rev. Lett. 74, 534
49. Dimonte G 2000 Spanwise homogeneous buoyancy-drag model for Rayleigh–Taylor mixing and experimental evaluation. Phys. Plasmas 7, 2255
50. Besnard D C, Harlow F H, Rauenzahn R M and Zemach C 1996 Spectral transport model for turbulence. Theor. Comput. Fluid Dyn. 8, 1
51. Steinkamp M J, Clark T T and Harlow F H 1999 Two-point description of two-fluid turbulent mixing—I. Model formulation Int. J. Multiph. Flow 25, 599 and Two-point description of two-fluid turbulent mixing—II Numerical solutions and comparisons with experiments Int. J. Multiph. Flow 25, 639
52. Clark T T 2003, A numerical study of the statistics of a 2D Rayleigh–Taylor mixing layer. Phys. Fluids 15, 2413.

53. Ristorcelli J R and Clark T T 2004 Rayleigh–Taylor turbulence: self-similar analysis and direct numerical simulations. J. Fluid Mech. 507, 213
54. Dimotakis P E 2000 The mixing transition in turbulent flows. J. Fluid Mech. 409, 69
55. Zhou Y 2001, A scaling analysis of turbulent flows driven by Rayleigh-Taylor and Richtmyer-Meshkov instabilities. Physics of Fluids 13, 538.
56. Zhou Y, Remington B A, Robey H F, Cook A W, Glendinning S G, Dimits A, Buckingham A C, Zimmerman G B, Burke E W, Peyser T A, Cabot W, Eliason D 2003, Progress in understanding turbulent mixing induced by Rayleigh-Taylor and Richtmyer-Meshkov instabilities. Physics of Plasmas 10, 1883; Robey H F, Zhou Y, Buckingham A C, Keiter P, Remington B A, Drake R P, 2003, The time scale for the transition to turbulence in a high Reynolds number, accelerated flow. Physics of Plasmas 10, 614
57. Chertkov M 2003 Phenomenology of Rayleigh–Taylor turbulence. Phys. Rev. Lett. 91, 115001
58. Gauthier S and Bonnet M 1990 A k –e model for turbulent mixing in shocktube flows induced by Rayleigh–Taylor instability. Phys. Fluids A 2 1685
59. Abarzhi S I, Gorobets A, Sreenivasan K R 2005 Turbulent mixing in immiscible, miscible and stratified media, Phys. Fluids 17, 081705.
60. Abarzhi S I, Cadjun M, Fedotov S 2007 Stochastic model of Rayleigh–Taylor turbulent mixing. Phys. Lett. A 371, 457.
61. Abarzhi S I 2010, On fundamentals of Rayleigh-Taylor turbulent mixing, Europhysics leterrs, 91, 35000.
62. Abarzhi S I, Rosner R 2010, A comparative study of approaches for modeling Rayleigh-Taylor turbulent mixing, Physica Scripta T142, 014012
63. Taylor G I 1935 Statistical theory of turbulence. Proc. Roy Soc. London 151(A), 421.
64. Batchelor G K 1953 The Theory of Homogeneous Turbulence. Cambridge: Cambridge Univ. Press.
65. Monin A S, Yaglom A M 1975 Statistical Fluid Mechanics Vol. 2. MIT Press, Cambridge.
66. Frisch U 1995 Turbulence, the Legacy of A N Kolmogorov. Cambridge University Press, Cambridge.
67. Tennekes H and Lumley J L, 1972 A First Course in Turbulence. MIT Press.
68. Taylor G I 1929, The criterion for turbulence in curved pipes. Proc. Roy. Soc. A 124, 243.
69. Narasimha R, Sreenivasan K R 1973, Relaminarization in highly accelerated turbulent boundary layers. J. Fluid Mechanics, 61, 417.
70. Mazellier N, Vassilicos JC 2010, Turbulence without Richardson-Kolmogorov cascade, Physics of Fluids 22, 075101

Self-organization in a foliated phase space

Z. Yoshida[1] and S. M. Mahajan[2]

[1]*Graduate School of Frontier Sciences, The University of Tokyo,*
Kashiwa, Chiba 277-8561, Japan
[2]*Institute for Fusion Studies, The University of Texas at Austin,*
Austin, Texas 78712, U.S.A.

Abstract. Self-organization of a structure is, at its surface, an antithesis of the entropy *ansatz*. However, disorder can still develop at micro scale while a structure emerges on some macro scale; it seems more common in various nonlinear systems that order and disorder are simultaneous, and such coexistence may be possible if the self-organization and the entropy principle work on different scales. The self-organization of a magnetospheric plasma vortex is an example. A systematic formulation of a scale hierarchy is given by a "foliation" of the kinetic phase space in terms of actions (adiabatic invariants). Interpreting an action μ (the magnetic moment, for instance) as the number of quantized "quasi-particles," we can construct a grand-canonical distribution function $f_\alpha \propto e^{-\beta H - \alpha\mu}$ (H: Hamiltonian, β: inverse temperature, α: chemical potential of the quasi-particle) that maximizes entropy on a macroscopic leaf where the microscopic action-angle variables are abstracted as quasi-particle numbers. While embedding the macroscopic leaf in the (laboratory-frame) total phase space, the transforming Jacobian weight forces an inhomogeneous density profile in the laboratory flat space. An inhomogeneous magnetic field (typically a dipole) yields a strongly distorted invariant measure of the magnetized particles, creating a self- organized vortex with steep density gradient; this theory explains "inward diffusion" in magnetospheres, as well as their laboratory simulations [Z. Yoshida *et al.*, Phys. Rev. Lett. **104** (2010) 235004].

1 Introduction

Superficially, the process of self-organization of a structure may appear to be an antithesis of the maximum entropy *ansatz*. And yet various nonlinear systems display what may be viewed as the simultaneous existence of order and disorder [1]. This co-existence will begin to make sense if the self-organization processes and the entropy principle were to manifest on different scales; disorder can still develop at a microscopic scale while an ordered structure emerges on some appropriate macroscopic scale. Writing a theory of self-organization, then, will be an exercise in delineating and understanding the characteristic *scale hierarchy* of the physical system.

Scale hierarchy is a popular keyword in various arguments on "structures"; a biological body is a typical example in which an evident hierarchical structure is preprogrammed enabling effective consumption of energy and materials as well as emission of entropy and waste. A physical macrosystem —a collective system of "simple" elements (a gravitational system, a plasma, etc.)— is anchored on a different framework. An automatic emergence of scale hierarchy is not "programmed" and the structures are not assigned specific functions *a priori*; yet the controlling nonlinear dynamics can mimic a fundamental and elementary process of *creation*.

The ordering principal is generally epitomized in a "constraint" —a possible conservation law, a constant of motion— that, by restricting the class of motions available to the system, limits its ability to degenerate into general disorder. In complicated dynamics, the emergence of "complete" order would surely seem like a tall order; what one may, realistically, expect is the creation of order at some scale coming at the cost of enhanced disorder at another.

Although this scenario seems philosophically sensible, one must trace the theoretical path through which such a self-organization could occur. In this Letter we analyze the *creation* process embodied in the formation of a self-organized magnetospheric plasma. Through this example, we delineate a clear and distinct scale hierarchy in terms of Hamiltonian mechanics and foliation (provided by adiabatic invariants), and show how an ordered structure (heterogeneity) can emerge while maximizing the entropy.

Magnetospheres are self-organized structures found, commonly, in the Universe. The naturally occurring ones (the planetary magnetospheres [2, 3, 4], for instance) as well as their laboratory simulations [5, 6, 7, 8, 9] are built around the dipole magnetic fields. In a dipole magnetic field, the charged particles can cause a variety of interesting phenomena. Of particular interest is the often observed *inward diffusion* (or up-hill diffusion) of magnetized particles. This process is driven by some spontaneous fluctuations (symmetry breaking) that violate the constancy of angular momentum. In a strong enough magnetic field, the canonical angular momentum P_θ is dominated by the magnetic part $q\psi$: the charge multiplied by the flux function (Gauss'potential). The conservation of $P_\theta \approx q\psi$, therefore, restricts the charged particle motion to the magnetic surface (level-set of ψ). It is only via randomly-phased fluctuations that the particles can diffuse across magnetic surfaces. Although the “diffusion” is normally a process of diminishing gradients, numerical experiments do exhibit preferential inward shifts through random motions of test particles [10, 11]. Detailed specification of the fluctuations or the microscopic motion of particles is not the subject of present effort. We plan to construct, instead, a clear-cut description of the self-organized state, which, through with entropy principle, allows steep gradients to form at the goal of diffusion. [1]

Here we describe the scale hierarchy by a phase-space foliation. Heterogeneity is, then, created by the distortion of the metric (invariant measure) dictating the *equipartition* on the leaf of the macroscopic hierarchy; in a strongly inhomogeneous magnetic field (typically a dipole magnetic field), the phase-space metric of *magnetized particles* is distorted, thus the projection of the equipartition distribution onto the flat space of the laboratory frame yields peaked profile by the Jacobian weight (this idea was proposed by Hasegawa [12, 13]; in later discussion we will put the present theory in perspective). The theoretical path for the self-organization scenario will be charted invoking a Hamiltonian formalism of the magnetized charged particles and the Boltzmann distribution on a foliated phase space endowed with a *non-canonical* Poisson bracket [14].

2 Separation of action-angle variables and scale hierarchy

To analyze the effect of magnetization in an inhomogeneous magnetic field (specifically, a dipole magnetic field), we invoke the hierarchical Hamiltonian structure built by adiabatic invariants (actions).

2.1 Hamiltonian of charged particle

The Hamiltonian of a charged particle is a sum of the kinetic energy and the potential energy:

$$H = \frac{m}{2}v^2 + q\phi, \tag{1}$$

---

[1] A density f (on an n-dimensional space) is an extensive quantity (n-form), which differs from an intensive quantity (scalar, or 0-form). A diffusion equation for f, with respect to an invariant measure $dx^1 \wedge \cdots \wedge dx^n$, is written as $\partial_t f = d(\mathcal{D}\delta f)$, where $\mathcal{D}$ is a diffusion coefficient, d is the exterior derivative (gradient) and $\delta = (-1)^{n+1}\ {}^*d^*$ is the codifferential (* is the Hodge star); a diffusion equation for a scalar ϕ is such that $\partial_t \phi = \delta(\mathcal{D}d\phi)$. Thus, the diffusion of f is a process of flattening ${}^*f$, while that of ϕ simply flattens ϕ. The Hodge star converts $f = f(y^1, \cdots, y^n)$ to${}^*f = f(y^1, \cdots, y^n)D(y^1, \cdots, y^n)/D(x^1, \cdots, x^n)$.

where $\boldsymbol{v} := (\boldsymbol{P}-q\boldsymbol{A})/m$ is the velocity, $\boldsymbol{P}$ is the canonical momentum, $(\phi, \boldsymbol{A})$ is the electromagnetic 4-potential, m (q) is the particle mass (charge). In the present work, we may treat electrons and ions equally (in later discussion, we will neglect ϕ assuming charge neutrality, but generalization to a non-neutral plasma will be interesting [7, 15]). Denoting by $\boldsymbol{v}_{\|}$ and $\boldsymbol{v}_{\perp}$ the parallel and perpendicular (with respect to the local magnetic field) components of the velocity, we may write

$$H = \frac{m}{2}v_{\perp}^2 + \frac{m}{2}v_{\|}^2 + q\phi. \tag{2}$$

The velocities are related to the mechanical momentum as $\boldsymbol{p} := m\boldsymbol{v}$, $\boldsymbol{p}_{\|} := m\boldsymbol{v}_{\|}$, and $\boldsymbol{p}_{\perp} := m\boldsymbol{v}_{\perp}$.

2.2 Creation of an action-angle pair by magnetization

In a strong magnetic field, $\boldsymbol{v}_{\perp}$ can be decomposed into a small-scale cyclotron motion $\boldsymbol{v}_c$ and a macroscopic guiding-center drift motion $\boldsymbol{v}_d$. The periodic cyclotron motion $\boldsymbol{v}_c$ can be *quantized* to write $(m/2)v_c^2 = \mu\omega_c(\boldsymbol{x})$ in terms of the magnetic moment μ and the cyclotron frequency $\omega_c(\boldsymbol{x})$; the adiabatic invariant μ and the gyration phase $\vartheta_c := \omega_c t$ constitute an action-angle pair. In the standard interpretation, in analogy with the Landau levels in quantum theory, ω_c is the *energy level* and μ is the *number* of quasi-particles (quantized periodic motions) at the corresponding energy level.

For an axisymmetric system with a poloidal (but no toroidal) magnetic field, let (ψ, ζ, θ) be a magnetic coordinate system such that $\boldsymbol{B} = \nabla\psi\times\nabla\theta$ (θ is the toroidal angle). An approximately-vacuum magnetic field may also be written as $\boldsymbol{B} = \nabla\xi = B\nabla\zeta$. [2] The macroscopic part of the perpendicular kinetic energy is expressed as $mv_d^2/2 = (P_\theta - q\psi)^2/(2mr^2)$, where P_θ is the angular momentum in the θ direction and r is the radius from the geometric axis. In terms of the canonical-variable set $\boldsymbol{z} = (\vartheta_c, \mu, \zeta, p_{\|}, \theta, P_\theta)$ the Hamiltonian of the guiding center (or, the quasi-particle) becomes

$$H_c = \mu\omega_c + \frac{1}{2m}\frac{(P_\theta - q\psi)^2}{r^2} + \frac{1}{2m}p_{\|}^2 + q\phi. \tag{3}$$

Note that the energy of the cyclotron motion has been quantized in term of the frequency $\omega_c(\boldsymbol{x})$ and the action μ; the gyro-phase ϑ_c has been coarse grained (integrated to yield 2π).

---

[2] The flux function ψ is equal to rA_θ (A_θ is the θ component of $\boldsymbol{A}$). For a point dipole of magnetic moment M, $\psi(r,z) = Mr^2(r^2+z^2)^{-3/2}$. On the other hand, the scalar potential is $\xi(r,z) = Mz(r^2+z^2)^{-3/2}$. The magnetic field strength is $B = M\sqrt{(r^4+5r^2z^2+4z^4)/(r^2+z^2)^5}$.

2.3 Boltzmann distribution

The standard Boltzmann distribution function is derived when we assume that the Lebesgue measure d^3vd^3x is an invariant measure and the Hamiltonian H is the determinant of the ensemble. Maximizing the entropy $S = -\int f \log f d^3vd^3x$ keeping the total energy $E = \int Hfd^3vd^3x$ and the total particle number $N = \int fd^3vd^3x$ constant, we obtain

$$f(\boldsymbol{x}, \boldsymbol{v}) = Z^{-1}e^{-\beta H}, \tag{4}$$

where Z is the normalization factor ($\log Z - 1$ is the Lagrange multiplier on N) and β is the inverse temperature (the Lagrange multiplier on E). The corresponding configuration-space density,

$$\rho(\boldsymbol{x}) = \int fd^3v \propto e^{-\beta q\phi}, \tag{5}$$

becomes constant for a charge neutral system ($\phi = 0$).

Needless to say that the Boltzmann distribution or the corresponding configuration-space density, with an appropriate Jacobian multiplication, is independent of the choice of phase-space coordinates. Moreover, the density is invariant no matter whether we quantize the cyclotron morion or not. Let us confirm this fact by a direct calculation. For the Boltzmann distribution of the "guiding-center plasma"

$$\begin{aligned} f(\mu, v_d, v_\parallel; \boldsymbol{x}) &= Z^{-1}e^{-\beta H_c} \\ &= Z^{-1}e^{-\beta\left(\mu\omega_c(\boldsymbol{x}) + mv_d^2/2 + mv_\parallel^2/2 + q\phi(\boldsymbol{x})\right)}, \end{aligned} \tag{6}$$

the density is given by

$$\rho(\boldsymbol{x}) = \int fd^3v = \int f\,\frac{2\pi\omega_c}{m}d\mu dv_d dv_\parallel \propto e^{-\beta q\phi}, \tag{7}$$

exactly reproducing (5).

2.4 Equilibrium on macroscopic hierarchy

The adiabatic invariance of the magnetic moment μ (the *number* of the quantized quasi-particles) imposes a *topological constraint* on the motion of particles; it is this constraint that is the root-cause of a macroscopic hierarchy and of structure formation. Mathematically, the *scale hierarchy* is equivalent to a foliation of the phase space. To explain how the scale hierarchy is formulated, we start by the general (micro-macro total) formulation, and then separate the microscopic action-angle pair μ-ϑ_c; the *macroscopic phase space* is the remaining sub-manifold immersed in the general phase space, which we delineate as a leaf of the foliation in terms of a *Casimir element* [14].

The Poisson bracket on the total phase space, spanned by the canonical variables $\boldsymbol{z} = (\vartheta_c, \mu, \zeta, p_{||}, \theta, P_\theta)$, is

$$\{F, G\} := \langle \mathcal{J} \partial_{\boldsymbol{z}} F, \partial_{\boldsymbol{z}} G \rangle,$$

where $\langle \boldsymbol{u}, \boldsymbol{v} \rangle := \int u_j v^j \, d^6 z$ is the inner-product and $\mathcal{J}$ is the canonical symplectic matrix (Poisson tensor):

$$\mathcal{J} := \begin{pmatrix} J & 0 & 0 \\ 0 & J & 0 \\ 0 & 0 & J \end{pmatrix}, \quad J := \begin{pmatrix} 0 & 1 \\ -1 & 0 \end{pmatrix}. \tag{8}$$

The equation of motion for the Hamiltonian H_c is written as $dz^j/dt = \{H_c, z^j\}$. Notice that the quantization of the cyclotron motion (i.e., the replacement of the microscopic variables ϑ_c-v_c by ϑ_c-μ) suppresses change in μ. Liouville's theorem determines the invariant measure $d^6 z$, by which we obtain the Boltzmann distribution (6).

To extract the macroscopic hierarchy, we "separate" the microscopic variables (ϑ_c, μ) by modifying the symplectic matrix as

$$\mathcal{J}_{nc} = \begin{pmatrix} 0 & 0 & 0 \\ 0 & J & 0 \\ 0 & 0 & J \end{pmatrix}. \tag{9}$$

The Poisson bracket, determining the kinematics on the macroscopic hierarchy, is defined as $\{F, G\}_{nc} := \langle \mathcal{J}_{nc} \partial_{\boldsymbol{z}} F, \partial_{\boldsymbol{z}} G \rangle$. The macroscopic kinetic equation, $\partial_t f + \{H_c, f\}_{nc} = 0$, reproduces the familiar drift-kinetic equation (see for example [16]).

$$\begin{aligned} &\partial_t f + \{H_c, f\}_{nc} \\ &\quad = \partial_t f + v_{||} \frac{\partial f}{\partial \zeta} + F_{||} \frac{\partial f}{\partial v_{||}} + \frac{v_d}{r} \frac{\partial f}{\partial \theta} + F_\theta \frac{\partial f}{\partial P_\theta} = 0, \end{aligned}$$

where $F_{||} := -\partial_\zeta H_c$ and $F_\theta := -\partial_\theta H_c$ (the last two terms on the right-hand side vanishes because of the symmetry $\partial_\theta = 0$).

The nullity of $\mathcal{J}_{nc}$ makes the Poisson bracket $\{\,,\,\}_{nc}$ *non-canonical* [14], i.e., there is a nontrivial $C(\boldsymbol{z})$ such that $\{G, C\}_{nc} = 0$ for every G. We call

$C(\boldsymbol{z})$ a Casimir element (since $\{H_c, C\} \equiv 0$, C is an invariant). Evidently, μ is a Casimir element (more generally $C = g(\mu)$ with g being any smooth function). The level-set of $C(\boldsymbol{z}) = \mu$, a leaf of the Casimir foliation, identifies what we may call the *macroscopic hierarchy*.

By applying Liouville's theorem to the Poisson bracket $\{\ ,\ \}_{nc}$, the invariant measure on the macroscopic hierarchy is $d^4 z = d^6 z/(2\pi d\mu)$, the the total phase-space measure modulo the microscopic measure. The most probable state (statistical equilibrium) on the macroscopic ensemble must maximize the entropy with respect to this invariant measure. The variational principle is set up following the standard procedure —immersing the macroscopic hierarchy into the general phase space, and incorporating the constraints through the Lagrange multipliers: We maximize entropy $S = -\int f \log f \, d^6 z$ for a given particle number $N = \int f d^6 z$, a quasi-particle number $M = \int \mu f d^6 z$, and an energy $E = \int H_c f d^6 z$, to obtain the distribution function

$$f = f_\alpha := Z^{-1} e^{-(\beta H_c + \alpha\mu)}, \tag{10}$$

where α, β, and $\log Z - 1$ are, respectively the Lagrange multipliers on M, E, and N. In this "grand-canonical" distribution function, α is the chemical potential associated with the quasi-particles. [3]

The factor $e^{-\alpha\mu}$ in f_α yields a direct ω_c dependence of the configuration-space density:

$$\rho = \int f_\alpha \frac{2\pi\omega_c}{m} d\mu dv_d dv_{\|} \propto \frac{\omega_c(\boldsymbol{x})}{\beta\omega_c(\boldsymbol{x}) + \alpha}, \tag{11}$$

which may be compared with the density (7) evaluated for the Boltzmann distribution ($\phi = 0$ assuming charge neutrality). Notice that the Jacobian $(2\pi\omega_c/m)d\mu$ multiplying the macroscopic measure $d^4 z$ reflects the distortion of the macroscopic phase space (Casimir leaf) caused by the magnetic field; see Fig. 1.

3 Macro-scale action-angle pairs in an axisymmetric system

In an axisymmetric system, the quasi-particle motion, periodic in both the parallel and θ directions, may be described in terms of the macroscopic

---

[3] We can also derive (10) by an *energy-Casimir function.* With a Casimir element μ, we can transform the Hamiltonian as $H_c \mapsto H_\alpha := H_c + \alpha\mu$ (α is an arbitrary constant) without changing the macroscopic dynamics; H_α is called an energy-Casimir function [14]. The Boltzmann distribution with respect to H_α is equivalent to (10).

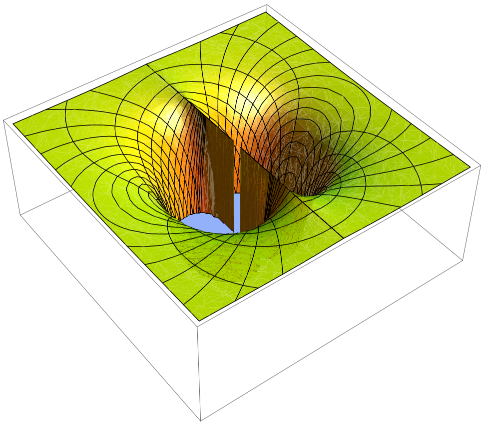

Figure 1: Jacobian weight on the foliated phase space of quasi-particles —the macroscopic hierarchy of magnetized charged particles.

action-angle pairs: $J_{\|}$-$\vartheta_{\|}$ ($:= \sin^{-1}(\zeta/\ell_{\|})$; $\ell_{\|}$ is the bounce orbit length) and P_θ ($\approx q\psi$)-θ (for a hierarchy of adiabatic invariants, see [17] and papers cited there). To find explicit expressions for the parallel action-angle variables, we invoke the Hamiltonian H_c of (3) in which the gyration action-angle pair μ-ϑ_c is "quantized" in a sense that $\omega_c = \dot{\vartheta}_c$ is given as a function of $\boldsymbol{x}$ (configuration space coordinate). Neglecting the curvature effect [4] and putting $\phi = 0$, the equation of the parallel motion reads as

$$\left\{ \begin{aligned} \frac{d\zeta}{dt} &= \frac{\partial H_c}{\partial p_{\|}} = \frac{p_{\|}}{m}, \\ \frac{dp_{\|}}{dt} &= -\frac{\partial H_c}{\partial \zeta} = -\mu \nabla_{\|}\omega_c, \end{aligned} \right. \tag{12}$$

which combine to yield

$$m\frac{d^2}{dt}\zeta = -\mu \nabla_{\|}\omega_c. \tag{13}$$

In the vicinity of $\zeta = 0$, where ω_c has a minimum on each magnetic surface, we may expand

$$\omega_c = \Omega_c(\psi) + \Omega_c''(\psi)\zeta^2/2,$$

---

[4] With $\boldsymbol{b} = \boldsymbol{B}/B$, we define $\boldsymbol{v}_{\|} = \boldsymbol{b}\cdot\boldsymbol{v}$, and hence, $\partial/\partial\zeta$ operates on $\boldsymbol{b}$. If $v_{\|}/R$ (R: curvature) is comparable to the bounce-frequency (14), we have to take into account the centrifugal force; see for example [16].

where $\Omega_c(\psi)$ is the minimum of ω_c and $\Omega_c''(\psi) := d^2\omega_c/d\zeta^2|_\psi$. In terms of the length

$$L_{||}(\psi) := \left(\frac{2\Omega_c(\psi)}{\Omega_c''(\psi)}\right)^{1/2},$$

which scales the variation of ω_c along ζ, (13) is integrated to identify the corresponding action-angle variables: $\zeta = \ell_{||}\sin\vartheta_{||}$, $\vartheta_{||} = \omega_b t$ with the bounce frequency

$$\omega_b = \sqrt{\frac{\Omega_c''(\psi)\mu}{m}} = \frac{v_\perp}{L_{||}(\psi)}. \tag{14}$$

The bounce amplitude $\ell_{||} = [2E_{||}/(m\omega_b^2)]^{1/2}$ is evaluated in terms of the parallel energy $E_{||} := (mv_{||}^2)/2|_{\zeta=0}$. Assuming $E_{||} \approx E_\perp := \mu\Omega_c$, we estimate $\ell_{||} \approx L_{||}$. The action

$$J_{||} := \frac{1}{2\pi}\oint mv_{||}d\zeta$$

is related to $E_{||} = J_{||}\omega_b$, and $dv_{||} = \left[\omega_b/(mv_{||})\right] dJ_{||}$. Using the relation $\omega_b/(mv_{||}) = v_\perp/(L_{||}mv_{||}) \approx 1/(mL_{||})$, we may write

$$dv_{||} \approx \frac{1}{mL_{||}}dJ_{||}.$$

The quantization of the parallel action-angle pair $J_{||}$-$\vartheta_{||}$, adds an additional constraint leading to a new equilibrium distribution function:

$$f_{\alpha,\gamma} = Z^{-1}e^{-(\beta H_c + \alpha\mu + \gamma J_{||})}, \tag{15}$$

and the corresponding density

$$\begin{aligned} \rho &= \int f_{\alpha,\gamma}\frac{2\pi\omega_c d\mu}{m}\frac{dJ_{||}}{mL_{||}(\psi)}dv_d \\ &\propto \frac{\omega_c(\boldsymbol{x})}{m^2}\int_0^\infty \frac{e^{-(\beta\omega_c+\alpha)\mu}d\mu}{\beta\sqrt{2\omega_c\mu/m} + \gamma L_{||}(\psi)}. \end{aligned} \tag{16}$$

Through $L_{||}(\psi)$, the density ρ acquires a dependence on ψ. We may estimate $L_{||}(\psi) \sim \psi^{-1}$.

The second part of the macroscopic dynamics is contained in the equation of motion in the θ direction. Solving the θ motion reveals that the self-organized clump of density turns out to be a *vortex*. Averaging the cyclotron and bounce motions, the Hamiltonian becomes (neglecting ϕ and approximating $P_\theta \approx q\psi$)

$$H_{cb} = \mu\omega_c(\psi,\zeta) + J_{||}\omega_b(\psi,\mu). \tag{17}$$

The governing equations for the canonical pair $q\psi$-θ

$$\begin{cases} \dfrac{d}{dt}\theta = \dfrac{\partial H_{cb}}{\partial(q\psi)} = \dfrac{\mu}{q}\dfrac{\partial\omega_c}{\partial\psi} + \dfrac{J_{||}}{q}\dfrac{\partial\omega_b}{\partial\psi} =: \omega_d, \\ \\ \dfrac{d}{dt}(q\psi) = -\dfrac{\partial H_{cb}}{\partial\theta} = 0 \end{cases} \tag{18}$$

tell us that a particle involved in the density clump rotates with a frequency ω_d.

4 Concluding remarks

We have constructed a grand-canonical distribution function f_α (or $f_{\alpha,\gamma}$) that maximizes entropy on a macroscopic leaf where the microscopic action-angle variables are abstracted as quasi-particle numbers. While embedding the macroscopic leaf in the (laboratory-frame) total phase space, the transforming Jacobian weight forces an inhomogeneous density profile in the laboratory flat space. Evidently, f_α (or $f_{\alpha,\gamma}$) is a "particular" solution of the stationary kinetic equation $\{H_c, f\}_{nc} = 0$; the general solution, freed from the maximum-entropy condition, is any arbitrary function of the constants of motion, $f = F(H_c, \mu, J_{||}, \psi)$. The solution $f = F(\mu, J_{||})$, for instance, yields a density function $\rho \propto \omega_c/L_{||}$. In a dipole magnetic field, this function scales as $\propto r^{-4}$, precisely the density profile given by Hasegawa [12, 13], and is the asymptotic form of (16) in the limit $r \to \infty$ ($\omega_c \to 0$ so that $\beta H_c \ll \alpha\mu + \gamma J_{||}$).

The chosen example of self-organization, simultaneous with maximum entropy, is distinguished from the standard narrative based on the integral fluid invariants (like a helicity) with motion taking place in the 3-dimensional space [1]. Here the domain is the 6-dimensional phase space, and the constants of motion are the adiabatic invariants (actions) associated with particle motion. The conserved actions force the trajectories in the action-angle space to be straight lines. It is the translation of these straight action-angle trajectories (microscopic) into configuration space of observation (macroscopic) that connect the micro with the macro with the emergence of structure in the latter while the former may be totally structureless.

Acknowledgment

The authors acknowledge the stimulating discussions and suggestions of Professor A. Hasegawa and Professor Philip. J Morrison. ZY's research was supported by Grant-in-Aid for Scientific Research (23224014) from MEXT-Japan. SMM's research was supported by the U.S. DOE Grant DE-FG02-04ER54742.

References

[1] A. Hasegawa, Adv. Phys. **34**, 1 (1985).

[2] M. Schulz and L. J. Lanzerotti, *Particle Diffusion in the Radiation Belts* (Springer, New York, 1974).

[3] D. H. Brautigam and J. M. Albert, J. Geophys. Res. **105**, 291 (2000).

[4] Y. Chen, G. D. Reeves, and R. H. W. Friedel, Nature Phys. **3**, 614 (2007).

[5] D. T. Garnier *et al.*, Phys. Plasmas **13**, 056111 (2006).

[6] A. C. Boxer *et al.*, Nature Phys. **6**, 207 (2010).

[7] Z. Yoshida, H. Saitoh, J. Morikawa, Y. Yano, S. Watanabe and Y. Ogawa, Phys. Rev. Lett. **104**, 235004 (2010).

[8] H. Saitoh *et al.*, Phys. Plasmas **17**, 112111 (2010).

[9] H. Saitoh *et al.*, Nucl. Fusion **51**, 063034 (2011).

[10] T.J. Birmingham, T.G. Northrop, and C.-G. Falthammar, Phys. Fluids **10**, 2389 (1967).

[11] M. Walt, Space Sci. Rev. **12**, 446 (1971).

[12] A. Hasegawa, Comments Plasma Phys. Contr. Fusion **1**, 147 (1987).

[13] A. Hasegawa, Phys. Scr. **T116**, 72 (2005).

[14] P. J. Morrison, Rev. Mod. Phys. **70**, 467 (1998).

[15] D. H. E. Dubin and T. M. O'Neil, Rev. Mod. Phys. **71**, 87 (1999).

[16] K. Nishikawa and M. Wakatani, *Plasma Physics*, 3rd ed. (Springer-Verlag, Berlin-Heidelberg, 2000), Sec. 4.3.

[17] A.J. Lichtenberg and M.A. Lieberman, *Regular and Chaotic Dynamics*, 2nd ed. (Springer-Verlag, New York, 1992), Sec. 2.3b.